Technical Physics, Vol. 48, No. 7, 2003, pp. 801–806. Translated from Zhurnal Tekhnicheskoĭ Fiziki, Vol. 73, No. 7, 2003, pp. 1–6.

THEORETICAL AND MATHEMATICAL PHYSICS

Asymptotic Laws of Superdiffusion

A. I. Saichev and S. G. Utkin

Lobachevsky State University, pr. Gagarina 23, Nizhni Novgorod, 603600 Russia

e-mail: saichev@hotmail.ru

Received December 6, 2002

Abstract—The dynamic and statistical characteristics of diffusion trajectories are studied by introducing the notion "fractional drift." An equation for the random walk probability density for cases of subdiffusion and superdiffusion is derived. A solution to this equation is constructed on the basis of the Mittag–Leffler function properties. © *2003 MAIK "Nauka/Interperiodica".*

INTRODUCTION

Anomalous diffusion, whose distinctive feature is the nonlinear growth of the root-mean-square deviation with time, has been already discovered in a variety of physical processes. This phenomenon can be adequately described in terms of fractional differential equations. In this study, we consider the case

$$\langle X^2(t)\rangle \sim t^\gamma,$$

which is typical of most phenomena where anomalous diffusion is observed: the random dynamics of Hamiltonian systems [1], the motion of particles in a plasma [2], turbulent diffusion [3], and the motion of high-energy charged particles in a crystal [4] (see also [5, 6]). Such a dependence is closely related to the violation of the central limit theorem. In the case of anomalous diffusion, it should be replaced by the Levy–Gnedenko generalized central limit theorem, which is valid when the moments of some orders are absent.

An effective method of describing diffusion phenomena is the detailed study of a model process for which the probability distribution is an exact solution to a certain diffusion equation. A prominent example is the Wiener process with its probability density adhering to the classical diffusion equation.

In this study, we construct several model processes to derive a general asymptotical equation for the random walk probability distribution that is applicable to both subdiffusion ($0 < \gamma < 1$) and superdiffusion ($1 < \gamma < 2$) cases and seek its solution.

THE KINETICS OF A DIFFUSING PARTICLE

Consider a diffusion process similar to the diffusion of gas molecules. We will concentrate on the one-dimensional case, bearing in mind that the results obtained can be easily generalized to diffusion in a multidimensional space.

Let $\{\ldots, t_0, t_1, t_2, \ldots, t_n, \ldots\}$ be the instants of "collisions," between which the velocity of a particle is constant and changes stepwise from v_k to v_{k+1} at an instant t_k. Let also $\{\tau_1, \tau_2, \ldots\}$ be the intervals between collisions: $\tau_k = t_k - t_{k-1}$. At zero time $t = 0$, the particle is taken to be at the origin ($X(t = 0) = 0$); the initial time instant is assumed to be between the collision instants t_0 and t_1 ($t_0 < 0$, $t_1 > 0$).

We are interested in the probabilistic properties of the coordinate $X(t)$ of the diffusing particle. The detailed statistics of $X(t)$ is defined by the properties of the random time intervals $\{t_1, \tau_2, \ldots, \tau_n, \ldots\}$ and velocities $\{v_1, v_2, \ldots, v_n, \ldots\}$ between collisions. Our aim, however, is to study the asymptotical "macroscopic" properties of $X(t)$ at the time scale $t \gg \langle\tau\rangle$, where $\langle\tau\rangle = \langle\tau_k\rangle$ is the mean time between collisions, which characterizes the "microscopic" scale of the problem.

For the sake of simplicity, the macroscopic properties of diffusion will be analyzed under the assumption that the measurement of the coordinate $X(t)$ is also a macroscopic process. That is, the coordinate of the particle at a given time t is taken to be its coordinate at the instant t_n of the last collision; accordingly, the coordinate $X(t_n)$ plays the role of $X(t)$. Then, the coordinate measured at a given time instant t is expressed as

$$X_-(t) = X(t_N) = \begin{cases} v_1 t_1, & t_1 > t \\ v_1 t_1 + \sum_{k=1}^{N} v_k \tau_k, & t_1 < t. \end{cases}$$

Here, $N = N(t)$ is the number of collisions within the interval $[0, t]$. The subscript "–" designates the measuring procedure applied to the coordinate of a diffusing

particle. In further consideration, the function

$$t = T(n) = \begin{cases} 0 & n = 0 \\ t_1, & n = 1 \\ t_1 + \sum_{k=1}^{N} \tau_k, & n \geq 2 \end{cases}$$

(the time to an nth jump), which is the inverse to $n = N(t)$, will be of crucial importance.

A relationship between the functions $n = N(t)$ and $t = T(n)$ is evident:

$$N(t) \geq n \Longleftrightarrow T(n) < t. \tag{1}$$

THE STATISTICS OF A DIFFUSING PARTICLE

Consider the characteristic function of the $X(t)$ process:

$$\Theta_-(u, t) = \langle e^{iuX_-(t)} \rangle. \tag{2}$$

The broken brackets mean statistical averaging over an ensemble of random instants of collisions and particle velocities between collisions. In order to represent average (2) in a form more convenient for analysis, we employ the expansion of the unit function:

$$\chi(z) = \sum_{n=0}^{\infty} \Pi_n(z), \tag{3}$$

where

$$\Pi_n(z) = \chi(z-n) - \chi(z-n-1),$$
$$\chi(z) = \begin{cases} 1, & z \geq 0 \\ 0, & z < 0. \end{cases} \tag{4}$$

With expansion (3), average (2) is recast as

$$\Theta_-(u, t) = \sum_{n=0}^{\infty} \langle e^{iuX(n)} \Pi_n(N(t)) \rangle. \tag{5}$$

Expression (5) involves one more function of integer argument:

$$X(n) = \begin{cases} v_1 t_1, & n = 1 \\ v_1 t_1 + \sum_{k=1}^{n} v_k t_k, & n \geq 2. \end{cases}$$

Let us discuss an nth term of sum (5) (at $n \geq 1$) in more detail. In view of (4), it can be written as

$$\langle e^{iuX(n)} \Pi_n(N(t)) \rangle = \langle e^{iuX(n)} \chi(N(t)-n) \rangle - \langle e^{iuX(n)} \chi(N(t)-n-1) \rangle. \tag{6}$$

Taking advantage of the equivalence of inequalities (1), we may change (6) for the expression

$$\langle e^{iuX(n)} \Pi_n(N(t)) \rangle = \langle e^{iuX(n)} \chi(t - T(n)) \rangle - \langle e^{iuX(n)} \chi(t - T(n+1)) \rangle. \tag{7}$$

Now, we apply the Laplace transformation to both parts of Eq. (5):

$$\hat{\Theta}_-(u, s) = \int_0^{\infty} e^{-st} \Theta_-(u, t) dt.$$

In view of (7), this function becomes

$$\hat{\Theta}_-(u, s) = \frac{1}{2} \sum_{n=0}^{\infty} [\langle e^{iuX(n) - sT(n)} \rangle - \langle e^{iuX(n) - sT(n+1)} \rangle]. \tag{8}$$

INDEPENDENT COLLISIONS

Assume that the velocities between the collisions are statistically independent and have the same distribution $w(v)$. The random intervals $\{t_1, \tau_2, \ldots, \tau_n, \ldots\}$ are also considered to be independent. The distribution of the time t_1 (from the beginning of observation to the first collision) is $f_+(\tau)$, and the distributions of the intervals τ_k are taken to be the same and equal to $f(\tau)$. Then, the averages in (8) split up into the product of averages and the function $\hat{\Theta}_-(u, s)$ appears as

$$\hat{\Theta}_-(u, s) = \frac{1}{s}\left[1 - \hat{f}_+(s) + \frac{g(u, s)[1 - \hat{f}(s)]}{1 - g(u, s)}\right]. \tag{9}$$

Here,

$$g_+(u, s) = \langle \hat{w}(ut_1) e^{-st_1} \rangle,$$
$$g(u, s) = \langle \hat{w}(u\tau) e^{-st} \rangle,$$
$$g_+(u) = g_+(u, 0) = \langle \hat{w}(ut_1) \rangle, \tag{10}$$
$$g(u) = g(u, 0) \langle \hat{w}(u\tau) \rangle.$$

In (9) and (10), the angular brackets stand for averaging over the statistics of the intervals t_1 and $\tau = \tau_k$; $\hat{w}(z)$ is the characteristic function of the particle's velocity:

$$\hat{w}(z) = \int_{-\infty}^{\infty} w(v) e^{ivz} dv;$$

and $\hat{f}(s)$ and $\hat{f}_+(s)$ are the Laplace transforms of the distributions $f(\tau)$ and $f_+(\tau)$.

For example,

$$\hat{f}(s) = g(0, s) = \langle e^{-s\tau} \rangle = \int_0^{\infty} f(\tau) e^{-s\tau} d\tau.$$

In the following discussion, we make use of an expression akin to (9). Setting $g_+ = g$ and $\hat{f}_+ = \hat{f}$ in (9) yields

$$\hat{\Theta}_-(u, s) = \frac{1}{s}\frac{1-\hat{f}(s)}{1-g(u, s)}. \quad (11)$$

This formula is legitimate when zero time and the instant of a collision coincide ($t_0 = 0$).

ASYMPTOTICAL LAWS OF DIFFUSION

For now, we will perform a detailed analysis of statistical results stemming from Eq. (11), which is the simplest of the expressions presented above. Note first of all that expression (11) matches the normalization condition

$$\int_{-\infty}^{\infty} W(x, t)dx = 1. \quad (12)$$

Here, $W(x, t)$ is the sought probability distribution for the coordinate of the particle, which is equal to the inverse Fourier and Laplace transform of the function $\hat{\Theta}(u, s)$. Since $g(0, s) = \hat{f}(s)$, Eq. (11) gives $\hat{\Theta}(0, s) = 1/s$, which is the Laplace transform of unity. This is a direct indication that Eq. (11) matches normalization condition (12).

Similarly, the Laplace transform of the mean square of the particle's coordinate can be found from the formula

$$\hat{X}_-^2(s) = \int_{-\infty}^{\infty} \langle X_-^2(t)\rangle e^{-st}dt = -\frac{\partial^2\hat{\Theta}(u, s)}{\partial u^2}\bigg|_{u=0}. \quad (13)$$

To calculate this Laplace transform, we expand the original function in the Taylor series in the vicinity of $u = 0$, substitute the first terms of the series into Eq. (11), and assume for simplicity that $\langle v\rangle = 0$ and $\langle v^2\rangle = \sigma^2$. Eventually, we find

$$g(u, s) = \hat{f}(s) - \frac{\sigma^2}{2}u^2\hat{f}''(s) + \ldots, \quad (14)$$

where the primes denote derivatives with respect to s.

Substituting (14) into (11) and then (11) into (13) yields the Laplace transform of the mean square in the form

$$\hat{X}_-^2(s) = \frac{\sigma^2}{s\varphi(s)}, \quad \varphi(s) = \frac{1-\hat{f}(s)}{\hat{f}''(s)}. \quad (15)$$

Our concern is with the asymptotic behavior of the mean square $\langle X^2(t)\rangle$ at $t \longrightarrow \infty$. Since it is defined by the asymptotics of Laplace transform (15) at $s \longrightarrow 0$, we will take a closer look at the behavior of Eq. (15). Let us first consider the standard situation where $f(\tau)$ tends to zero at $t \longrightarrow \infty$ so rapidly that the first two moments of the intervals between collisions are limited:

$$\langle\tau\rangle < \infty, \quad \langle\tau^2\rangle < \infty. \quad (16)$$

In this case, the following expansion is valid:

$$\hat{f}(s) = 1 - \langle\tau\rangle s + \frac{1}{2}\langle\tau^2\rangle s^2 + \ldots \longrightarrow \hat{f}''(s) = \langle\tau^2\rangle + \ldots. \quad (17)$$

Substituting (17) into (15), we have

$$\hat{X}_-^2(s) \sim \sigma^2\frac{\langle\tau^2\rangle}{\langle\tau\rangle}\frac{1}{s^2}, \quad s \longrightarrow 0. \quad (18)$$

Using the tabulated formula for the Laplace transform

$$\frac{1}{s^\gamma} \rightleftharpoons \frac{t^{\gamma-1}}{\Gamma(\gamma)}, \quad (19)$$

we get the conventional linear law of diffusion from (18):

$$\langle X_-^2(t)\rangle \sim Dt, \quad t \longrightarrow \infty, \quad D = \sigma^2\frac{\langle\tau^2\rangle}{\langle\tau\rangle}. \quad (20)$$

Anomalous superdiffusion, which we are interested in, takes place when one or both inequalities (16) are violated. For this to occur, the distribution of the intervals between collisions must have a power asymptotics:

$$f(\tau) \sim \kappa^\beta\tau^{-\beta-1}, \quad \tau \longrightarrow \infty, \quad 0 < \beta \le 2.$$

Here, κ has the dimension of time. We consider the cases $0 < \beta < 1$ and $1 < \beta < 2$ separately (the cases $\beta = 1$ and 2, which include logarithmic corrections, need special analysis). In the first case, the desired asymptotics looks like

$$\hat{f}(s) \sim 1 - \kappa^\beta\frac{\Gamma(1-\beta)}{\beta}s^\beta, \quad s \longrightarrow 0, \quad 0 < \beta < 1; \quad (21)$$

for the second derivative, we have

$$\hat{f}''(s) \sim \kappa^\beta\Gamma(2-\beta)s^{\beta-2}, \quad s \longrightarrow 0, \quad 0 < \beta < 1. \quad (22)$$

Substituting (21) and (22) into (15) yields

$$\hat{X}_-^2(s) \sim \sigma^2\beta(1-\beta)\frac{1}{s^3}, \quad s \longrightarrow 0, \quad 0 < \beta < 1.$$

The inverse Laplace transform of this asymptotics is found by standard formula (19):

$$\langle X_-^2(t)\rangle \sim \sigma^2\frac{\beta(1-\beta)}{2}t^2, \quad t \longrightarrow \infty, \quad 0 < \beta < 1. \quad (23)$$

The result obtained has a clear physical meaning. For $0 < \beta < 1$, collisions occur so rarely that the motion of a particle can be considered as collision-free, i.e., uniform:

$$X(t) \sim vt, \quad \langle X^2(t)\rangle \sim \sigma^2t^2.$$

Let us now turn to the case $1 < \beta < 2$. The corresponding asymptotics can be written as

$$\hat{f}(s) \sim 1 - \langle\tau\rangle s + \kappa^\beta \frac{\Gamma(2-\beta)}{\beta(\beta-1)} s^\beta, \quad s \longrightarrow 0, \quad 1 < \beta < 2. \tag{24}$$

The asymptotics of $\hat{f}$" is also described by formula (22). Substituting Eqs. (24) and (22) into (15), we have

$$\hat{X}_-^2(s) \sim \sigma^2 \frac{\kappa^\beta}{\langle\tau\rangle} \Gamma(2-\beta) \frac{1}{s^{4-\beta}}, \quad s \longrightarrow 0, \quad 1 < \beta < 2.$$

Using tabulated formula (19), we finally arrive at

$$\langle X_-^2(t)\rangle \sim \sigma^2 \frac{\kappa^\beta}{\langle\tau\rangle} \frac{\Gamma(2-\beta)}{\Gamma(4-\beta)} t^{3-\beta}.$$

Thus, at $1 < \beta < 2$, the mean square of the particle's coordinate obeys the law of superdiffusion:

$$\langle X_-^2(t)\rangle \sim t^\gamma, \quad \gamma = 3 - \beta.$$

As would be expected, this function transforms into collision-free formula (23) and formula (20) of linear diffusion at $\beta = 1$ and 2, respectively.

FRACTIONAL DIFFUSION EQUATION

We now derive an equation for $W(x, t)$. To do this, we replace the functions in formula (11) by their expansions (14), (22), and (21) or (24) for $0 < \beta < 1$ or $1 < \beta < 2$, respectively. In the first case, this leads to

$$s^2 \hat{\Theta}_-(u, s) + Du^2 \hat{\Theta}_-(u, s) = s,$$

$$D = \frac{\beta(1-\beta)}{2} \sigma^2, \quad 0 < \beta < 1.$$

Applying inverse Fourier and Laplace transformations, we come to the desired equation:

$$\frac{\partial^2 W(x, t)}{\partial t^2} = D \frac{\partial^2 W(x, t)}{\partial x^2} + \delta'(t)\delta(x).$$

It can be solved via the inverse Fourier–Laplace transformation of the function

$$\hat{\Theta}_-(u, s) = \frac{s}{s^2 + Du^2} \rightleftharpoons W(x, t)$$

$$= \frac{1}{2}[\delta(x - \sqrt{D}t) + \delta(x + \sqrt{D}t)].$$

In the second case ($1 < \beta < 2$), Eq. (11) leads to the asymptotic equation

$$s^\gamma \hat{\Theta}_-(u, s) + \frac{\sigma^2}{2\delta} u^2 \hat{\Theta}_-(u, s) = s^{\gamma-1},$$

$$\delta = \frac{\langle\tau\rangle}{\kappa^{3-\gamma}\Gamma(\gamma-1)}, \quad \gamma = 3 - \beta.$$

Hence, it follows that

$$\frac{\partial^\gamma W(x, t)}{\partial t^\gamma} = \frac{\sigma^2}{2\delta} \frac{\partial^2 W(x, t)}{\partial x^2} + \frac{t^{-\gamma}}{\Gamma(1-\gamma)} \chi(t)\delta(x).$$

By properly choosing the time and coordinate scales, $\tilde{t} = t/\delta^{1/\gamma}$ and $\tilde{x} = x\sqrt{2}/\sigma$ with β replaced by $\gamma = 3 - \beta$, this equation can be reduced to the equation

$$\frac{\partial^\gamma \tilde{W}(\tilde{x}, \tilde{t})}{\partial \tilde{t}^\gamma} = \frac{\partial^2 \tilde{W}(\tilde{x}, \tilde{t})}{\partial \tilde{x}^2} + \frac{\tilde{t}^{-\gamma}}{\Gamma(1-\gamma)} \chi(\tilde{t})\delta(\tilde{x}), \tag{25}$$

which will be referred to as the fractional-diffusion equation.

FRACTIONAL DRIFT

Before we solve the fractional-diffusion equation obtained in the previous section, it would be useful to discuss the properties of the fractional drift process. To begin with, we introduce β-stable time $t(\varrho)$ with the stable parent distribution $f_\beta(t)$:

$$t(\varrho) = \lim_{n \to \infty} \sum_{k=1}^{\lfloor \varrho n \rfloor} T_k^{(1/n)}.$$

Here, $T_k^{(1/n)}$ are infinitely divisible nonnegative random quantities for which the Laplace transforms of the probability densities are equal to $\hat{f}^{1/n}(s)$, where $\hat{f}(s) = \exp[-s^\beta]$ is the parent Laplace transform ($0 < \beta < 1$). In view of the stability of $f_\beta(t)$, the probability density of the random function $t(\varrho)$ is given by

$$f_\beta(t, \varrho) = \frac{1}{\varrho^{1/\beta}} f_\beta\left(\frac{t}{\varrho^{1/\beta}}\right). \tag{26}$$

Let us consider a function $\varrho(t)$ that is inverse to $t(\varrho)$. Given the probability density $f(t, \varrho)$ of the values of $t(\varrho)$, we determine the probability density $Q(\varrho, t)$ of the values of the inverse function $\varrho(t)$. The relation between $t(\varrho)$ and $\varrho(t)$ is based on the equivalence of the inequalities

$$t(\varrho) < t \rightleftharpoons \varrho(t) \geq \varrho.$$

In probabilistic terms, the same can be written as

$$F(t, \varrho) = P(t(\varrho) < t) = P(\varrho(t) \geq \varrho) = \int_\varrho^\infty Q(\varrho', t) d\varrho'.$$

This allows one to find the desired relationship between the probability densities of the random processes $t(\varrho)$ and $\varrho(t)$:

$$Q(\varrho, t) = -\frac{\partial F(t, \varrho)}{\partial \varrho} = -\frac{\partial}{\partial \varrho} \int_{-\infty}^t f(t', \varrho) dt'. \tag{27}$$

Substituting distribution (26) into (27), we find the probability density of the inverse function $\rho(t)$:

$$Q_\beta(\rho, t) = \frac{1}{t^\beta} Q_\beta\left(\frac{\rho}{t^\beta}\right),$$
$$Q_\beta(\rho) = \frac{1}{\beta\rho^{1+1/\beta}} f_\beta\left(\frac{1}{\rho^{1/\beta}}\right). \quad (28)$$

As follows from the definition of $Q_\beta(\rho)$ and the Laplace transform of the distribution $f_\beta(t)$,

$$\exp(-\rho s^\beta) = \beta\int_0^\infty e^{-st}\frac{\rho}{t^{\beta+1}} Q_\beta\left(\frac{\rho}{t^\beta}\right)dt. \quad (29)$$

Let a quantity $\mathcal{R}$ be characterized by the distribution $Q_\beta(\rho)$. We will seek the moments of $\mathcal{R}$ by multiplying (29) by $\rho^{\nu-1}$ and integrating the result with respect to ρ from 0 to ∞. Eventually, we obtain

$$\frac{\Gamma(\nu)}{s^{\nu\beta}} = \beta\langle\mathcal{R}^\nu\rangle\int_0^\infty e^{-st}t^{\nu\beta-1}dt = \beta\langle\mathcal{R}^\nu\rangle\frac{\Gamma(\nu\beta)}{s^{\nu\beta}}.$$

Finally, we have

$$\langle\mathcal{R}^\nu\rangle = \int_0^\infty \rho^\nu Q_\beta(\rho)d\rho = \frac{\Gamma(\nu)}{\beta\Gamma(\nu\beta)} = \frac{\Gamma(\nu+1)}{\Gamma(\nu\beta+1)}.$$

Consequently, the Taylor expansion of the Laplace transform of the distribution $Q_\beta(\tau)$ has the form

$$\hat{Q}_\beta(s) = \langle s^{-s\mathcal{R}}\rangle = \sum_{n=0}^\infty \frac{(-1)^n}{\Gamma(n\beta+1)}s^n = E_\beta(-s). \quad (30)$$

Here, we use the Mittag–Leffler function $E_\beta(s)$, which is defined as

$$E_\beta(z) = \sum_{n=0}^\infty \frac{z^n}{\Gamma(n\beta+1)}.$$

The function $E_\beta(-(t/\tau)^\beta)$ is known [6–8] to be a solution to equation

$$\frac{d^\beta\Phi(t)}{dt^\beta} + \tau^{-\beta}\Phi(t) = \frac{t^{-\beta}}{\Gamma(1-\beta)}\chi(t), \quad 0<\beta<1. \quad (31)$$

This equation is a fractional generalization of the ordinary differential equation

$$\frac{d\Phi(t)}{dt} = -\frac{1}{\tau}\Phi(t),$$

which has the exponential solution $e^{-t/\tau} = E_1(-t/\tau)$.

It follows from Eqs. (28) and (30) that the Laplace transform of the distribution $Q(\rho, t)$ with respect to ρ is given by

$$Q(\rho, t) = \langle e^{-\gamma\rho(t)}\rangle = E_\beta(-\gamma t^\beta). \quad (32)$$

Let us consider a random process $\mathcal{X}(t) = \rho(t)$ with the probability density

$$W(x, t) = \frac{1}{t^\beta} Q_\beta\left(\frac{\rho}{t^\beta}\right). \quad (33)$$

This process will be called fractional drift. According to (32), its characteristic function can be written as

$$\Theta(u, t) = \langle e^{iu\rho(t)}\rangle = E_\beta(iut^\beta).$$

As follows from Eq. (31), this function satisfies the equation

$$\frac{\partial^\beta\Theta}{\partial t^\beta} = iu\Theta + \frac{t^{-\beta}}{\Gamma(1-\beta)}\chi(t). \quad (34)$$

The introduction of the fractional drift process enables one to find the probability density of the fractional diffusion $\mathcal{X}(t) = V(\rho(t))$. Here, $V(\rho)$ is the Wiener process ($\langle V^2(\rho)\rangle = 2\rho$). Clearly, the desired probability density obeys fractional diffusion equation (25) and the characteristic function, the equation

$$\frac{d^\beta\Theta}{dt^\beta} + u^2\Theta = \frac{t^{-\beta}}{\Gamma(1-\beta)}\chi(t).$$

We will solve it using the fractional drift characteristic function. This function is divided into two (even and odd) components,

$$\Theta = \Theta_{\text{even}} + \Theta_{\text{odd}},$$

and is substituted into Eq. (34). This yields two equations:

$$\frac{d^\beta\Theta_{\text{even}}}{dt^\beta} = iu\Theta_{\text{odd}} + \frac{t^{-\beta}}{\Gamma(1-\beta)}\chi(t),$$
$$\frac{d^\beta\Theta_{\text{odd}}}{dt^\beta} = iu\Theta_{\text{even}}.$$

Taking the β-order derivative of the first equation with respect to t and excluding the odd component, we arrive at a closed equation for $Q_{\text{even}}(u, t)$:

$$\frac{\partial^{2\beta}\Theta_{\text{even}}}{\partial t^{2\beta}} + u^2\Theta_{\text{even}} = \frac{t^{-2\beta}}{\Gamma(1-2\beta)}\chi(t).$$

Accordingly, the even component of the fractional drift probability density

$$W_{\text{even}}(x, t) = \frac{1}{2}[W(x, t) + W(-x, t)] = \frac{1}{2}W(|x|, t) \quad (35)$$

satisfies the equation

$$\frac{\partial^{2\beta}W_{\text{even}}}{\partial t^{2\beta}} = \frac{\partial^2 W_{\text{even}}}{\partial x^2} + \frac{t^{-2\beta}}{\Gamma(1-2\beta)}\chi(t)\delta(x),$$

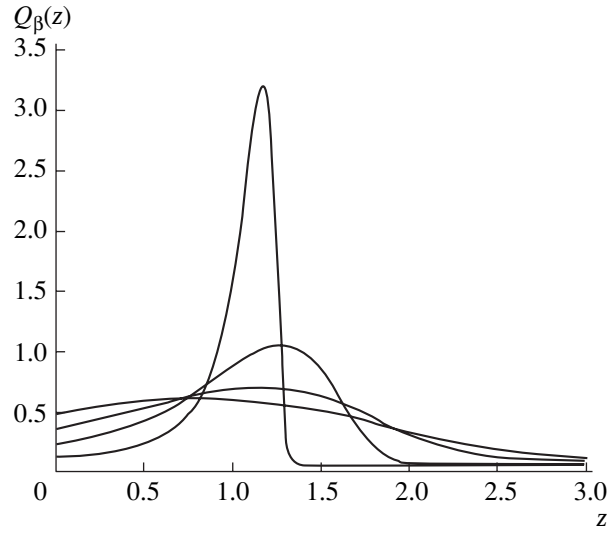

Distributions $Q_\beta(z)$ with $\beta = 0.65$–0.95. The exponential drop of the functions with z assures the finiteness of the moments $\langle \mathcal{R}^\nu \rangle$.

which is reduced to Eq. (25) when β is replaced by $\gamma/2$. Thus, in view of Eqs. (33) and (35), the solution of fractional diffusion equation (25) can be written in the form

$$W(x, t) = \frac{1}{2t^{\gamma/2}} Q_{\gamma/2}\left(\frac{|x|}{t^{\gamma/2}}\right).$$

The distribution $Q_{\gamma/2}(z)$ is found by applying inverse Fourier transformation to $E_{\gamma/2}(iu)$ $(1 < \gamma < 2)$. From the properties of the Mittag–Leffler function, one finds that

$$Q_{\gamma/2}(z) = \frac{2}{\pi\gamma} \mathrm{Re} \int_0^\infty \exp(ixz + x^{2/\gamma} e^{-i\pi/\gamma}) dx.$$

The two last equalities define the probability density of superdiffusion. The figure depicts the function $Q_\beta(z)$ for different β.

CONCLUSIONS

A typical diffusion process, the random walk of a particle, is described under the assumption that its velocity between collisions is constant. Based on the asymptotic properties of its characteristic function, the statistical characteristics of the process are obtained and the macroscopic kinetic equations are derived. The fractional drift process constructed makes it possible to solve the fractional diffusion equation in terms of the Mittag–Leffler function.

ACKNOWLEDGMENTS

This work was supported by the program "Scientific Schools of Russia" (project no. 00-15-96619).

REFERENCES

1. G. M. Zaslavsky, M. Edelman, and B. Niyazov, Chaos **7**, 159 (1997).
2. V. Yu. Zaburdaev and K. V. Chukbar, Zh. Éksp. Teor. Fiz. **121**, 299 (2002) [JETP **94**, 252 (2002)].
3. J. Klafter, M. F. Shlesinger, and G. Zumofen, Phys. Today **49** (2), 33 (1996).
4. V. V. Uchaĭkin, Teor. Mat. Fiz. **115**, 154 (1998).
5. E. Barkai, Phys. Rev. E **63**, 046118 (2001).
6. R. Metzler and J. Klafter, Phys. Rep. **339**, 1 (2000).
7. A. I. Saichev and G. M. Zaslavsky, Chaos **7**, 753 (1997).
8. A. I. Saichev and W. A. Woyczynski, *Distributions in the Physical and Engineering Sciences* (Birkhäuser, Boston, 1997), Vol. 1.

Translated by A. Sidorova

Technical Physics, Vol. 48, No. 7, 2003, pp. 807–812. Translated from Zhurnal Tekhnicheskoĭ Fiziki, Vol. 73, No. 7, 2003, pp. 7–12.

THEORETICAL AND MATHEMATICAL PHYSICS

Generation of Thermonuclear Energy by Fusing Hydrogen and Lithium Atoms

V. E. Tyrsa and L. P. Burtseva

Engineering Institute, Autonomous University of Baja California, 21280 Mexicali, Mexico

e-mail: v_tyrsa@iing.mxl.uabc.mx

Received December 24, 2002

Abstract—A method of designing a thermonuclear reactor based on the modified Cockroft–Walton accelerator, where the lithium–proton fusion was first observed, is considered. It is proposed that the reactor have the form of a spherical capacitor with a point lithium cathode used as the inner electrode and a spherical anode, as the outer electrode. The interelectrode space is filled with hydrogen. A high-voltage electric pulse applied to the electrodes is used as a driver. The reactor parameters providing an ion temperature of 100 keV and a proton flux of 8.6×10^{15} W/cm^2 to the cathode are determined. The basic elements of a system generating thermonuclear fusion energy, including those of the energy conversion chamber with a fusion chamber inside, are listed, and possible applications of the system are indicated. © *2003 MAIK "Nauka/Interperiodica".*

INTRODUCTION

Two approaches to controllable thermonuclear fusion are studied today: the confinement of a high-temperature plasma using a toroidal magnetic field (tokamak) [1, 2] and inertial confinement fusion (ICF) [3]. The latter is the subject of investigation in this paper.

The simplest ICF scheme is as follows. A spherical capsule (target) filled with either deuterium or a deuterium–tritium mixture is synchronously irradiated by driving pulses from high-power lasers arranged spherically symmetrically. The nuclear fusion occurs as a limited-power thermonuclear explosion [3]. In the Laboratory for Laser Energetics, University of Rochester (USA), 60 Omega lasers with a total energy of 40 kJ are used [4]. The laser intensity at a target diameter of 1 mm and a pulse duration of 1 ns is 1.27×10^{15} W/cm^2. In the Russian Federal Nuclear Center (Sarov) [5], an intensity of 10^{15}–10^{16} W/cm^2 was achieved using the Iskra-5 facility with 12 lasers generating 0.3-ns pulses.

The ideas underlying controllable thermonuclear synthesis have not been changed for many years, and research is currently aimed at increasing the dimensions of the facilities and quantity of the reactants. The project of International Thermonuclear Experimental Reactor (giant tokamak) and the National Ignition Facility Program (USA) [1] are examples. Tens of billions of dollars have already been spent on these programs. It is, however, clear even now that the National Ignition Facility Program will not be much more profitable than its predecessors, at least because the efficiency of converting the laser pump energy into radiant energy for pulse durations of about 1 ns is smaller than 1% [6]. It is easy to check that the energy used to initiate the reaction is comparable to the released energy.

In this paper, the design of a system generating thermonuclear fusion energy with a reactor based on the modification of the Cockroft–Walton experiment is proposed.

FIELD LINE FOCUSING IN A SPHERICAL CAPACITOR

The artificial conversion of lithium nuclei due to accelerated protons,

$$^{7}_{3}\mathrm{Li} + p \longrightarrow 2^{4}_{2}\mathrm{He} + 17.35\ \mathrm{Mev}, \qquad (1)$$

was first performed in the Cockroft–Walton accelerator.

The Cockroft–Walton experiment has demonstrated (1) the feasibility of energy production in reaction where lithium atoms bombarded by hydrogen nuclei are converted to helium nuclei and (2) the possibility of using an electrostatic accelerator as a driver. In this experiment, only a few particles out of millions enter into the nuclear reaction because of the low density of the accelerated proton beam; therefore, the bombardment of a solid target by accelerated nuclei is considered to be inefficient for producing fusion energy.

If electrostatic field lines are focused on a point lithium target in this experiment, the Cockroft–Walton accelerator becomes a prototype of an electric-driver reactor. This idea can be implemented in a reactor made in the form of a spherical capacitor. Its capacitance is found by the formula [7]

$$C = 4\pi\varepsilon\varepsilon_0\frac{rR}{R-r}, \qquad (2)$$

where $\varepsilon_0 = 8.85 \times 10^{-12}$ C/(V m) is the electric constant; ε is the relative permittivity; and r and R are the inner and outer electrode radii, respectively.

1063-7842/03/4807-0807$24.00

The potential difference U across the electrodes of a spherical capacitor induces the charge

$$Q = CU. \quad (3)$$

The electrostatic field intensity E_r on the cathode surface of a spherical capacitor is

$$E_r = \frac{U}{r}\frac{R}{R-r}. \quad (4)$$

The electrostatic field intensity between the cathode surface and a sphere placed at a distance x from the center inside the capacitor is given by

$$E_x = \frac{1}{4\pi\varepsilon_0\varepsilon}\frac{Q}{x^2}, \quad r < x < R.$$

In view of (2) and (3),

$$E_x = U\frac{r}{x^2}\frac{R}{R-r}, \quad r < x < R. \quad (5)$$

In the limit $x = R$,

$$E_x = E_R = U\frac{r}{R}\frac{1}{R-r}. \quad (6)$$

The ratio of the intensities $k = E_r/E_R = R^2/r^2$ shows that the field is nonuniform and its intensity at the cathode is k times higher than that at the anode at a fixed potential difference U across the electrodes. The field lines of the nonuniform electrostatic field between the electrodes of a regularly shaped spherical capacitor are straight lines propagating from the anode inner surface to the vertex of the solid angle 4π sr in the center of the cathode; i.e., they are focused on the cathode. The smaller the radius of the cathode, the higher the field line density on its surface at a constant potential difference across the electrodes.

CONDITIONS FOR CARRYING OUT THE THERMONUCLEAR REACTION

The focused electrostatic field is a field of conservative forces. If not too high, this field does not influence the state of cathode atoms. When protons are injected into the interelectrode space, as in the Cockroft–Walton experiment, they are accelerated in the focused field and gain kinetic energy. Under certain conditions, this energy on the cathode surface may be sufficient for lithium–proton fusion to occur. Because of the high energy of fusion, it seems impossible to produce it continuously over a small cathode area; therefore, it is appropriate to conduct this process as limited-power thermonuclear explosions at regular intervals, as is done in other relevant systems. The explosion energy is accumulated and used over a period of time.

In the method proposed, a high-voltage pulse (HVP) from a special power pulser is applied to the electrodes of the spherical capacitor. The electrostatic field energy is then injected into the space between the electrodes for a short time. This energy must be sufficient to (1) generate hydrogen ions and (2) accelerate these ions to velocities at which the protons and lithium atoms of the cathode fuse together. Since the hydrogen–lithium fusion is planned to have the form of a destructive thermonuclear explosion, the reactor should be placed into a special energy-conversion chamber (ECC), where the fusion energy is converted to the energy of superheated steam (see figure).

We impose restrictions on the energy released in the explosion, thereby considering the fusion energy given. On this basis, we will determine (1) the masses of the reactants; (2) the dimensions of the reactor, which depend on of these masses; (3) the potential difference and the electrostatic field intensity that are necessary for (i) the ionization of hydrogen atoms and (ii) the acceleration of the protons to energies sufficient for proton–lithium fusion; and (4) the reaction time, the HVP leading edge time, and the intensity of the proton flux to the cathode.

MASSES OF THE REACTANTS AND DIMENSIONS OF THE FUSION CHAMBER

Let the energy to be released in the course of the thermonuclear reaction be equal to $W_r = 1$ MJ. In view of the energy 17.35 MeV, which is released in reaction (1) of nuclear fusion, and under the assumption that 100% of the lithium atoms are involved in the reaction, the number of lithium atoms in the target is given by

$$N = \frac{W_r 6.24\times10^{18}}{17.35\times10^6} = 3.60\times10^{17}.$$

Here, 6.24×10^{18} eV = 1 J. From the formula $N = m/(M \times 1u)$, which relates the number of atoms N to atomic weight M and the mass m of a material [7], we find the lithium mass m_{Li}:

$$m_{\mathrm{Li}} = M_{\mathrm{Li}} 1u N_{\mathrm{Li}} = 4.19\times10^{-9}\ \mathrm{kg},$$

since $M_{\mathrm{Li}} = 7.016$ and $1u = 1.66\times10^{-27}$ kg for ^{7}Li. For the lithium density $\rho = 530$ kg/m^3, the volume of the lithium cathode is

$$V = \frac{m_{\mathrm{Li}}}{\rho} = 7.91\times10^{-12}\ \mathrm{m}^3.$$

The cathode radius is found from the formula for the volume of a sphere: $r = 0.124$ mm. Let us find the hydrogen volume V_{H} at standard pressure $p_n = 0.1$ MPa for the number of hydrogen atoms taken to be equal to $N_{\mathrm{H}} \geq N = 3.60\times10^{17}$. In view of the Loschmidt constant $N_{\mathrm{L}} = 2.69\times10^{25}$ m^{-3},

$$V_{\mathrm{H}} = \frac{N_{\mathrm{H}}}{2N_{\mathrm{L}}} = 6.69\times10^{-9}\ \mathrm{m}^3.$$

The distance between the electrodes may be decreased by increasing the hydrogen pressure. For example, let p_r be equal to 1 MPa. Then, the hydrogen volume is

$$V_{\mathrm{Hp}} = V_{\mathrm{H}}\frac{p_n}{p_r} = 6.69\times10^{-10}\ \mathrm{m}^3,$$

according to the Boyle–Mariotte law.

The radius of the anode sphere is then equal to $R = \sqrt[3]{(3\times6.69\times10^{-10})/(4\times3.14)} = 5.43\times10^{-4}$ m. Actually, the radius of the anode must be larger if one takes into account the volumes of the lithium cathode and insulated metallic rod to which the cathode is attached. However, in our case, this is of no significance.

HYDROGEN IONIZATION

An HVP applied to the reactor's electrodes generates a rapidly increasing interelectrode electrostatic field with an intensity $E(t)$ rising with the HVP amplitude. In this field, each hydrogen atom gains an additional induced energy [7]

$$W_{\mathrm{ind}}(t) = \frac{\alpha E(t)^2}{2}, \qquad (7)$$

where α is the atomic polarizability.

In the case of hydrogen, $\alpha = 7\times10^{-41}$ F m^2. When the energy $W_{\mathrm{ind}}(t)$ becomes equal to the total energy of the hydrogen electron occupying the orbit with $n = 1$ ($W_{\mathrm{ind}}(t) = W_{\mathrm{H}} \le 13.60$ eV), the atom ionizes. The energy required for the ionization of N_{H} hydrogen atoms is

$$W_{i\mathrm{H}} = N_{\mathrm{H}}W_{\mathrm{H}} = 3.60\times10^{17}\times13.60\times1.60\times10^{-19} = 0.78\ \mathrm{J}. \qquad (8)$$

From (7), we find the threshold intensity of ionization:

$$E_{\mathrm{th}} = \sqrt{\frac{2W_{\mathrm{H}}}{\alpha}} = \sqrt{\frac{2\times13.61\times1.60\times10^{-19}}{7\times10^{-41}}} = 2.49\times10^{11}\ \mathrm{V/m}.$$

It is reasonable to propose that the field intensity needed to ionize all the hydrogen, i.e., to break it down, is substantially lower. The threshold intensity $E_{\mathrm{th}} = 2.49\times10^{11}$ V/m corresponds to an individual hydrogen atom rather than to many atoms that are in thermal motion and, hence, are partially excited. The Earth's atmosphere serves as an indirect confirmation of this statement. The field intensity at which air breaks down is $E_{\mathrm{th,\,a}} \approx 3\times10^6$ V/m at normal atmospheric pressure. The Earth's atmosphere consists of oxygen and nitrogen with insignificant amounts of other gases and water vapor. The ionization potentials of oxygen ($W_{\mathrm{O}} = 13.56$ eV), nitrogen ($W_{\mathrm{N}} = 14.47$ eV), and hydrogen atoms ($W_{\mathrm{H}} = 13.60$ eV) are comparable. The polarizability of an oxygen atom is $\alpha = 3.5\times10^{-40}$ F m^2. The threshold field intensity for oxygen that is found with (7) is $E_{\mathrm{th,\,O}} = 1.13\times10^{11}$ V/m. The parameters of nitrogen atoms are similar. Therefore, the threshold ionization intensity for hydrogen may be taken to be equal to the intensity of air breakdown $E_{\mathrm{th}} \approx E_{\mathrm{th,\,a}} \approx 6.3\times10^6$ V/m. If necessary, this value may be refined experimentally.

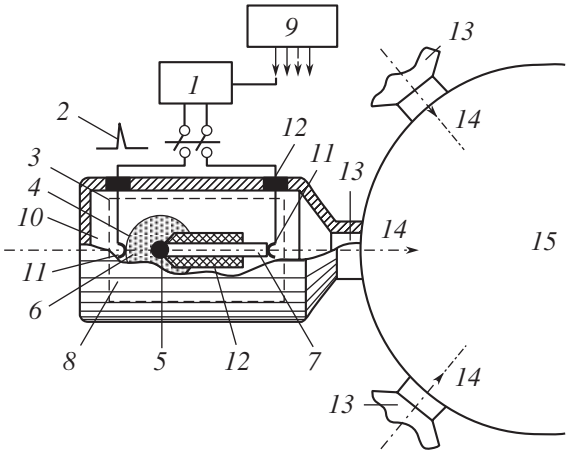

(*1*) Driver (power pulser), (*2*) high-voltage pulse, (*3*) fusion chamber (reactor), (*4*) metallic anode, (*5*) lithium cathode, (*6*) hydrogen, (*7*) electrode, (*8*) energy-conversion chamber, (*9*) control system, (*10*) water, (*11*) contact, (*12*) insulator, (*13*) discharge outlet receiver, (*14*) superheated steam, and (*15*) receiver.

PROCESS PARAMETERS IN THE FUSION CHAMBER AFTER HYDROGEN IONIZATION

The force acting on an electric charge q_i placed in an electrostatic field of intensity $\mathbf{E}$ is $\mathbf{F}_i = q_i\mathbf{E}$. Collinear forces $\mathbf{F}_i$ act on electrons and protons appeared as a result of ionization. At a certain time instant t_x, these charged particles will start moving in the opposite directions with different velocities. The direction of their motion coincides with that of the field lines.

The work needed to accelerate an electron is expressed as $A = e^+U$, where $e^+ = 1.60\times10^{-19}$ C is the proton charge and U is the potential difference between the anode and cathode. It is believed that the proton kinetic energy W_{p} becomes sufficient to overcome the Coulomb barrier at a temperature $T \approx 10^9$ K. Since 1 keV $= 11.6\times10^6$ K,

$$W_{\mathrm{p}} = \frac{T}{11.6\times10^6} = 86.21\ \mathrm{keV}.$$

Therefore, the work needed to accelerate a proton may be taken to be equal to the above kinetic energy: $A = e^+U = W_p = 86.21$ keV. Hence, the potential differ-

ence required is

$$U = \frac{W_p}{e^+} = 86\,207 \text{ V}.$$

The effective cross sections of the reactions approach the maximum value at $W_p \approx 100$ keV [7]. Therefore, the amplitude of the HVP applied to the reactor's electrodes is taken to be $U \le 100$ kV. Then, according to (4) and (6), the field intensity at the cathode is

$$E_r = \frac{10^5 \times 5.43 \times 10^{-4}}{1.24 \times 10^{-4}(5.43 \times 10^{-4} - 1.24 \times 10^{-4})} = 1.045 \times 10^9 \text{ V/m}$$

and at the anode,

$$E_R = \frac{10^5 \times 1.24 \times 10^{-4}}{5.43 \times 10^{-4}(5.43 \times 10^{-4} - 1.24 \times 10^{-4})} = 5.45 \times 10^7 \text{ V/m}.$$

These values exceed the field intensity of hydrogen ionization conventionally taken above.

The energy needed to transfer protons to the cathode is written as

$$W_{\Sigma p} = N_H W_p = 3.60 \times 10^{17} \times 10^5 \times 1.60 \times 10^{-19} = 5.76 \times 10^3 \text{ J}.$$

The field energy spent on the ionization of hydrogen atoms (expression (8)), as well as on the transfer of electrons to the anode and protons to the cathode, is given by

$$W_{\Sigma H} = W_{iH} + 2W_{\Sigma p} = 0.78 + 2 \times 5.76 \times 10^3 = 11\,520.78 \le 1.20 \times 10^4 \text{ J}.$$

Finally, the efficiency of the reactor is

$$\eta = \frac{W_r - W_{\Sigma H}}{W_r} = \frac{10^6 - 1.20 \times 10^4}{10^6} = 0.988.$$

A most important parameter of the reactor is the reaction time. We will determine it as follows. Let a charged particle move along the x axis. The one-dimensional equation for a particle with a charge e and a mass m moving in a uniform field of constant intensity E has the form

$$m\frac{d^2x}{dt^2} = eE. \quad (9)$$

In our case, the electrostatic field is nonuniform. Its intensity depends on the coordinate x varying between r and R (see (5)). To simplify the calculations, we will use a certain conventional value $\bar{E}$ of the field intensity: $\sim E_{R\text{Li}} \le \bar{E} < E_{r\text{Li}}$. Assuming that the initial proton velocity is $v_0 = 0$, we find from Eq. (9) both the velocity $v(t) = e\bar{E}t/m_p$ and the path x_i traveled by each of the particles over the time t_i

$$x_i = \frac{e\bar{E}}{2m_p}t_i^2.$$

The mean path to the cathode traveled by a proton over the time t_i is given by

$$\bar{x} = \frac{R-r}{2} = \frac{1}{N_H}\sum_{N_H} x_i = \frac{e\bar{E}}{2m_p N_H}\sum_{N_H} t_i^2.$$

We assume that the intervals t_i are uniformly distributed along the field line in the interval $[0, \tau_p]$. The time $t_p = t_{i\max}$ is the time taken for a proton to pass from one electrode to the other with the velocity $v(t)$ when $v_0 = 0$.

The arithmetic mean of the intervals t_i is written as $\bar{t} = (\sum_{N_H} t_i)/N_H = \tau_r/2$. We put $\sum_{N_H} t_i^2 = \sum_{N_H}(\bar{t} - \Delta t_i)^2$, where $\Delta t_i = \bar{t} - t_i$. Bearing in mind that $\sum_{N_H} \Delta t_i \approx 0$ and, for uniformly distributed intervals, $\sum_{N_H}(\Delta t_i)^2 = N_H \tau_p^2/12$, we find

$$\bar{x} = \frac{e\bar{E}}{3m_p}\tau_p^2 = \frac{R-r}{2}.$$

Hence,

$$\tau_p = \sqrt{\frac{3m_p(R-r)}{2e\bar{E}}}.$$

In the worst case, taking $\bar{E} = E_R = 5.45 \times 10^7$ V/m, we arrive at

$$\tau_p = \sqrt{\frac{3 \times 4.19 \times 10^{-4} \times 1.007 \times 1.66 \times 10^{-27}}{2 \times 1.60 \times 10^{-19} \times 5.45 \times 10^7}} = 3.47 \times 10^{-10} \text{ s}.$$

We will consider this time as the reaction time in the reactor, since all protons arrive at the cathode in this time and the nuclei fuse within hundreds of femtoseconds [5].

The intensity of the proton flux toward the lithium cathode is

$$I = \frac{W_{\Sigma p}}{\tau_p S}.$$

Here, $S = 4\pi r^2 = 4 \times 3.14 \times (1.24 \times 10^{-4})^2 = 1.93 \times 10^{-7}$ m^2 $= 1.93 \times 10^{-3}$ cm^{-2} is the surface area of the

spherical cathode. Calculations yield

$$I = \frac{5.76 \times 10^3}{3.47 \times 10^{-10} \times 1.93 \times 10^{-3}} = 8.60 \times 10^{15}\ \text{W/cm}^2.$$

More detailed estimates show that the actual cathode surface area where the field lines are focused may differ from the surface area of the sphere. However, this point does not change the order of the proton flux density value at the cathode.

TIME PARAMETERS OF THE VOLTAGE PULSE

The HVP rise time is defined by the time parameters of the reaction. Hydrogen atoms may stay excited for the time $\tau \approx 10^{-8}$ s [7]. If an electron on the orbit $n = 1$ gains energy, it will pass on the orbit $m = \infty$ (i.e., leave the atom) when the energy gained reaches the value $\Delta W \leq W_H = 13.60$ eV. In accordance with the Heisenberg uncertainty principle [7], the transition time Δt and the energy ΔW are related by the expression $\Delta W \Delta t \approx \hbar$, where $\hbar = 1.055 \times 10^{-34}$ J s is the Planck constant. Hence, we can assume that the ionization time of an atom is $\Delta t \approx \hbar/W_H = 1.055 \times 10^{-34}/(13.60 \times 1.60 \times 10^{-19}) = 4.85 \times 10^{-17}$ s. At first sight, it appears that all hydrogen atoms must ionize over the same time because of their similarity. However, this is not true and the total ionization time for all the atoms subjected to the field simultaneously will be longer than Δt, because the electrons in hydrogen atoms occupy the orbits at random at any time instant. If the electron velocity on the orbit is $\Delta v_x = 10^6$ m/s and the atom size is $\Delta x = 10^{-10}$ m [7], the period of electron motion over the orbit may be considered as the maximum time delay between the ionization of a particular atom and the time instant the ionization starts: $\Delta t_x = \pi \Delta x/\Delta v_x = 3.14 \times 10^{-10}/10^6 = 3.14 \times 10^{-16}$ s. Therefore, the total ionization time of the atomic ensemble is equal to $\Delta t_\Sigma \leq \Delta t + \Delta t_x = 3.63 \times 10^{-16}$ s. This time falls in the worst-case interval $\tau_p \leq 0.35$ ns, since the protons start moving toward the cathode immediately after the beginning of ion generation. Thus, the HVP rise time must be comparable to $\tau_p \leq 0.35$ ns and its duration must be $t_p \geq 2\tau_p = 0.7$ ns.

CONVERSION OF THE ATOMIC ENERGY TO THE ENERGY OF SUPERHEATED STEAM

ECCs for laser ICF are being developed. One idea is that the radiation due to thermonuclear microexplosions heats up the spherical walls of the chamber and water-filled pipes built in the walls absorb the heat. The drawback of such a solution is the highly (by many orders of magnitude) different rates of nuclear and thermal processes. Therefore, the spherical surface of the chamber has to be distant enough from the radiation source to avoid the melting of the chamber walls subjected to high-power radiation pulses during the fusion. This fact would restrict the applicability of the system if the problem of laser ICF is successfully solved.

The ECC suggested in this work is a metal vessel filled with water and air. The reactor mounted on a special holder is placed into the water. The ECC has two electrodes to feed a pulser and a steam outlet firmly closed by the exhaust valve. Such a design is to some extent similar to the charge chamber in a piece of ordnance as regards durability and reusability when it is reloaded by new reactors and water.

A manipulator sets the ECC into the position in which the electrodes are connected to the pulser and the outlet, to one port of the steam receiver. The receiver may have several ports for connecting several ECCs depending on the power of the steam turbine connected to the receiver through a secondary converter.

On the command of the control system, an HVP is applied to the reactor to initiate the explosive thermonuclear reaction. The fusion-induced radiant energy evaporates water in the ECC almost instantly. In the course of the isochoric process in the ECC, the steam may be heated up above the critical temperature. As the steam parameters approach given values, it will be transferred to the receiver. The manipulator detaches the ECC from the receiver and sends it to reload.

DISCUSSION AND CONCLUSIONS

(1) The problem of inertial confinement fusion has advanced from the area of fundamental physics to the stage of engineering solutions. The calculations show that the thermonuclear reaction between hydrogen and lithium can be carried out by applying a high-voltage pulse to the electrodes of the reactor made in the form of a small spherical capacitor. The pulse-induced electrostatic field provides the impact ionization of the hydrogen atoms and their instantaneous fusion with lithium nuclei at the reactor's cathode. The driver energy required to carry out the reaction is applied to the reactor directly without being converted into other forms. That is why this energy is two orders of magnitude smaller than the energy consumed by a laser driver, in which less than 1% of the pumping energy is converted to the radiant energy [6].

(2) If the equipment to be used with the reactor admits an increase in the reactor energy W_r (explosion energy) by a factor of n, then the increase is provided by a proportional increase in the masses of the reactants (reactor volume) and in the power applied to the reactor from the pulser (i.e., driver). The amplitude of the HVP applied to the electrodes and the proton flux intensity at the cathode remain constant in this case. The linear sizes of the reactor and the reaction time (pulse duration) τ_p will increase by a factor of $\sqrt[3]{n}$. For instance, if

W_r = 10 MJ in the example considered, then n = 10 and $\sqrt[3]{10}$ = 2.15. Laser-driven ICF lacks such capabilities.

(3) Current technologies can easily turn the method into an industry platform. Accordingly, the introduction of this method of energy production into industry would require much smaller time and much lower costs than in the case of laser-driver ICF. The reactants needed for the fusion are readily available. Lithium is sold on the market at $220 per 1 kg [8].

(4) The method proposed does not alter the current technology of power generation owing to the direct conversion of nuclear fusion energy to the energy of superheated steam. It only adds a new system of steam generation. After being introduced into industry, this technology can be immediately used at new and already existing thermal and nuclear power plants. The new technology is simpler than laser-driven ICF. Unlike laser ICF, it allows one to control the energy in a wide range; therefore, it is also applicable to marine crafts and land vehicles.

REFERENCES

1. General Atomic Fusion Group, http://fusion.gat.com/icf/concept/
2. Fusion Energy Research, http://www-afrd.lbl.gov/fusion.html.
3. J. D. Lindl, *Inertial Confinement Fusion: The Quest for Ignition and Energy Gain Using Indirect Drive* (AIP, Springer-Verlag, New York, 1997).
4. About OMEGA, http://www.lle.rochester.edu/03_omega/_03omega.html.
5. I. A. Andryushin, A. K. Borodin, Yu. K. Zavalishin, *et al.*, *Sarov: The Nuclear Center of Russia* (Sarov, 2000).
6. N. G. Basov, I. G. Lebo, V. B. Rozanov, *et al.*, Kvantovaya Élektron. (Moscow) **25**, 327 (1998).
7. V. E. Kuz'michev, *Laws and Formulas of Physics* (Kiev, 1989).
8. *Handbook of Chemistry and Physics: A Ready-Reference Book of Chemical and Physical Data. The Elements* (CRC, 1995–1996, 76th ed.), p. 4.

Translated by M. Fofanov

Technical Physics, Vol. 48, No. 7, 2003, pp. 813–821. Translated from Zhurnal Tekhnicheskoĭ Fiziki, Vol. 73, No. 7, 2003, pp. 13–20.

GASES AND LIQUIDS

On Acoustic Radiation from a Nonlinearly Vibrating Charged Drop

A. P. Gaibov and A. I. Grigor'ev

Demidov State University, Sovetskaya ul. 14, Yaroslavl, 150000 Russia

e-mail: grig@uniyar.ac.ru

Received July 10, 2002; in final form, December 18, 2002

Abstract—An expression for the time-varying shape of an incompressible liquid drop immersed in a compressible dielectric medium is derived to the second-order approximation in drop vibration amplitude. It is shown that the acoustic radiation spectrum of the drop has a monopole component, which makes a considerable contribution to the integral radiation intensity. Its appearance is associated with the time variation of the zeroth-mode vibration amplitude, showing up in the second order of smallness. *© 2003 MAIK "Nauka/Interperiodica".*

(1) An incompressible liquid drop vibrating in a compressible medium may radiate acoustic waves. To an approximation linear in vibration amplitude, the zeroth and first modes do not contribute to the vibration spectrum [1]. When the drop volume is invariable, the fundamental mode dominates in the spectrum of acoustic radiation [2]. The dipole radiation, which is caused by the excitation of the translational mode, appears only in the second-order approximation in vibration amplitude, when the spectrum of modes responsible for the initial deformation has two adjacent modes (for example, jth and $j + 1$th). This is because the amplitude of the translational mode excited in the second order of smallness is proportional to the Clebsch–Gordan coefficients, which are other than zero only if adjacent modes are among initially excited modes [3, 4].

The idea of acoustic radiation by a vibrating drop stems from the fact that each vibration mode is responsible for a distortion of the equilibrium (spherical) drop surface in the form $\sim P_n(\mu)\exp(i\omega_n t)$, where $\mu \equiv \cos\theta$, θ is the polar angle of the spherical coordinate system, $P_n(\mu)$ are Legendre polynomials, and ω_n is the frequency of an nth mode. The periodical motion of the drop surface causes periodical disturbances of the pressure in the compressible environment, that is, generates acoustic waves. The vibration frequencies for drops of sizes typical of natural liquid-drop systems (fogs, clouds, and rain) fall into the frequency range of acoustic waves and long-wavelength ultrasonic waves (see, for example, [5, 6] and the references cited therein). The charge present on the drops, the deviation of their shape from spherical, their movement relative to the ambient medium, and the influence of their viscosity all cause a shift of the capillary vibration spectrum toward lower frequencies [4, 5, 7], that is, toward the range of acoustic waves perceptible to the ear.

(2) Let a perfectly conducting drop of equilibrium radius R, density ρ_1, surface tension coefficient γ, and charge Q be immersed in an ideal compressible dielectric medium with a density ρ_2 and permitivity ε. The sound velocity in the environment is c.

We use the spherical coordinate system with the origin at the drop center and assume that, at the initial time instant, a perturbation $\xi(\theta, t)$ of the equilibrium (spherical) drop shape has the form $\xi(\theta, t) = \alpha P_2(\mu)$, where α is the small perturbation amplitude ($\alpha/R \ll 1$).

The equation of the vibrating drop surface at any time instant is written in the form

$$r = R + \xi(\theta, t); \quad (|\xi|/R \le \alpha/R \ll 1).$$

Flows inside the drop and in the environment are assumed to be potential with velocity potentials ψ_1 and ψ_2, respectively.

Mathematically the problem is stated as

$$\Delta\phi = 0; \quad \Delta\psi_1 = 0; \quad \frac{1}{c^2}\frac{\partial^2\psi_2}{\partial t^2} - \Delta\psi_2 = 0;$$

$$r = R + \xi: \frac{\partial\psi_1}{\partial n} = \frac{\partial\psi_2}{\partial n}; \quad \frac{\partial\psi_1}{\partial r_1} = \frac{\partial\xi}{\partial t} + \frac{1}{r^2}\frac{\partial\psi_1}{\partial\theta}\frac{\partial\xi}{\partial\theta};$$

$$\Delta p - \rho_1\frac{\partial\psi_1}{\partial t} - \rho_1\frac{1}{2}(\nabla\psi_1)^2 + \rho_2\frac{\partial\psi_2}{\partial t} - \frac{\rho_2}{2c^2}\left(\frac{\partial\psi_2}{\partial t}\right)$$

$$+ \frac{1}{2}\rho_2(\nabla\psi_2)^2 + \frac{\varepsilon}{8\pi}(\nabla\phi)^2 = \gamma\nabla\cdot\mathbf{n};$$

$$\phi = \text{const};$$

$$r \longrightarrow \infty: \frac{\partial\psi_2}{\partial t} + ik\psi_2 = o\left(\frac{1}{r}\right);$$

1063-7842/03/4807-0813$24.00

$$t = 0: r = R + \xi_0 + \alpha P_2(\mu); \quad \psi_1 = 0;$$

$$-\frac{1}{4\pi}\oint_S (\mathbf{n}\cdot\nabla\phi)ds = Q,$$

$$S = [r = R + \xi(\theta, t),\ 0 \le \theta \le \pi,\ 0 \le \varphi \le 2\pi];$$

$$\int_V r^2 dr \sin\theta d\theta d\varphi = \frac{4}{3}\pi R^3,$$

$$V = [0 \le r \le R + \xi(\theta, t),\ 0 \le \theta \le \pi,\ 0 \le \varphi \le 2\pi];$$

$$\int_V e_r r^3 dr \sin\theta d\theta d\varphi = 0.$$

Here, ϕ is the electric field potential; $\mathbf{n}$ is the unit vector directed normally to the drop surface, Δp is the difference between the hydrostatic pressures inside the drop and in the environment, γ is the surface tension coefficient, and ξ_0 is a normalizing constant that is determined from the constancy condition for the drop volume. In the first row of this set, Δ stands for the Laplacian operator.

We will solve the problem using conventional methods of the perturbation theory (see, e.g., [4, 6, 8–10]).

The time dependences of ψ_1 and ψ_2 are introduced through the factor $\exp(i\omega t)$. Then, the wave equation for the potential ψ_2 can be transformed into the Helmholtz equation

$$\Delta\psi_2 + k^2\psi_2 = 0.$$

(3) We will seek the velocity potentials inside and outside the drop, the perturbation of the drop surface, and the electrical potential in the form of expansions

$$\psi_1 = \psi_1^{(1)} + \psi_1^{(2)}; \quad \psi_2 = \psi_2^{(1)} + \psi_2^{(2)}; \quad \xi = \xi^{(1)} + \xi^{(2)};$$
$$\phi = \phi^{(0)} + \phi^{(1)} + \phi^{(2)}, \tag{1}$$

where the superscripts denote the order of smallness in α/R.

Since $\phi^{(0)}$ is the electric potential of the unperturbed drop surface, it must be equal to $\phi^{(0)} = Q/\varepsilon r$; then, the expansion for electrical potential ϕ can be written in the form

$$\phi = \frac{Q}{\varepsilon r} + \phi^{(1)} + \phi^{(2)}. \tag{2}$$

Taking into account (1) and (2) and expanding the boundary conditions into the series in α/R in the vicinity of the unperturbed drop surface $r = R$ and leaving the expansion terms up to the second order of smallness inclusive, we decompose the problem into subproblems of the first and second orders of smallness.

The first approximation is stated as follows:

$$\Delta\phi^{(1)} = 0; \quad \Delta\psi_1^{(1)} = 0; \quad \Delta\psi_2^{(1)} + k^2\psi_2^{(1)} = 0;$$

$$r = R: \frac{\partial\psi_1^{(1)}}{\partial r} = \frac{\partial\psi_2^{(1)}}{\partial r}; \quad \frac{\partial\psi_1^{(1)}}{\partial r} = \frac{\partial\xi^{(1)}}{\partial t};$$

$$-\rho_1\frac{\partial\psi_1^{(1)}}{\partial t} + \rho_2\frac{\partial\psi_2^{(1)}}{\partial t} + P_e^{(1)} = P_L^{(1)};$$

$$P_e^{(1)} = -\frac{Q}{4\pi R^2}\left[\frac{\partial\phi^{(1)}}{\partial r} + 2\xi^{(1)}\frac{Q}{\varepsilon R^2}\right];$$

$$P_L^{(1)} = \gamma\left[-\frac{2\xi^{(1)}}{R^2} - \frac{1}{R^2}\Delta_\Omega\xi^{(1)}\right];$$

$$\phi^{(1)} + \xi^{(1)}\frac{\partial\phi^{(0)}}{\partial r} = 0;$$

$$-\frac{1}{4\pi}\int_0^{2\pi}\int_0^{\pi}\varepsilon\left[R^2\frac{\partial\phi^{(1)}}{\partial r}\right]\sin\theta d\theta d\varphi = 0;$$

$$r \to \infty: \frac{\partial\psi_2^{(1)}}{\partial r} + ik\psi_2^{(1)} = o\left(\frac{1}{r}\right);$$

$$t = 0: \xi^{(1)} = \alpha P_2(\mu); \quad \psi_1^{(1)} = 0.$$

The second approximation is given by

$$\Delta\phi^{(2)} = 0; \quad \Delta\psi_1^{(2)} = 0; \quad \Delta\psi_2^{(2)} + k^2\psi_2^{(2)} = 0;$$

$$r = R: \frac{\partial\psi_1^{(2)}}{\partial r} + \xi^{(1)}\frac{\partial^2\psi_1^{(1)}}{\partial r^2} - \frac{1}{R^2}\frac{\partial\psi_1^{(1)}}{\partial\theta}\frac{\partial\xi^{(1)}}{\partial\theta}$$
$$= \frac{\partial\psi_2^{(2)}}{\partial r} + \xi^{(1)}\frac{\partial^2\psi_1^{(1)}}{\partial r^2} - \frac{1}{R^2}\frac{\partial\psi_2^{(1)}}{\partial\theta}\frac{\partial\xi^{(1)}}{\partial\theta};$$

$$\frac{\partial\psi_1^{(2)}}{\partial r} + \xi^{(1)}\frac{\partial^2\psi_1^{(1)}}{\partial r^2} = \frac{1}{R^2}\frac{\partial\xi^{(1)}}{\partial\theta}\frac{\partial\psi_1^{(1)}}{\partial\theta} + \frac{\partial\xi^{(2)}}{\partial\theta};$$

$$-\rho_1\left[\frac{\partial\psi_1^{(2)}}{\partial t} + \xi^{(1)}\frac{\partial^2\psi_1^{(1)}}{\partial r\partial t}\right] - \frac{1}{2}\rho_1(\nabla\psi_1^{(1)})^2$$
$$+ \rho_2\left[\frac{\partial\psi_2^{(2)}}{\partial t} + \xi^{(1)}\frac{\partial^2\psi_2^{(1)}}{\partial r\partial t}\right] - \frac{\rho_2}{2c^2}\left(\frac{\partial\psi_2^{(1)}}{\partial t}\right)^2$$
$$+ \frac{1}{2}\rho_2(\nabla\psi_2^{(1)})^2 + P_e^{(2)} = P_L^{(2)};$$

$$P_e^{(2)} = \frac{\varepsilon}{8\pi}\left(\frac{\partial\phi^{(1)}}{\partial r}\right)^2 - \frac{Q}{4\pi R^2}\left[\frac{\partial\phi^{(2)}}{\partial r} + 2\xi^{(2)}\frac{Q}{\varepsilon R^3}\right]$$
$$+ \frac{5Q^2}{4\pi\varepsilon R^6}\xi^{(1)^2} + 2\xi^{(1)}\frac{Q}{4\pi R^3}\frac{\partial\phi^{(1)}}{\partial r}$$
$$- \xi^{(1)}\frac{Q}{4\pi R^2}\frac{\partial^2\phi^{(1)}}{\partial r^2} + \frac{\varepsilon}{8\pi R^2}\left(\frac{\partial\phi^{(1)}}{\partial\theta}\right)^2;$$

$$P_L^{(2)} = -\gamma\frac{2\xi^{(2)}}{R^2} - \gamma\frac{1}{R^2}\Delta_\Omega\xi^{(2)} + \gamma\frac{2}{R^3}\xi^{(1)}(\xi^{(1)} + \Delta_\Omega\xi^{(1)});$$

$$\phi^{(2)} + \xi^{(1)}\frac{\partial\phi^{(1)}}{\partial r} - \xi^{(2)}\frac{Q}{\varepsilon R^2} + \xi^{(1)^2}\frac{Q}{\varepsilon R^3} = 0;$$

$$-\frac{1}{4\pi}\int_0^{2\pi}\int_0^{\pi}\varepsilon\left[R^2\frac{\partial\phi^{(2)}}{\partial r} + R^2\frac{\partial^2\phi^{(1)}}{\partial r^2}\xi^{(1)} - \frac{\partial\xi^{(1)}}{\partial\theta}\frac{\partial\phi^{(1)}}{\partial\theta} + 2R\xi^{(1)}\frac{\partial\phi^{(1)}}{\partial r}\right]\sin\theta d\theta d\varphi;$$

$$r \longrightarrow \infty: \frac{\partial\psi_2^{(2)}}{\partial r} + ik\psi_2^{(2)} = o\left(\frac{1}{r}\right);$$

$$t = 0: \xi^{(2)} = -\frac{1}{5}\frac{\alpha^2}{R}; \quad \psi_1^{(2)} = 0.$$

Here, Δ_Ω is the angular part of the Laplacian operator.

(4) The first-order problem is easy to solve [11]. A solution is sought in the form of the expansions

$$\psi_1^{(1)} = A_0 + \sum_{n=1}^{\infty} A_n r^n P_n(\mu);$$

$$\psi_2^{(1)} = B_0 h_0^{(2)}(kr) + \sum_{n=1}^{\infty} B_n h_n^{(2)}(kr) P_n(\mu);$$

$$\phi^{(1)} = F + \frac{F_0}{r} + \sum_{n=1}^{\infty} F_n r^{-(n+1)} P_n(\mu);$$

$$\xi^{(1)} = a_0 + \sum_{n=1}^{\infty} a_n P_n(\mu),$$

where $h_n^{(2)}(x)$ are the spherical Hankel functions of the second kind. The final form of the solution [2] is

$$\xi^{(1)} = \kappa_2\exp(-\omega_2^* t)\cos(\omega_2 t + \beta_2)P_2(\mu);$$

$$\psi_1^{(1)} = -\frac{1}{2R}\kappa_2\exp(-\omega_2^* t)[\omega_2\sin(\omega_2 t + \beta_2) + \omega_2^*\cos(\omega_2 t + \beta_2)]r^2 P_2(\mu);$$

$$\psi_2^{(1)} = \kappa_2\exp(-\omega_2^* t)\{M\cos[\omega_2 t + \beta_2 - k(r-R)] + X\sin[\omega_2 t + \beta_2 - k(r-R)]\}P_2(\mu) + \{[\beta_2 - k(r-R)]\}P_2(\mu);$$

$$\phi^{(1)} = \kappa_2\frac{QR}{\varepsilon r^3}\exp(-\omega_2^* t)\cos(\omega_2 t + \beta_2)P_2(\mu).$$

Expressions for the coefficients κ_2, ω_2, ω_2^*, β_2, M, and X, which are dependent on the physical parameters of the problem, are presented in Appendix 1.

(5) A solution to the second-order problem will be sought by means of direct expansion [12]. We substitute $\psi_1^{(1)}$, $\psi_2^{(1)}$, and $\xi^{(1)}$ found by solving the first-order problem into the boundary conditions for the second-order problem to obtain a set of inhomogeneous boundary conditions:

$$\frac{\partial\psi_1^{(2)}}{\partial r} - \frac{\partial\psi_2^{(2)}}{\partial r} = \kappa_2^2\exp(-2\omega_2^* t)\{[K_0 + K_0\cos(\Theta) + K_1\sin(\Theta)] + [K_2 + K_2\cos(\Theta) + K_3\sin(\Theta)]P_2(\mu) + [K_4 + K_4\cos(\Theta) + K_5\sin(\Theta)]P_4(\mu)\}; \quad (3)$$

$$\frac{\partial\psi_1^{(2)}}{\partial r} - \frac{\partial\xi^{(2)}}{\partial t} = \frac{1}{2R}\kappa_2^2\exp(-2\omega_2^* t)[\omega_2\sin(\Theta) + \omega_2^*\cos(\Theta)]\left(-\frac{2}{5} - \frac{1}{7}P_2(\mu) + \frac{54}{35}P_4(\mu)\right); \quad (4)$$

$$\Theta = (2\omega_2 t + 2\beta_2);$$

$$-\rho_1\frac{\partial\psi_1^{(2)}}{\partial t} + \rho_2\frac{\partial\psi_2^{(2)}}{\partial t} - \frac{Q}{4\pi R^2}\left[\frac{\partial\phi^{(2)}}{\partial r} + 2\xi^{(2)}\frac{Q}{\varepsilon R^3}\right] + \gamma\frac{2\xi^{(2)}}{R^2} + \gamma\frac{1}{R^2}\Delta_\Omega\xi^{(2)} = \kappa_2^2\exp(-2\omega_2^* t) \times\left\{\frac{1}{5}[\mathfrak{B}_0 + \mathfrak{B}_1\cos(\Theta) + \mathfrak{B}_2\sin(\Theta)] + \frac{1}{7}[\mathfrak{B}_3 + \mathfrak{B}_4\cos(\Theta) + \mathfrak{B}_5\sin(\Theta)]P_2(\mu) + \frac{1}{35}[\mathfrak{B}_6 + \mathfrak{B}_7\cos(\Theta) + \mathfrak{B}_8\sin(\Theta)]P_4(\mu)\right\}; \quad (5)$$

$$\phi^{(2)} - \xi^{(2)}\frac{Q}{\varepsilon R^2} = \kappa_2^2\frac{Q}{\varepsilon R^3}\exp(-2\omega_2^* t)[1 + \cos(\Theta)] \times\left(\frac{1}{5} + \frac{2}{7}P_2(\mu) + \frac{18}{35}P_4(\mu)\right);$$

$$-\frac{1}{4\pi}\int_0^{2\pi}\int_0^{\pi}\varepsilon\left[R^2\frac{\partial\phi^{(2)}}{\partial r}\right]\sin(\theta)d\theta d\varphi = 0. \quad (6)$$

Expressions for the coefficients K_0, K_1,…, K_5 and $\mathfrak{B}_0$, $\mathfrak{B}_1$, …, $\mathfrak{B}_8$ are given in Appendix 2.

The second-order corrections $\psi_1^{(2)}$, $\psi_2^{(2)}$, and $\xi^{(2)}$ will be sought in the same form as in the first-order

problem:

$$\psi_1^{(2)} = A_0^{(2)} + \sum_{n=1}^{\infty} A_n^{(2)} r^n P_n(\mu);$$

$$\psi_2^{(2)} = B_0^{(2)} h_0^{(2)}(kr) + \sum_{n=1}^{\infty} B_n^{(2)} h_n^{(2)}(kr) P_n(\mu);$$

$$\phi^{(2)} = F^{(2)} + \frac{F_0^{(2)}}{r} + \sum_{n=1}^{\infty} F_n^{(2)} r^{-(n+1)} P_n(\mu); \quad (7)$$

$$\xi^{(2)} = a_0^{(2)} + \sum_{n=1}^{\infty} a_n^{(2)} P_n(\mu).$$

Substituting (7) into (3)–(6) subject to the radiation condition and the initial condition for the second-order problem yields a set of equations for the coefficients $A_0^{(2)}$, $A_n^{(2)}$, $B_0^{(2)}$, $B_n^{(2)}$, $F^{(2)}$, $F_0^{(2)}$, $F_n^{(2)}$, $a_0^{(2)}$, and $a_n^{(2)}$. Solving this set gives an expression for the generatrix of an axisymmetric vibrating drop as a function of time:

$$\xi^{(2)}(\mu, t) = a_0^{(2)}(t) P_0(\mu) + a_2^{(2)}(t) P_2(\mu) + a_4^{(2)}(t) P_4(\mu);$$

$$a_0^{(2)}(t) = -\frac{1}{10R}\kappa_2^2 \exp(-2\omega_2^* t)[1 + \cos(\Theta)] + \frac{1}{10R}[-2\alpha^2 + \kappa_2^2 \cos(2\beta_2) + \kappa_2^2];$$

$$a_2^{(2)}(t) = \kappa_2^{(2)} \exp(-\omega_2^* t)\cos(\omega_2 t + \beta_2^{(2)}) - \kappa_2^{(2)} \exp(-2\omega_2^* t)[N + L\cos(\Theta) + M\sin(\Theta)]; \quad (8)$$

$$a_4^{(2)}(t) = \kappa_4^{(2)} \exp(-\omega_4^* t)\cos(\omega_4 t + \beta_4^{(2)}) - \kappa_2^{(2)} \exp(-2\omega_2^* t)[\Re + \Omega\cos(2\omega_2 t + \beta_2) + \Im\sin(2\omega_2 t + \beta_2)].$$

Expressions for the coefficients $\kappa_2^{(2)}$, $\beta_2^{(2)}$, $\kappa_4^{(2)}$, $\beta_4^{(2)}$, N, L, M, $\Re$, Ω, and $\Im$ are given in Appendix 2.

It is easy to see that the initial perturbation of the fundamental mode causes the zeroth and fourth modes to excite because of the second-order interaction. Of most interest for the study of acoustic radiation from a vibrating drop is the time dependence of the zeroth mode amplitude. This allows us to consider of the drop as a monopole acoustic radiator. The time dependence of the zeroth mode amplitude follows from the constancy of the vibrating drop volume.

(6) From expressions (8), it is seen, in particular, that the zeroth mode amplitude is quadratic in the small parameter α; that is, this mode is excited because of the mode interaction only in the second order of smallness, whereas the problem linear in α gives the time-invariable amplitude of the zeroth mode. It is also seen that the component of the amplitude periodically varying with time and generating acoustic radiation decays with time with the damping decrement ω^*. The decay depends on the acoustic radiation loss of the capillary vibrations.

For numerical calculations, we assume, as in [2, 3], that $\rho_1 = 1$ g/cm^3, $\rho_2 = 1.3 \times 10^{-3}$ g/cm^3, $\gamma = 73$ dyn/cm, $\alpha = 0.1R$, $kR \ll 1$, $R = 250$ μm, and the concentration of rain drops of this radius is $N = 0.3$ cm^{-3}. Let us also assume that the drop charge is much less than the limiting one in terms of Rayleigh stability ($W \ll 1$) [6, 13].

The expression for the power J of the acoustic radiation emitted by a sphere vibrating with an amplitude a_0 has the form [12]

$$J = \frac{2\pi\rho_2 R^4 \omega^4 a_0^2}{c(1 + \omega^2 R^2/c^2)}. \quad (9)$$

From (8) and (9), it follows that $a_0 \approx 10^{-3}R$ and the power of the monopole acoustic radiation emitted by a single drop with the above parameters at a frequency of $\omega \approx 6 \times 10^3$ s^{-1} is on the order of 10^{-7} erg/s. At the same time, the power of the acoustic radiation emitted by a rainy space of 1 km^3 equals ≈3 W, that is, considerably exceeds both the power of the dipole acoustic radiation associated with the excitation of the translational mode [3] and the power of quadrupole acoustic radiation generated by the fundamental mode in the approximation linear in oscillation amplitude [2]. The integral monopole acoustic radiation at the boundary of such a cloud has a loudness of ≈60 dB, which corresponds to the loudness of human speech. The charge on the drop surface lowers the acoustic radiation frequency, as follows from (8).

CONCLUSIONS

We analyzed nonlinear capillary vibrations of an ideal incompressible liquid drop immersed in an ideal compressible medium. In the approximation quadratic in initial deviation of the drop shape from equilibrium spherical, it was found that the spectrum of modes induced by nonlinear interaction has the zeroth mode. Because of this, the drop can be viewed as a monopole radiator of acoustic waves. The intensity of the monopole radiation in the audio frequency range substantially exceeds the linear intensity of the acoustic radiation associated with the excitation of higher vibration modes. From this it follows that the monopole acoustic radiation dominates in the total intensity of the acoustic radiation from liquid-drop systems, such as a rainy space.

APPENDIX 1

The coefficients involved in the solution to the first-order problem are as follows:

$$\omega_n^2 = (n-1)(n+2)\frac{\gamma}{R^3}(1-W_n)$$

$$\times\left[\frac{\rho_1}{n} - \frac{\rho_2 h_n^{(2)}(rR)}{kRh_{n-1}^{(2)}(kR) - (n+1)h_n^{(2)}(kR)}\right];$$

$$W_n = \frac{Q^2}{4\pi\varepsilon R^3(n+2)\gamma}; \quad \omega_n = \mathrm{Re}(\sqrt{\tau_n + i\tau_n^*});$$

$$\omega_n^* = \mathrm{Im}(\sqrt{\tau_n + i\tau_n^*}) \ (n = 2, 4);$$

$$\tau_2 = \mathrm{Re}(\omega_n^2) = \frac{4\gamma(1-W_2)}{R^3}[2\rho_1\Lambda_1 + 4\rho_2\Lambda_2]$$

$$\times[\Lambda_1\rho_1^2 + 4\Lambda_2\rho_1\rho_2 + 4\Lambda_3\rho_2^2]^{-1};$$

$$\tau_2^* = \mathrm{Im}(\omega_n^2) = \frac{4\gamma(1-W_2)}{R^3}[4\rho_2 k^5 R^5]$$

$$\times[\Lambda_1\rho_1^2 + 4\Lambda_2\rho_1\rho_2 + 4\Lambda_3\rho_2^2]^{-1};$$

$$\Lambda_1 = (81 + 9k^2R^2 - 2k^4R^4 + k^6R^6);$$

$$\Lambda_2 = (27 + 6k^2R^2 + k^4R^4);$$

$$\lambda_3 = (9 + 3k^2R^2 + k^4R^4);$$

$$\kappa_2 = \alpha^2\sqrt{1 + (\omega_2^*/\omega_2)^2}; \quad \beta_2 = \arctan\left(-\frac{\omega_2^*}{\omega_2}\right);$$

$$M = (\Lambda_4\omega_2 + \Lambda_5\omega_2^*)\Lambda_6^{-1};$$

$$X = (\Lambda_5\omega_2 - \Lambda_4\omega_2^*)\Lambda_6^{-1};$$

$$\Lambda_4 = (3k^3R^3 - k^5r^2R^3 - 27kR + 9k^3r^2R - 12k^3rR^2 + 27kr);$$

$$\Lambda_5 = (-12k^2R^2 + 4k^4r^2R^2 + 27 - 9k^2r^2 - 3k^4rR^3 + 27k^2rR);$$

$$\Lambda_6 = \left[k^8r^3R^4\left(\frac{1}{k^2R^2} - \frac{2}{k^4R^4} + \frac{9}{k^6R^6} + \frac{81}{k^8R^8}\right)\right].$$

APPENDIX 2

The coefficients involved in the solution to the second-order problem are expressed as

$$K_0 = \left(\frac{1}{10}\mathfrak{U} - \frac{6}{10R^2}\mathfrak{M} - \frac{2}{10R}\omega_2^*\right);$$

$$K_1 = \left(\frac{1}{10}\mathfrak{R} - \frac{6}{10R^2}\mathfrak{Z} - \frac{2}{10R}\omega_2^*\right);$$

$$K_2 = \left(\frac{1}{7}\mathfrak{U} - \frac{3}{7R^2}\mathfrak{M} - \frac{1}{14R}\omega_2^*\right);$$

$$K_3 = \left(\frac{1}{7}\mathfrak{R} - \frac{3}{7R^2}\mathfrak{Z} - \frac{1}{14R}\omega_2\right);$$

$$K_4 = \left(\frac{9}{35}\mathfrak{U} + \frac{36}{35R^2}\mathfrak{M} + \frac{27}{35R}\omega_2^*\right);$$

$$K_5 = \left(\frac{9}{35}\mathfrak{R} + \frac{36}{35R^2}\mathfrak{Z} + \frac{27}{35R}\omega_2\right);$$

$$\mathfrak{B}_0 = \left(\frac{1}{2}(\rho_1-\rho_2)(\omega_2^{*2} - \omega_2^2) + \frac{1}{4}(\rho_1-\rho_2)(\omega_2^2 + \omega_2^{*2})\right.$$

$$+ \frac{11Q^2}{16\pi\varepsilon R^6} - \gamma\frac{5}{R^3} + \frac{\rho_2}{4c^2}(\omega_2\mathfrak{Z} - \omega_2^*\mathfrak{M})^2 + \frac{\rho_2}{4c^2}$$

$$\times(\omega_2^*\mathfrak{Z} + \omega_2\mathfrak{M})^2 + \frac{6}{16}\rho_1(\omega_2^2 + \omega_2^{*2})$$

$$\left. - \frac{6}{4R^2}\rho_2(\mathfrak{M}^2 + \mathfrak{Z}^2)\right);$$

$$\mathfrak{B}_1 = \left(\frac{3}{4}(\rho_1-\rho_2)(\omega_2^{*2} - \omega_2^2) + \frac{11Q^2}{16\pi\varepsilon R^6} - \gamma\frac{5}{R^3}\right.$$

$$+ \frac{\rho_2}{4c^2}(\omega_2\mathfrak{Z} - \omega_2^*\mathfrak{M})^2 - \frac{\rho_2}{4c^2}(\omega_2^*\mathfrak{Z} + \omega_2\mathfrak{M})^2$$

$$\left. - \frac{6}{16\rho_1}(\omega_2^{*2} - \omega_2^2) - \frac{6}{4R^2}\rho_2(\mathfrak{M}^2 - \mathfrak{Z}^2)\right);$$

$$\mathfrak{B}_2 = \left(\frac{3}{4}(\rho_1-\rho_2)2\omega_2^*\omega_2 - \frac{\rho_2}{4c^2}2(\omega_2\mathfrak{Z} - \omega_2^*\mathfrak{M})\right.$$

$$\left.\times(\omega_2^*\mathfrak{Z} + \omega_2\mathfrak{M}) + \frac{6}{16}\rho_1 2\omega_2\omega_2^* - \frac{6}{4R^2}\rho_2 2\mathfrak{M}\mathfrak{Z}\right);$$

$$\mathfrak{B}_3 = \left((\rho_1-\rho_2)(\omega_2^{*2} - \omega_2^2) + \frac{1}{2}(\rho_1-\rho_2)(\omega_2^2 + \omega_2^{*2})\right.$$

$$+ \frac{14Q^2}{8\pi\varepsilon R^6} - \gamma\frac{10}{R^3} + \frac{\rho_2}{2c^2}(\omega_2\mathfrak{Z} - \omega_2^*\mathfrak{M})^2 + \frac{\rho_2}{2c^2}$$

$$\times(\omega_2^*\mathfrak{Z} + \omega_2\mathfrak{M})^2 + \frac{6}{16}\rho_1(\omega_2^2 + \omega_2^{*2})$$

$$\left. - \frac{6}{4R^2}\rho_2(\mathfrak{M}^2 + \mathfrak{Z}^2)\right);$$

$$\mathfrak{B}_4 = \left(\frac{3}{2}(\rho_1-\rho_2)(\omega_2^{*2}-\omega_2^2)+\frac{14Q^2}{8\pi\varepsilon R^6}-\gamma\frac{10}{R^3}\right.$$
$$+\frac{\rho_2}{2c^2}(\omega_2\mathfrak{Z}-\omega_2^*\mathfrak{M})^2-\frac{\rho_2}{2c^2}(\omega_2^*\mathfrak{Z}+\omega_2\mathfrak{M})^2$$
$$\left.+\frac{6}{16}\rho_1(\omega_2^{*2}-\omega_2^2)-\frac{6}{4R^2}\rho_2(\mathfrak{M}^2-\mathfrak{Z}^2)\right);$$

$$\mathfrak{B}_5 = \left(3(\rho_1-\rho_2)\omega_2^*\omega_2-\frac{\rho_2}{c^2}(\omega_2\mathfrak{Z}-\omega_2^*\mathfrak{M})\right.$$
$$\left.\times(\omega_2^*\mathfrak{Z}+\omega_2\mathfrak{M})+\frac{3}{4}\rho_1\omega_2\omega_2^*-\frac{3}{R^2}\rho_2\mathfrak{M}\mathfrak{Z}\right);$$

$$\mathfrak{B}_6 = \left(9(\rho_1-\rho_2)(\omega_2^{*2}-\omega_2^2)+\frac{9}{2}(\omega_2^2+\omega_2^{*2})(\rho_1-\rho_2)\right.$$
$$+\frac{189Q^2}{8\pi\varepsilon R^6}-\gamma\frac{90}{R^3}+\frac{9\rho_2}{2c^2}(\omega_2\mathfrak{Z}-\omega_2^*\mathfrak{M})^2+\frac{9\rho_2}{2c^2}$$
$$\times(\omega_2^*\mathfrak{Z}+\omega_2\mathfrak{M})^2-\frac{9}{2}\rho_1(\omega_2^2+\omega_2^{*2})$$
$$\left.+\frac{18}{R^2}\rho_2(\mathfrak{M}^2+\mathfrak{Z}^2)\right);$$

$$\mathfrak{B}_7 = \left(\frac{27}{2}(\rho_1-\rho_2)(\omega_2^{*2}-\omega_2^2)+\frac{189Q^2}{8\pi\varepsilon R^6}-\frac{90\gamma}{R^3}\right.$$
$$+\frac{9\rho_2}{2c^2}(\omega_2\mathfrak{Z}-\omega_2^*\mathfrak{M})^2-\frac{9\rho_2}{2c^2}(\omega_2^*\mathfrak{Z}+\omega_2\mathfrak{M})^2$$
$$\left.-\frac{9}{2}\rho_1(\omega_2^{*2}-\omega_2^2)+\frac{18}{R^2}\rho_2(\mathfrak{M}^2-\mathfrak{Z}^2)\right);$$

$$\mathfrak{B}_8 = \left[27(\rho_1-\rho_2)\omega_2^*\omega_2-\frac{9\rho_2}{c^2}(\omega_2\mathfrak{Z}-\omega_2^*\mathfrak{M})\right.$$
$$\left.\times(\omega_2^*\mathfrak{Z}+\omega_2\mathfrak{M})-9\rho_1\omega_2\omega_2^*+\frac{36}{R^2}\rho_2\mathfrak{M}\mathfrak{Z}\right];$$

$$N = \frac{Z_i\tau_2^*+Z_r(\tau_2+4\omega_2^{*2})}{\tau_2^{*2}+(\tau_2+4\omega_2^{*2})^2};$$

$$\mathfrak{U} = \frac{-6k^5R^5\omega_2+k^7R^7\omega_2+324\omega_2^*+27k^2R^2\omega_2^*-4k^4R^4\omega_2^*+k^6R^6\omega_2^*}{R(81+9k^2R^2-2k^4R^4+k^6R^6)};$$

$$\mathfrak{R} = \frac{324\omega_2+27k^2R^2\omega_2-4k^4R^4\omega_2+k^6R^6\omega_2+6k^5R^5\omega_2^*-k^7R^7\omega_2^*}{R(81+9k^2R^2-2k^4R^4+k^6R^6)};$$

$$\mathfrak{M} = \frac{-k^5R^6\omega_2+27R\omega_2^*+6k^2R^3\omega_2^*+k^4R^5\omega_2^*}{81+9k^2R^2-2k^4R^4+k^6R^6};$$

$$\mathfrak{Z} = \frac{27R\omega_2+6k^2R^3\omega_2+k^4R^5\omega_2+k^5R^6\omega_2^*}{81+9k^2R^2-2k^4R^4+k^6R^6};$$

$$L = [-\tau_2^{*3}T_i+\tau_2^{*2}(-\tau_2T_r+4T_r\omega_2^2+8S_r\omega_2\omega_2^*-4T_r\omega_2^{*2})$$
$$-(\tau_2T_r-4T_r\omega_2^2+8S_r\omega_2\omega_2^*+4T_r\omega_2^{*2})(\tau_2^2-8\tau_2\omega_2^2$$
$$+16\omega_2^4+8\tau_2\omega_2^{*2}+32\omega_2^2\omega_2^{*2}+16\omega_2^{*4})-\tau_2^*$$
$$\times(\tau_2^2T_i-8\tau_2T_i\omega_2^2+16T_i\omega_2^4+16S_i\tau_2\omega_2\omega_2^*-64S_i\omega_2^3\omega_2^*$$
$$+8\tau_2T_i\omega_2^{*2}-96T_i\omega_2^2\omega_2^{*2}+64S_i\omega_2\omega_2^{*3}+16T_i\omega_2^{*4})]\Lambda_7^{-1};$$

$$M = [-S_i\tau_2^*(\tau_2^{*2}+\tau_2^2-8\tau_2\omega_2^2$$
$$+16\omega_2^4+8\tau_2\omega_2^{*2}-96\omega_2^2\omega_2^{*2}+16\omega_2^{*4})$$
$$-S_r(\tau_2-4\omega_2^2+4\omega_2^{*2})(\tau_2^{*2}+\tau_2^2-8\tau_2\omega_2^2$$
$$+16\omega_2^4+8\tau_2\omega_2^{*2}+32\omega_2^2\omega_2^{*2}+16\omega_2^{*4})+8\omega_2\omega_2^*$$
$$\times(2\tau_2^*\tau_2T_i-\tau_2^{*2}T_r+\tau_2^2T_r-8\tau_2^*T_i\omega_2^2-8\tau_2T_r\omega_2^2$$
$$+16T_r\omega_2^4+8\tau_2^*T_i\omega_2^{*2}+8\tau_2T_r\omega_2^{*2}$$
$$+32T_r\omega_2^2\omega_2^{*2}+16T_r\omega_2^{*4})]\Lambda_7^{-1};$$

$$\Lambda_7 = [(\tau_2^{*2}+\tau_2^2-8\tau_2\omega_2^2+16\omega_2^4-16\tau_2^*\omega_2\omega_2^*$$
$$+8\tau_2\omega_2^{*2}+32\omega_2^2\omega_2^{*2}+16\omega_2^{*4})(\tau_2^{*2}+\tau_2^2-8\tau_2\omega_2^2$$
$$+16\omega_2^4+16\tau_2^*\omega_2\omega_2^*+8\tau_2\omega_2^{*2}+32\omega_2^2\omega_2^{*2}+16\omega_2^{*4})];$$

$$\Lambda_8 = \frac{\rho_1\omega_2\omega_2^*}{7}+\frac{1}{7}\left[3(\rho_1-\rho_2)\omega_2^*\omega_2-\frac{\rho_2}{c^2}(\omega_2\mathfrak{Z}-\omega_2^*\mathfrak{M})\right.$$
$$\left.\times(\omega_2^*\mathfrak{Z}+\omega_2\mathfrak{M})+\frac{6}{8}\rho_1\omega_2\omega_2^*-\frac{6}{2R^2}\rho_2\mathfrak{M}\mathfrak{Z}\right];$$

$$S_r = \mathfrak{A}\Lambda_8-\mathfrak{B}\Lambda_9; \quad S_i = \mathfrak{A}^*\Lambda_8-\mathfrak{B}^*\Lambda_9;$$

$$\Lambda_9 = \frac{\rho_2 2\omega_2\omega_2^*}{7Rk}+\frac{\rho_2}{k}\left[2\omega_2^*\left(\frac{1}{7}\mathfrak{R}-\frac{3}{7R^2}\mathfrak{Z}-\frac{1}{14R}\omega_2\right)\right.$$
$$\left.+2\omega_2\left(\frac{1}{7}\mathfrak{U}-\frac{3}{7R^2}\mathfrak{M}-\frac{1}{14R}\omega_2^*\right)\right];$$

$$T_r = \mathfrak{A}\Lambda_{10}-\mathfrak{B}\Lambda_{11}; \quad T_i = \mathfrak{A}^*\Lambda_{10}-\mathfrak{B}^*\Lambda_{11};$$

$$\Lambda_{10} = \frac{\rho_1(2\omega_2^{*2} - 2\omega_2^2)}{28} - \frac{3Q^2}{14\pi\varepsilon R^6} + \frac{1}{7}\left[\frac{3}{2}(\rho_1 - \rho_2)\right.$$
$$\times(\omega_2^{*2} - \omega_2^2) + \frac{14Q^2}{8\pi\varepsilon R^6} - \gamma\frac{10}{R^3} + \frac{\rho_2}{2c^2}$$
$$\times(\omega_2\mathfrak{Z} - \omega_2^*\mathfrak{M})^2 - \frac{\rho_2}{2c^2}(\omega_2^*\mathfrak{Z} + \omega_2\mathfrak{M})^2$$
$$\left. + \frac{6}{16}\rho_1(\omega_2^{*2} - \omega_2^2) - \frac{6}{4R^2}\rho_2(\mathfrak{M}^2 - \mathfrak{Z}^2)\right];$$

$$\Lambda_{11} = \frac{2\rho_2(\omega_2^{*2} - \omega_2^2)}{14Rk} + \frac{\rho_2}{k}\left[2\omega_2^*\left(\frac{1}{7}\mathfrak{U} - \frac{3}{7R^2}\mathfrak{M}\right.\right.$$
$$\left.\left. - \frac{1}{14R}\omega_2^*\right) - 2\omega_2\left(\frac{1}{7}\mathfrak{R} - \frac{3}{7R^2}\mathfrak{Z} - \frac{1}{14R}\omega_2\right)\right];$$

$$Z_r = \mathfrak{A}\Lambda_{12} - \mathfrak{B}\Lambda_{13}; \quad Z_i = \mathfrak{A}^*\Lambda_{12} - \mathfrak{B}^*\Lambda_{13};$$

$$\Lambda_{12} = \rho_1\frac{2\omega_2^{*2}}{28} - \frac{3Q^2}{14\pi\varepsilon R^6} + \frac{1}{7}\left[(\rho_1 - \rho_2)(\omega_2^{*2} - \omega_2^2)\right.$$
$$+ \frac{1}{2}(\rho_1 - \rho_2)(\omega_2^2 + \omega_2^{*2}) + \frac{14Q^2}{8\pi\varepsilon R^6} - \gamma\frac{10}{R^3} + \frac{\rho_2}{2c^2}$$
$$\times(\omega_2\mathfrak{Z} - \omega_2^*\mathfrak{M})^2 + \frac{\rho_2}{2c}(\omega_2^*\mathfrak{Z} + \omega_2\mathfrak{M})^2$$
$$\left. + \frac{6}{16}\rho_1(\omega_2^2 + \omega_2^{*2}) - \frac{6}{4R^2}\rho_2(\mathfrak{M}^2 + \mathfrak{Z}^2)\right];$$

$$\Lambda_{13} = \frac{2\rho_2\omega_2^{*2}}{14Rk} + \frac{2\rho_2\omega_2^*}{k}\left(\frac{1}{7}\mathfrak{U} - \frac{3}{7R^2}\mathfrak{M} - \frac{1}{14R}\omega_2^*\right);$$

$$\mathfrak{A} = (\rho_1\Lambda_{13}^* + 4\rho_2\Lambda_{14})(R\rho_1^2\Lambda_{13}^* + 4R\rho_1\rho_2\Lambda_{14} + 4R\rho_2^2\Lambda_{15})^{-1};$$

$$\mathfrak{A}^* = (4k^5R^4\rho_2)(\rho_1^2\Lambda_{13}^* + 4\rho_1\rho_2\Lambda_{14} + 4\rho_2^2\Lambda_{15})^{-1};$$

$$\mathfrak{B} = -(2k\rho_1\Lambda_{14} + 4k\rho_2\Lambda_{15})$$
$$\times(\rho_1^2\Lambda_{13}^* + 4\rho_1\rho_2\Lambda_{14} + 4\rho_2^2\Lambda_{15})^{-1};$$

$$\mathfrak{B}^* = (2k^6R^5\rho_1)(\rho_1^2\Lambda_{13}^* + 4\rho_1\rho_2\Lambda_{14} + 4\rho_2^2\Lambda_{15})^{-1};$$

$$\Lambda_{13}^* = (81 + 9k^2R^2 - 2k^4R^4 + k^6R^6);$$

$$\Lambda_{14} = (27 + 6k^2R^2 + k^4R^4);$$

$$\Lambda_{15} = (9 + 3k^2R^2 + k^4R^4);$$

$$\kappa_2^{(2)} = \kappa_2^2$$
$$+ \left[1 + \left(\frac{N(\omega_2^*\omega_2^2 + \omega_2^{*3}) + L(3\omega_2^*\omega_2^2 + \omega_2^{*3}) + 2M\omega_2^3}{(\omega_2^3 + \omega_2^{*2}\omega_2)N - L(\omega_2^3 - \omega_2^{*2}\omega_2) + 2M\omega_2^*\omega_2^2}\right)^2\right]^{1/2}$$
$$\times\left(N - L\frac{\omega_2^2 - \omega_2^{*2}}{\omega_2^2 + \omega_2^{*2}} + M\frac{2\omega_2^*\omega_2}{\omega_2^2 + \omega_2^{*2}}\right);$$

$$\mathfrak{R} = \frac{G_i\tau_4^* + G_r\tau_4 + 4G_r\omega_2^{*2}}{\tau_4^{*2} + \tau_4^2 + 8\tau_4\omega_2^{*2} + 16\omega_2^{*4}};$$

$$\tan(\beta_2^{(2)})$$
$$= \frac{N(\omega_2^*\omega_2^2 + \omega_2^{*3}) + L(3\omega_2^*\omega_2^2 + \omega_2^{*3}) + 2M\omega_2^3}{(\omega_2^3 + \omega_2^{*2}\omega_2)N - L(\omega_2^3 - \omega_2^{*2}\omega_2) + 2M\omega_2^*\omega_2^2};$$

$$\mathfrak{L} = -[-\tau_4^{*3}H_i - \tau_4^*\tau_4^2H_i - \tau_4^{*2}\tau_4H_r - \tau_4^3H_r$$
$$+ 8\tau_4^*\tau_4H_i\omega_2^2 + 4\tau_4^{*2}H_r\omega_2^2 + 12\tau_4^2H_r\omega_2^2$$
$$- 16\tau_4^*H_i\omega_2^4 - 48\tau_4H_r\omega_2^4 + 64H_r\omega_2^6 + 8U_r\tau_4^{*2}\omega_2\omega_2^*$$
$$- 16U_i\tau_4^*\tau_4\omega_2\omega_2^* - 8U_r\tau_4^2\omega_2\omega_2^* + 64U_i\tau_4^*\omega_2^3\omega_2^*$$
$$+ 64U_r\tau_4\omega_2^3\omega_2^* - 128U_r\omega_2\omega_2^5\omega_2^* - 8\tau_4^*\tau_4H_i\omega_2^{*2}$$
$$- 4\tau_4^{*2}H_r\omega_2^{*2} - 12\tau_4^2H_r\omega_2^{*2} + 96\tau_4^*H_i\omega_2^2\omega_2^{*2}$$
$$+ 32\tau_4H_r\omega_2^2\omega_2^{*2} + 64H_r\omega_2^4\omega_2^{*2} - 64U_i\tau_4^*\omega_2\omega_2^{*3}$$
$$- 64U_r\tau_4\omega_2\omega_2^{*3} - 256U_r\omega_2^3\omega_2^{*3} - 16\tau_4^*H_i\omega_2^{*4}$$
$$- 48\tau_4H_r\omega_2^{*4} - 64H_r\omega_2^2\omega_2^{*4} - 128U_r\omega_2\omega_2^{*5}$$
$$- 64H_r\omega_2^{*6}]\Lambda_{16}^{-1};$$

$$\mathfrak{C} = -[-U_i\tau_4^{*3} - U_r\tau_4^{*2}\tau_4 - U_i\tau_4^*\tau_4^2 - U_r\tau_4^3 + 4U_r\tau_4^{*2}\omega_2^2$$
$$+ 8U_i\tau_4^*\tau_4\omega_2^2 + 12U_r\tau_4^2\omega_2^2 - 16U_i\tau_4^*\omega_2^4 - 48U_r\tau_4\omega_2^4$$
$$+ 64U_r\omega_2^6 + 16\tau_4^*\tau_4H_i\omega_2\omega_2^* - 8\tau_4^{*2}H_r\omega_2\omega_2^*$$
$$+ 8\tau_4^2H_r\omega_2\omega_2^* - 64\tau_4^*H_i\omega_2^3\omega_2^* - 64\tau_4H_r\omega_2^3\omega_2^*$$
$$+ 128H_r\omega_2^5\omega_2^* - 4U_r\tau_4^{*2}\omega_2^{*2} - 8U_i\tau_4^*\tau_4\omega_2^{*2}$$
$$- 12U_r\tau_4^2\omega_2^{*2} + 96U_i\tau_4^*\omega_2^2\omega_2^{*2} + 32U_r\tau_4\omega_2^2\omega_2^{*2}$$
$$+ 64U_r\omega_2^4\omega_2^{*2} + 64\tau_4^*H_i\omega_2\omega_2^{*3} + 64\tau_4H_r\omega_2\omega_2^{*3}$$
$$+ 256H_r\omega_2^3\omega_2^{*3} - 16U_i\tau_4^*\omega_2^{*4} - 48U_r\tau_4\omega_2\omega_2^{*4}$$
$$- 64U_r\omega_2^2\omega_2^{*4} + 128H_r\omega_2\omega_2^{*5} - 64U_r\omega_2^{*6}]\Lambda_{16}^{-1};$$

$$\Lambda_{16} = [256\omega_2^8 + 256\omega_2^6(-\tau_4 + 4\omega_2^{*2}) + (\tau_4^{*2} + \tau_4^2 + 8\tau_4\omega_2^{*2} + 16\omega_2^{*4})^2 + 32\omega_2^4(\tau_4^{*2} + 3\tau_4^2 - 8\tau_4\omega_2^{*2} + 48\omega_2^{*4}) + 16\omega_2^2(-\tau_4^{*2}\tau_4 - \tau_4^3 - 12\tau_4^{*2}\omega_2^{*2} - 4\tau_4^2\omega_2^{*2} + 16\tau_4\omega_2^{*4} + 64\omega_2^{*6})];$$

$$U_r = \Re\Lambda_{17} + \Im\Lambda_{18}; \quad U_i = -\Re^*\Lambda_{17} + \Im^*\Lambda_{18};$$

$$H_r = -\Re\Lambda_{19} + \Im\Lambda_{20};$$

$$H_i = -\Re^*\Lambda_{19} + \Im^*\Lambda_{20};$$

$$\Lambda_{17} = \frac{2\rho_2}{k}\left[\frac{9}{35}(\omega_2^*\Re + \omega_2\mathfrak{U}) + \frac{36}{35R^2}(\Im\omega_2^* + \mathfrak{M}\omega_2)\right];$$

$$\Lambda_{18} = \frac{1}{35}\left[-9(\rho_1 + 3\rho_2)\omega_2\omega_2^* - \frac{9\rho_2}{c^2}(\omega_2\Im - \omega_2^*\mathfrak{M}) \times (\omega_2^*\Im + \omega_2\mathfrak{M}) + \frac{36}{R^2}\rho_2\mathfrak{M}\Im\right];$$

$$\Lambda_{19} = \frac{2\rho_2}{k}\left[\frac{9}{35}(\omega_2^*\mathfrak{U} - \omega_2\Re) + \frac{36}{35R^2}(\omega_2^*\mathfrak{M} - \omega_2\Im)\right];$$

$$\Lambda_{20} = \frac{1}{35}\left[\frac{9}{2}(\rho_1 + 3\rho_2)(\omega_2^2 - \omega_2^{*2}) + \frac{9Q^2}{8\pi\varepsilon R^6} - \frac{90\gamma}{R^3} + \frac{9\rho_2}{2c^2}(\omega_2\Im - \omega_2^*\mathfrak{M})^2 - \frac{9\rho_2}{2c^2} \times (\omega_2^*\Im + \omega_2\mathfrak{M})^2 + \frac{18}{R^2}\rho(\mathfrak{M}^2 - \Im^2)\right];$$

$$G_r = -\Re\Lambda_{21} + \Im\Lambda_{22};$$

$$G_i = -\Re^*\Lambda_{21} + \Im^*\Lambda_{22};$$

$$\Lambda_{21} = \frac{2\rho_2}{k}\omega_2\left(\frac{9}{35}\mathfrak{U} + \frac{36}{35R^2}\mathfrak{M}\right);$$

$$\Lambda_{22} = \frac{1}{35}\left[-\frac{9}{2}\rho_1(2\omega_2^2 + \omega_2^{*2}) - \frac{9}{2}\rho_2(3\omega_2^{*2} - \omega_2^2) + \frac{9Q^2}{8\pi\varepsilon R^6} - \frac{90\gamma}{R^3} + \frac{9\rho_2}{2c^2}(\omega_2\Im - \omega_2^*\mathfrak{M})^2 + \frac{9\rho_2}{2c^2}(\omega_2^*\Im + \omega_2\mathfrak{M})^2 + \frac{18}{R^2}\rho_2(\mathfrak{M}^2 + \Im^2)\right];$$

$$\Im = (4\Lambda_{23}\rho_1 + 16\Lambda_{24}\rho_2) \times (\Lambda_{23}R\rho_1^2 + \Lambda_{24}8R\rho_1\rho_2 + \Lambda_{25}16R\rho_2^2)^{-1};$$

$$\Im^* = (16k^9R^8\rho_2)(\Lambda_{23}\rho_1^2 + \Lambda_{24}8\rho_1\rho_2 + \Lambda_{25}16\rho_2^2)^{-1};$$

$$\Re = -(4k\rho_1\Lambda_{24} + 16k\rho_2\Lambda_{25}) \times (\Lambda_{23}\rho_1^2 + \Lambda_{24}8\rho_1\rho_2 + \Lambda_{25}16\rho_2^2)^{-1};$$

$$\Re^* = (4k^{10}R^9\rho_1)(\Lambda_{23}\rho_1^2 + \Lambda_{24}8\rho_1\rho_2 + \Lambda_{25}16\rho_2^2)^{-1};$$

$$\tau_4 = \frac{18\gamma(1 - W_4)}{R^3}[(1\,102\,500k^2R^2 + 94\,500k^4R^4 + 3600k^6R^6 - 20k^8R^8 - 36k^{10}R^{10} + 4k^{12}R^{12})\rho_1 + (882\,000k^2R^2 + 100\,800k^4R^4 + 6480k^6R^6 + 320k^8R^8 + 16k^{10}R^{10})\rho_2] \times (\Lambda_{23}k^2R^2\rho_1^2 + \Lambda_{26}\rho_1\rho_2 + \Lambda_{27}\rho_2^2)^{-1};$$

$$\tau_4^* = \frac{18\gamma(1 - W_4)}{R^3}(16k^{11}R^{11}\rho_2) \times (\Lambda_{23}k^2R^2\rho_1^2 + \Lambda_{26}\rho_1\rho_2 + \Lambda_{27}\rho_2^2)^{-1};$$

$$\Lambda_{23} = (275\,625 + 23\,625k^2R^2 + 900k^4R^4 - 5k^6R^6 - 9k^8R^8 + k^{10}R^{10});$$

$$\Lambda_{24} = (55\,125 + 6300k^2R^2 + 405k^4R^4 + 20k^6R^6 + k^8R^8);$$

$$\Lambda_{25} = (11025 + 1575k^2R^2 + 135k^4R^4 + 10k^6R^6 + k^8R^8);$$

$$\Lambda_{26} = (441\,000k^2R^2 + 50\,400k^4R^4 + 3240k^6R^6 + 160k^8R^8 + 8k^{10}R^{10});$$

$$\Lambda_{27} = (176\,400k^2R^2 + 25200k^4R^4 + 2160k^6R^6 + 160k^8R^8 + 16k^{10}R^{10});$$

$$\kappa_4^{(2)} = \kappa_2^2\sqrt{1 + \tan^2(\beta_4^{(2)})}\left[\Re - \mathfrak{Q}\frac{\omega_2^2 - \omega_2^{*2}}{\omega_2^2 + \omega_2^{*2}} + \mathfrak{C}\frac{2\omega_2^*\omega_2}{\omega_2^2 + \omega_2^{*2}}\right];$$

$$\tan(\beta_4^{(2)}) = [\Re(\omega_4^*\omega_2^2 + \omega_4^*\omega_2^{*2} - 2\omega_2^*\omega_2^2 - 2\omega_2^{*3}) + \mathfrak{Q}(-2\omega_2^*\omega_2^2 - \omega_4^*\omega_2^2 - 2\omega_2^{*3} + \omega_4^*\omega_2^{*2}) + \mathfrak{C}(-2\omega_2^3 - 2\omega_2\omega_2^{*2} + 2\omega_4^*\omega_2^*\omega_2)] \times [-\Re(\omega_4\omega_2^2 + \omega_4\omega_2^{*2}) + \mathfrak{Q}(\omega_4\omega_2^2 - \omega_4\omega_2^{*2}) - 2\mathfrak{C}\omega_4\omega_2^*\omega_2]^{-1}.$$

ACKNOWLEDGMENTS

This work was supported by the President of the Russian Federation (grant no. 00-15-9925).

REFERENCES

1. L. D. Landau and E. M. Lifshitz, *Course of Theoretical Physics*, Vol. 6: *Fluid Mechanics* (Nauka, Moscow, 1986; Pergamon, Oxford, 1987).
2. A. I. Grigor'ev and A. R. Gaibov, Zh. Tekh. Fiz. **71** (11), 6 (2001) [Tech. Phys. **46**, 1351 (2001)].
3. A. I. Grigor'ev, S. O. Shiryaeva, A. R. Gaibov, and D. F. Belonozhko, Pis'ma Zh. Tekh. Fiz. **21** (22), 7 (2001) [Tech. Phys. Lett. **27**, 934 (2001)].
4. S. O. Shiryaeva, Zh. Tekh. Fiz. **72** (4), 15 (2002) [Tech. Phys. **47**, 389 (2002)].
5. Won-Kyu Rhim, Song Kun Chung, M. T. Hyson, *et al.*, IEEE Trans. Ind. Appl. **23**, 975 (1987).
6. A. I. Grigor'ev and S. O. Shiryaeva, Izv. Ross. Akad. Nauk, Mekh. Zhidk. Gaza, No. 3, 3 (1994).
7. V. P. Shagapov, Izv. Akad. Nauk SSSR, Fiz. Atmos. Okeana **24**, 506 (1988).
8. E. H. Trinh, R. G. Holt, and D. B. Thiessen, Phys. Fluids **8**, 43 (1996).
9. S. O. Shiryaeva, Zh. Tekh. Fiz. **71** (2), 27 (2001) [Tech. Phys. **46**, 158 (2001)].
10. D. F. Belonozhko and A. I. Grigor'ev, Zh. Tekh. Fiz. **70** (8), 45 (2000) [Tech. Phys. **45**, 1001 (2000)].
11. L. F. Lependin, *Acoustics* (Vysshaya Shkola, Moscow, 1978).
12. A. H. Nayfeh, *Perturbation Methods* (Wiley, New York, 1973; Mir, Moscow, 1976).
13. C. D. Hendricks and J. M. Schneider, Am. J. Phys. **1**, 450 (1963).

Translated by N. Mende

Technical Physics, Vol. 48, No. 7, 2003, pp. 822–828. Translated from Zhurnal Tekhnicheskoĭ Fiziki, Vol. 73, No. 7, 2003, pp. 21–27.

GASES AND LIQUIDS

On the Appearance of Ions near the Charged Surface of an Intensely Evaporating Electrolyte

S. O. Shiryaeva, A. I. Grigor'ev, and V. V. Morozov

Demidov State University, Sovetskaya ul. 14, Yaroslavl, 150000 Russia

e-mail: shir@uniyar.ac.ru

Received December 3, 2002

Abstract—Two mechanisms behind the appearance of ions in the vapor–gas sheath around a hot electrode immersed in an electrolyte, electrolyte surface instability against the surface charge and field evaporation, are considered. It is shown that the concept of the thermally activated field evaporation of ions provides a better approximation to experimental conditions. A dispersion relation for capillary–barogravity waves at the electrolyte–saturated vapor charged interface is derived. Critical conditions for the instability of these waves are found. © *2003 MAIK "Nauka/Interperiodica".*

(1) Let a metallic electrode be immersed in a conducting vessel with a liquid electrolyte and a voltage difference $U \approx 150$ V be applied to the vessel. Under such conditions, the electrode temperature will increase above the boiling point of the electrolyte because of Joule heat evolution, and a vapor sheath of thickness $h \approx 100$ μm, which separates the electrode from the electrolyte, will form (Fig. 1). The further evolution of Joule heat will heat the electrode to $T \approx 1000$ K and the vapor sheath to ≈1400 K, and the process will then become steady-state. In such a system, the current density may reach $\approx(4–6) \times 10^4$ A/m^2. The electrode heats up largely by heat exchange with the vapor sheath, which, in turn, heats up due to its poor electrical conductivity and low specific heat. Away from the electrode, the electrolyte temperature is 310–330 K.

If the heat flux toward the electrolyte is intense and the pressure of the superheated vapor is significant, the temperature of the electrolyte surface near the electrode is presumably very high, while lower than the temperatures of the electrode and vapor. Note that the vapor is hard to remove from the evaporating surface, since the sheath is narrow. This phenomenon is however essentially nonequilibrium, and the notion of surface temperature for a liquid being in contact with a highly superheated vapor fails in this case. High-energy vapor molecules turning back from the interface to the electrolyte will exchange energy with molecules of the liquid electrolyte. Eventually, energetic molecules will prevail in the nonequilibrium velocity distribution of liquid electrolyte molecules in the narrow surface layer. Because of this, to describe kinetic processes in the narrow surface layer of the electrolyte in conventional physical terms, we introduce the concept of effective temperature, which is assumed to be much greater than the equilibrium boiling point of the electrolyte but lower than the temperature of the superheated vapor. The effective temperature will be used below to estimate the surface tension of the electrolyte, as well as the rates of field and thermal evaporation.

(2) The phenomenon under discussion has been known since the late 19th century and has found wide application in many devices (see, e.g., [1–12] and the references cited there). Yet a theoretical treatment of it that is adequate to the current status of science is lacking. In particular, transient and steady-state processes of current passage and electrode heating have been poorly understood.

Many theoretical models [1–12] consider this phenomenon in terms of the theory of electrical discharge in gases, ignoring its electrohydrodynamic features. If, however, attention is drawn to the fact that the discharge is initiated between a metallic electrode and the heavily charged surface of an electrolyte that is intensely evaporating due to heat exchange, it will become obvious that the vapor pressure in such a system must be substantially higher than the atmospheric pressure. The same follows from the fact that the geometry of the vapor sheath around the electrode is similar to that of the electrode (Fig. 1) and the gravitational

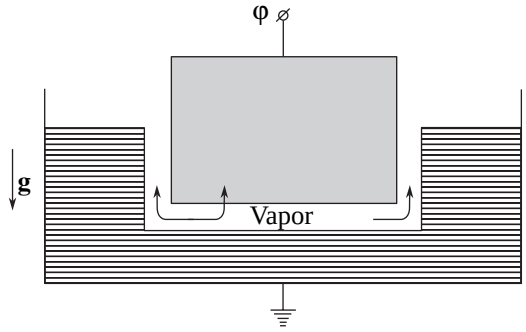

Fig. 1. Experimental scheme.

1063-7842/03/4807-0822$24.00 © 2003 MAIK "Nauka/Interperiodica"

field (and also the field of surface tension forces) affects the shape of the liquid–vapor interface insignificantly.

The aforesaid leads us to conclude that (1) the effective temperature of the intensely evaporating electrolyte surface is fairly high, i.e., much greater than the equilibrium temperature averaged over the electrolyte volume; (2) the geometry of the vapor sheath, which separates the electrolyte from the electrode, depends on the pressure of the evaporating electrolyte (vapor pressure) to the greatest extent. The gravity forces and the surface tension forces play a minor part in this process; (3) the pressure of the vapor sheath, which separates the electrode from the electrolyte, far exceeds the atmospheric pressure; (4) the vapor flowing out of the electrode–electrolyte gap follows the tangent to the electrolyte surface, and its motion may generate Kelvin–Helmholtz oscillatory instability; and (5) the electrode–electrolyte interface in the separating sheath has a high charge density $\kappa \approx U/4\pi h$, which may cause Tonks–Frenkel aperiodic instability of the electrolyte surface.

Since the vapor pressure at the electrolyte surface is very high (the free path of charge carriers, which are ions instead of electrons according to the physical picture of the process, is low), the initiation of a glow, corona, spark, or arc discharge between the electrolyte and electrode is hardly possible under the conditions mentioned above. At the same time, the field evaporation of ions from the electrolyte surface and the electrohydrodynamic instability of the charged liquid surface merit detailed consideration as possible mechanisms underlying the phenomenon [13–16].

Although the phenomenon considered is essentially nonequilibrium, the role of electrohydrodynamic effects will subsequently be analyzed in terms of a simplified equilibrium model, which allows us to use thermodynamic notions.

(3) Let an electrical charge uniformly distributed over the equilibrium planar surface of an electrolyte produce a uniform electrostatic field $\mathbf{E}_0$ that is normal to the surface. The temperature and pressure of the system are kept constant and close to the critical values for the solvent (water). In such a system, the evaporation and condensation processes are in equilibrium, allowing us to study the field evaporation of ions from the electrolyte surface and the instability of the vapor–liquid interface against the surface charge.

The electrolyte and vapor are simulated by incompressible immiscible fluids, of which the former occupies the lower domain $z \le 0$ in the gravity force ($\mathbf{g}$) field and the latter occupies the upper domain $z > 0$ and moves with a constant finite velocity $\mathbf{V} = V \cdot \mathbf{n}_x$ relative to the lower domain ($\mathbf{n}_x$ is the unit vector in Cartesian coordinates). Let the unperturbed fluid–fluid interface be coincident with the *XOY* plane of the Cartesian coordinate system where the unit vector $\mathbf{n}_z$ is pointing upward, i.e., is in opposition to the gravitational force ($-\mathbf{g} \parallel \mathbf{n}_z$). The lower fluid of density ρ_1 is assumed to be viscous, perfectly conducting, and incompressible. The upper fluid of density ρ_2 is assumed to be nonviscous and incompressible. We also assume that the unperturbed interface, which is described by the equation $z = 0$, is uniformly charged with a surface charge density $\kappa = E_0/4\pi$ and has a surface tension coefficient σ. The equation for an interface disturbed by low-amplitude thermal capillary wave motion has the form

$$F(\mathbf{r}, t) \equiv z - \zeta(x, y, t) = 0, \tag{1}$$

where $|\zeta| \sim (kT/\sigma)^{1/2} \ll \kappa^{-1}$, κ is the wavenumber, k is the Boltzmann constant, and T is absolute temperature.

The velocity fields of the wave motion of the fluids that is induced by a small perturbation $\zeta(x, y, t)$ will be denoted by $\mathbf{U}_j(\mathbf{r}, t)$, where $j = 1, 2$ (the fields are of the same order of smallness as the perturbation). Without loss in generality, we may assume that the perturbation ζ of the equilibrium surface is y independent and is due to capillary waves $D\exp(i\kappa x - i\omega t)$ traveling along the abscissa (ω is the complex frequency, t is time, and i is the imaginary unit).

Finally, the liquid is assumed to be in thermodynamic equilibrium with the vapor.

In such a system, the stability of the interface is defined by the balance of five forces: the force of gravity; surface tension; saturated vapor pressure; electrostatic field pressure; and aerodynamic pressure, which is associated with the tangential discontinuity of the velocity field. The first three stabilize the interface, while the other two destabilize it. Bearing in mind the specific features of the phenomenon being simulated, we will assume that the force of gravity and the surface tension force are negligible compared with the saturated vapor pressure force.

Eventually, the instability conditions in the system are found from the set of linearized equations

$$\frac{\partial \mathbf{U}_1}{\partial t} = -\frac{1}{\rho_1}\nabla P_1 + \nu\Delta\mathbf{U}_1 + \mathbf{g}; \tag{2}$$

$$\frac{\partial \mathbf{U}_2}{\partial t} + (\mathbf{V}\cdot\nabla)\mathbf{U}_2 = -\frac{1}{\rho_2}\nabla P_2 + \mathbf{g}; \tag{3}$$

$$\mathrm{div}\mathbf{U}_j = 0; \quad j = 1, 2; \tag{4}$$

$$z \longrightarrow -\infty: \mathbf{U}_1 \longrightarrow 0; \tag{5}$$

$$z \longrightarrow \infty: \mathbf{U}_2 \longrightarrow 0; \tag{6}$$

$$z = 0: U_{2z} \approx V\frac{\partial\zeta}{\partial x} + \frac{\partial\zeta}{\partial t}; \tag{7}$$

$$U_{1z} \approx \frac{\partial\zeta}{\partial t}; \tag{8}$$

$$\boldsymbol{\tau}\cdot(\mathbf{n}\cdot\nabla)\mathbf{U}_1 + \mathbf{n}\cdot(\boldsymbol{\tau}\cdot\nabla)\mathbf{U}_1 = 0; \tag{9}$$

$$P_2(\mathbf{r}, t) - P_1(\mathbf{r}, t) + 2\nu\rho_1\frac{\partial U_{1z}}{\partial z} + P_\kappa - P_\sigma - P_* = 0. \quad (10)$$

Here, $P_i = P_j(\mathbf{r}, t)$ is the pressure inside an ith fluid; P_* is the saturated vapor pressure; ν is the kinematic viscosity of the lower fluid; $P_\sigma = -\sigma(\partial^2\zeta/\partial x^2)$ and $P_\kappa = 4\pi\kappa^2\kappa\zeta$ are, respectively, the surface tension force pressure under the liquid surface curved by the wave motion and the electrostatic pressure on the liquid surface because of the presence of the surface charge [17]; $\boldsymbol{\tau}$ and $\mathbf{n}$ are, respectively, the unit vectors of the tangent and normal to the surface of the lower fluid; and Δ is the Laplacian. The flow of the lower fluid will be sought by dividing the velocity field $\mathbf{U}_1 = \mathbf{U}_1(\mathbf{r}, t)$ into two components: potential (with velocity potential $\psi_1(\mathbf{r}, t)$) and vortical (described by the stream function). The flow of the upper perfect fluid is purely potential with the velocity potential ψ_2. Then, the expressions for the pressures P_2 and P_1 in the upper and lower fluids in (10) can be written in the form

$$\begin{aligned} P_1 &= -\rho_1\frac{\partial\psi_1}{\partial t} - \rho_1 g\zeta; \\ P_2 &= -\rho_2\frac{\partial\psi_2}{\partial t} - \rho_2 g\zeta - \rho_2 V\frac{\partial\psi_2}{\partial x}. \end{aligned} \quad (11)$$

It should also be noted that the saturated vapor pressure P_* on the surface of the fluid depends on its local curvature according to the well-known formula [18, 19]

$$P_* = P_\infty\exp(C_*/r); \quad C_* = 2\mu\sigma/\rho_1 RT,$$

where R is the gas constant, μ is the molecular weight, P_∞ is the saturated vapor pressure at infinity, and r is the mean radius of curvature at a given point.

In the approximation linear in small quantities, the mean surface curvature in the vicinity of a given point is expressed as

$$\frac{1}{r} \approx -\frac{1}{2}\frac{\partial^2\zeta}{\partial x^2};$$

accordingly, for the saturated vapor pressure, we have

$$P_* \approx P_\infty\exp\left(-C_*\frac{1}{2}\frac{\partial^2\zeta}{\partial x^2}\right).$$

Since for all real liquids, the exponent in the exponential is much less than unity, this expression simplifies to

$$P_* \approx P_\infty\left(1 - C_*\frac{1}{2}\frac{\partial^2\zeta}{\partial x^2}\right). \quad (12)$$

(4) In the approximation linear in the small quantities U_j and ζ, a solution to the problem stated by (1)–(12) is naturally sought in the form [20]

$$\begin{aligned} \psi_2(x, z, t) &= Vx + A\exp(-\kappa z)\exp(i\kappa x - i\omega t); \\ U_{1x}(x, z, t) &= (i\kappa B\exp(\kappa z) - lC\exp(lz))\exp(i\kappa x - i\omega t); \\ U_{1z}(x, z, t) &= (\kappa B\exp(\kappa z) + ilC\exp(lz))\exp(i\kappa x - i\omega t); \\ l^2 &= k^2 - i\omega\nu^{-1}; \quad \zeta(x, t) = D\exp(i\kappa x - i\omega t); \end{aligned} \quad (13)$$

where A, B, C, and D are unknown constants.

Substituting (13) into boundary conditions (7)–(12) yields a set of homogeneous algebraic equations for the unknown constants A, B, C, and D. The solvability condition for such a set provides a dispersion relation for capillary–barogravity waves in the system:

$$\begin{aligned} &\omega^2\left(1 + \frac{\rho_2}{\rho_1}\right) + \omega\left(4i\nu\kappa^2 - 2\frac{\rho_2}{\rho_1}\kappa V\right) \\ &- 4\nu^2\kappa^4\left(1 - \sqrt{1 - \frac{i\omega}{\nu\kappa^2}}\right) = \omega_0^2, \\ &\omega_0^2 = \frac{\kappa}{\rho_1}\left[g\rho_1\left(1 - \frac{\rho_2}{\rho_1}\right)\right. \\ &\left. + \sigma\kappa^2\left(1 + \frac{2\mu P_\infty}{\rho_1 RT}\right) - \kappa(\rho_2 V^2 + 4\pi\kappa^2)\right]. \end{aligned} \quad (14)$$

A solution to dispersion relation (14) can be expressed in analytical form for the case of a low-viscosity fluid (i.e., when the condition $|\omega/\nu\kappa^2| \gg 1$ is met):

$$\begin{aligned} \omega_{1,2} &= \left(1 + \frac{\rho_2}{\rho_1}\right)^{-1}\left[-\left(2i\nu\kappa^2 - \frac{\rho_2}{\rho_1}\right)\right. \\ &\left. \pm\left(\left(2i\nu\kappa^2 - \frac{\rho_2}{\rho_1}\kappa V\right)^2 + \omega_0^2\left(1 + \frac{\rho_2}{\rho_1}\right)\right)^{1/2}\right]. \end{aligned}$$

It is seen that, when ω_0^2 passes through zero and falls into the negative range, the complex frequency ω acquires an imaginary part. This means the appearance of wave solutions that exponentially grow with time, i.e., interface instability, which may be aperiodic (Tonks–Frenkel instability against surface charge [17]) at $V = 0$ or oscillatory (Kelvin–Helmholtz instability due to a tangential discontinuity in the velocity field [21]) at $V \neq 0$.

It follows that the electrolyte–saturated vapor interface will execute oscillatory motions that exponentially decrease ($\omega_0^2 > 0$) and exponentially increase ($\omega_0^2 < 0$) with time. The instability increment will grow with increasing V and κ.

Taking into account the processes of evaporation and condensation augments ω_0^2 by a term proportional to $2\mu P_\infty/\rho RT$. From (14), it is seen that this ratio stands for an increase in the pressure under the curved surface.

This correction can formally be included by introducing the effective surface tension coefficient $\sigma_* = \sigma(1 + 2\mu P_\infty/\rho RT)$, since this correction depends on the wavenumber in the same way as that taking into account the Laplace pressure under the curved liquid surface.

(5) The critical condition for the development of interface instability against the disturbing forces due to the electric field and the tangential discontinuity of the velocity field at the interface has the form $\omega_0^2 = 0$ (i.e., when ω_0^2 passes through zero) [13, 14, 19]. In the dimensionless variables such that $\rho_1 = \sigma = g = 1$, this conditions is recast as

$$x^2(1+\gamma) - x(W + \mathrm{We}) + (1-\rho) = 0, \qquad (15)$$

where

$$W \equiv \frac{4\pi\kappa^2 a}{\sigma}; \quad \mathrm{We} \equiv \frac{\rho_2 a V^2}{\sigma}; \quad x \equiv \kappa a;$$

$$a^2 \equiv \frac{\sigma}{\rho_1 g}; \quad \gamma \equiv \frac{2\mu P_\infty}{\rho_1 RT}; \quad \rho \equiv \frac{\rho_2}{\rho_1}.$$

Equating the first derivative of ω_0 with respect to κ to zero yields a relationship for the wavenumber κ of the most unstable capillary mode (i.e., the value of κ for the highest increment mode). This relationship is easy to write in the dimensionless variables:

$$3x^2(1+\gamma) - 2(W + \mathrm{We})x + (1-\rho) = 0. \qquad (16)$$

Solutions to set (15)–(16) has the form

$$W_{\mathrm{cr}} = 2[1 + (\gamma - \rho) - \gamma\rho]^{1/2} - \mathrm{We};$$
$$x_{\mathrm{cr}} = \left(\frac{1-\rho}{1+\gamma}\right)^{1/2}. \qquad (17)$$

Thus, as the saturated vapor pressure grows (the parameters γ and ρ increases), so does the wavelength of the most unstable capillary mode. The results of calculation by (17) are given in Fig. 2. The effect of the parameters γ and ρ on the critical value W_{cr} (which characterizes the electric field pressure on the interface) depends on a relationship between their magnitudes and may both increase and decrease W_{cr}, as follows from Fig. 3. The parameters γ and ρ are always less than unity: at the critical point for water, $\gamma \approx 0.5$ and $\rho = 1$ [22] (in subsequent physicochemical estimations, we assume that the parameters of the electrolyte coincide with those of water). Taking for definiteness that $T = 546$ K and $P = 58.8 \times 10^5$ Pa, we find $\gamma \approx 0.06$ and $\rho \approx 0.04$. Under these conditions (and also under lower temperatures), a slight increase in the saturated vapor pressure (a slight increase in γ and ρ) causes W_{cr} to grow. When approaching the critical point ($\gamma \longrightarrow 0.5$ and $\rho \longrightarrow 1$), ρ exceeds γ and a rise in the saturated vapor pressure decreases W_{cr}. An increase in the Weber number We always decreases W_{cr} and does not have an effect on x_{cr}, according to (17).

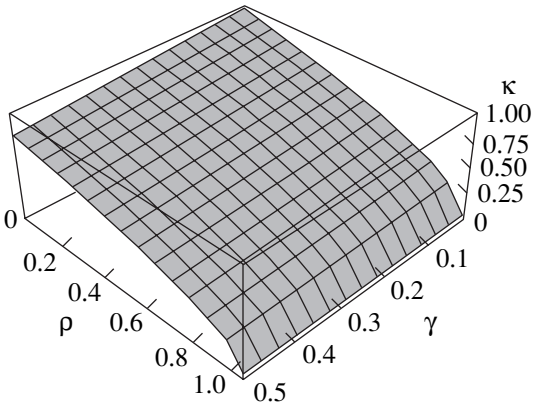

Fig. 2. Dimensionless wavenumber κ vs. vapor-to-electrolyte density ratio ρ and dimensionless parameter γ, which characterizes the vapor pressure.

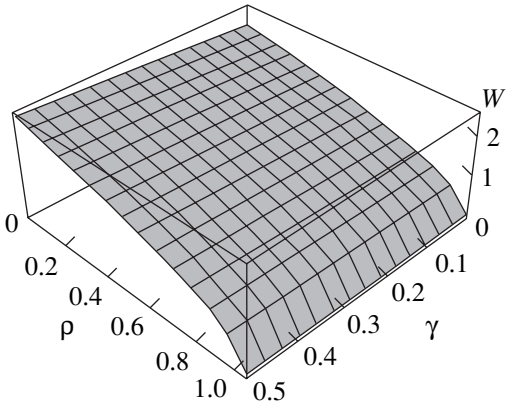

Fig. 3. Dimensionless parameter W, which characterizes the stability of the charged interface against the surface charge, vs. vapor-to-electrolyte density ratio ρ and dimensionless parameter γ, which characterizes the vapor pressure. We = 0.

From (15), it follows that the critical parameter of instability W_{cr} for a capillary mode with a wavenumber κ is related to x, γ, and ρ through the relationship

$$W_{\mathrm{cr}} = x(1+\gamma) + \frac{1-\rho}{x} - \mathrm{We}.$$

Hence, as x grows, the effect of the saturated vapor pressure on the onset of instability builds up. In other words, under a sufficiently strong electric field, when a continuous sequence of capillary modes from a certain wavenumber range becomes unstable, the shortest length modes are affected by the saturated vapor pressure to the greatest extent.

From Fig. 3 and the estimates made above, it can be inferred that the effect of the saturated vapor pressure (the parameter γ) and density (ρ) on the instability of the charged interface is insignificant if the temperature and pressure are far from the critical values for the elec-

trolyte. For $T = 546$ K and $P = 58.8 \times 10^5$ Pa (in this case, $\gamma \approx 0.06$ and $\rho \approx 0.04$), the critical value of W is $W_{cr} \approx 2$ (with $V \leq 30$ cm/s, when We $\ll 1$ and its influence on W_{cr} can be neglected). This value of W_{cr} corresponds to the critical electric field strength $E_{cr} \approx 18$ kV/cm at $\sigma = 21$ dyn/cm (such a low surface tension coefficient for water is associated with its fast decrease with increasing temperature [22]). In the experiments where $U = 150$ V and $h \approx 100$ μm, the electric field strength at the interface was ≈15 kV/cm.

Thus, the electrolyte–saturated vapor interface is stable at the values of T and P considered. The electric current passing between the electrodes in the phenomenon under study is unrelated to the instability of the charged liquid surface. Such instability may yet arise when the potential difference is increased. Indeed, as follows from Fig. 3, the parameter W_{cr} drops fast when the temperature and pressure approach their critical values (i.e., when the parameters γ and ρ grow). This means that the interface may become unstable in the oscillatory regime when the potential applied to the electrodes is raised. The onset of oscillatory instability will lead to the instability and oscillations of the current passing in the circuit, as observed in experiments [1, 2, 5].

(6) Earlier, we considered and rejected an ion source delivering ions to the vapor–gas sheath through the interface instability that is accompanied by the emission of heavily charged droplets, clusters, and ions from the electrolyte surface. Another source of ions to sustain the electric current in the sheath may be the field or thermal evaporation of ions [23–25] from the liquid electrolyte surface.

Iribarne and Thomson [23] suggested a mechanism of the field evaporation of ions and charged clusters from electrolyte solutions. This mechanism is physically similar to the mechanism of field ion evaporation from the metal surface that was developed theoretically for field ion microscopy [24] and liquid-metal ion sources [25] and is related to the thermal activation of the process. According to this mechanism, metal ions evaporate by means of electric-field-assisted thermal activation above the Schottky barrier (which arises in the presence of an electric field E at the metal surface). The rate constant K of metal ion evaporation here is given by

$$K = \omega \exp\left[-\frac{Q - (z_*^3 |q|^3 E)^{1/2}}{kT}\right], \qquad (18)$$

$$Q \equiv \Lambda + J - \varphi,$$

where k is the Boltzmann constant, T is absolute temperature, ω is the atomic oscillation frequency, q is the charge of an ion, and z_* is the charge number.

In the exponent, Q is the energy of activation of ion evaporation. In a virtual thermionic cycle of field emission microscopy [24], this parameter is estimated as follows. A neutral atom evaporates from the metal surface, absorbing the energy of sublimation Λ; the atom ionizes, which requires an additional energy of ionization J; and the electron released returns to the metal, giving off an energy φ equal to the electron work function. The second term in the numerator of the exponent describes a decrease in the activation energy due to the Schottky effect.

Expression (18) may also be used to describe the field evaporation of ions or ionic clusters from electrolyte solutions [23, 26]. In this case, ω (used in terms of the absolute reaction rate theory) is replaced by kT/h, where h is the Planck constant, and Q (the energy of activation of ion evaporation from the metal surface) is replaced by ΔH_+ (the change in the enthalpy when an ion or ionic cluster passes from the solution to free space). The value of ΔH_+ is equal in value but opposite in sign to ΔH_* (the change in the enthalpy upon the solvation of an ion or cluster in the solution). In this case, however, the energy of activation of evaporation turns out to be excessively high and cannot provide satisfactory agreement with experimental data. Therefore, another evaluation of Q based on the model that is applied in the theory of field metal evaporation [24] was suggested [16, 27].

Following [16, 27], consider the possibility of an Na^+ ion thermally evaporating from aqueous sodium solutions (NaI and NaCl). We will calculate the activation energy of the field evaporation of the ion from the solution surface in a virtual thermionic cycle involving NaI and NaCl molecules, as is done when field ion evaporation from the metal surface is analyzed [24]. However, unlike [24], of interest to us is not the breakaway of the ion from the continuous metal surface by the field but the field-stimulated decay of a neutral NaCl or NaI molecule on the electrolyte surface (where the field is high) into a Na^+ cation and I^- (or Cl^-) anion with the subsequent evaporation of the Na^+ ion. Let Λ be the energy of sublimation; D, the energy of molecule dissociation into two neutral atoms (Na and I or Cl); J, the energy of Na atom ionization; L, the affinity of electrons for a I or Cl atom; and φ, the electron work function for water. Then, the energy of field evaporation of a Na^+ ion from the electrolyte solution is given by

$$Q = \Lambda + D + J - \varphi - L. \qquad (19)$$

In other words, the salt molecule sublimates from the solution and dissociates into two atoms; the Na atom ionizes, and the electron and the neutral I (or Cl) atom return to the solution, where the electron combines with the I (Cl) atom to form an anion. It is remembered that the thermochemical process is virtual. Actually, under the action of the field, the salt molecule decays into a Na^+ cation and I^- (Cl^-) anion immediately on the surface of the solution. According to [28], with $T = 300$ K, $\lambda = 2.08$ eV and $D = 3.76$ eV for a NaI molecule and $\lambda = 2.39$ eV and $D = 4.22$ eV for a NaCl molecule. In addition, the ionization potential of a Na atom is $J = 5.14$ eV, and the electron affinity for I and Cl atoms is $L = 3.06$ and 3.61 eV, respectively [22]. The

electron work function for water is $\varphi = 6.13$ eV [29]. Substituting these values into (19) yields the energy of activation of the field evaporation of a Na^+ ion from NaI and NaCl aqueous electrolytes: $Q_{NaI} = 1.78$ eV and $Q_{NaCl} = 2.01$ eV. Eventually, the rate constant of field ion evaporation from the electrolyte solution must be calculated by the formula

$$K = (kT/h)\exp\left[-\frac{Q-(z_*^3|q|^3E)^{1/2}}{kT}\right], \qquad (20)$$

where

$$Q = \Lambda + D + J - \varphi - L.$$

To find the rate V of field ion evaporation from the unit surface area of the solution based on the rate constant defined by (20), one must multiply the rate constant K by N, where N is the number of nondissociated salt molecules on the solution surface subjected to a high electric field: $V = KN$. The dimension of V is [s^{-1} cm^{-2}] (i.e., the number of ions evaporating from one square centimeter per second).

Let us evaluate the rate of the field evaporation of Na^+ ions from a NaCl solution with a concentration of several tens of weight percent for the field strength at the solution surface $E = 15$ kV/cm and $T = 546$ K. It is easy to check that N (the number of nondissociated NaCl molecules per square centimeter of the interface) is $\sim 10^{15}$ cm^{-2}. According to the above, the activation energy for the field evaporation of a Na^+ ion is $Q_{NaCl} = 2.01$ eV at $T = 300$ K. We also take into account that the heat of sublimation decreases with increasing temperature. Using analytical approximations $\Lambda = \Lambda(T)$ (see, e.g., [30]), we find that $Q_{NaCl} \approx 1.6$ eV with $T = 546$ K. Then, according to (20), $K \approx 2$ s^{-1} and the rate of the field evaporation of Na^+ ions from the unit surface area of the electrolyte is found to be $V \approx 2 \times 10^{15}$ s^{-1} cm^{-2}. This corresponds to the current density at the electrolyte surface $J \approx 3 \times 10^{-4}$ A/cm^2. This value is four orders of magnitude lower than that observed in experiments [1–12]. However, the disagreement is related to the choice of the model electrolyte used in the qualitative estimations. If we had taken an aqueous solution of NaBr, for which the energy of activation of Na^+ ion evaporation is much lower ($Q_{NaBr} = 1.03$ eV for $T = 300$ K [27]), the current density due to Na^+ ion evaporation would have been ~ 10 A/cm^2 at $T = 546$ K.

CONCLUSIONS

The electric current in the vapor–gas sheath around the electrode immersed in an electrolyte is due to the field and thermal evaporation of ions from the electrolyte surface. The instability of the electrolyte surface against the surface charge and oscillatory tangential flow of the vapor causes current oscillations in the circuit.

When the saturated vapor pressure on the interface plays a decisive role in shaping the interface, the critical conditions for the onset of the instability of the charged interface depend significantly on both the saturated vapor pressure and the ratio of the vapor and liquid densities.

ACKNOWLEDGMENTS

The authors thank P.N. Belkin, who called their attention to the problem discussed in this paper.

This work was supported by a grant from the President of the Russian Federation (grant no. 00-15-9925).

REFERENCES

1. P. Ludewig, Ann. Phys. (Leipzig), No. 25, 467 (1908).
2. H. H. Kellog, J. Electrochem. Soc. **97** (4), 133 (1950).
3. V. S. Vanin, Elektrotermiya, No. 55, 18 (1967).
4. K. Jnoue and U. Shima, J. Jpn. Inst. Met. **32**, 755 (1969).
5. O. J. Garbarz and C. Guilpin, J. Chem. Phys. **72**, 207 (1975).
6. P. N. Belkin, E. A. Pasinkovskiĭ, and A. A. Faktorovich, Izv. Akad. Nauk Mold. SSR, Ser. Fiz.-Tekh. Mat. Nauk, No. 1, 82 (1977).
7. P. N. Belkin, V. I. Ganchar, and Yu. N. Petrov, Dokl. Akad. Nauk SSSR **291**, 1116 (1986) [Sov. Phys. Dokl. **31**, 1001 (1986)].
8. P. N. Belkin and V. I. Ganchar, Élektron. Obrab. Mater., No. 5, 59 (1988).
9. P. N. Belkin and S. N. Belkin, Inzh.-Fiz. Zh. **57**, 159 (1989).
10. V. I. Ganchar, Inzh.-Fiz. Zh. **60**, 92 (1991).
11. P. N. Belkin and A. K. Tovarkov, Vestn. Kostromsk. Gos. Univ., No. 3, 8 (2001).
12. S. Yu. Shadrin and P. N. Belkin, Élektron. Obrab. Mater., No. 3, 24 (2002).
13. A. I. Grigor'ev, O. A. Grigor'ev, and S. O. Shiryaeva, Zh. Tekh. Fiz. **62** (9), 12 (1992) [Sov. Phys. Tech. Phys. **37**, 904 (1992)].
14. O. A. Grigor'ev and S. O. Shiryaeva, Zh. Tekh. Fiz. **66** (2), 23 (1996) [Tech. Phys. **41**, 124 (1996)].
15. A. I. Grigor'ev, Pis'ma Zh. Tekh. Fiz. **27** (7), 89 (2001) [Tech. Phys. Lett. **27**, 305 (2001)].
16. A. I. Grigor'ev, V. V. Morozov, and S. O. Shiryaeva, Zh. Tekh. Fiz. **72** (10), 33 (2002) [Tech. Phys. **47**, 1237 (2002)].
17. L. D. Landau and E. M. Lifshitz, *Course of Theoretical Physics*, Vol. 8: *Electrodynamics of Continuous Media* (Nauka, Moscow, 1982; Pergamon, New York, 1984).
18. P. Reist, *Introduction to Aerosol Science* (Macmillan, New York, 1984; Mir, Moscow, 1987).
19. S. O. Shiryaeva, Pis'ma Zh. Tekh. Fiz. **22** (13), 43 (1996) [Tech. Phys. Lett. **22**, 540 (1996)].
20. V. G. Levich, *Physicochemical Hydrodynamics* (Fizmatgiz, Moscow, 1959).
21. L. D. Landau and E. M. Lifshitz, *Course of Theoretical Physics*, Vol. 6: *Fluid Mechanics* (Nauka, Moscow, 1986; Pergamon, New York, 1987).

22. A. P. Babichev, N. A. Babushkina, A. M. Bratkovskiĭ, *et al.*, *Handbook of Physical Quantities*, Ed. by I. S. Grigoriev and E. Z. Meilikhov (Énergoatomizdat, Moscow, 1991; CRC, Boca Raton, 1997).
23. J. V. Iribarne and B. A. Thomson, J. Chem. Phys. **64**, 2287 (1976).
24. E. W. Muller and T. T. Tsong, *Field Ion Microscopy: An Introduction to Principles, Experiments, and Applications* (Elsevier, New York, 1969; Metallurgiya, Moscow, 1972).
25. R. Gomer, Appl. Phys. **19**, 365 (1979).
26. N. B. Zolotoĭ, Zh. Tekh. Fiz. **65** (11), 159 (1995) [Tech. Phys. **40**, 1175 (1995)].
27. A. I. Grigor'ev, Pis'ma Zh. Tekh. Fiz. **27** (7), 89 (2001) [Tech. Phys. Lett. **27**, 305 (2001)].
28. L. V. Gurvich, I. V. Veĭts, V. A. Medvedev, *et al.*, *Thermodynamic Properties of Substances: A Reference Book* (Nauka, Moscow, 1982), Vol. 4, Part 1.
29. V. S. Fomenko, *Emissive Properties of Materials: A Handbook* (Naukova Dumka, Kiev, 1981).
30. M. M. Viktorov, *Calculation of Physicochemical Quantities: Methods and Applications* (Khimiya, Leningrad, 1977).

Translated by V. Isaakyan

Technical Physics, Vol. 48, No. 7, 2003, pp. 829–836. Translated from Zhurnal Tekhnicheskoĭ Fiziki, Vol. 73, No. 7, 2003, pp. 28–36.

GASES AND LIQUIDS

Prediction of the Penetrating Power of Metallic Shaped Charge Jets Subjected to an Intense Electric Current Pulse

S. V. Fedorov*, A. V. Babkin*, S. V. Ladov*, G. A. Shvetsov, and A. D. Matrosov****

** Bauman State Technical University, Vtoraya Baumanskaya ul. 5, Moscow, 107005 Russia*
e-mail: sm4@sm.bmstu.ru
*** Lavrent'ev Institute of Hydrodynamics, Siberian Division, Russian Academy of Sciences, pr. Akademika Lavrent'eva 15, Novosibirsk, 630090 Russia*

Received December 6, 2002

Abstract—A method for evaluating the penetrating (piercing) power of shaped charges under the condition when an intense electric current pulse is applied to a shaped charge jet is developed. The buildup of waist-type MHD instability and the volume damage of the jet material are viewed as possible mechanisms behind a reduction of the penetrating power of a shaped charge jet under the current action. With this method, electrodynamic action parameters that provide a significant reduction of the penetrating power of a shaped charge jet are calculated for shaped charges of various penetrability. © *2003 MAIK "Nauka/Interperiodica"*.

INTRODUCTION

It is known that a short high-intensity electrodynamic action (EDA) on a fast metallic shaped-charge jet (hereafter jet for brevity) produced by the explosion of shaped charges (SCs) with a metal-coated charge hollow [1] may reduce its penetrating power [2–6]. Such an action is carried out by passing an intense electric current pulse through the jet immediately before it strikes an obstacle.

The simplest EDA device consists of two plates (electrodes) spaced by an insulating layer and connected to an electric power supply (Fig. 1). Such an element is placed before an obstacle and, after the jet has penetrated the insulator and the electrical circuit has been closed, provides a current action on the jet moving in the electrode gap.

The pioneering investigation into this problem was performed more than 20 years ago in the Lavrent'ev Institute of Hydrodynamics (Siberian Division, Russian Academy of Sciences) [7]. It was suggested that an EDA on a jet be used to reduce the penetration of the jet. In past years, a large body of experimental data has been gathered [2–9]. The emphasis in the experiments was on a two-electrode EDA device (Fig. 1) with a capacitor bank as an electric energy source. In [8], the feasibility of a magnetic cumulative generator for the current action was considered. Experimental results were obtained for SCs of diameter d_0 (Fig. 1) varying from 30 to 100 mm and are represented mainly as data on the reduction of the SC penetrability, curves of the discharge current in the electrode gap, and X-ray patterns of SCs subjected to an intense current action.

However, the available experimental data are too scarce for any practically valuable generalizations to be made. The parameters of the electrode system (e.g., the distance h to the shaped charge and the electrode gap δ, Fig. 1), as well as the amplitude and duration of the current pulse, were chosen almost arbitrarily without any substantiation and can by no means be considered optimal in terms of accomplishing the desired effect (jet

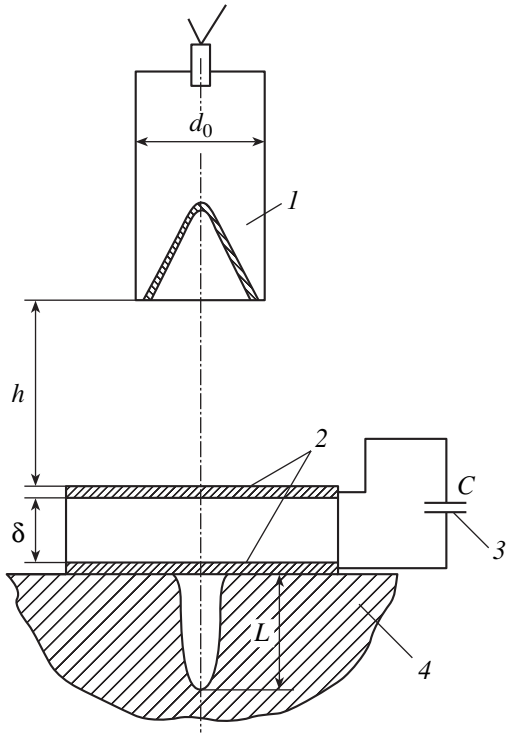

Fig. 1. Two-electrode configuration for the application of a current pulse to a shaped charge jet: (*1*) shaped charge, (*2*) plane electrodes, (*3*) electric energy source (capacitor bank), and (*4*) obstacle.

1063-7842/03/4807-0829$24.00 © 2003 MAIK "Nauka/Interperiodica"

damage) with a minimal energy consumption. Also, the available experimental data are insufficient to reveal the partial effects of the EDA parameters on the reduction of the jet penetrability (any appreciable studies on this issue were not carried out).

In the experiments with jets of diameter 100 mm, noticeable damage of the jets was observed at a capacitor bank energy of 1 MJ or higher [5] (the huge dimensions of such a capacitive energy storage eliminate its practical use). Obviously, the current action conditions should be optimized in order to decrease the energy spent on the reduction of the jet's penetrating power and make such an approach practically feasible. The optimization cannot be accomplished without knowing the physical reasons why the penetrating power of a jet subjected to a current pulse decreases. In addition, there is an acute need for physicomathematical models of the EDA-induced deformation of the jet and numerical methods for predicting the results of the current action on the jet.

This work is an attempt to elaborate a behavioral model of a jet exposed to EDA and to reveal the partial effects of the EDA parameters on the penetrating power of the jets produced by different shaped charges.

PHYSICAL MODELS

As follows from the experiments, high-intensity EDAs may substantially reduce the penetrating power of the jet. The X-ray pattern of a jet exposed to an intense EDA [2, 5, 7] suggests that the most plausible mechanisms responsible for a decrease in the penetrability of the jet are the buildup of waist-type MHD instability and the volume damage of the jet material. Both are due to compressive ponderomotive stresses and the thermal effect that arises when a current passes through the jet.

The analysis of MHD instability under the current action was based on the model [10], where individual portions of the jet are considered as elements of an incompressible variable-radius rigid–plastic rod under the assumption that its cross section remains plane throughout the deformation process. The force action of the current is taken into account by specifying the surface magnetic pressure. The model also includes the thermal softening of the rod material, with the current density uniformly distributed over the cross section in this case.

Numerical calculations showed that the EDA may not only accelerate the development of the jet's natural plastic instability, causing the jet to decay into fragments, but also, if sufficiently intense, favor the disk formation process [9], when the jet fragments shrink along the axis and extend in the radial direction. Because of this process, the effective length of the jet decreases considerably. To describe the MHD instability due to the current action on the quantitative level, we introduced the shape factor, which characterizes the deviation of the jet fragment shape from cylindrical, and the coefficient of velocity inversion, which characterizes the variation of the axial velocity along the fragment length [11]. These coefficients depend on three dimensionless process-controlling parameters

$$u = \frac{\rho \dot{\varepsilon}_{z,\,\mathrm{in}}^2 R_{\mathrm{in}}^2}{\sigma_{Y0}}, \quad s = \frac{\mu_0 J^2}{8\pi^2 R_{\mathrm{in}}^2 \sigma_{Y0}},$$

$$q = \frac{J^2 \eta_0 (1 + \gamma(T_{\mathrm{in}} - T_0))}{\pi^2 \dot{\varepsilon}_{z,\,\mathrm{in}} R_{\mathrm{in}}^4 \rho c_{\mathrm{v}} (T_{\mathrm{melt}} - T_{\mathrm{in}})}.$$

Here, $\mu_0 = 4\pi \times 10^{-7}$ is the magnetic constant; ρ is the jet material density; R_{in}, $\dot{\varepsilon}_{z,\,\mathrm{in}}$, and T_{in} are, respectively, the initial radius, axial strain rate, and temperature of a jet fragment by the time of current action; σ_{Y0} is the initial value of the yield strength of the jet fragment; J is the current strength; η_0 is the resistivity of the jet material at normal temperature T_0; γ is the temperature coefficient of resistance; c_{v} is the heat capacity at constant volume of the jet material; and T_{melt} is the melting point of the jet material.

The parameter u, which equals the ratio of inertial forces acting in the jet to the yield strength, reflects the natural deformation of the jet [12]. The parameter s (the ratio of the magnetic pressure to the yield strength) characterizes the force action of the current, and the parameter q (the ratio of the Joule heat evolving in the rod of radius R_{in} for the characteristic time $1/\dot{\varepsilon}_{z,\,\mathrm{in}}$ to the amount of heat necessary to heat the rod to the melting point) describes the thermal action of the current.

It is noteworthy that, under typical EDA conditions, jet fragments take on a disk-like form not in the electrode gap but beyond the EDA region because of the jet material inertia. Once the current action has been switched off, the dynamics of the disk formation process, which can be followed from the variation of the shape factor, depends on the value of the velocity conversion coefficient by the end of the action and on the degree of the thermal softening of the jet. In the calculation of the penetrability of the jet, the shape factor, according to the hydrodynamic theory [13], was used to determine the effective length of jet fragments subjected to the current action.

The conditions for the volume damage of the jet appear when it leaves the electrode gap, since the compressive action of the electromagnetic forces suddenly ceases. This may cause the dispersion of the thermally softened jet material in the radial direction [3, 14]. When considering this mechanism of damage, we applied the model of a uniformly elongating cylindrical compressible elastic–plastic rod, where it is assumed that the yield strength of the material decreases linearly with growing temperature [14, 15]. By numerical calculations, it was found that the rate of jet material radial dispersion may be estimated with a simple energy rela-

tionship. This relationship implies that, when the magnetic pressure dies out, the potential energy of the jet uniformly compressed by the magnetic pressure is spent on material damage; on quenching the kinetic energy of jet fragments, which radially converge to the axis of symmetry of the motion; and, on the contrary, on imparting the kinetic energy of radial expansion to the fragments. In this case, the work needed to damage the material was assumed to be equal to the potential energy of its uniform extension with a mean stress depending on the instantaneous value of the yield strength [11].

The penetrating power of the damaged portion of the jet was calculated based on the hydrodynamic theory of penetration combined with the concept of critical penetration velocity. It was assumed that, once the jet has come out of the EDA region, (1) the mean density of the material decreases continuously with a rate depending on the rate of radial expansion and (2) the lower limit of the jet velocity with which it can penetrate an obstacle rises with decreasing density [13].

The factors that are responsible for the volume damage and for MHD instability come into play at roughly equal parameters of the current pulse [9]. In the computational technique for finding the penetration power of a shaped charge under electrodynamic action, we therefore took into account the possibility of their joint effect. The rate of the radial dispersion of the damaged jet fragments was evaluated with allowance for variations in their shape and the rate of axial deformation due to MHD instability. The geometric and kinematic parameters of the jet were calculated by the technique given in [16].

Figure 2 compares the calculated data for the reduction of the penetration depth for shaped charges when the jet was subjected to electrodynamic action with experimental results obtained in the Lavrent'ev Institute of Hydrodynamics (Siberian Division, Russian Academy of Sciences) [17, 18] (Figs. 2a, 2b) and also in the All-Russia Research Institute of Experimental Physics, Russian Federal Nuclear Center [4, 5] (Sarov, Nizhegorodsk oblast) (Figs. 2c, 2d). The data in Figs. 2a–2c were obtained for SCs of diameter 50 mm; those in Fig. 2d, for SCs with a coating base diameter of 100 mm.

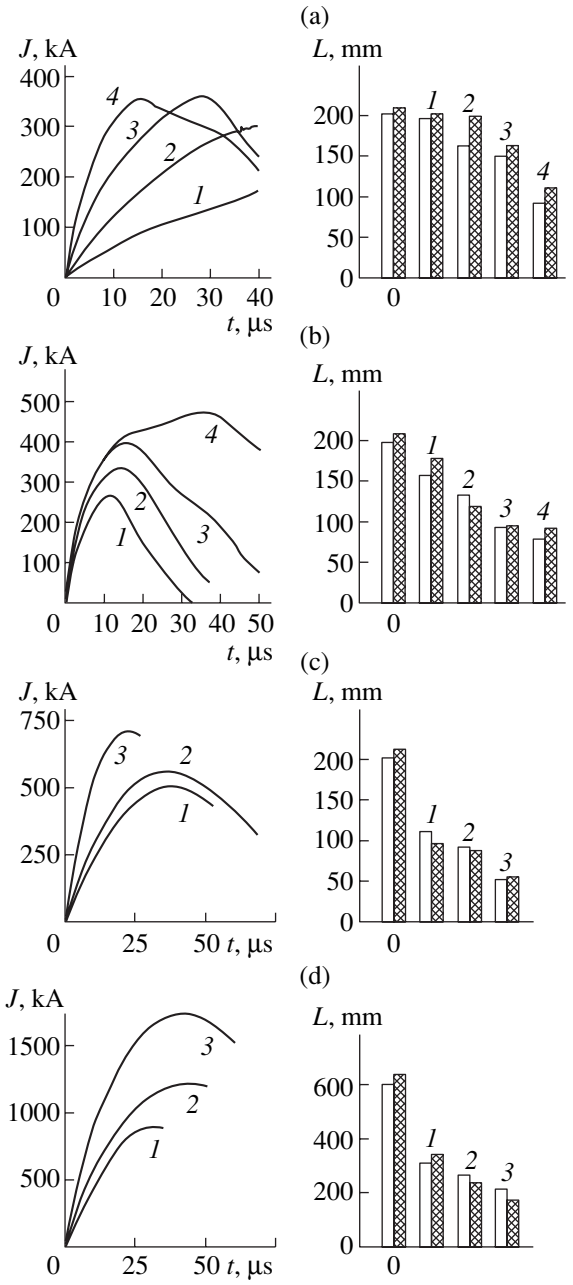

Fig. 2. Experimental vs. calculated data for the penetration power of the jet subjected to the pulsed current action. (a, b) h = 40 mm, δ = 21 mm; (c) h = 50 mm, δ = 30 mm; and (d) h = 115 mm, δ = 45 mm. (The figures by the bar graphs for the penetration L correspond to the numbers of the discharge current curves recorded in the experiments. "0" marks the bar graph obtained in the absence of current action.)

OPTIMAL CONDITIONS FOR THE CURRENT DISCHARGE

Good agreement between the analytical and experimental results over a wide range of current pulse parameters (Fig. 2) has spurred the determination of optimal EDA parameters to decrease the piercing power of various SCs. The charges had diameters d_0 = 70 mm (the depth of penetration into a homogeneous steel obstacle is L_0 = 440–500 mm), 115 mm (L_0 = 700–750 mm), and 150 mm (L_0 = 950–1100 mm). Below, they will be designated as SC_1 (d_0 = 70 mm), SC_2 (d_0 = 115 mm), and SC_3 (d_0 = 150 mm).

The EDA on the jet was accomplished with a capacitor bank as an energy source and a two-electrode EDA device (Fig. 1).

The equivalent electrical circuit of the discharge initiated by the jet-closed EDA device comprises the

inductance L_g and resistance R_g of the electrode gap, as well as the inductance L_r and resistance R_r of the remaining part of the discharge network (including the energy source). The total inductance $L_t = L_r + L_g$ and resistance $R_t = R_r + R_g$ of the discharge circuit distort the current pulse shape and, hence, affects the EDA efficiency. As the inductance and resistance grow, the discharge current strength in the circuit diminishes. Therefore, the L_r and R_r components should be minimized as much as possible in a given setup.

For an electrode gap of width δ, the inductance L_g can be estimated by the formula for an isolated cylindrical conductor [19]:

$$L_g \approx \frac{\mu_0}{2\pi}\left(\ln\left(\frac{2\delta}{r_f}\right) - 1\right)\delta,$$

where r_f is the radius of the jet fragment closing the gap.

For an electrode spacing δ of no more than 100 mm and a jet radius of several millimeters (which is typical of SCs of diameter $d_0 \approx 100$ mm), the inductance L_r varies between 0.05 and 0.1 μH. The total inductance L_t of the EDA system may reach several tenths of a microhenry, as indicated by the results of laboratory experiments [5]. Thus, in actual conditions, the inductance L_r somewhat exceeds the inductance L_g of the electrode gap.

The active resistance R_g of the gap closed by the jet fragment was measured as 0.01 Ω [5]. For the resistance of the jet fragment between the electrodes, simple estimators yield values that are more than one order of magnitude lower. It appears that a major contribution to the interelectrode resistance is from plasma contacts between the jet and electrodes: the jet punches holes in the electrodes, with a hole diameter far exceeding the transverse dimension of the jet, and a gas discharge between the electrode and jet fragment closes the circuit. Under these conditions, the resistance R_r, which usually does not exceed 0.001 Ω, may be neglected.

Based on the experimental data and estimates made, we took the following control values of the total inductance and resistance: $L_t = 0.25$ μH and $R_t = 0.01$ Ω. The variation of the inductance L_g and resistance R_g when jet fragments with various diameters (cross sections) passed through the electrode spacing was neglected, since it is small.

When L_t and R_t are constant, the discharge current law in the circuit with a capacitance C depends on the dimensionless parameter $\gamma = 0.5R_t\sqrt{C/L_t}$: with $\gamma < 1$, the oscillatory discharge regime is established; for $\gamma \geq 1$, the discharge is aperiodic. The time variation of the pulsed current J in the circuit, as well as its maximal value J_m and rise time t_m, are defined by well-known relationships from the theory of transients [19]. As for the efficiency of the current action on the jet, it depends on the initial voltage U_0 and capacitance C of the capacitor bank, as well as on the inductance L_t and resistance R_t of the discharge circuit.

Among the design parameters of the EDA device that influence the efficiency of jet decay are the electrode spacing δ and the distance h of the electrode system to the shaped charge (Fig. 1). When selecting the electrode–charge spacing, we considered the presence and absence of a screen in front of the EDA device. In the former case, it was assumed that the shaped charge detonates upon striking the screen and the distance h between the front electrode and the SC base is $h = F + h_1$, where F is the design "focus" length [1, 13] of an SC (1.5–2.0 charge diameters) and h_1 is the spacing between the screen and front electrode. In the absence of the screen, $h = F$.

The screening of the electrode system is expected to favor the current-induced decay of the jet, since its transverse dimensions decrease with distance from the charge because of extension. However, since the shaped charge jet eventually decays into gradientless fragments [1, 12, 13], the possibility of the fragments entering into the electrode gap [20] must be taken properly into account in selecting the electrode–screen spacing. Breaks between the jet fragments increase the gap resistance R_g and ultimately may quench the current discharge. Because of this, we considered a small screen–electrode separation ($h_1 = 100$ mm).

In almost all the experiments where the jet decayed under the action of a current pulse, the relative electrode spacing was varied in the interval $\delta/d_0 = 0.4$–0.6 [5, 17, 18]. In our calculations, values of the electrode spacing δ were similar or slightly larger (up to $\delta/d_0 \approx 1$). As the electrode gap widens, the time during which the jet fragments experience the current action increases, enhancing the jet decay effect. Simultaneously, however, the discharge initiation conditions may deteriorate especially if the jet decays directly between the electrodes. In the calculations, the effect of the jet state in the electrode spacing on the discharge parameters and the possibility of discharge quenching were not taken into account. Accordingly, values of the gap that were used in the calculations did not differ from those employed in the experiments.

In all the calculations, it was assumed that the SC axis at the time of detonation is perpendicular to the electrode plane and that the obstacle placed behind the EDA device is made of steel.

COMPUTATIONAL RESULTS

The factors influencing the EDA efficiency were considered more carefully using SC_2 as an example, whose depth of penetration is intermediate between those of SC_1 and SC_3. Figure 2 shows the reduction of the penetration vs. the energy $W = CU_0^2/2$ of the capacitive storage with various capacitances (for the

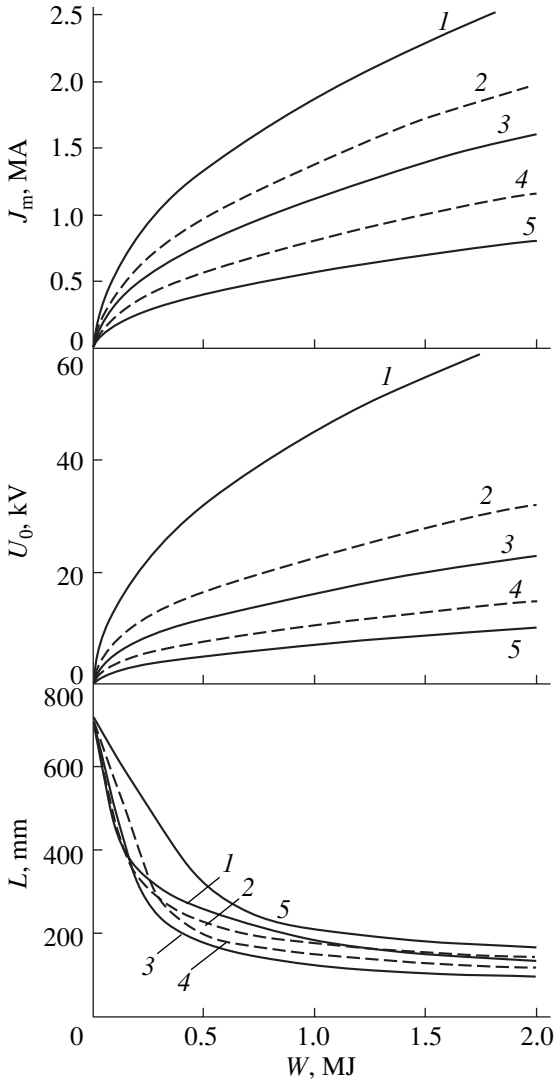

Fig. 3. Maximal discharge current, initial voltage across the capacitor bank, and depth of SC_2 penetration vs. source energy. The bank capacitance C = (*1*) 1, (*2*) 4, (*3*) 8, (*4*) 20, and (*5*) 50 mF.

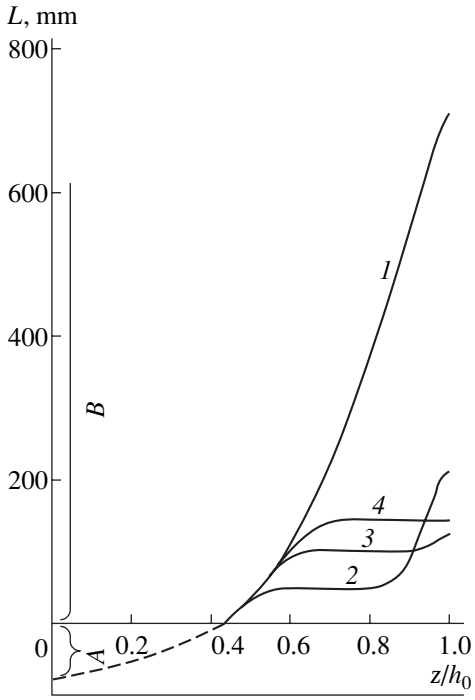

Fig. 4. Increase in the SC_2 jet penetration as the integrated effect of the fragments from different parts of the metal coating (the z coordinate is measured from the coating top along its axis; h_0 is the coating height) (*1*) under natural conditions and under the action of the capacitor bank with C = (*2*) 4, (*3*) 8, and (*4*) 20 mF. *A*, EDA device; *B*, obstacle.

unscreened electrode gap, $\delta = 75$ mm, $L_t = 0.25$ μH, and $R_t = 0.01$ Ω). Also shown are the initial voltages across the bank and the amplitudes J_m of the discharge current (under real conditions, equipment-related restrictions may be imposed on the voltages and allowable currents).

As follows from Fig. 3, at the given electrode spacing and discharge loop, there is an optimal capacitance of the bank (C = 8 mF) at which the penetrating power is the lowest. With smaller or higher capacitances, the EDA efficiency declines. The presence of the optimum is due to the fact that the efficiency of interaction (synchronization) between the current pulse and jet fragments passing through the gap depends on the bank capacitance. As follows from the analysis of the penetrability of different fragments, the EDA device with an optimum-capacitance energy storage provides the most appropriate distribution of the current pulse energy when it is spent on the destruction of the front and tail of the jet. Figure 4 shows how the SC_2 penetration increases because of the sequential strikes of jet elements in the absence of the current action and in the presence of the EDA device fed by a capacitor bank with the energy W = 1 MJ and different capacitances. It is seen that, when the capacitance is lower than optimal (C = 4 mF), the current rises rapidly and front fragments of the jet are effectively destroyed. However, the discharge is too short in this case and the tail of the jet remains intact, keeping its penetrating power. Conversely, if the capacitance is too large (C = 20 mF), the tail of the jet breaks up, while a significant part of the front has a chance to break through the electrode gap that is undestroyed because of the slow rise time.

The penetration vs. energy of the storage curves in Fig. 3 clearly demonstrate that the amount of the desired effect tends toward saturation as the energy grows. The EDA efficiency markedly increases with energy up to a certain threshold value. For example, when the capacitance is optimal (C = 8 mF), the penetration of the SC_2 can be reduced by more than thrice (from 700 to 200 mm) with W = 350–400 kJ. In this case, the initial voltage U_0 across the bank is about 10 kV and the maximal discharge current J_m, no more

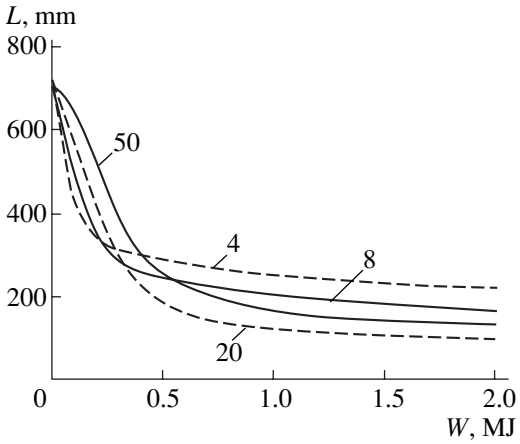

Fig. 5. Penetrating power of SC_2 vs. the energy and capacitance of the capacitor bank with a screen placed in front of the EDA device. The figures by the curves are the values of C in mF.

than 750 kA. The further fivefold increase in the energy to 2 MJ ($U_0 \approx 22$ kV, $J_m \approx 1.6$ MA) additionally reduces the depth of penetration by only 100 mm (it is of interest that the total kinetic energy of the jet produced by SC_2 is roughly 700 kJ). Thus, as the bank energy grows, the effect of penetration reduction is saturated, indicating that the penetration cannot be eliminated completely. As the length of the residual penetration approaches the SC diameter d_0, a further increase in the energy of the storage becomes inefficient, since the penetration decreases very slightly. The residual penetration is associated with the front end of the jet, which is impossible to decay completely, since it has a high velocity and breaks through the electrode gap at the very beginning of the current discharge, when the amplitude has not yet reached the jet-breaking value.

The optimal capacitance of the bank, which provides the maximal conversion of the bank energy to the jet decay energy, depends on the EDA parameters (design parameters of the EDA device and electrical parameters of the discharge circuit). Figure 5 shows the depth of penetration vs. energy and capacitance of the storage when the EDA device is away from the SC (h_1 = 100 mm; the other parameters are the same as in Fig. 3). As the electrode–SC distance grows, so does the time it takes for jet fragments to fall into the electrode gap. The total time the jet takes to pass through the EDA area also increases. Because of this, much longer current pulses are needed to effectively act on the tail of the jet. Therefore, for the remote EDA device (h_1 = 100 mm), the optimal capacitance should be increased: in our experiments, the least penetration was obtained with C = 20 mF (Fig. 5). For C = 50 mF, the EDA efficiency of the remote device was also improved. In the case of C = 4 and 8 mF, the jet decay effect weakens: the current pulses are too short to entirely "cover" the jet.

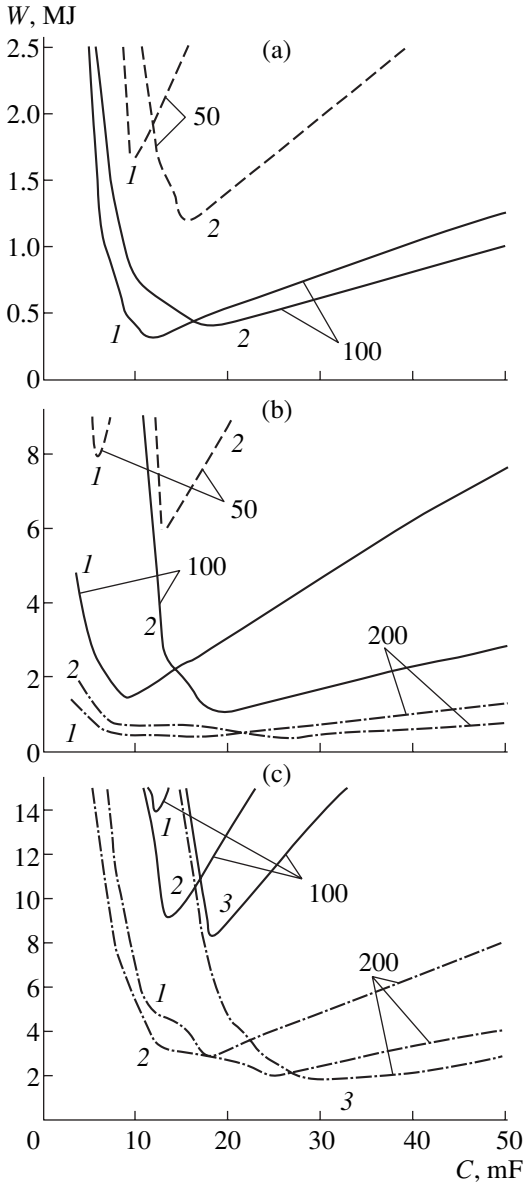

Fig. 6. Energy vs. capacitance relationships needed to achieve a desired level of the residual penetration when the jet is subjected to the current action. (a) SC_1: (*1*) δ = 50 mm, h_1 = 0 and (*2*) δ = 50 mm, h_1 = 100 mm; (b) SC_2: (*1*) δ = 75 mm, h_1 = 0 and (*2*) δ = 125 mm, h_1 = 100 mm; and (c) SC_3: (*1*) δ = 75 mm, h_1 = 0; (*2*) δ = 125 mm, h_1 = 0; and (*3*) δ = 125 mm, h_1 = 100 mm. The figures by the curves give the values of L (≥50) in millimeters.

For the shaped charges SC_1, SC_2, and SC_3, we determined the parameters of the EDA system that provide the reduction of the penetration to 50, 100, and 200 mm (Fig. 6) with discharge circuit parameters being equal to the control values: L_t = 0.25 μH and R_t = 0.01 Ω. The capacitance of the energy source was used as a varied parameter. For each capacitance value, we found the initial voltage U_0 across the capacitor bank and the stored energy $W = CU_0^2/2$ that allowed for the

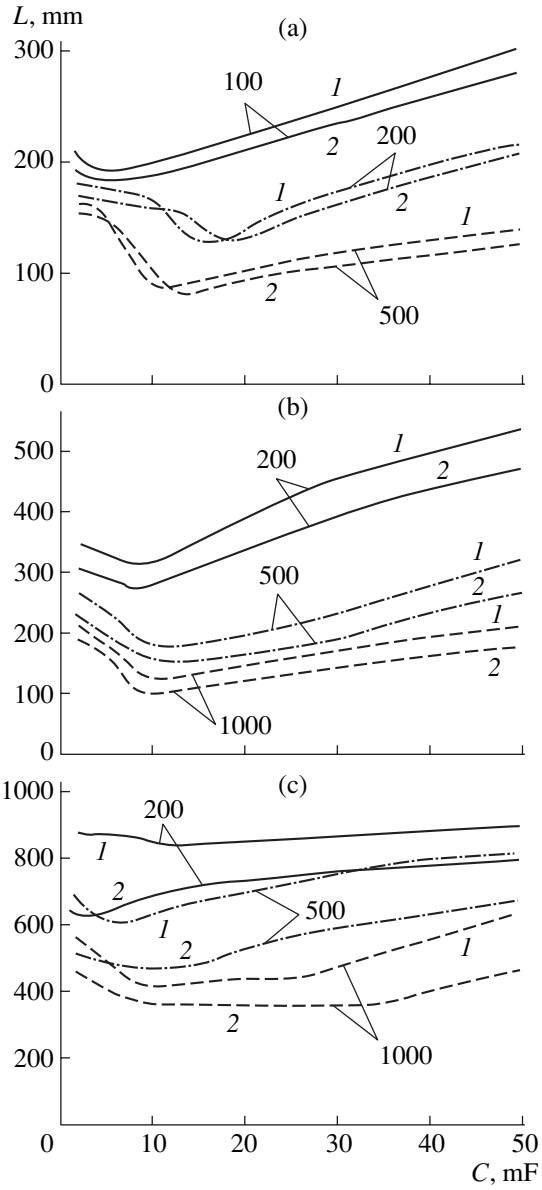

Fig. 7. Reduction of the penetrating power for SC_1, SC_2, and SC_3 by the unscreened EDA element at a given source energy: (a) SC_1 (δ = (*1*) 50 and (*2*) 75 mm), (b) SC_2 (δ = (*1*) 75 and (*2*) 125 mm); and (c) SC_3 (δ = (*1*) 75 and (*2*) 125 mm). The figures by the curves give the values of W (≥100) in kilojoules.

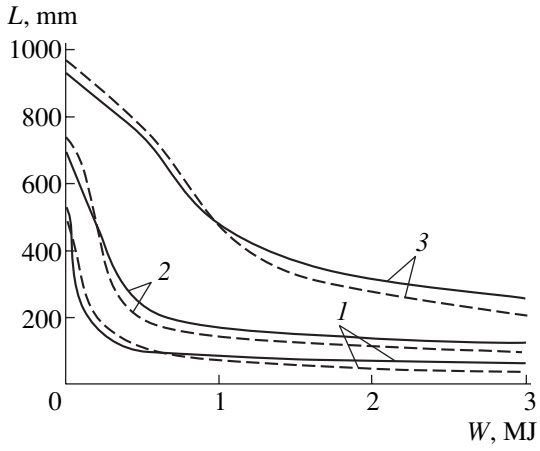

Fig. 8. Reduction of the penetrating power for various SCs by the EDA device with δ = 75 mm vs. the energy of the 30-mF capacitor bank. h_1 = 0 (continuous lines) and 100 mm (dashed lines). (*1*) SC_1, (*2*) SC_2, and (*3*) SC_3.

reduction of the penetration to a desired level. We considered various designs of the EDA device (h_1 = 0 and 100 mm and different electrode spacings δ).

As follows from Fig. 6, optimal energy source parameters appear in this case too: namely, there is a capacitance of the source that provides a desired efficiency at a minimal energy consumption. As requirements for the reduction become more stringent, the minimum at the energy–capacitance curves sharpens: even small deviations from the optimal capacitance cause much extra energy consumption. As the electrode spacing δ grows and the distance h of the EDA device to the charge increases, the optimal capacitance rises because the time the jet takes to pass through the electrode system rises. By varying these two design parameters simultaneously, one can minimize the energy needed to reach a desired reduction. For SC_1 and the unscreened (h_1 = 0) EDA device with δ = 50 mm, the residual penetration L = 50 mm is achieved at an energy of 1.6 MJ and a capacitance C = 10 mF. The presence of the screen (h_1 = 100 mm) with the optimal capacitance C = 15 mF decreases this energy by more than 0.5 MJ. For SC_3, which has the highest penetrating power, the residual penetration L = 200 mm is provided by using the EDA device with the electrode spacing δ = 125 mm, a source capacitance of 25–35 mF, and a source energy of somewhat higher than 2 MJ. In this case, the penetration L = 100 mm is unfeasible: this would require a capacitor bank of energy about 10 MJ. At the same time, to decrease the penetration of SC_2 to the same level requires 1.2–1.5 MJ and to L = 200 mm, 300–400 kJ.

Of practical interest is a relationship between the penetration of shaped charges of various diameters and the capacitor bank energy. We constructed penetration curves for bank energies of 100, 200, 500, and 1000 kJ (Fig. 7). The capacitance of the bank and the electrode distance of the unscreened EDA devices were varied.

As follows from the calculations, the penetration may be minimized by selecting an appropriate capacitance value of the source at a given source energy (Fig. 7). The penetration may be decreased still further by expanding the electrode gap. For SC_1 and an energy of 100 kJ, the least possible penetration is roughly 200 mm (L/L_0 = 0.4). At an energy of 200 kJ, the penetration of SC_1 and SC_2 may be reduced to 125–150 mm (L/L_0 = 0.25–0.30) and 300–350 mm (L/L_0 = 0.43–0.50), respectively. With this energy and δ = 75 mm, the

penetrability of SC_3 remains nearly the same. For δ = 125 mm, the residual penetration of SC_3 with W = 200 kJ may be decreased to 650–700 mm (L/L_0 = 0.68–0.74), with the capacitance being relatively small (within 5 mF). The bank of energy 500 kJ makes it possible to reduce the penetration powers of SC_1, SC_2, and SC_3 to L = 75–100 mm (L/L_0 = 0.15–0.20), 150–200 mm (L/L_0 = 0.21–0.29), and 500–600 mm (L/L_0 = 0.53–0.63), respectively.

Of practical value is to compare the efficiencies of the same EDA system (with fixed parameters) when it "opposes" various SCs. We considered the EDA system with C = 30 mF, L_t = 0.25 μH, and R_t = 0.01 Ω. It was assumed that the penetrability of SC_1, SC_2, and SC_3 is quenched by a screened (h_1 = 100 mm) of unscreened EDA device with the electrode spacing δ = 75 mm. From the penetration vs. bank energy curves depicted in Fig. 8, one can evaluate capacitor bank parameters that can attenuate the cumulative action of the charges to a desired level.

CONCLUSIONS

Thus, a simple engineering analysis makes it possible to predict the penetrating power of metallic shaped charge jets subjected to the pulsed current action. In addition, the approach suggested allows one to consider the effects of the EDA device parameters and the parameters of shaped charges on the penetration both separately and in combination. At the same time, the results presented in this work should be considered only as a first approximation to the solution of the optimization problem for EDA devices. They need analytical refinement and experimental verification. However, our results may serve as a guide in experiments on shaped charge jet decay by electric current pulses.

REFERENCES

1. W. P. Walters and J. A. Zukas, *Fundamentals of Shaped Charges* (Wiley, New York, 1989).
2. A. D. Matrosov and G. A. Shvetsov, Prikl. Mekh. Tekh. Fiz. **37** (4), 9 (1996).
3. C. E. Pollock, *Megagauss Magnetic Field Generation and Pulsed Power Applications*, Ed. by M. Cowan and R. B. Spielman (Nova Science, New York, 1994), pp. 309–316.
4. A. I. Pavlovskiĭ, L. N. Plyashkevich, A. M. Shuvalov, and A. Ya. Brodskiĭ, Zh. Tekh. Fiz. **64** (2), 76 (1994) [Tech. Phys. **39**, 157 (1994)].
5. A. I. Pavlovskiĭ, L. N. Plyashkevich, A. M. Shuvalov, and A. Ya. Brodskiĭ, Zh. Tekh. Fiz. **64** (5), 43 (1994) [Tech. Phys. **39**, 479 (1994)].
6. G. A. Shvetsov, A. D. Matrosov, A. V. Babkin, and A. Ya. Brodskiĭ, in *Proceedings of the 19th International Symposium on Ballistics, Interlaken, 2001*, Vol. 2, p. 851.
7. G. A. Shvetsov and A. D. Matrosov, in *Proceedings of the 7th International Conference on Megagauss Magnetic Field Generation and Related Topics* (VNIIÉF, Sarov, 1997), Part 2, p. 948.
8. G. A. Shvetsov, Yu. L. Bashkatov, A. S. Matrosov, *et al.*, in *Proceedings of the 7th International Conference on Megagauss Magnetic Field Generation and Related Topics* (VNIIÉF, Sarov, 1997), Part 2, p. 956.
9. A. V. Babkin, V. A. Kruzhkov, S. V. Ladov, *et al.*, in *Proceedings of the 7th International Conference on Megagauss Magnetic Field Generation and Related Topics* (VNIIÉF, Sarov, 1997), Part 2, p. 961.
10. S. V. Fedorov, A. V. Babkin, and S. V. Ladov, Oboronnaya Tekh., Nos. 1–2, 49 (1998).
11. G. A. Shvetsov, A. D. Matrosov, S. V. Fedorov, *et al.*, in *Proceedings of the 3rd International Conference "Khariton Topical Lectures"* (VNIIÉF, Sarov, 2002), p. 263.
12. A. V. Babkin, S. V. Ladov, V. M. Marinin, and S. V. Fedorov, Prikl. Mekh. Tekh. Fiz. **40** (4), 25 (1999).
13. *Physics of Explosion*, Ed. by K. P. Stanyukovich (Nauka, Moscow, 1975).
14. A. V. Babkin, M. E. Kolychev, S. V. Ladov, and S. V. Fedorov, Oboronnaya Tekh., No. 4, 47 (1995).
15. A. V. Babkin, V. A. Kruzhkov, É. V. Lugovoĭ, and S. V. Fedorov, Oboronnaya Tekh., No. 9, 36 (1993).
16. V. M. Marinin, A. V. Babkin, and V. I. Kolpakov, Oboronnaya Tekh., No. 4, 34 (1995).
17. G. A. Shvetsov, A. D. Matrosov, A. V. Babkin, *et al.*, Prikl. Mekh. Tekh. Fiz. **41** (3), 19 (2000).
18. S. V. Fedorov, A. V. Babkin, S. V. Ladov, *et al.*, Fiz. Goreniya Vzryva **36** (6), 126 (2000).
19. H. Knoepfel, *Pulsed High Magnetic Fields* (North-Holland, Amsterdam, 1970; Mir, Moscow, 1972).
20. L. N. Plyashkevich, A. M. Shuvalov, G. M. Spirov, *et al.*, Fiz. Goreniya Vzryva **38** (5), 124 (2002).

Translated by V. Isaakyan

Technical Physics, Vol. 48, No. 7, 2003, pp. 837–845. Translated from Zhurnal Tekhnicheskoĭ Fiziki, Vol. 73, No. 7, 2003, pp. 37–45.

GASES AND LIQUIDS

Analytical Solution to the Problem of a Temperature Jump in a Metal

A. V. Latyshev and A. A. Yushkanov

Moscow State Regional University, ul. Radio 10a, Moscow, 105005 Russia

e-mail: latyshev@orc.ru, yushkanov@mtu-net.ru

Received October 31, 2002

Abstract—An analytical solution to the problem of a temperature jump in a metal is obtained. The jump is caused by a heat flow to the surface. An exact expression for the heat-induced electric field is derived. Based on the exact expressions, the electric field profiles are plotted for different ratios of the electron free path to the Debye length. It is shown that the field profile near the surface may differ substantially from the Debye profile. © *2003 MAIK "Nauka/Interperiodica".*

INTRODUCTION

The temperature distribution near a metal surface is of primary importance in considering problems of heat exchange between a metal and its environment, especially at low temperatures. This problem is also topical for small-size metallic samples, which are widely encountered in microelectronics. For small metallic samples, taking into account the influence of the surface on the temperature distribution becomes of crucial importance.

Consider the plane interface between a metal and its environment. We assume that there is a heat flux to (or from) the metal surface. Let us introduce the Cartesian coordinate system centered on the surface with the x axis normal to the surface and directed into the metal. Then, the heat flux at distances from the surface far exceeding the electron free path l_0 is described by a constant temperature gradient $K_t = dT/dx$ (hereafter the anisotropy of the metal properties is neglected). This gradient is assumed to be small enough; that is, the relative temperature drop over the length l_0 is much smaller than unity.

In the kinetic theory, the layer that is adjacent to the interface and has a thickness of about l_0 is usually referred to as the Knudsen layer. Outside the Knudsen layer, the temperature profile takes the form $T = T_0 + K_t x$. Let us denote the surface temperature as T_s. The value $\Delta T = T_0 - T_s$ is called the temperature jump. At small temperature gradients, it is proportional to the gradient K_t:

$$\Delta T = C_t l_0 K_t. \qquad (1)$$

The K_t-independent coefficient C_t is named the temperature jump coefficient. To determine C_t, a kinetic equation near the metal surface in the Knudsen layer must be solved. In practice, the relative jump $\varepsilon_t = C_t l_0 k_t$, where $k_t = K_t/T_s$ is the relative temperature gradient ΔT, is usually used instead of the absolute temperature jump.

In the general case, the process of heat conduction in metals produces an electric field [1]. As a result, the problem of the temperature distribution near the surface arises along with the problem of electric field behavior in the Knudsen layer.

In [2], we considered the behavior of the electric field at the interface between crystallites in a metal with an electric current. The analysis [2] was performed for zero temperature, i.e., for the case when the temperature is much lower than the temperature of the degenerate electron gas. No other studies in this area have come to our notice.

The aim of this paper is to calculate a temperature jump in a metal based on an analytical solution to the kinetic equation for electrons and to construct the electric field profile near the surface.

Note that we consider the general case of an arbitrary degree of electron gas degeneration. Therefore, the results reported are valid in a wide range of temperatures and for a wide class of materials including semimetals.

KINETIC EQUATION

Consider a metal with a spherical Fermi surface. In the kinetics of metals, the electron kinetic equation is often used in the so-called τ approximation [1, 3, 4]:

$$\frac{\partial f}{\partial t} + (\mathbf{v}\cdot\nabla) f + e_0\mathbf{E}\cdot\frac{\partial f}{\partial \mathbf{p}} = \frac{1}{\tau}(f_F^0 - f). \qquad (2)$$

Here, f is the electron distribution function, e_0 is the electron charge, $\mathbf{p}$ is the electron momentum, $\mathbf{E}$ is the electric field, $\mathbf{v}$ is the electron velocity, and τ is the time of electron relaxation to the Fermi equilibrium distribution function f_F^0.

1063-7842/03/4807-0837$24.00 © 2003 MAIK "Nauka/Interperiodica"

For a finite temperature, the dependence of the relaxation time τ on the electron velocity should be taken into account. If electron scattering by impurities dominates, the assumption that the electron free path remains constant seems to be the most reasonable. In this case, the relaxation time τ is inversely proportional to the electron velocity; i.e., $\tau = l_0/w$. Here, l_0 is the electron free path, $w = |\mathbf{v} - \mathbf{u}|$, and $\mathbf{u}$ is the mean electron velocity. In metals, the condition $u \ll v$ is fulfilled in all physically realizable cases. Below, we shall use v instead of w.

In addition, at a finite temperature, the kinetic equation describing the phonon behavior should, in general, be taken into account together with the electron kinetic equation.

Let the phonon distribution function f_{ph} satisfy the kinetic equation [1, 4]

$$\frac{\partial f_{\text{ph}}}{\partial t} + (\mathbf{C} \cdot \nabla) f_{\text{ph}} = J(f_{\text{ph}}, f). \quad (3)$$

Here, $\mathbf{C}$ is the phonon velocity and $J(f_{\text{ph}}, f)$ is the collision integral taking into account phonon scattering by electrons and lattice defects, as well as phonon–phonon scattering.

At a finite temperature, the Fermi distribution function with some effective temperature T_* and effective chemical potential μ^* must be used as the electron equilibrium distribution function in Eq. (2) instead of f_{F}^0, which corresponds to zero temperature. In this case, the kinetic equation for electrons in the τ approximation is expressed as

$$\frac{\partial f}{\partial t} + (\mathbf{v} \cdot \nabla) f + e_0 \mathbf{E} \cdot \frac{\partial f}{\partial \mathbf{p}} = \frac{v}{l_0}(f_{\text{F}}^* - f). \quad (4)$$

Here,

$$f_{\text{F}}^* = f_{\text{F}}(\mu^*, T_*) = \left[\exp\left(\frac{mv^2}{2k_0T_*} - \frac{\mu^*}{k_0T_*}\right) + 1\right]^{-1}$$

is the Fermi distribution function (Fermian) and k_0 is the Boltzmann constant.

The electron conversion law leads to the equality

$$\int v f \, d\Omega_{\text{F}} = \int v f_{\text{F}}^* \, d\Omega_{\text{F}}. \quad (5)$$

which follows from Eq. (4). Here, $d\Omega_{\text{F}} = (2s + 1)(2\pi\hbar)^{-3} dp$, $\hbar$ is the Planck constant, and s is the electron spin. The integrals are taken over the entire velocity space. For most metals, the contribution of the electron subsystem to heat transfer dominates [4]. Therefore, the phonon contribution to heat transfer will be neglected.

In the stationary case, electron kinetic equation (4) yields

$$\nabla \cdot \mathbf{Q}_{\text{e}} = \frac{v}{l_0}\left(\int v \frac{m}{2} v^2 f_{\text{F}}^* d\Omega_{\text{F}} - \int v \frac{m}{2} v^2 f \, d\Omega_{\text{F}}\right), \quad (6)$$

where $\mathbf{Q}_{\text{e}}$ is the heat flux transferred by electrons and m is the electron effective mass. In the absence of heat sources, the total heat flux remains constant: $\nabla \cdot \mathbf{Q} = 0$. When the phonon contribution to heat transfer in a metal can be neglected, $\nabla \cdot \mathbf{Q}_e = 0$, according to Eq. (6). Then, Eq. (5) yields

$$\int v \frac{m}{2} v^2 f \, d\Omega_{\text{F}} = \int v \frac{m}{2} v^2 f_{\text{F}}^* d\Omega_{\text{F}}. \quad (7)$$

Equations (5) and (7) define the parameters T_* and μ^* of kinetic equation (4).

In the approximation considered, the kinetic equations for electrons, (4), and phonons, (3), are mutually independent. In this case, a number of fine effects, for example, the entrapment of electrons by phonons, may be missed and the τ approximation, which is considered in this paper, fails. Let us suppose that the mass velocity is much lower than the electron velocity and the resulting temperature drops over the length l_0 are small in comparison with the electron gas temperature. Under these assumptions, the problem can be linearized. The distribution function will be looked for in the form $f = f_{\text{F}}^{\text{s}} + \varphi(t, \mathbf{r}, \mathbf{v})g$. Here, $f_{\text{F}}^{\text{s}} = f_{\text{F}}(\mu_{\text{s}}, T_{\text{s}})$, φ is a new unknown function, μ_{s} is the chemical potential of electrons scattered by the surface,

$$g = -\frac{\partial}{\partial \varepsilon_{\text{s}}} f_{\text{F}}^{\text{s}}; \quad \varepsilon_{\text{s}} = \frac{mv^2}{2k_0T_{\text{s}}} - \frac{\mu_{\text{s}}}{k_0T_{\text{s}}}.$$

Introducing the designations

$$\mathbf{c} = \sqrt{\frac{m}{2k_0T_{\text{s}}}}\mathbf{v}, \quad \alpha = \frac{\mu_{\text{s}}}{k_0T_{\text{s}}}, \quad \varepsilon_* = \frac{mv^2}{2k_0T_*} - \frac{\mu_*}{k_0T_*},$$

we have

$$f_{\text{F}}^*(\varepsilon_*) = \frac{1}{\exp(\varepsilon_*) + 1}, \quad f_{\text{F}}^{\text{s}}(c, \alpha) = \frac{1}{\exp(c^2 - \alpha) + 1},$$

$$g = g(c, \alpha) = \frac{\exp(c^2 - \alpha)}{[\exp(c^2 - \alpha) + 1]^2}.$$

Let us linearize the local Fermian f_{F}^* by passing to dimensionless variables. Note that

$$\varepsilon_* = \frac{T_{\text{s}}}{T_*}\left[\frac{m}{2k_0T_{\text{s}}}v^2 - \frac{\mu_*}{k_0T_{\text{s}}}\right] = \frac{T_{\text{s}}}{T_*}(c^2 - \alpha_*),$$

$$\alpha_* = \frac{\mu_*}{k_0T_{\text{s}}}.$$

Taking into account that $T_* = T_s + \delta T_s$ and $\alpha_* = \alpha + \delta\alpha_*$, we obtain

$$\varepsilon_* = c^2 - \alpha - \frac{\delta T_*}{T_s}(c^2 - \alpha) - \delta\alpha_*,$$

hence,

$$\delta\varepsilon_* = -\delta\alpha_* - (c^2 - \alpha)\frac{\delta T_*}{T_s},$$

where

$$\delta\varepsilon_* = \varepsilon_* - \varepsilon_s, \quad \varepsilon_s = c^2 - \alpha.$$

Consequently,

$$f_F^* = f_F^s + \left(\frac{\partial f_F^*}{\partial \varepsilon_*}\right)_{\varepsilon_* = \varepsilon_s}\delta\varepsilon_*$$

or

$$f_F^* = f_F^s + g\left[\delta\alpha_* + (c^2 - \alpha)\frac{\delta T_*}{T_s}\right].$$

Now we introduce the dimensionless variables

$$\mathbf{e} = \frac{e_0 l_0}{k_0 T_s}\mathbf{E}, \quad t_* = t\sqrt{\frac{2k_0 T_s}{m l_0^2}}, \quad \mathbf{r}_* = \frac{\mathbf{r}}{l_0}.$$

Hereafter, the asterisks will be omitted. In the dimensionless variables, Eq. (4) takes the form

$$\frac{\partial\varphi}{\partial t} + (\mathbf{c}\cdot\nabla)\varphi - \mathbf{c}\cdot\mathbf{e} = c\left[\delta\alpha_* + (c^2 - \alpha)\frac{\delta T_*}{T_s} - \varphi\right]. \quad (8)$$

The parameters of this equation, $\delta\alpha_*$ and δT_*, are found from the conservation laws (Eqs. (5) and (7)), which can now be expressed as

$$\int\left[\delta\alpha_* + (c^2 - \alpha)\frac{\delta T_*}{T_s} - \varphi\right]cg d^3c = 0,$$

$$\int\left[\delta\alpha_* + (c^2 - \alpha)\frac{\delta T_*}{T_s} - \varphi\right]c^3 g d^3c = 0.$$

From this system, we find

$$\frac{\delta T_*}{T_s} = -\frac{r_1(\alpha)}{2\pi\Delta(\alpha)}\int\varphi cg d^3c + \frac{l(\alpha)}{2\pi\Delta(\alpha)}\int\varphi c^3 g d^3c,$$

$$\delta\alpha_* - \alpha\frac{\delta T_*}{T_s} = \frac{r_3(\alpha)}{2\pi\Delta(\alpha)}\int\varphi cg d^3c - \frac{r_1(\alpha)}{2\pi\Delta(\alpha)}\int\varphi c^3 g d^3c.$$

Here,

$$r_1(\alpha) = 4\int_0^\infty c\ln[1 + \exp(\alpha - c^2)]dc,$$

$$l(\alpha) = \ln(1 + e^\alpha),$$

$$r_3(\alpha) = 12\int_0^\infty c^3\ln[1 + \exp(\alpha - c^2)]dc,$$

$$\Delta(\alpha) = l(\alpha)r_3(\alpha) - r_1^2(\alpha).$$

Let us represent Eq. (8) in the conventional form. Using the above formulas, we obtain for the right of Eq. (8)

$$c^2\frac{\delta T_*}{T_s} + \left(\delta\alpha_* - \alpha\frac{\delta T_*}{T_s}\right) = \frac{1}{2\pi}\int\left[\frac{l^2(\alpha)}{\Delta(\alpha)}c^2 c'^2 - (c^2 + c'^2)\frac{r_1(\alpha)l(\alpha)}{\Delta(\alpha)} + \frac{r_3(\alpha)l(\alpha)}{\Delta(\alpha)}\right]\frac{g(c', \alpha)c'}{l(\alpha)}d^3c'.$$

Note that

$$\frac{l^2(\alpha)}{\Delta(\alpha)}c^2 c'^2 - (c^2 + c'^2)\frac{r_1(\alpha)l(\alpha)}{\Delta(\alpha)} + \frac{r_3(\alpha)l(\alpha)}{\Delta(\alpha)} = 1 + \frac{l^2(\alpha)}{\Delta(\alpha)}\left(c^2 - \frac{r_1(\alpha)}{l(\alpha)}\right)\left(c'^2 - \frac{r_1(\alpha)}{l(\alpha)}\right).$$

With the designations

$$k(c, c') = 1 + \frac{l^2(\alpha)}{\Delta(\alpha)}\left(c^2 - \frac{r_1(\alpha)}{l(\alpha)}\right)\left(c'^2 - \frac{r_1(\alpha)}{l(\alpha)}\right),$$

$$d\Omega(\alpha) = \frac{g(c', \alpha)c'}{l(\alpha)}d^3c',$$

we can express Eq. (8) as

$$\frac{\partial\varphi}{\partial t} + c\varphi(t, \mathbf{r}, \mathbf{c}) - \mathbf{c}\cdot\mathbf{e}(\mathbf{r}) = \frac{c}{2\pi}\int k(c, c')\varphi(t, \mathbf{r}, \mathbf{c})d\Omega(\alpha). \quad (9)$$

STATEMENT OF THE PROBLEM

Let the half-space $x > 0$ be filled with a metal and the plane xy be coincident with the metal boundary. We assume that electrons reflect from the surface purely diffusively [4] and that the heat flux is directed perpendicularly to the surface. Then, the electric field related to the heat flux is also normal to the surface and all the parameters of the problem depend on the coordinate x alone.

A set of equations describing this problem consists of kinetic equation (9) for electrons (in view of the time invariance of the problem) and an equation for the electric field. In dimensionless form, these equations have the form

$$\mu\frac{\partial\varphi}{\partial x} + \varphi(x, \mu, c) - \mu e(x)$$

$$= \frac{1}{l(\alpha)}\int_{-1}^{1}\int_{0}^{\infty} k(c, c')\varphi(x, \mu', c')g(c')c'^3 d\mu' dc',$$

$$e'(x) = a_0^2 \int_{-1}^{1}\int_{0}^{\infty} \varphi(x, \mu, c)g(c)c^2 d\mu dc, \tag{10}$$

$$a_0^2 = \frac{e_0^2 m^2 l_0^2}{\pi^2 \hbar^3 \varepsilon_0}\sqrt{\frac{2k_0 T_s}{m}},$$

where ε_0 is the permittivity and $\mu = c_x/c$. The boundary-value conditions taking into account the diffusive scattering of electrons by the surface [4, 5] and the conditions in the bulk of the metal are

$$\begin{gathered}\varphi(0, \mu, c) = A_0, \quad 0 < \mu < 1,\\ \varphi(x, \mu, c) = \varphi_h(x, \mu, c) + o(1),\\ x \longrightarrow +\infty, \ -1 < \mu < 0,\\ e(0) = 0, \quad e(x) = e_h + o(1), \quad x \longrightarrow +\infty.\end{gathered} \tag{11}$$

Here,

$$\varphi_h = \varepsilon_t\left(c^2 - \frac{r_0(\alpha)}{s(\alpha)}\right) + k_t(x - \mu)\left(c^2 - \frac{r_0(\alpha)}{s(\alpha)}\right) - h_0(\alpha)k_t\mu,$$

$$e_h = -k_t h_0(\alpha), \quad \Delta_0(\alpha) = r_0(\alpha)l(\alpha) - s(\alpha)r_1(\alpha),$$

$$h_0(\alpha) = \frac{\Delta_0(\alpha)}{s(\alpha)l(\alpha)},$$

$$r_0(\alpha) = \frac{3}{2}\int_0^\infty [1 + \exp(\alpha - c^2)]dc,$$

$$s(\alpha) = \int_0^\infty \frac{\exp(\alpha - c^2)}{1 + \exp(\alpha - c^2)}dc.$$

The function φ_h stands for the thermal conductivity of the electron gas in the bulk of the metal. The process of heat conduction generates an electric field e_h (the thermoelectric effect [1]). The condition $e(0) = 0$ assumes the absence of an electric field outside the metal. The constant A_0 is not preset: it is determined from a solution to the problem. This constant is related to the condition that electrons do not cross the surface. In such a statement, the current equals zero everywhere at $x > 0$; i.e.,

$$\int (c\mu)\varphi(x, \mu, c)g(c)c^2 d\mu dc = 0.$$

We stress that the functions φ_h, e_h are solutions to system (10).

DECOMPOSITION OF THE PROBLEM

According to the structure of the function φ_h, we look for the function φ in the form

$$\varphi(x, \mu, c) = h_1(x, \mu) + (c^2 - r_0(\alpha)/s(\alpha))h_2(x, \mu).$$

Substituting this expression into Eqs. (10) and calculating the right-hand side of the first of Eqs. (10) yields

$$\frac{1}{l(\alpha)}\int_{-1}^{1}\int_{0}^{\infty} k(c, c')\varphi(x, \mu', c')g(c')c'^3 dc' d\mu'$$

$$= \frac{1}{l(\alpha)}\int_{-1}^{1}\int_{0}^{\infty} h_1(x, \mu')g(c')c'^3 dc' d\mu'$$

$$+ \frac{1}{l(\alpha)}\int_{-1}^{1}\int_{0}^{\infty}\left(c'^2 - \frac{r_1(\alpha)}{l(\alpha)}\right)h_2(x, \mu')g(c')c'^3 dc' d\mu' + \frac{l(\alpha)}{\Delta(\alpha)}$$

$$\times\left(c^2 - \frac{r_1(\alpha)}{l(\alpha)}\right)\int_{-1}^{1}\int_{0}^{\infty}\left(c'^2 - \frac{r_1(\alpha)}{l(\alpha)}\right)h_1(x, \mu')g(c')c'^3 dc' d\mu'$$

$$+ \frac{l(\alpha)}{\Delta(\alpha)}\left(c^2 - \frac{r_1(\alpha)}{l(\alpha)}\right)$$

$$\times\int_{-1}^{1}\int_{0}^{\infty}\left(c'^2 - \frac{r_1(\alpha)}{l(\alpha)}\right)^2\left(c'^2 - \frac{r_0(\alpha)}{s(\alpha)}\right)h_2(x, \mu')g(c')c'^3 dc' d\mu'$$

$$= \frac{1}{2}\int_{-1}^{1} h_1(x, \mu')d\mu' + \left(c'^2 - \frac{r_1(\alpha)}{l(\alpha)}\right)\frac{1}{2}\int_{-1}^{1} h_2(x, \mu')d\mu'$$

(the second and third integrals vanished after integration with respect to c'). The right-hand side of the second of Eqs. (10) is calculated in a similar way.

We arrive at the set of equations

$$\begin{gathered}\mu\frac{\partial h_1}{\partial x} + h_1(x, \mu) = \bar{h}_1(x) + \mu e(x),\\ \mu\frac{\partial h_2}{\partial x} + h_2(x\mu) = \bar{h}_2(x);\end{gathered} \tag{12}$$

$$\bar{h}_j(x) = \frac{1}{2}\int_{-1}^{1} h_j(x, \mu)d\mu, \quad j = 1, 2; \tag{13}$$

$$e'(x) = a^2(\alpha)\bar{h}_1(x), \quad a^2(\alpha) = a_0^2 s(\alpha). \tag{14}$$

Boundary conditions (11) can now be expressed as

$$\begin{gathered}h_1(0, \mu) = A_0, \quad 0 < \mu < 1,\\ h_1(x, \mu) = -h_0(\alpha)k_t\mu + o(1),\\ x \longrightarrow +\infty, \quad -1 < \mu < 0;\end{gathered} \tag{15}$$

$$h_2(0, \mu) = 0, \quad 0 < \mu < 1,$$
$$h_2(x, \mu) = \varepsilon_t + k_t(x - \mu) + o(1), \quad x \longrightarrow +\infty, \quad -1 < \mu < 0; \tag{16}$$

$$e(0) = 0, \quad e(x) = e_h + o(1), \quad x \longrightarrow +\infty. \tag{17}$$

The problem given by Eqs. (10), (11) splits into two that are related to each other only through the boundary conditions: the problem of a temperature jump in a metal (Eqs. (13) and (16)) and the problem of electric field behavior near the surface under the action of temperature gradient k_t (Eqs. (12), (14), (15), (17)). We will start with the former.

TEMPERATURE JUMP IN A METAL

Consider the problem given by Eqs. (13) and (16). The method of its solution was developed in [6]. Following [6], we will seek a solution in the form $h_{2\eta}(x, \mu) = \exp(-x/\eta)\Phi(\eta, \mu)$ and obtain the characteristic equation

$$(\eta - \mu)\Phi(\eta, \mu) = \eta\frac{1}{2}m(\eta), \quad m(\eta) = \int_{-1}^{1}\Phi(\eta, \mu)d\mu. \tag{18}$$

Due to the homogeneity of Eq. (13), we may assume that $m(\eta) \equiv 1$. Then, for $\eta \in \sigma_c$, $\sigma_c = (-1, 0) \cup (0, 1)$, we can determine from (18) the Case eigenfunctions corresponding to the continuous spectrum σ_c:

$$\Phi(\eta, \mu) = \frac{1}{2}\eta P\frac{1}{\eta - \mu} + \lambda(\eta)\delta(\eta - \mu).$$

Here, the symbol Px^{-1} means the distribution, the principal value of the integral with respect to x^{-1}; $\delta(x)$ is the Dirac delta function; and $\lambda(z)$ is the Case dispersion function [6]:

$$\lambda(z) = 1 + \frac{z}{2}\int_{-1}^{1}\frac{du}{u - z}.$$

Two solutions to Eq. (13), 1 and $z = \infty$, correspond to the double zero $x - \mu$ of the function $\lambda(z)$. A solution to Eqs. (13) and (16) is found in the form of the expansion in eigensolutions:

$$h_2(x, \mu) = \varepsilon_t + k_t(x - \mu) + \int_0^1 \exp\left(-\frac{x}{\eta}\right)\Phi(\eta, \mu)m(\eta)d\eta. \tag{19}$$

In expansion (19), the temperature jump ε_t and the function $m(\eta)$ are unknowns.

Using boundary-value conditions (16), we pass from expansion (19) to a singular integral equation with the Cauchy kernel:

$$\varepsilon_t - k_t\mu + \frac{1}{2}\int_0^1\frac{\eta m(\eta)}{\eta - \mu}d\eta + \lambda(\mu)m(\mu) = 0. \tag{20}$$

To solve Eq. (20), we introduce the auxiliary function

$$M(z) = \frac{1}{2}\int_0^1\frac{\eta m(\eta)d\eta}{\eta - z}, \tag{21}$$

which is analytical in the complex plane with the cut [0, 1]. The upper and lower extremes of $M(z)$ on this cut are related by the Sokhotsky formulas [7]

$$M^+(\mu) - M^-(\mu) = \pi i\mu m(\mu), \quad 0 < \mu < 1,$$
$$\frac{1}{2}[M^+(\mu) + M^-(\mu)] = M(\mu), \tag{22}$$

where

$$M(\mu) = \frac{1}{2}\int_0^1\frac{\eta m(\eta)d\eta}{\eta - \mu}, \quad 0 < \mu < 1.$$

We also need the Sokhotsky formulas for the dispersion function $\lambda(z)$:

$$\lambda^+(\mu) - \lambda^-(\mu) = \pi i\mu, \quad -1 < \mu < 1,$$
$$\frac{1}{2}[\lambda^+(\mu) + \lambda^-(\mu)] = \lambda(\mu),$$

where

$$\lambda(\mu) = 1 + \frac{\mu}{2}\ln\frac{1 - \mu}{1 + \mu}, \quad -1 < \mu < 1.$$

Using the four last equalities, we can reduce Eq. (20) to the Riemann inhomogeneous boundary-value problem [7, 8]

$$\lambda^+(\mu)[M^+(\mu) + \varepsilon_t - k_t\mu] = \lambda^-(\mu)[M^-(\mu) + \varepsilon_t - k_t\mu], \quad 0 < \mu < 1.$$

Solve first the corresponding homogeneous boundary-value problem

$$\frac{X^+(\mu)}{X^-(\mu)} = \frac{\lambda^+(\mu)}{\lambda^-(\mu)}, \quad 0 < \mu < 1.$$

The curve $z = \lambda^+(\mu)/\lambda^-(\mu) = \exp(2i\theta(\mu))$ $(0 \le \mu \le 1)$, where $\theta(\mu) = \arg\lambda^+(\mu)$, runs around the unit circle in the positive direction once. From a family of solutions to such problems, we choose the so-called canonical solution (the solution whose order at infinity is equal to

the problem index):

$$X(z) = \frac{1}{z}\exp V(z), \quad V(z) = \frac{1}{\pi}\int_0^1 \frac{\zeta(u)du}{u-z},$$

$$\zeta(u) = \theta(\mu) - \pi = -\frac{\pi}{2} - \arctan\frac{2\lambda(u)}{\pi u}.$$

Using the homogeneous boundary-value problem, we can reduce the inhomogeneous problem to the problem of definition of an analytical function by its zero jump on the cut:

$$X^+(\mu)[M^+(\mu) + \varepsilon_t - k_t\mu]$$
$$= X^-(\mu)[M^-(\mu) + \varepsilon_t - k_t\mu], \quad 0 < \mu < 1.$$

A general solution to this problem contains one arbitrary constant C:

$$M(z) = -\varepsilon_t + k_t z + C/X(z). \tag{23}$$

We require this solution to be taken as an auxiliary function like (21). The constant C is chosen such that the pole of solution (23) at the point $z = \infty$, $C = -k_t$, is eliminated. The value of ε_t is now determined from the condition $M(\infty) = 0$. Expanding the function $1/X(z)$ into the Laurent series in the vicinity of the point $z = \infty$, we equate the free term on the right of solution (23) to zero and obtain

$$\varepsilon_t = V_1 k_t, \quad V_1 = -\frac{1}{\pi}\int_0^1 \zeta(u)du = 0.71045\ldots. \tag{24}$$

This formula gives the sought temperature jump in a metal. Comparing Eqs. (24) and (1), we estimate the temperature jump coefficient as $C_t = 0.71045$. Note that this coefficient does not depend on the electron gas degeneration.

ELECTRIC FIELD BEHAVIOR IN A METAL

Let us now solve the problem stated by Eqs. (12) and (14) with boundary conditions (15) and (17). We shall seek solutions to Eqs. (12) and (14) in the form

$$h_{1\eta}(x, \mu) = \exp\left(-\frac{x}{\eta}\right)F(\eta, \mu),$$

$$e_\eta(x) = \exp\left(-\frac{x}{\eta}\right)E(\eta).$$

The characteristic set is

$$(\eta - \mu)F(\eta, \mu) = \frac{1}{2}(1 - a^2(\alpha)\eta\mu)\eta n(\eta), \tag{25}$$

$$E(\eta) = -\frac{1}{2}a^2(\alpha)\eta n(\eta), \quad n(\eta) = \int_{-1}^1 F(\eta, \mu)d\mu. \tag{26}$$

Assuming $\eta n(n) \equiv 1$, we take a solution to Eq. (25) in the space of generalized functions (for $\eta \in (-1, 0) \cup (0, 1)$):

$$F(\eta, \mu) = \frac{1}{2}a^2(\alpha) + \frac{1 - a^2(\alpha)\eta^2}{\eta}\Phi(\eta, \mu), \tag{27}$$

where Φ is the Case eigenfunction introduced earlier.

The dispersion function of this problem, $(1 - a^2(\alpha)z^2)\lambda(z)/z$, has three zeros: $z = \infty$ and $z = \pm 1/a(\alpha)$. To these zeros, there correspond three solutions to Eqs. (12) and (14): $\{h_1 = \mu, e = 1\}$ and $\{h_1 = \exp(\mp a(\alpha)x), e = \mp a(\alpha)\exp(\mp a(\alpha)x)\}$. These solutions correspond to the discrete spectrum, while the eigenfunctions (27) and (26) correspond to the continuous spectrum.

Now we will seek a solution to the problem in the form of the expansion in the eigenfunctions of the discrete and continuous spectra:

$$h_1(x, \mu) = -k_t h_0(\alpha)\mu + A_1\exp(-a(\alpha)x) + \int_0^1 \exp\left(-\frac{x}{\eta}\right)F(\eta, \mu)n(\eta)d\eta, \tag{28}$$

$$e(x) = -k_t h_0(\alpha) - a(\alpha)A_1\exp(-a(\alpha)x) - \frac{1}{2}a^2(\alpha)\int_0^1 \exp\left(-\frac{x}{\eta}\right)n(\eta)d\eta. \tag{29}$$

The constants A_0 and A_1, as well as the function $n(\eta)$, are unknowns in expansions (28) and (29), with A_0 also entering boundary condition (15).

Note that expansions (28) and (29) meet the relevant boundary conditions automatically for $x \longrightarrow +\infty$. The substitution of these expansions into the boundary conditions at $x = 0$ yields

$$A_0 = -k_t h_0(\alpha)\mu + A_1 + A_2 + \frac{1}{2}\int_0^1 (1 - a^2(\alpha)\eta^2)\frac{n(\eta)d\eta}{\eta - \mu} + (1 - a^2(\alpha)\mu^2)\frac{\lambda(\mu)}{\mu},$$

$$A_2 = \frac{1}{2}a^2(\alpha)\int_0^1 \eta n(\eta)d\eta, \tag{30}$$

$$a(\alpha)A_1 = -k_t h_0(\alpha) - \frac{1}{2}a^2\int_0^1 n(\eta)d\eta. \tag{31}$$

Let us solve Eq. (30). We introduce the auxiliary function

$$N(z) = \frac{1}{2}\int_0^1 (1 - a^2(\alpha)\eta^2)\frac{n(\eta)d\eta}{\eta - z} \tag{32}$$

and, as before, reduce Eq. (30) to the Riemann boundary-value problem

$$X^+(\mu)[N^+(\mu) - A_0 + A_1 + A_2 - h_0(\alpha)k_t\mu] = X^-(\mu)[N^-(\mu) - A_0 + A_1 + A_2 - h_0(\alpha)k_t\mu], \quad 0 < \mu < 1.$$

This problem has the solution

$$N(z) = -A_1 + A_0 - A_2 + k_t h_0(\alpha)(z - 1/X(z)),$$

from which we find the last unknown function $n(\eta)$,

$$\pi i(1 - a^2(\alpha)\eta^2)n(\eta) = -k_t h_0(\alpha)\left[\frac{1}{X^+(\eta)} - \frac{1}{X^-(\eta)}\right] \quad (33)$$

and the constant A_0: $A_0 = -k_t h_0(\alpha)V_1 + A_1 + A_2$. The integral in the expression for A_2 is transformed according to Eq. (33). Then,

$$A_0 = A_1 - k_t h_0(\alpha) \times \left[V_1 - \frac{1}{2\pi i}\int_0^1\left(\frac{1}{X^+(\eta)} - \frac{1}{X^-(\eta)}\right)\frac{\eta\, d\eta}{\eta^2 - a^{-2}(\alpha)}\right]. \quad (34)$$

Let us calculate the integral in Eq. (34). For most metals, the value of $1/\alpha(\alpha)$ belongs to the cut: $1/\alpha(\alpha) \in (0, 1)$; hence, the integral on the right of Eq. (34) is singular. The value of this singular integral is denoted as $J(a)$:

$$J(a) = \frac{1}{2\pi i}\int_0^1\left[\frac{1}{X^+(u)} - \frac{1}{X^-(u)}\right]\frac{u\,du}{u^2 - a^{-2}(\alpha)}.$$

Let us construct a function $f(z) = z/[X(z)(z^2 - a^2(\alpha))]$ that is analytical in the entire complex plane, except for the cut [0, 1] and simple poles at the points $\pm 1/a(\alpha)$. We take an intricate contour (Fig. 1) consisting of a circle γ_R with a sufficiently large radius $R = 1/\varepsilon$ ($\varepsilon > 0$), a circle γ_{-1} given by $|z + 1/a(\alpha)| = 2\varepsilon$, and a contour γ_ε encircling the cut [0, 1]. The contour γ_ε is placed at a distance ε from the cut; is passed clockwise (unlike the other two contours); and contains a part of the circle γ_{+1}, which is given by $|z - 1/a(\alpha)| = 2\varepsilon$. According to the Cauchy theorem for multiply connected domains,

$$\frac{1}{2\pi i}\oint_{\gamma_R} f(z)dz = \frac{1}{2\pi i}\oint_{\gamma_1} f(z)dz - \frac{1}{2\pi i}\oint_{\gamma_\varepsilon} f(z)dz.$$

In the limit $\varepsilon \longrightarrow 0$, we obtain

$$J(a) = \operatorname*{Res}_\infty f(z) + \operatorname*{Res}_{-1/a} f(z) + \operatorname*{Res}_{1/a} f(z).$$

It is easy to see that $\operatorname*{Res}_\infty f(z) = V_1$ and $\operatorname*{Res}_{1/a} f(z) = 1/[2X(-1/a)]$. Since the point $1/a$ falls into the cut, we have

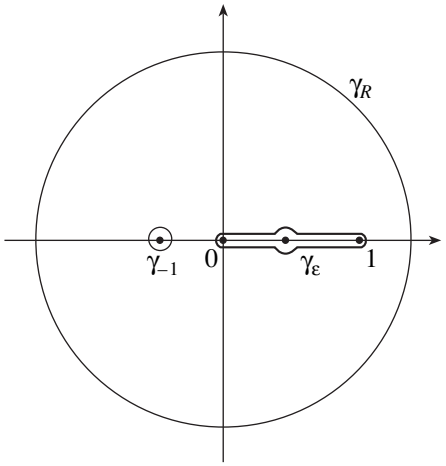

Fig. 1.

$$\operatorname*{Res}_{1/a} f(z) = \frac{1}{2}\left[\frac{1}{2X^+(1/a)} + \frac{1}{2X^-(1/a)}\right] = \frac{\cos\zeta(1/a)}{2X(1/a)}.$$

Thus,

$$J(a) = V_1 + \frac{1}{2}\left[\frac{\cos\zeta(1/a)}{X(1/a)} + \frac{1}{X(-1/a)}\right].$$

Hence, according to Eq. (34),

$$A_0 = A_1 + k_t h_0(\alpha)\frac{1}{2}\left[\frac{\cos\zeta(1/a)}{X(1/a)} + \frac{1}{X(-1/a)}\right].$$

Now we return to Eq. (31) and recast it, according to Eqs. (26) and (33), in the form

$$a(\alpha)A_1 = -k_t h_0(\alpha) \times \left[1 + \frac{1}{2\pi i}\int_0^1\left(\frac{1}{(X^+(u))} - \frac{1}{X^-(u)}\right)\frac{du}{u^2 - a^{-2}(\alpha)}\right].$$

The integral in this equality is also singular. Using the above method for taking a special integral, we come to

$$a(\alpha)A_1 = -k_t h_0(\alpha) \times \left[1 + (\operatorname*{Res}_\infty + \operatorname*{Res}_{-1/a} + \operatorname*{Res}_{1/a})\frac{1}{X(z)(z^2 - a^{-2}(\alpha))}\right].$$

These residues are

$$\operatorname*{Res}_\infty \frac{1}{X(z)(z^2 - a^{-2}(\alpha))} = -1,$$

$$\operatorname*{Res}_{-1/a} \frac{1}{X(z)(z^2 - a^{-2}(\alpha))} = -\frac{a}{2X(-1/a)},$$

$$\operatorname*{Res}_{1/a} \frac{1}{X(z)(z^2 - a^{-2}(\alpha))} = \frac{a\cos\zeta(1/a)}{2X(1/a)}.$$

Hence,

$$A_1 = -k_t h_0(\alpha)\frac{1}{2}\left[\frac{\cos\zeta(1/a)}{X(1/a)} - \frac{1}{X(-1/a)}\right]$$

and the expression for A_0 simplifies to $A_0 = k_t h_0(\alpha)/X(-1/a)$. All the unknown constants and functions in expansions (28) and (29) are now determined, and the problem described by Eqs. (12), (14), (15), and (17) is thus solved. With Eq. (22), the expansion coefficients found allow us to build the distribution function for electrons on the metal surface in explicit form:

$$\varphi(0, \mu, c) = k_t\left[\frac{h_0(\alpha)}{X(-1/a)} - \frac{\theta_+(-\mu)}{X(\mu)}\left(c^2 - \frac{r_1(\alpha)}{l(\alpha)}\right)\cos\theta(\mu)\right],$$

$\theta_+(\mu) = 1$, $\mu > 0$; $\theta_+(\mu) = 0$, $\mu < 0$.

As is seen from this expression, $\varphi(0, \mu, c) = A_0$ $(0 < \mu < 1)$, which completely coincides with the first boundary condition in (15).

Let us now construct the electric field profile in the half-space. According to Eqs. (28) and (33), we have

$$e(x) = k_t h_0(\alpha)\left[-1 + \frac{1}{2}a(\alpha)\left(\frac{f_0(a)}{X(1/a)} - \frac{1}{X(-1/a)}\right)\right.$$

$$\left.\times \exp(-a(\alpha)x) - \frac{1}{2\pi i}\int_0^1 \exp\left(-\frac{x}{u}\right)\right. \qquad (35)$$

$$\left.\times\left(\frac{1}{X^+(u)} - \frac{1}{X^-(u)}\right)\frac{du}{u^2 - a^{-2}(\alpha)}\right].$$

The condition $e(0) = 0$ is obviously fulfilled, since,

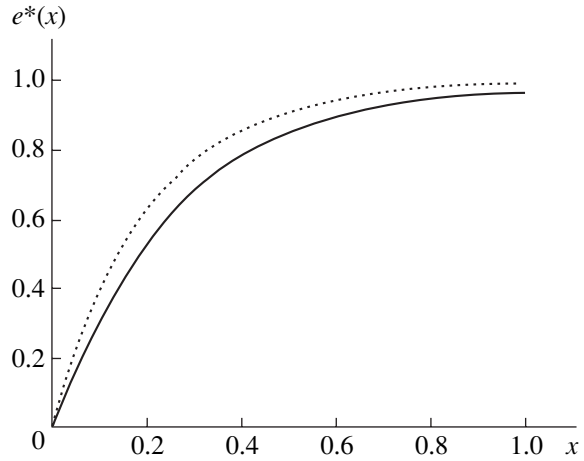

Fig. 2.

upon calculating A_1, it was shown that

$$\frac{1}{2\pi i}\int_0^1\left[\frac{1}{X^+(u)} - \frac{1}{X^-(u)}\right]\frac{du}{u^2 - a^{-2}(\alpha)}$$

$$= \frac{1}{2}a(\alpha)\left[\frac{\cos\zeta(1/a)}{X(1/a)} - \frac{1}{X(-1/a)}\right] - 1.$$

ELECTRIC FIELD PROFILE

Consider the case of typical metals, where the value of the chemical potential $\alpha \gg 1$. To estimate the integrals entering into Eq. (35), we apply the well-known asymptotics [9, p. 191, Eq. (58.1)]

$$\int_0^\infty \frac{f(x)dx}{e^{x-\alpha}+1} = \int_0^\alpha f(x)dx + \frac{\pi^2}{6}f'(\alpha) + \frac{7\pi^2}{360}f'''(\alpha) + \ldots,$$

$$\alpha \gg 1.$$

For $\alpha \gg 1$, we have

$$r_0(\alpha) = \alpha^{3/2} + \frac{\pi^2}{8}\alpha^{-1/2} + \ldots, \quad r_1(\alpha) = \alpha^2 + \frac{\pi^2}{3} + \ldots,$$

$$s(\alpha) = \alpha^{1/2} - \frac{\pi^2}{24}\alpha^{-1/2} + \ldots, \quad l(\alpha) = \alpha + \ldots.$$

Hence, for $\alpha \gg 1$,

$$a(\alpha) = a_0\sqrt[4]{\alpha}, \quad h_0(\alpha) \sim -\pi^2/6\alpha$$

and the electric field can be expressed as

$$e(x) = -k_t\frac{\pi^2}{6\alpha}\left[-1 + \frac{1}{2}a_0\sqrt[4]{\alpha}\exp(-a_0\sqrt[4]{\alpha}x)\right.$$

$$\left.\times\left(\frac{\cos\zeta(1/a)}{X(1/a)} - \frac{1}{X(-1/a)}\right) - \frac{1}{2}\int_0^1 \exp\left(-\frac{x}{\eta} - V(\eta)\right)\right.$$

$$\left.\times\frac{\eta^2}{\sqrt{\lambda^2(\eta) + (\pi\eta/2)^2}\,\eta^2 - 1/a_0^2\sqrt{\alpha}}\frac{d\eta}{}\right],$$

$$a = a(\alpha) = a_0\sqrt[4]{\alpha}.$$

The quantity a is defined as $a = 3\omega_p^2 l_0^2 v_F^{-2}$, where ω_p is the plasma frequency, $\omega_p^2 = e_0^2 n/m\varepsilon_0$, and n is the electron density. Then,

$$e(x) = -k_t\frac{\pi^2}{6\alpha}\left[-1 + \frac{1}{2}a\exp(-ax)\right.$$

$$\left.\times\left(\frac{\cos\zeta(1/a)}{X(1/a)} - \frac{1}{X(-1/a)}\right) - \frac{1}{2}\int_0^1 \exp(-x/\eta - V(\eta))\right. \qquad (36)$$

$$\left.\times\frac{\eta}{\sqrt{\lambda^2(\eta) + (\pi\eta/2)^2}\,\eta^2 - a^{-2}}\frac{d\eta}{}\right].$$

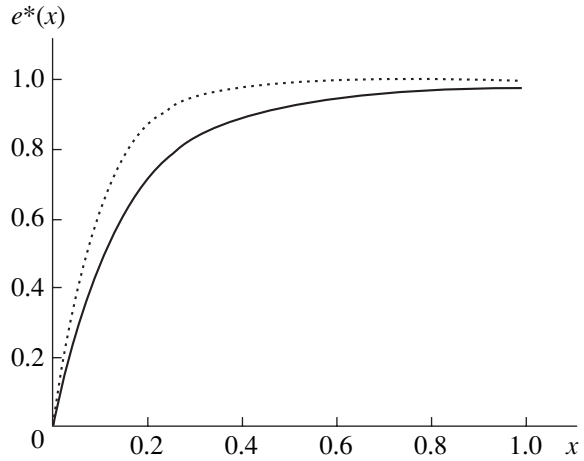

Fig. 3.

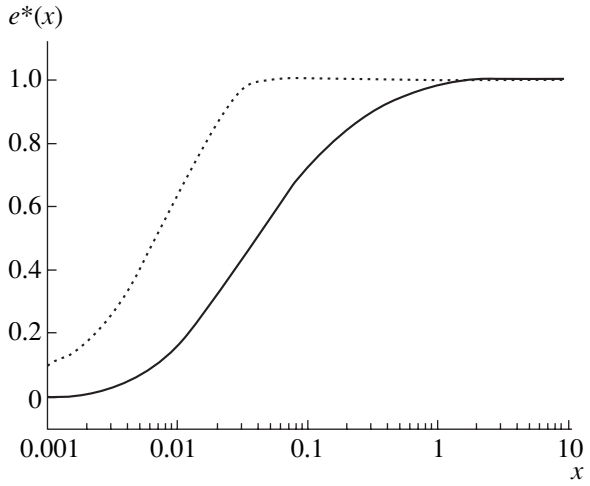

Fig. 4.

The dependences of the reduced electric field $e_*(x) = -\frac{1}{4}\alpha e(x)$ (where x is the distance from the surface) are shown in Figs. 2–4 (continuous curves) for a = 5 (Fig. 2), 10 (Fig. 3), and 100 (Fig. 4). The physical meaning of a is the ratio of the electron free path to the Debye screening length ($a = l_0/r_D$). The profiles corresponding to Debye screening (dotted lines) are also shown for comparison. All the curves are normalized to the field away the surface.

It is seen from the figures that, as the parameter a (i.e., the electron free path) increases, so does the difference between the behavior of the field near the surface (exact solution (36)) and in the case of purely Debye screening. For a = 100, this difference is essential. Such a behavior of the field is associated with kinetic effects modifying the electron behavior near the surface. If Debye screening is localized in a range on the order of r_D, the kinetic effects tell at distances on the order of the electron free path from a wall (Knudsen layer). In the dimensionless coordinates, the size of the Knudsen layer is $x \sim 1$.

CONCLUSIONS

In this paper, the problem of a temperature jump caused by a heat flux toward or from the surface of a metal is solved analytically for the first time. An exact expression for the electric field produced by thermal processes is found. The distribution function of electrons near the metal surface is constructed in explicit form. The limiting case of typical metals is considered. The dependence of the electric field on the distance from the surface is studied for different ratios of the electron free path to the Debye screening length.

The difference between the field behavior corresponding to the analytical solution and in the case of Debye screening is revealed. It is found that kinetic effects show up at a distance on the order of the electron free path. For typical metals, this distance is much greater than the Debye screening length. Thus, the effect of the metal surface on the electric field behavior is appreciable at distances far exceeding the classical screening length.

ACKNOWLEDGMENTS

This work was partly supported by the Russian Foundation for Basic Research (project no. 03-01-00286).

REFERENCES

1. E. M. Lifshitz and L. P. Pitaevsky, *Physical Kinetics* (Nauka, Moscow, 1979; Pergamon, Oxford, 1981).
2. A. V. Latyshev and A. A. Yushkanov, Fiz. Tverd. Tela (St. Petersburg) **43**, 1744 (2001) [Phys. Solid State **43**, 1816 (2001)].
3. A. A. Abrikosov, *Fundamentals of the Theory of Metals* (Nauka, Moscow, 1987; North-Holland, Amsterdam, 1998).
4. J. M. Ziman, *Electrons and Phonons* (Clarendon, Oxford, 1960; Inostrannaya Literatura, Moscow, 1962).
5. V. S. Vladimirova, *Generalized Functions in Mathematical Physics* (Nauka, Moscow, 1976).
6. K. M. Case and P. F. Zweifel, *Linear Transport Theory* (Addison-Wesley, Reading, 1967; Mir, Moscow, 1972).
7. F. D. Gakhov, *Boundary Value Problems* (Nauka, Moscow, 1977, 3rd ed.; Addison-Wesley, Reading, 1966).
8. A. V. Latyshev and A. A. Yushkanov, Zh. Vychisl. Mat. Mat. Fiz. **41**, 1239 (2001).
9. L. D. Landau and E. M. Lifshitz, *Course of Theoretical Physics*, Vol. 5: *Statistical Physics* (Nauka, Moscow, 1976; Pergamon, Oxford, 1980).

Translated by M. Astrov

Technical Physics, Vol. 48, No. 7, 2003, pp. 846–853. Translated from Zhurnal Tekhnicheskoĭ Fiziki, Vol. 73, No. 7, 2003, pp. 46–54.

GAS DISCHARGES, PLASMA

Two-Pulse Generation of High-Current Relativistic Electron Beams and Their Transportation in the Gaseous Medium of a Plasmochemical Reactor

N. A. Kondrat'ev and V. I. Smetanin[†]

Nuclear Physics Institute, Tomsk Polytechnical University, pr. Lenina 2a, Tomsk, 634050 Russia

e-mail: alex@npi.tpu.ru

Received December 15, 2002

Abstract—Experimental results on two-pulse generation and transportation of high-current relativistic electron beams (REBs) through the gaseous medium of a plasmochemical reactor (PR) are presented. The generation of two consecutive high-current REB pulses with a duration of 60 ns was achieved at the Tonus accelerator with modified schemes of high-voltage pulse formation. The first version of the formation scheme enabled pulse powers of 2 and 4.0–9.6 GW with a time interval between the pulses of 500 ns. The second version enabled one to generate pulses with powers of 1.8 and 16 GW and time interval between the pulses of 160 μs. The transportation parameters of an REB injected into a 1.4-m-long PR filled with an $N_2 : O_2$ gas mixture are studied. The conductance of the plasma produced under the action of the electron beams is measured. It is shown that the schemes proposed provide more efficient (by 35–45%) transportation of the REBs in the reactor volume as compared to single-pulse high-current REBs of the same power and pulse duration. © *2003 MAIK "Nauka/Interperiodica".*

INTRODUCTION

The results of numerous studies and application developments in the field of plasmochemical technologies based on high-current relativistic electron beams (REBs) show great promise for applying these technologies in industry [1, 2]. The main problem related to the implementation of these technologies is the problem of controlling the reactions proceeding in plasmochemical reactors (PRs). A particular application requires not only providing specific conditions in the reactor (namely, the pressure, temperature, and working medium composition), but also imposes certain requirements on the characteristics of the PR itself (the wall material, reactor dimensions, and diagnostic facility). Such an important PR parameter as the production rate, which depends on the geometrical parameters of the reactor, can be limited by the onset of various REB instabilities, in particular, large-scale resistive instability, due to which the beam falls out onto the reactor wall over a relatively short propagation length. A number of plasmochemical technologies that are employed in metallurgy (for waste utilization) and hydrocarbon synthesis require stable transportation of the beam through the PR. This paper is devoted to the experimental study of the possible ways of the efficient transportation of high-current REBs propagating through the gaseous medium of a PR. Here and below, the REB transportation efficiency is defined as the ratio I_e/I_{inj} of the electron beam current I_e passed through the reactor to the beam current at the point of injection. We note that, in this study, no external focusing magnetic field was applied. Instead, we used the so-called passive methods for increasing the REB transportation efficiency in the gaseous medium of a PR, namely, the gas-dynamic propagation method and a method in which the beam propagates in a preformed plasma channel.

The gas-dynamic method for increasing the transportation efficiency of a high-current REB in the gaseous medium of a PR requires creating a low-density gas channel along which the REB propagates. The gas pressure P_1 in the channel should be much lower than the pressure P_0 of the surrounding gas ($P_1/P_0 \ll 1$). Ideally, the pressure P_1 should be so low as to provide the forceless drift of the REB (for air, this is $P_1 = 1$ torr). Previously, gas heating and the dynamics of the gas density under the action of an REB were studied in [3–5]. In [3], it was noted that, for an REB with an electron energy of $E_e = 1$ MeV, a beam current of $I_b = 8$ kA, and a pulse duration of 60 ns (such a beam provides an energy input into the gas of about $Q = 0.3$ J/cm^3), the decrease in the pressure inside the propagation channel was $P_1/P_0 = 0.4$ (where P_0 is the atmospheric pressure and P_1 is the pressure in the channel); this value was reached in 80–100 μs. The low-pressure channel can also be formed under intense pulsed gas heating due to the dissipation of energy deposited by an external source. The energy deposition can be provided by a thin-wire electrical explosion, an electric gas discharge, an extended laser spark, or gas heating with a high-cur-

[†] Deceased.

rent REB. All these methods have their own advantages and drawbacks, and the aim of this study is to investigate their comparative efficiencies. In our opinion, the last method (gas heating with a high-current REB) is the most challenging from the technological standpoint. In this case, the beam accelerator must provide the formation of several consecutive REBs (with given time intervals between them) that are then injected into the PR channel. The efficient transportation of the REB through the PR is possible if the REB propagates along a low-density channel produced by the preceding beams. The optimum time interval between the pulses is determined by the REB parameters and the conditions of energy deposition in the gas.

An alternative passive method that allows one to keep the REB transportation parameters unchanged throughout the entire PR is the electron beam injection into a preformed plasma channel with a prescribed conductivity. In this case, the processes of charge and current neutralization are determined by the parameters of the beam and plasma. In early experimental studies [6, 7], it was noted that, after the beam is injected into plasma, the beam magnetic field is highly neutralized and the REB current can greatly exceed the Alfvén limiting current. However, the higher the density of the plasma into which the electron beam is injected, the shorter the mean free path of the plasma electrons and the higher the dissipation of the return current [8]. As a result, the magnetic field neutralization comes to an end a certain time after the beam injection. Hence, to provide stable transportation of an REB through a PR with a preformed plasma, it is necessary to find the optimum relation between the plasma density and the beam parameters. This optimum relation was, first, found numerically [9] and, then, experimentally [10], which enabled one to increase the REB transportation efficiency by a factor of more than 2.

In the present study, both the gas-dynamic regime of REB propagation through the PR gas volume and the regime of beam injection into a preformed plasma were investigated using a generation scheme that allowed two consecutive high-current pulsed REBs to be formed. The optimum propagation conditions, which enable efficient REB transportation, were found by varying the power of the beams and the time interval between them.

EXPERIMENTAL SETUP

In the experiments, the Tonus high-current electron accelerator [11] was used as an REB generator. The main components of the accelerator are a Marx generator (MG), a double pulse-forming line (DPFL), and the vacuum diode of an electron gun (EG). After switching on the MG, the stored electric energy (up to 28 kJ) is supplied through a charging inductance to the DPFL designed according to the Blumlein scheme [12] with a wave impedance of $p_1 = p_2 = 12\ \Omega$ (Fig. 1a). After switching on spark gap *1*, a high-voltage pulse with the duration $t_p = 2L/V$ and the amplitude equal to the charging voltage is formed in a time $t = L/V$ (where L is the line length and V is the propagation velocity of an electromagnetic wave in the line) at the load $Z = p_1 + p_2$. Then, this pulse is switched to the planar vacuum diode of the EG. In the DPFL, a transformer oil was used as a dielectric. The diameter of the stainless-steel EG cathode was 2.5 cm. A 50-μm-thick Ti foil, which separated the EG from the PR gas volume, acted as an anode. Vacuum in the EG was sustained at a level of 4×10^{-5} torr. In the experiments, the generated single-pulse REB had an electron energy of $(1.0–1.2) \times 10^6$ eV, a beam current of $I_b = (12–20)$ kA, and a pulse duration of $t_p = 60$ ns. The DPFL voltage and the EG accelerating voltage were measured with the help of capacitive voltage dividers *6–8*. Return-current shunt *9* and a vacuum Faraday cup (FC) were used to monitor the total diode current and the current of the produced electron beam, respectively. A 1.4-m-long 9.2-cm-diameter metallic cylinder served as a PR. The PR was attached to the anode of the EG accelerator (Fig. 1d) and filled with the $N_2 : O_2 = 4 : 1$ gas mixture at different pressures.

To carry out experiments with an REB propagating in a preformed plasma produced in the dense gaseous medium of the PR by the first high-current electron beam, the generation scheme of the Tonus accelerator was modified as is shown in Fig. 1c. The principal difference between this scheme and the previous version used for single-pulse generation is that the discharger D_1, which previously switched the middle forming line to the grounded accelerator housing, now serves as a switch between the middle and inner forming lines. The discharge inductance L_2 is separated from the inner line by the discharger D_2, which is set between the accelerator housing and the flange of the EG cathode holder. This scheme allows the generation of two high-current pulsed REBs in a time equal to the MG pulse rise time t_f = 1–2 μs. The scheme operates as follows. After switching on (energy commutation), the MG begins to charge the DPFL through the charging inductance L_1. After the voltage amplitude reaches a value corresponding to the first pulse, at the instant t_1 (Fig. 1c), the discharger D_2 is switched on, the high-voltage pulse is applied to the EG cathode, and the first high-current REB is generated in the anode–cathode gap. After switching on the discharger D_2, the inner forming line becomes connected to the accelerator housing through the inductance L_2.

The amplitude U_1 of the first voltage pulse is regulated by adjusting the switching time t_1 of the discharger D_2, which, in turn, is varied by varying the pressure of the gas mixture (N_2 + 10% SF_6) in the discharger. The first high-current REB is then injected into the PR through the anode foil.

At the instant t_2, when the voltage applied from the MG to the middle line reaches its maximum value U_2,

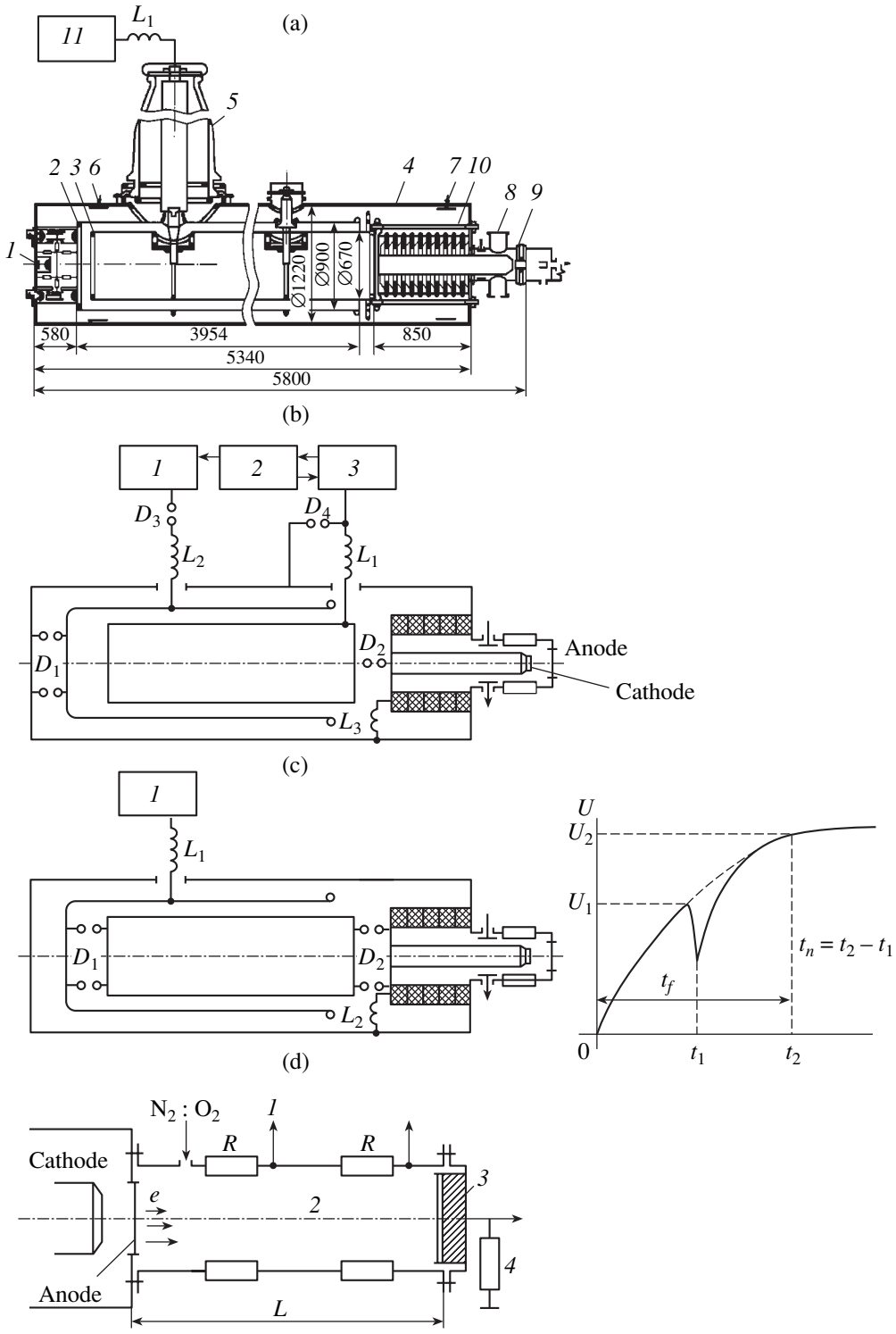

Fig. 1. Schematic of the experimental facility. (a) A schematic of the Tonus high-current electron accelerator operating in the single-pulse mode: (*1*) discharger, (*2*) middle pulse-forming line, (*3*) inner pulse-forming line, (*4*) accelerator housing, (*5*) high-voltage insulator, (*6–8*) capacitive voltage dividers, (*9*) return current shunt, (*10*) electron gun, and (*11*) Marx generator (MG_1). (b) A circuit diagram of the generator of two consecutive high-current REB pulses separated by the time interval t_n = 160 μs: (*1*) MG_1, (*2*) synchronization scheme, and (*3*) MG_2. (c) A circuit diagram of the generator of two consecutive high-current REB pulses separated by a time interval t_n of up to 500 ns: (*1*) MG_1. (d) A schematic of the PR and a system for recording the REB parameters: (*1*) to an oscilloscope, (*2*) PR, (*3*) Faraday cup, and (*4*) R_{FC}.

the discharger D_1 switches on and the second high-voltage pulse is applied through the discharger D_2 (whose electric strength has not yet recovered) to the anode–cathode gap, where the second high-current REB is formed. The amplitude U_2 of the second high-voltage pulse can also be regulated by adjusting the switching time t_2 of the discharger D_1, which is varied by varying the pressure in the discharger.

This generation scheme allows the formation of two high-voltage pulses of either equal amplitudes (if the discharger D_1 is switched on with a time delay $t_n = t_2 - t_1 = 10$–100 ns with respect to the switching-on of the discharger D_2) or with an elevated amplitude of the second pulse, which can be done by increasing the time t_n to 500 ns. As the time interval between the pulses increases further ($t_n > 500$ ns), the operation conditions of the accelerator vacuum diode become close to the short-circuit conditions because of the filling of the entire anode–cathode gap with a dense explosive-emission plasma produced during the formation of the first REB. When studying the transportation of REBs generated by this scheme through the PR, we used high-current electron beams with the following parameters. The first REB had the electron energy $E_e = (0.5$–$0.6) \times 10^6$ eV, beam current $I_e = 3$–4 kA, and pulse duration $t_p = 60$ ns. In the second REB, the electron energy was $E_e = (0.5$–$0.6) \times 10^6$ eV, the beam current I_e was 8–16 kA, and the pulse duration was $t_p = 60$ ns. The time interval between the pulses was varied in the range $t_n = 60$–500 ns. In the experiments, we measured the propagation efficiency of the second high-current REB defined as the ratio of the beam current I_e passed through a PR filled with $N_2 : O_2$ gas mixtures at different pressures and recorded with a vacuum Faraday cup to the injection current I_{inj} measured at the point where the beam entered the PR (behind the accelerator anode foil). The propagation efficiency was measured as a function of the gas pressure in the PR, the beam propagation length L, and the time interval between the REBs.

Another modification of the scheme for generating two high-current REBs is a version shown in Fig. 1b. This scheme allowed one to investigate the gas-dynamic regime of the propagation of two electron beams with a time interval between them of up to 500 μs. The scheme included an additional oil-filled Marx generator (MG_2) with the maximum pulsed output voltage $U_2 = 0.75 \times 10^6$ V and the stored energy $W = 18.5$ kJ. The MG_2 charged the inner pulse-forming line via the charging inductance L_1. The charging of the DPFL from the MG_1 and MG_2 generators was provided by using a synchronization system allowing one to control the switching times of the D_1, D_2, and D_3 dischargers. After switching on the discharger D_2, the MG_2 charged the inner pulse-forming line, a high-voltage pulse was applied to the EG, and the first REB was generated in the anode–cathode gap. The subsequent switching-on of the discharger D_3 (within a time interval controlled by the synchronization system) gave rise to the charging of the middle pulse-forming line from the MG_1. Then, after triggering the discharger D_1, a high-voltage pulse was applied to the EG through the discharger D_2 and a second REB was generated in the anode–cathode gap. The parameters of the high-current REBs were as follows. The electron energy in the first beam was $E_e = 0.7 \times 10^6$ eV, the beam current was $I_e = 6$–7 kA, and the pulse duration was $t_p = 60$ ns. The electron energy in the second beam was $E_e = (0.9$–$1.0) \times 10^6$ eV, the beam current was $I_e = 10$–16 kA, and the pulse duration was $t_p = 60$ ns. The time interval between the pulses was up to 500 μs. However, the propagation of these REBs was first studied only for the time intervals between the beams $300 < t_n < 500$ μs, because it was impossible to reduce the time interval due to the presence of a dense explosion-emission plasma in the anode–cathode gap, the recombination time of this plasma being no less than 300 μs. Preliminary experiments showed that it was possible to reduce the time interval between the pulses to $t_n < 300$ μs by reducing the density of the explosion-emission plasma produced in the diode during the formation of the first high-current REB. This reduction was achieved by decreasing the power of the first pulse from 4.8 to 1.8 GW. In this way, a 160-μs time interval between the beams was achieved with the aim of increasing the parameter range in which the gas-dynamic method for REB propagation was investigated. This time interval is comparable with the optimum time within which the maximum decrease in the gas density inside the PR channel is reached after a high-current electron beam has passed through the channel (as was first observed in [3]). For both modifications of the REB generation scheme, the possible values of the time interval between the beams were limited by the frequency characteristics of the accelerator vacuum diode with a field-emission cathode.

To obtain additional information about the parameters of the plasma formed by the first and second REBs in the volume of a PR, we used a facility (described in detail in [13]) that allowed us to determine the conductance of the plasma channels and the plasma decay time.

RESULTS AND DISCUSSION

Figures 2 and 3 show the transportation characteristics of the second high-current REB for the scheme with a preformed plasma channel. The beam transportation efficiency was defined as the ratio of the beam current I_e passed through the PR and recorded with a vacuum Faraday cup to the injection current at the entrance to the PR (behind the accelerator anode foil). This characteristic was measured at different distances from the injection point as a function of the pressure of the $N_2 : O_2$ gas mixture and the time interval t_n between

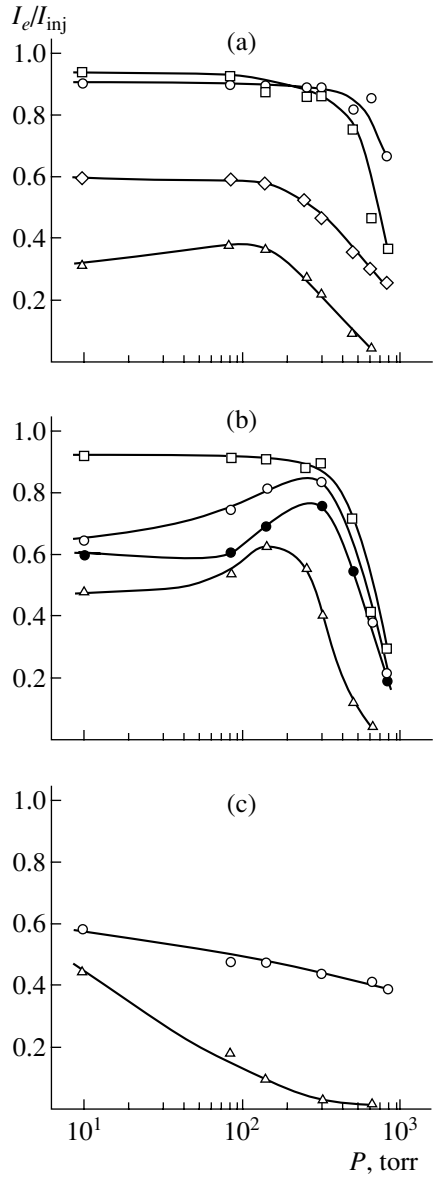

Fig. 2. Transportation efficiency of the second high-current REB vs. gas pressure in the PR for different time intervals t_n between the pulses and different transportation lengths L: (a) t_n of up to 100 ns and L = (○) 0.4, (□) 0.75, (◇) 1.2, and (△) 1.4 m; (b) t_n = 100–250 ns and L = (□) 0.75, (○) 0.85, (●) 1.2, and (△) 1.4 m; and (c) t_n = 250–500 ns and L = (○) 0.4 and (△) 1.0 m.

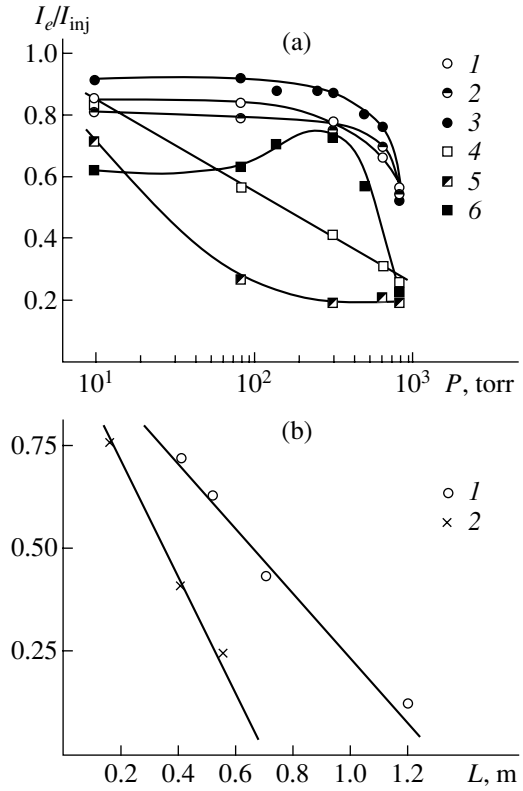

Fig. 3. (a) Transportation efficiency for the single-pulse and two-pulse regimes of high-current REB generation and propagation vs. gas mixture pressure in a PR for different electron energies E_e and injection currents I_{inj} at the transportation lengths L = (*1–3*) 0.6 and (*4–6*) 1.4 m: (*1, 4*) E_e = 1 MeV and I_{inj} = 17 kA, (*2, 5*) E_e = 1 MeV and I_{inj} = 24 kA, and (*3, 6*) two pulses with E_e = 0.5 MeV and the injection current of the second REB I_{inj} = 15 kA. (b) Transportation efficiency for the single-pulse and two-pulse regimes of high-current REB generation and propagation vs. beam transportation length L in a PR filled with an $N_2 : O_2$ gas mixture at atmospheric pressure: (*1*) two-pulse regime with E_e = 0.5 MeV and the injection current of the second REB I_{inj} = 8 kA and (*2*) single-pulse regime with E_e = 0.6 MeV and I_{inj} = 10 kA.

the beams. These experimental data can be conventionally divided into three groups corresponding to the time intervals lying in the ranges <100, 100–250, and 250–500 ns. Such a wide range of the time intervals between high-current REBs was used in order to determine the optimum conditions for the propagation of the second REB for different parameters of the plasma produced by the first beam. The change in the plasma density and its spatial homogeneity along the pathway of the second beam due to plasma expansion and recombination in the reactor volume could be varied by varying the t_n value. It can be seen from Fig. 2b that, over a wide range of gas pressure (P = 10–400 torr), the REB transportation efficiency is the highest at time intervals of t_n = 100–250 ns. For example, for the propagation length L = 1.2 m and the gas mixture pressure P = 300 torr, the efficiency is I_e/I_{inj} = 0.75. Typical waveforms of the accelerating voltage and REB currents in this regime are shown in Fig. 4. The beam transportation efficiency obtained in the two-pulse regime at such a high gas mixture pressure is significantly higher than that obtained in previous experiments, including experiments on the propagation of single-pulse 1-MeV REBs. For comparison, the efficiencies for single-pulse and two-pulse regimes of REB generation and propagation are shown in Fig. 3. The transportation characteristics of high-current REBs were investigated over a wide range of gas mixture pressure in the PR (up to atmo-

spheric pressure). It can be seen from Fig. 3b that, in the two-pulse regime with an optimum time interval between the REBs, the beam transportation efficiency increases by 35–45% as compared to the single-pulse generation regime with an electron energy of E_e = 0.6 MeV. Moreover, the transportation length increases by 50%. These results are certainly of great interest and can be used in designing industrial plasmochemical reactors with an elevated output capacity.

When measuring the transportation characteristics of two high-current REBs with a time interval between them of up to 500 ns, we also measured the conductance of the plasma created in the gas exposed to the beam. For this purpose, we used a facility and technique that were approved earlier in [13]. The results of these measurements are shown in Fig. 5 for the REB transportation length L = 0.3 m. The data on the plasma conductance in the PR and the REB transportation characteristics allow us to suggest the following scenario of the beam–plasma interaction.

When the time interval between the two high-current electron beams is less than 100 ns, the density of the plasma created by the first beam is relatively high. As a result, the plasma beam current is also high, which can lead to the onset of REB instabilities (most probably, resistive hose instability [14]). Since, in this case, the repulsion caused by the magnetic fields of the counter-directed and spatially separated beam current and beam-induced return plasma current increases, this can result in the excitation of transverse beam oscillations and, finally, to the departure of the beam onto the reactor wall. Such oscillations prevent the beam transportation over lengths longer than one to three betatron lengths [11] ($L_{\text{bet}} = \pi r_e/(I_A/I_b)^{0.5}$, where I_A is the Alfvén current, I_b is the beam current, and r_e is the beam radius). For beams with parameters similar to those used in our experiments, L_{bet} is no longer than 0.1–0.15 m. Nevertheless, the interaction of the second high-current REB with a high-density plasma ensures the complete charge neutralization of the beam and reduces the time over which the complete current neutralization is reached. However, the onset of REB instability can significantly decrease the beam transportation efficiency.

When the time interval between the pulses is in the range t_n = 100–250 ns, the density of the plasma created by the first beam is much lower because, over this time interval, the plasma has time to recombine and expand under the action of the temperature and density gradients. Within a rather wide range of the gas mixture pressures in the PR (P = 100–400 torr), the optimum relation between the beam electron density n_e and the plasma ion density n_i is established (as occurred in [10]), which significantly increases the transportation efficiency of the second REB. As the gas mixture pressure increases to P > 400 torr, this optimum relation fails to hold because the recombination rate of the plasma created by the first beam changes. The measurements of the plasma conductance (see Fig. 5) indicate that, for gas pressures P > 100 torr, the plasma created by the first beam decays over a time no longer than 200

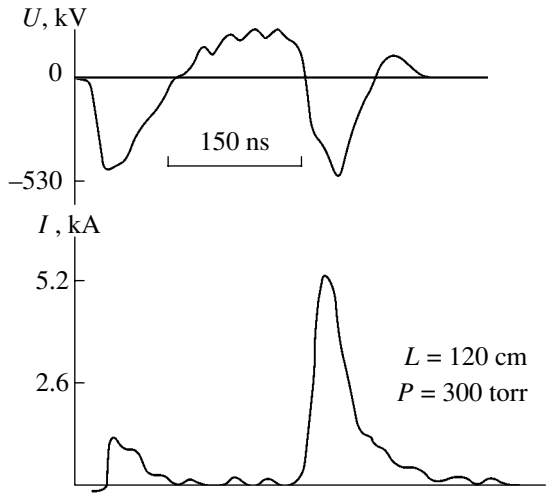

Fig. 4. Waveforms of the current and voltage for the time interval between the pulses t_n = 150 ns, the gas pressure in the PR P = 300 torr, and the propagation length L = 1.2 m. The injection current of the second REB is I_{inj} = 8 kA.

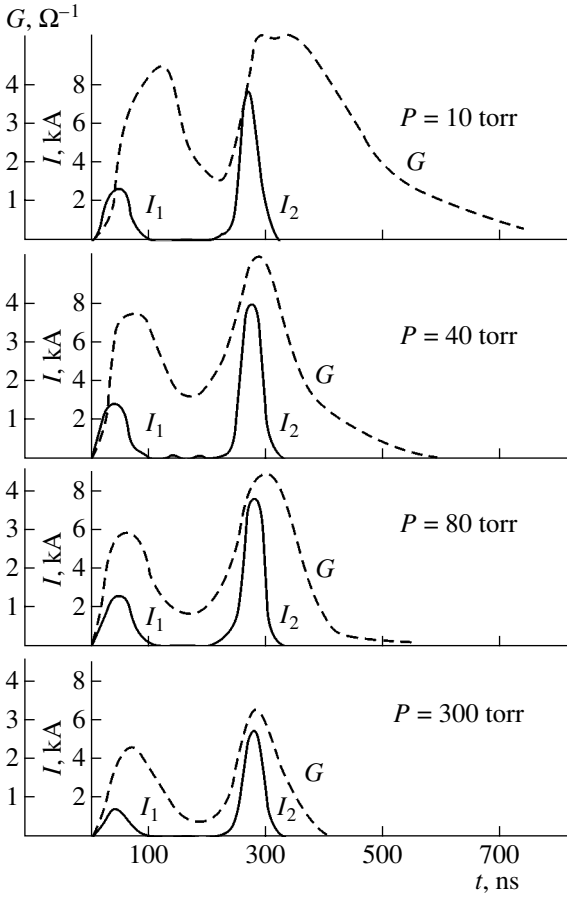

Fig. 5. Waveforms of the currents (I_1 and I_2 refer to the first and second REBs, respectively) and the plasma conductance G for L = 0.3 m and different gas pressures in a PR.

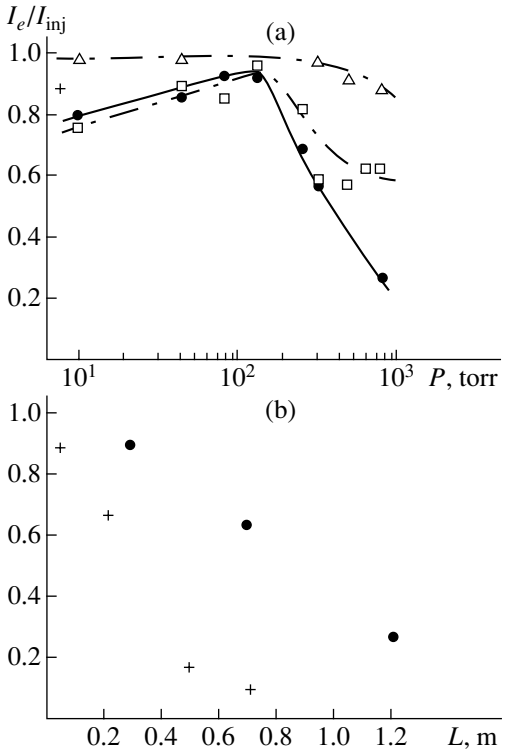

Fig. 6. (a) Transportation efficiency of the second high-current REB vs. gas pressure P in a PR for the time interval between the pulses t_n = 160 μs and different propagation lengths: L = (△) 0.3, (□) 0.7, and (●) 1.4 m. (b) Transportation efficiency of the second high-current REB vs. propagation length in the PR gas mixture at atmospheric pressure for different time intervals between the pulses: t_n = (+) 500 and (●) 160 μs.

ns. Hence, when the time interval between the pulses is in the range 250–500 ns, this plasma only slightly affects the propagation of the second beam. This is also confirmed by the measurements of the REB transportation characteristics in the above range of time intervals. In this case, the propagation of the second high-current electron beam through the PR gaseous medium is similar to the propagation of an REB in the single-pulse generation regime.

Figure 6 shows the transportation efficiency of the second REB under conditions of gas-dynamic propagation, when the first electron beam creates a low-density channel in the PR gaseous medium through which the second high-current electron beam propagates. We investigated the transportation efficiency of two high-current REBs with the time interval between them t_n = 160 μs in a PR filled with an $N_2 : O_2 = 4 : 1$ gas mixture at different pressures. It is interesting that the transportation efficiency of the second REB for gas pressures in the range P = 80–150 torr and propagation lengths L = 0.7 and 1.2 m is fairly high and the ratio I_e/I_{inj} smoothly increases from 0.8 to 0.95 as the gas pressure increases from 10 to 150 torr (Fig. 6a). It is reasonable to suggest that, in the initial stage of beam propagation (for L less than 0.5 m), when the energy deposition in the gas from the first electron beam is fairly high and the ionization losses of the second REB are low, the formation of a low-density channel increases the transportation efficiency I_e/I_{inj} of the second REB to 0.95–0.98 at gas pressures in the range P = 10–250 torr. As the gas pressure increases to 500–700 torr, the efficiency slightly decreases to 0.9 because of the increase in the ionization losses. The ionization losses play a decisive role at REB propagation lengths up to L = 0.7–1.2 m and decrease the transportation efficiency to 0.8 at pressures as low as P = 10 torr. The increase in the REB ionization losses is certainly related to a significant decrease in the gas mixture density in the propagation channel created by the fist electron beam at these pressures. As the gas mixture pressure in the PR increases to P = 10–150 torr, the gas density in the channel created by the first beam decreases to the optimum level; as a result, the transportation efficiency of the second REB increases to 0.96. With gas mixture pressures P > 150 torr and the REB propagation length equal to the reactor length (L = 1.2 m), the energy deposition in the gas from the first beam is not sufficient to provide the optimum decrease in the gas mixture density, which leads to a significant increase in the ionization losses of the second REB and, hence, a decrease in its transportation efficiency. Nevertheless, the results obtained for the gas-dynamic method of REB transportation in gas mixtures at pressures close to atmospheric show that the transportation efficiency of the second REB increases by 40–45% as compared to the single-pulse regime of beam generation and propagation at the same beam powers (Fig. 6b). Certainly, in order to increase the propagation efficiency of the second electron beam and, thus, the output capacity of the PR as a whole, it is necessary to further increase the power of the first REB, i.e., the energy deposited in the gas from the first electron beam over the propagation lengths L > 1 m.

CONCLUSIONS

The results of the experimental studies of the two-pulse generation regime of high-current REBs and their transportation characteristics in the PR gaseous medium can be formulated as follows:

(i) Two consecutive high-current REBs with powers of 2 and 4.0–9.6 GW, pulse durations of 60 ns, and a time interval t_n between the pulses of up to 500 ns are generated, and their propagation efficiency in a gaseous medium at different pressures is investigated. It is shown that, for PRs filled with an $N_2 : O_2 = 4 : 1$ gas mixture at nearly atmospheric pressure, the beam transportation efficiency for this generation method is higher by 35–45% than that obtained for the single-pulse generation regime at the same level of beam power. For electron beams in the power range under study, the maximum beam transportation efficiency for the given scheme of beam generation and propagation is I_e/I_{inj} = 0.75. This transportation efficiency is attained with the

time intervals between the beams $100 < t_n < 250$ ns, the gas pressure in the PR $P = 300$ torr, and the propagation length $L = 1.2$ m.

(ii) Two consecutive high-current REBs with powers of 1.8 and 16 GW, pulse durations of 60 ns, and a time interval between the pulses of $t_n = 160$ μs are generated, and their propagation efficiency in a gaseous medium at different pressures is investigated. It is shown that, for PRs filled with an $N_2 : O_2 = 4 : 1$ gas mixture at atmospheric pressure, the beam transportation efficiency for this generation method is higher by 40–45% than that obtained for the single-pulse generation regime at the same level of the beam power. It is found that, with the given beam powers, the propagation length $L = 1.4$ m, and gas pressures in the range $P =$ 80–150 torr, the transportation efficiency of the second high-current REB attains $I_e/I_{inj} = 0.95$.

In authors' opinion, the results obtained can be used in practice and will be useful in designing plasmochemical reactors and estimating their possible efficiency.

REFERENCES

1. G. E. Norman, L. S. Polak, P. I. Sopin, and G. A. Sorokin, in *Synthesis of Compounds in a Plasma Containing Hydrocarbons*, Ed. by L. S. Polak (Inst. Neftekhim. Sint. Akad. Nauk SSSR, Moscow, 1985), p. 33.
2. N. A. Kondratiev, V. A. Krasilnikov, Yu. A. Medvedev, *et al.*, in *Proceedings of the 14th International Conference on Chemical Reactors, Tomsk, 1998*, Vol. 1, p. 191.
3. A. A. Ipatov, S. N. Kabanov, A. A. Korolev, *et al.*, Pis'ma Zh. Tekh. Fiz. **10**, 162 (1984) [Sov. Tech. Phys. Lett. **10**, 66 (1984)].
4. D. P. Murphy, M. Raleigh, R. E. Pechacek, *et al.*, Phys. Fluids **30**, 232 (1987).
5. J. M. Picone, S. Boris, J. H. Gardner, *et al.*, in *Proceedings of the 5th International Conference on High Power Particle Beams, San Francisco, 1983*, p. 384.
6. T. G. Roberts and W. H. Bennet, Plasma Phys. **10**, 381 (1968).
7. S. E. Graybill and I. R. Uglum, J. Appl. Phys. **41**, 236 (1970).
8. A. A. Rukhadze and V. G. Rukhlin, Zh. Éksp. Teor. Fiz. **61**, 177 (1971) [Sov. Phys. JETP **34**, 93 (1972)].
9. S. L. Ginzburg and K. V. Khodataev, in *Proceedings of the 15th International Conference on Phenomena in Ionized Gases, Minsk, 1981*, p. 237.
10. S. A. Korenev, N. B. Rubin, and K. V. Khodataev, in *Workshop on Cooperative Methods of Acceleration, Dubna, 1982*, Abstracts of Papers, p. 161.
11. I. Z. Gleĭzer, A. N. Didenko, L. P. Dronova, *et al.*, At. Énerg. **36**, 378 (1974).
12. A. D. Blumlein, US Patent No. 589127 (1941).
13. N. A. Kondratiev, G. I. Kotlyarevsky, V. I. Smetanin, *et al.*, Phys. Lett. A **14A**, 89 (1990).
14. L. E. Aranchuk, V. D. Vikharev, V. V. Gorev, *et al.*, Zh. Éksp. Teor. Fiz. **86**, 1180 (1984) [Sov. Phys. JETP **59**, 747 (1984)].

Translated by N. Ustinovskiĭ

Technical Physics, Vol. 48, No. 7, 2003, pp. 854–857. Translated from Zhurnal Tekhnicheskoĭ Fiziki, Vol. 73, No. 7, 2003, pp. 55–58.

GAS DISCHARGES, PLASMA

Study of the Influence of the Injection Section on the Stability of a High-Current Relativistic Electron Beam Propagating through the Gaseous Medium of a Plasmochemical Reactor

N. A. Kondrat'ev and V. I. Smetanin[†]

Nuclear Physics Institute, Tomsk Polytechnical University, pr. Lenina 2a, Tomsk, 634050 Russia

e-mail: alex@npi.tpu.ru

Received December 15, 2002

Abstract—Results are presented from experimental study of the influence of the injection section on the stability of a high-current relativistic electron beam (REB) propagating through the gaseous medium of a plasmochemical reactor (PR). An REB with the electron energy E_e = 1 MeV, beam current I_b = 10–22 kA, and pulse duration t = 60 ns was generated by the Tonus accelerator and, then, injected into a 0.1-m-diameter PR filled with air. The PR consisted of two sections with lengths L_1 = 0.3–1.0 m and L_2 = 1.1–2.5 m; the total length of the system was no longer than 3.5 m. The first section was filled with air at a pressure of P_1 = 0.8–1.5 torr, and the pressure in the second section was varied within the range P_2 = 0.1–760 torr. The current I_b of an REB passed through both sections of the PR was measured with the help of a sectioned vacuum Faraday cup. The transportation efficiency of the beam was determined as the ratio I_b/I_{inj}, where I_{inj} is the beam current measured at the point of injection into the PR. It is shown that, for the optimal dimensions of the first PR section, it has a stabilizing action on the REB with a current density of up to 3 kA/cm^2, which makes it possible to increase the effective length of the second (working) PR section, which is filled with a gas at various pressures, to $L_2 = (25–35)L_{bet}$, where L_{bet} is the beam betatron length. © *2003 MAIK "Nauka/Interperiodica".*

Application of high-current relativistic electron beams (REBs) interacting with various gaseous media is of great interest because of their unique potentialities for concentrated energy deposition in a gas and the performance of a number of selective plasmochemical reactions. An important aspect of these applications, which are the subject of numerous investigations [1–3], is the problem of the stability of REB propagation through a gaseous medium. The regime and features of the interaction of a high-current REB with a gaseous medium are determined by the operating conditions of the plasmochemical reactor (PR). In one case, it is necessary to ensure the efficient volume recuperation of the REB energy into a gas when performing particular chemical reactions; in this case, a regime with large-scale resistive instability of the beam [4] may be recommended. In another case, stringent requirements are imposed on the propagation stability of the beam with minimum possible losses during its transportation in the reactor volume with given parameters of the gaseous medium (composition, pressure, temperature, etc.). The propagation regimes of high-current REBs through the PR gaseous medium in the absence of strong external focusing magnetic fields can be varied over a wide range. This became possible due to previous investigations [5], which revealed the efficient stabilizing action of the initial (injection) section of a PR on the high-current REB transportation. In this paper, we study the applicability limits of this method for REB stabilization. The results obtained may be used in practice when choosing the operating regimes of PRs.

The experimental setup was similar to that used in [5]. The parameters of an REB generated by the Tonus accelerator were the following: the electron energy E_e = 1 MeV and the beam current I_b = 10–22.5 kA. By using apertures with different diameters at the accelerator outlet behind the anode foil, we could vary the current density within the range 0.5–3.0 kA/cm^2 at the same pulse duration (t_e = 60 ns). In the course of experiments, a high-current REB was injected into a PR made of a metal drift tube 0.1 m in diameter. The PR consisted of two sections with lengths L_1 = 0.3–1.0 m and L_2 = 1.1–2.5 m; the total length of the system was no longer than 3.5 m (Fig. 1). The sections were separated by a 50-μm

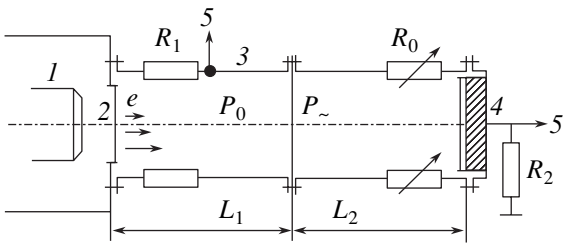

Fig. 1. Circuit diagram of the experiment: (*1*) cathode, (*2*) anode, (*3*) drift tube, (*4*) Faraday cup, and (*5*) to an oscillograph.

[†] Deceased.

titanium foil in order to have different pressures in them. The first section was filled with air at a pressure of P_1 = 0.8–1.5 torr. As was shown in [5], the REB transportation efficiency in the second (working) PR section is fairly high at this pressure. The air pressure in the second section was varied over the wide range P_2 = 0.1–760 torr.

It is well known that the onset of large-scale resistive instabilities of a high-current REB (first of all, hose instability) worsens the beam transportation. The hose instability of a beam in a finite-conductivity plasma was studied in many papers (see, e.g., [6]). The mechanism for this instability can be explained as follows. Small random oscillations (excursions) of the beam give rise to a centrifugal force that acts on the beam particles moving in the self-magnetic field. Under the action of this force, the REB shifts in the transverse direction over a distance on the order of the radius in a time longer than the diffusion time of the magnetic field in the ambient plasma, $t_d = 4\pi\sigma r_e/c^2$, where σ is the plasma conductivity and r_e is the beam radius. As the REB shifts in the transverse direction, its magnetic field shifts more slowly (the velocity of this shift is determined by the plasma conductivity), so that there is a phase lag between the shifts of the beam and its magnetic field. The beam motion with respect to its self-magnetic field induces the return plasma current I_p, which is spatially separated from the REB current I_b. The magnetic repulsion of the oppositely directed currents leads to a further shift of the beam. The increase in the amplitude of transverse REB oscillations is a consequence of the onset of resistive hose instability (RHI). These oscillations prevent the beam transportation over distances longer than one to three betatron lengths $L_{\text{bet}} = \pi r_e (I_A/I_b)^{0.5}$, where I_A is the Alfvén current, I_b is the beam current, and r_e is the beam radius [2]. For an REB with parameters similar to those in our experiments, L_{bet} is about 0.3–0.35 m. Based on this condition, the length of the first PR section was chosen so as to prevent the onset of large-scale REB instability.

The table gives the basic parameters of the high-current REBs and the generation regimes used in our experiments, as well as the betatron lengths corresponding to these regimes (L_{bet1} is equal to one betatron length, and L_{bet3} is equal to three betatron lengths). By analogy to [5], a high-current REB passed through the two PR sections was measured with the help of a sectioned vacuum Faraday cup placed at the end of the second section. This allowed us to determine both the amplitude of the REB current and its spatiotemporal evolution in the reactor. The beam transportation efficiency in the reactor was determined as the ratio I_b/I_{inj}, where I_b is the electron-beam current measured at the end of the PR (the PR length is L = 3–3.5 m) and I_{inj} is the REB current measured at the point of injection into the PR (behind the anode foil of the accelerator, at a distance of L = 0.01 m). The results of the measurements

Basic parameters and generation regimes of an REB

REB generation regime	REB current I_b, kA	REB diameter D_b, cm	REB current density J_e, kA/cm^2	Betatron length $L_{\text{bet1}}/L_{\text{bet3}}$, cm
1	22.5	5	1.14	11.5/34.4
2	17.5	5	0.89	13.0/39.0
3	12.8	5	0.65	15.2/45.6
4	18.5	2.8	3.00	7.0/21.5
5	10.1	2.8	1.64	9.8/28.7
With apertures on the accelerator anode				
6	5.0	2.8	0.81	13.62/40.8
7	15.5	2.8	2.52	7.73/23.2
8	5.0	4.0	0.41	19.48/58.45

of the REB transportation efficiency as a function of the air pressure in the second PR section are shown in Figs. 2 and 3. The air pressure in the first section was P_1 = 1 torr in all the experiments. The figures clearly demonstrate the main features of the propagation of a high-current REB in the reactor under different conditions. When choosing the regime of the interaction of an REB with the PR gaseous medium, the preference should evidently be given to a reactor scheme with the first section (gas cell) having the optimal gas pressure

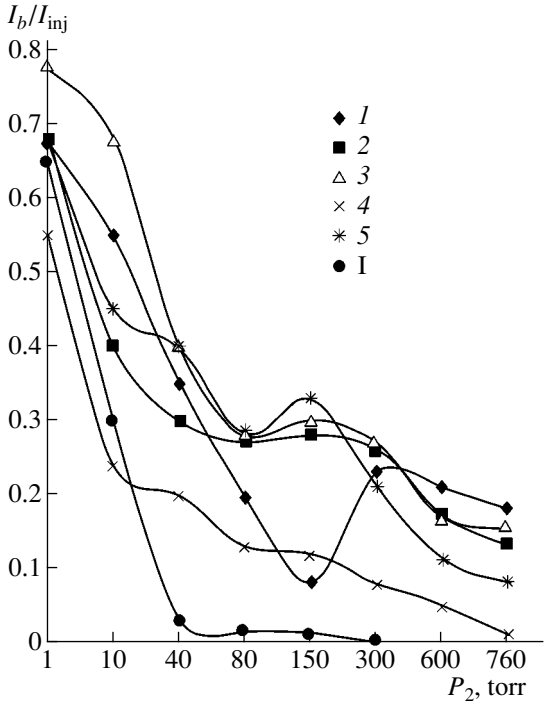

Fig. 2. Transportation efficiency of a high-current REB as a function of air pressure in the second PR section for generation regimes *1–5* (see table) at the gas pressure in the first section P_1 = 1 torr and (I) regime without a first section. The REB current is 22.5 kA.

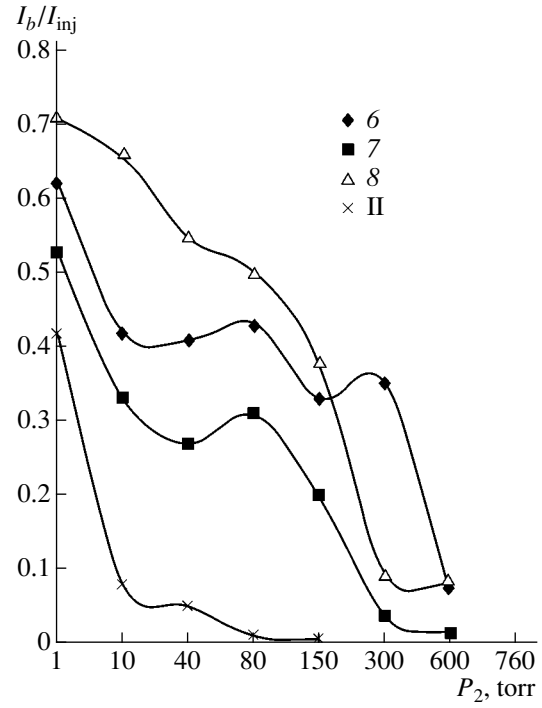

Fig. 3. Transportation efficiency of a high-current REB as a function of air pressure in the second PR section for generation regimes *6–8* (see table) at the gas pressure in the first section P_1 = 1 torr and (II) regime without a first section. The REB current is 15.5 kA.

P_1 and length L_1 in order to provide a relatively stable propagation of the electron beam over interaction lengths of about (20–30)L_{bet}.

A comparative analysis of the REB transportation efficiency for the gas-cell regime (Fig. 2, regimes *1–5*; Fig. 3, regimes *6–8*) and the regime without a first section at the REB currents I_b = 22.5 kA (Fig. 2) and I_b = 15.5 kA (Fig. 3) shows the advantages of the former PR scheme. With this scheme, the REB transportation efficiency can be increased by 40–50% as compared to the latter scheme. At gas pressures of P_2 > 80 torr, it is this scheme that allows one to achieve a relatively stable REB propagation in the reactor gas volume over interaction lengths of about 3 m. Choosing the optimum conditions for the REB transportation in the injection section, one can minimize the effect of the plasma processes that occur in the accelerating anode–cathode gap and are responsible for the onset of transverse beam oscillations [5]. In this case, the REB transportation through the PR gaseous medium is disturbed primarily by collisional ionization. At the same time, we cannot exclude a possible contribution of large-scale beam instability, which can be substantial under certain conditions. However, if this instability actually takes place, its spatial growth rate should be much smaller than that observed in the regime without a first PR section (gas cell). Thus, the increase in the current density to 3 kA/cm^2 or higher leads to both the appearance of

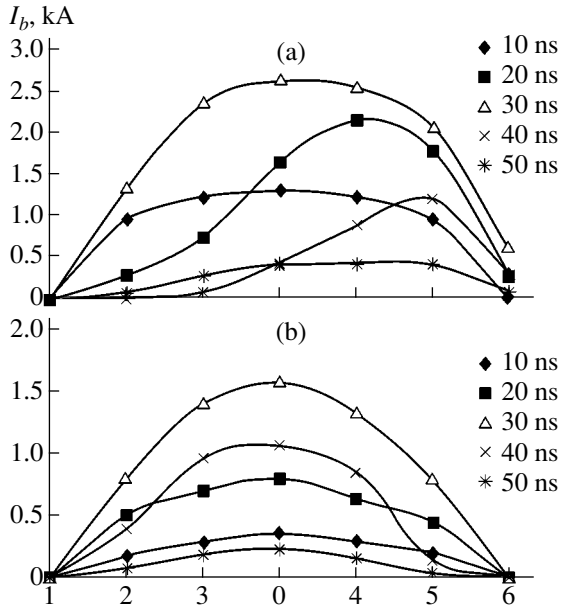

Fig. 4. Distribution of the beam current over the cross section of the PR transportation channel at the injection current I_b = 22.5 kA for the air pressure in the second PR section P_2 = (a) 150 and (b) 300 torr. The gas pressure in the first section is P_1 = 1 torr. The lengths of the first and second sections are L_1 = 0.3 m and L_2 = 2.5 m, respectively; the total length of the system is 3 m.

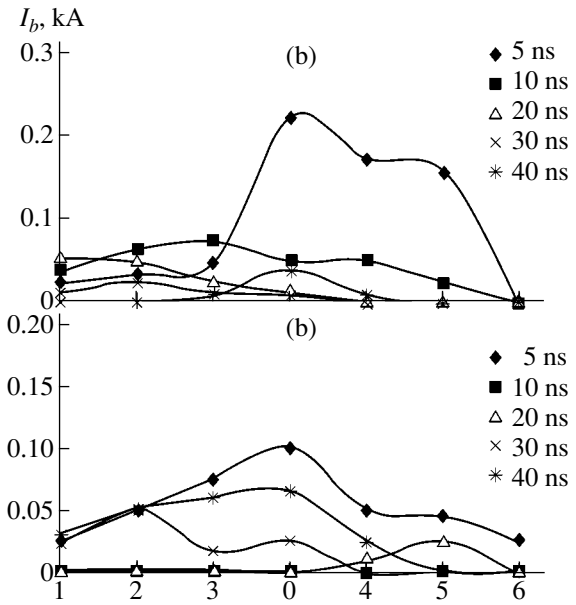

Fig. 5. Distribution of the beam current over the cross section of the PR transportation channel at the injection current I_b = 22.5 kA in the regime without a first PR section for the air pressure in the second PR section P_2 = (a) 40 and (b) 80 torr. The length of the second section is L_2 = 2.5 m.

transverse REB oscillations that are typical of the onset of large-scale instability and an abrupt decrease in the transportation efficiency (Fig. 2, regime *1*). The data on the regimes without a first section agree well with the onset of large-scale resistive REB instability, which was considered in detail in [7].

Figures 4 and 5 show the distributions of the beam current over the cross section of the interaction channel in these regimes. These distributions, which were measured with the help of a sectioned Faraday cup, confirm the results of the above comparison.

Hence, the results of our studies clearly demonstrate the possibility of efficiently controlling the interaction conditions of a high-current REB with a PR gaseous medium. The general features revealed in the course of these investigations are the following:

The stable regime of the interaction and transportation of a high-current REB in the PR gaseous volume can be achieved by using the first PR section, whose length is larger than $3L_{bet}$ and which is filled with air at an optimal pressure of $P_1 = 1$ torr.

The stabilizing action of the first PR section with these optimal parameters manifests itself at REB current densities of up to 3 kA/cm^2. In this case, the effective length of the second (working) PR section, which is filled with a gas at pressures of up to atmospheric pressure, can attain $L_2 = (25–35)L_{bet}$.

The increase in the REB current density to higher than 3 kA/cm^2, as well as the use of a reactor without a first section, can be recommended for PRs operating under conditions that admit the onset of large-scale instability with the amplitude of transverse beam oscillations substantially exceeding the beam diameter and, in particular cases, resulting in the departure of the beam onto the reactor wall.

REFERENCES

1. V. D. Rusanov and A. A. Fridman, *Physics of Chemically Active Plasmas* (Nauka, Moscow, 1984), p. 230.
2. G. E. Norman, L. S. Polak, P. I. Sopin, *et al.*, in *Synthesis of Compounds in a Plasma Containing Hydrocarbons*, Ed. by L. S. Polak (Inst. Neftekhim. Sint. Akad. Nauk SSSR, Moscow, 1985), p. 3.
3. R. F. Hubbard, R. F. Fernsler, S. P. Slinker, *et al.*, in *Proceedings of the 5th International Conference on High Power Particle Beams, San Francisco, 1983*, p. 370.
4. N. A. Kondrat'ev, G. I. Kotlyarevsky, and V. I. Smetanin, Zh. Tekh. Fiz. **58**, 1915 (1988) [Sov. Phys. Tech. Phys. **33**, 1164 (1988)].
5. N. A. Kondratiev, V. I. Smetanin, and Yu. P. Surikov, Nucl. Instrum. Methods Phys. Res. **53**, 229 (1991).
6. E. J. Lauer, R. J. Briggs, T. J. Fessenden, *et al.*, Phys. Fluids **21**, 1344 (1978).
7. E. P. Lee and J. E. Brandenburg, Phys. Fluids **31**, 3403 (1988).

Translated by E. Satunina

Technical Physics, Vol. 48, No. 7, 2003, pp. 858–865. Translated from Zhurnal Tekhnicheskoĭ Fiziki, Vol. 73, No. 7, 2003, pp. 59–66.

GAS DISCHARGES, PLASMA

Quasi-Stability of a Plasma Bicylinder

V. P. Vlasov and B. A. Trubnikov

Nuclear Fusion Institute, Russian Research Centre Kurchatov Institute, pl. Kurchatova 1, Moscow, 123182 Russia

e-mail: vlasov@nfi.kiae.ru, batrub@nfi.kiae.ru

Received October 1, 2002; in final form, December 6, 2002

Abstract—Observations seem to indicate that, in the plasmas of tokamaks and Z-pinches, short-lived closed current loops (filaments) can arise, each of which is composed of a pair of countercurrents flowing within the two halves of the cross section of the plasma cylinder in directions perpendicular to that of the main magnetic field. It is shown that such a plasma structure (which will be referred to as a bicylinder, for brevity) can, in fact, be stable (or quasi-stable, in the terminology used below). In the note added in proof, a possible mechanism for the generation of so-called blobs—peculiar perturbations that have relatively recently been discovered in tokamaks—is discussed. © *2003 MAIK "Nauka/Interperiodica".*

PLASMA BICYLINDER

The first scientific paper [1] by one of us (B.A. Trubnikov), entitled "On the Stability of a Plasma Cylinder" and published about fifty years ago, dealt with Z-pinch constrictions, the breaking of which releases nonthermonuclear neutrons in deuterium pinches. In the present work, we consider the equilibrium and stability of a plasma configuration having some properties similar to Z-pinches (see Fig. 1).

Figure 1 shows the cross section of a circular plasma cylinder in the (x, y) plane. The countercurrents $\pm I$, distributed over the plasma, flow within the two halves of the cylinder along the z axis. The cylinder is in an external uniform magnetic field $B_y = B_0$. For brevity, we will call this configuration a plasma bicylinder. The existence of such structures in tokamaks and Z-pinches has been discovered by A.B. Kukushkin and V.A. Rantsev-Kartinov (KRK) [2] (see also the literature cited therein). Figure 2 presents a photograph of the structures observed by them. On the left (*1*) and right (*2*) sides of the photograph, which is taken from [2], we can see tubular structures; KRK interpreted them as "cables of solid-state carbon nanotubes."

EQUILIBRIUM OF A PAIR OF COUNTERCURRENTS IN AN EXTERNAL MAGNETIC FIELD

We think, however, that there are no solid grounds for such an exotic interpretation, because these structures are most likely to be a pair of current filaments that form according to the mechanism illustrated schematically in Fig. 3.

We consider two formless loops of flexible conductors that are laid out on the table and whose ends are fixed (Fig. 3). We also assume that the magnetic field $B_y = B_0$ is directed upward; i.e., it is perpendicular to the table's surface. After switching on dc batteries, the loops start to interact with the magnetic field B_0, which thus drives them into motion (the friction between the loops and the table surface is neglected). Then, the right loop, in which the direction of the current with respect to the magnetic field is that of a right-handed screw, will smooth out to form a circle whose radius will increase without bound provided that the loop is perfectly elastic.

In turn, in the interaction with the field B_0, the left loop, in which the current flows in the direction opposite to that in the right loop, will form two parallel lines, which will approach one another until the repulsing forces produced by the oppositely directed currents in them come into play. We can easily see that the parallel lines stop moving when the total magnetic field across

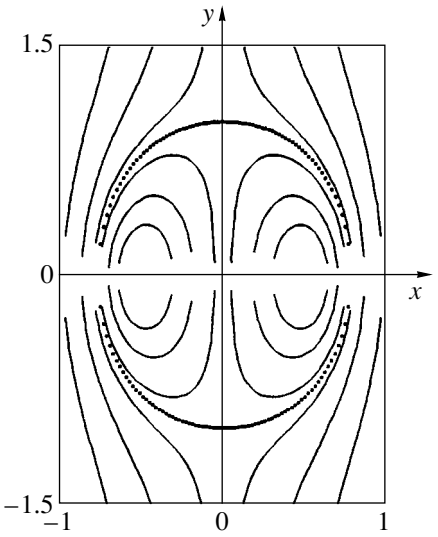

Fig. 1. Streamlines of two countercurrents flowing along the z axis in an external magnetic field B_0 directed along the y axis.

1063-7842/03/4807-0858$24.00 © 2003 MAIK "Nauka/Interperiodica"

them vanishes, i.e., when the distance between them becomes equal to $2a = 2I/cB_0$ (of course, when the conductors are thin, this configuration is unstable against their vertical displacements; however, this situation will be discussed below).

Now, we analyze the behavior of the bridge between the ends of the parallel lines on the left side of Fig. 3. At first glance, it appears that the interaction between the current I flowing in the bridge and the magnetic field B_0 should push the bridge toward the battery while simultaneously trying to crease it. Instead, the bridge indeed moves away from the battery. In order to convince ourselves of this, note that, along the line z = const that crosses the two parallel conductors and is far from the bridge, the total magnetic field is equal to $B_y = B_0[1 - 4a^2/(a^2 - x^2)]$. In the region between the conductors, the total field is negative; in particular, just between the conductors (at $x = 0$), we have $B_y = -3B_0 < 0$. In turn, the negative magnetic field pushes the bridge outward from the battery, thereby elongating the two parallel conductors. Figuratively speaking, the elongating conductors "germinate" in a direction perpendicular to the magnetic field.

Let us consider in more detail the equilibrium configuration of a pair of semi-infinite countercurrents. Using the Biot–Savart law, we can calculate the magnetic field of an arbitrarily thin, semi-infinite straight conductor in which the current I flows along the z axis from $z = -\infty$ to $z = 0$. In cylindrical coordinates (r, φ, z), we obtain the expression

$$B_\varphi = \frac{I}{cr}\left(1 - \frac{z}{\sqrt{r^2 + z^2}}\right). \quad (1)$$

At $z = -\infty$, this field, as expected, is equal to $B_\varphi = 2I/cr$; however, at $z = 0$, it turns out to be two times weaker. Consequently, under equilibrium conditions in the external magnetic field $B_0 = B_y$, the distance between the ends (at $z = 0$) of two semi-infinite straight conductors with oppositely directed currents $\pm I_z$ should be equal to $2a_{new} = I/cB_0$, which is two times shorter than the distance between two infinite ($-\infty \le z \le +\infty$) conductors in equilibrium.

If we introduce the dimensionless variables $Z = z/a$ and $X = x/a$ (where $a = I/cB_0$), then, from the above formula, we can readily find the equilibrium positions of two semi-infinite conductors that are in equilibrium with one another in an external magnetic field and the distance between which becomes progressively smaller toward their ends:

$$Z = (1 - 2|X|)\sqrt{|X|/(1 - |X|)}, \quad (2)$$

where $|X|$ is the absolute value of X.

In the photograph in Fig. 2, the upper parts of the right two filaments are distinctly seen to approach one another up to the points at which they terminate.

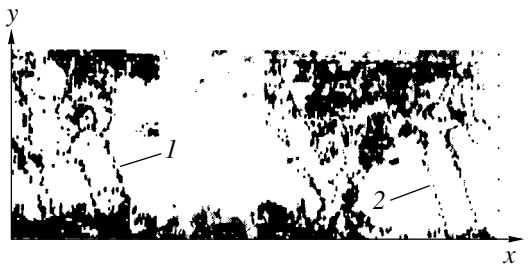

Fig. 2. Filaments at the plasma periphery in the T-6 tokamak (taken from [2]). The x axis is aligned with the toroidal field, and the y axis is directed from the wall toward the plasma column.

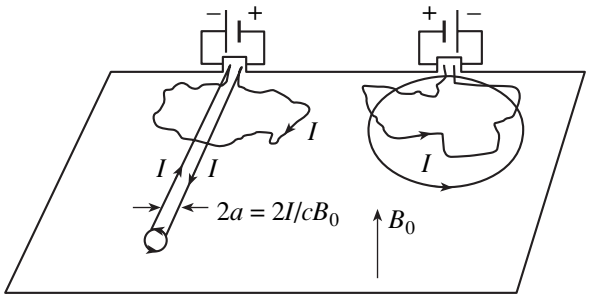

Fig. 3. Behavior of two current loops in a vertical magnetic field B_0.

SHORT-CIRCUITING OF TWO COUNTERCURRENTS AT THE ENDS

Moreover, the current in the bridge presumably tends to bifurcate (branch) in two directions and to flow along the two semicircles (Fig. 1). This possible structure is evidenced by the pattern of the magnetic field lines in the end cross section. If, for simplicity, we assume that the pattern is the same as that for two arbitrarily thin, infinite conductors with countercurrents $\pm I$ separated by the two times smaller distance $2a_{new} = I/cB_0$, then the magnetic field lines A = const are described by the simple formula

$$Y = \frac{y}{a_{new}} = \pm\sqrt{4X\coth(A + 2X) - 1 - 4X^2}. \quad (3)$$

The pattern of these field lines is shown in Fig. 1, where the separatrix is indicated by dots.

The tubular structures in the photographs presented by KRK are such that the possible current path may be as follows. First, the current $+I$ flows from minus infinity ($z = -\infty$) to the point $x = +a_{new}$. Second, the current flows to the right toward the nearer (right) equatorial point of the common circular separatrix. Third, at this point, the current bifurcates into two equal currents $I/2$, which flow along the upper and lower semicircles (i.e., along the separatrix of the magnetic field lines) toward the left equatorial point of the separatrix, where they merge. Finally, the current flows to the right toward the end $x = -a_{new}$, from where it flows to $z = -\infty$.

It is clear that, for straight-line segments of finite length, the separatrix in the form of two semicircles should also form at the remote end of the structure and should look like the left tubular structure in Fig. 2. On the whole, such a structure may resemble a "squirrel cage" with "wheel-like" ends and two "bridges" between then. Presumably, it is these structures that were revealed by KRK in tokamak plasmas and were mistakenly interpreted by them as solid-state nanotubes.

It seems that, in tokamak plasmas, such structures may result from short-term local fluctuations of the main longitudinal magnetic field: the fluctuations give rise to closed current loops that are perpendicular to the main field and evolve into pairs of countercurrents in the way described above. Another possible mechanism for the onset of squirrel-cage structures that have bridges and are oriented perpendicularly to the magnetic field may be associated with the fluctuation-driven local potential difference that arises between neighboring magnetic surfaces, especially in the vicinities of rational surfaces with integer values of the parameter q (in the tokamak theory, it is called the safety factor). At a certain time, the differential rotation of a plasma along the magnetic surfaces in the poloidal direction may result in the close opposition of two local spotlike regions with different potentials, as is the case with two capacitor plates. In turn, the potential difference can generate a local cross-field particle beam, which splits into individual filamentary bridges and thereafter forms wheel-like ends.

EQUILIBRIUM OF A PLASMA BICYLINDER IN AN EXTERNAL FIELD

Returning now to Fig. 1, note that two arbitrarily thin, infinite conductors with equal and oppositely directed currents in an external magnetic field are, of course, unstable against vertical displacements along the y axis. However, such a structure may be expected to be stable when the region inside the cylindrical separatrix is filled with plasma. We start by considering the equilibrium of a bicylinder.

For simplicity, we assume that there are no currents on the outside of the cylinder, so that the vector potential $A = A_z(r, \varphi)$ of the external magnetic field is described by the two-dimensional Laplace equation

$$\Delta A = 0, \quad A = -B_0\left(r - \frac{a^2}{r}\right)\cos\varphi, \tag{4}$$

which determines the field components in the form

$$B_r = \frac{\partial A}{r\partial\varphi} = B_0\left(1 - \frac{a^2}{r^2}\right)\sin\varphi,$$
$$B_\varphi = -\frac{\partial A}{\partial r} = B_0\left(1 + \frac{a^2}{r^2}\right)\sin\varphi. \tag{5}$$

At the cylinder surface $r = a$, we have $B_r = 0$, $B_\varphi = 2B_0\cos\varphi$, and $B^2/8\pi = (B_0^2/2\pi)\cos^2\varphi$. Assuming that there is a homogeneous plasma at constant pressure (p_0 = const) on the outside, we consider the situation inside the cylinder.

Since there are currents with the density $j = j_z$ within the separatrix, we can write the MHD equations

$$\Delta A = -\frac{4\pi}{c}j, \quad B_x = A_y', \quad B_y = -A_x',$$
$$p_x' = \frac{j}{c}A_x', \quad p_y' = \frac{j}{c}A_y', \tag{6}$$

according to which the plasma pressure $p = p(A)$ is an arbitrary function and the current density is equal to $j = cdp/dA$. Setting $p(A) = p_0 + |\beta|A^2$, we obtain the current density, $j = 2c|\beta|A$, and arrive at the following Bessel equation for the vector potential

$$A_{rr}'' + \frac{1}{r}A_r' + \frac{1}{r^2}A_{\varphi\varphi}'' + k^2A = 0, \tag{7}$$

where $k = \sqrt{8\pi|\beta|}$.

The solution with the first Bessel function yields the potential and field components inside the cylinder,

$$A = A_0 J\cos\varphi, \quad B_r = -\frac{A_0}{r}J\sin\varphi,$$
$$B_\varphi = -A_0 kJ'\cos\varphi, \tag{8}$$

where $J = J_1 = J_1(\rho)$ and $\rho = kr$, and satisfies all the requirements for equilibrium of the configuration. Specifically, at the cylinder surface $r = a$, the radial component of the internal magnetic field, B_r, vanishes if $J_1(ka) = 0$, where $ka = N_1 = 3.8317$ is the first zero of the first Bessel function, which is approximated by the expression $J_1(\rho) \approx (\rho/2)[1 - (\rho/3.8317)^2]$ across the region $0 < \rho < 3.8317$. In this case, at the cylinder surface, the vector potential vanishes, $A = 0$, and the pressure of the inner plasma is equal to $p_{A=0} = p_0$, as is the pressure in the entire region of the outer plasma.

At the cylinder surface, the magnetic field component $B_\varphi = B_a\cos\varphi$ with $B_a = -A_0kJ'(ka)$ produces the magnetic pressure $P_m = (B_a^2/8\pi)\cos^2\varphi$. Consequently, the complete equilibrium of a configuration with a dipole current-carrying cylindrical beam, which moves apart the lines of the external magnetic field, will be achieved when $B_a = 2B_0$. The tabulated values of the Bessel functions give $J'(N_1) = -0.4028$, which enables us to determine the amplitude of the vector potential, $A_0 = 1.3aB_0$, and, thereby, the current density $j = j_0J_1(kr)\cos\varphi$, where $j_0 = 1.5(cB_0/a)$. In such a configuration, the current flowing through the right half of the cylinder is about $I_+ \approx 0.8caB_0$, and the same current flows through the left part but in the opposite direction. If the current I_+ and the field B_0 are specified, we can

determine the equilibrium radius of the cylinder, $a = I_+/0.8cB_0$. Thus, in order for the dipole current $I_+ = -I_- =$ 10 kA to be in equilibrium with the tokamak magnetic field $B_0 = 10$ kGs, it should flow across the field B_0 inside the region with a diameter of about $2a \sim 3$ mm. The filaments of roughly the same diameter were observed by KRK [2].

STABILITY ANALYSIS BY EVALUATING THE INTEGRAL $J = \int dl/B$

Plasma–current filaments like a bicylinder of finite length may be conditionally referred to as "pseudotubular structures," because they resemble tubes. The existence of such structures is questioned by many critics of KRK's works (see, e.g., KRK's paper [2] and two critical comments published in the same issue). However, if these structures do indeed exist, it is relevant to study their stability. The main characteristic of the stability of a bicylinder is the correct behavior of the integral $J = \int dl/B$ near the cylinder surface. Below, it will be shown that, on the outside of the cylinder, the integral decreases with increasing distance from the cylinder surface.

For comparison, we begin by recalling that the magnetic field on the outside of an ordinary Z-pinch of radius a, with the current $I = I_z$, is equal to $B = 2I/cr$. In this case, the integral becomes $J_{ext} = \pi(c/I)r^2 \sim r^2$; i.e., it increases with distance from the cylinder surface, thereby indicating that the pinch is unstable against the development of constrictions. Inside the pinch, the current that is distributed uniformly over the pinch cross section produces the magnetic field $B = B_0 r/a$, in which case the integral is constant over the cross section, $J_{int} = \pi(c/I)a^2 =$ const, and thus does not affect the stability.

It may be, however, that a Z-pinch in which the current is nonuniformly distributed over the cross section and the pressure has the form $p = p(A) = p_0 + \beta A^2$ resembles the bicylinder in question more closely. In such a pinch, the current density is equal to $j = cdp/dA = 2c\beta A$, so that the vector potential satisfies the Bessel equation

$$\nabla \times \mathbf{B} = -\Delta A = (4\pi/c) j = k^2 A, \qquad A = A_z = A_0 J_0(z), \tag{9}$$

where $z = kr$ and $k^2 = 8\pi\beta$.

The pinch radius a is determined by the first zero of the first Bessel function, $ka = N_0 = 2.4$, and the magnetic field is equal to $B = B_\varphi = -\partial A/\partial r = -A_0 k J_0'(z) = A_0 k J_1(z)$, where $J_1(z)$ is the first Bessel function. For a given total current I, the amplitude of the vector potential is $A_0 = 2I/cN_0 J_1(N_0)$, where $J_1(N_0) = 0.52$ and $N_0 J_1(N_0) = 0.2166$. At the pinch boundary, the integral is equal to $J_a = \int dl/B = \pi a^2 c/I$, and, inside the pinch, it is equal to $J_{int} = \int dl/B = J_a f(r)$, where the factor $f(r) = 0.2166 z/J_i(z)$ increases from $f(0) = 2 \times 0.2166$ at the pinch axis to $f(r = a) = 1$ at the pinch boundary. On the outside of the pinch, the integral increases according to the law $J_{ext} = (r/a)^2 J_a$. We thus see that the integral is increasing everywhere, which indicates that the pinch is unstable against the development of constrictions.

On the outside of the bicylinder, the situation is opposite: the integral $J_{bc} = \int dl/B$ decreases away from the cylinder surface, thereby preventing the formation of constrictions. Calculating this integral for the outer region, in which the potential and the magnetic field are equal to

$$A = -B_0\left(r - \frac{a^2}{r}\right)\cos\varphi, \qquad B_r = \frac{\partial A}{r\partial\varphi} = B_0\left(1 - \frac{a^2}{r^2}\right)\sin\varphi, \tag{10}$$

yields

$$J_{bc} = \int \frac{dr}{B_r} = 2\int_{r_{min}}^{\infty} \frac{dr}{\sqrt{B_0^2[1-(a/r)^2]^2 - (A/r)^2}}, \tag{11}$$

where the integration should be carried out along the outer magnetic field line $A(r, \varphi) =$ const.

Introducing the variable $x = (r/a)^2$ and setting $x = x_{min} + (y/a)^2$, we rewrite integral (11) as

$$J_{bc} = \frac{a}{B_0}\int_{x_{min}}^{\infty} \frac{\sqrt{x}dx}{\sqrt{(x - x_{min})(x - x_{min}^{-1})}} = \frac{2}{B_0}\int_0^{\infty} R dy, \tag{12}$$

where $R = R(y) = (1-\xi)^{-1/2}$, $\xi = 1/x_{min}[x_{min} + (y/a)^2]$, and $x_{min} = (r_{min}/a)^2$. Since $r_{min} > a$, we have $x_{min} > 1$ and, accordingly, $\xi < 1$, which permits us to expand the function R in a series,

$$R = 1 + \sum_{n=1}^{\infty} \frac{(2n-1)!!}{(2n)!!}\xi^n. \tag{13}$$

The integral J_{bc} diverges because the outer magnetic field lines are infinite in length. However, the first term (the unity) in the expansion should be excluded from consideration since it produces the integral $J_{bc}^{(1)} = (2/B_0)\int_0^{\infty} dy$ over the straight lines of a uniform magnetic field unperturbed by the bicylinder. We finally arrive at the "effective" integral

$$J_{bc} \longrightarrow J_{eff} = \frac{2}{B_0}\sum_{n=1}^{\infty} \frac{(2n-1)!!}{(2n)!!}\int_0^{\infty}\xi dy = \frac{\pi a}{2B_0} z^3 F\left(\frac{1}{2}, \frac{3}{2}; 2; z^4\right), \tag{14}$$

where $z = a/r_{\min} < 1$ and F is a hypergeometric series.

In view of the fact that the effective integral J_{eff} decreases with distance from the cylinder surface ($r_{\min} > a$), the result obtained allows us to expect that the bicylinder will be stable at least against the development of constrictions at its boundary. Inside the bicylinder, the situation is unstable against snakelike perturbations. Let us, however, investigate this point in more detail.

ENERGY STABILITY PRINCIPLE

In what follows, we assume for simplicity that there is no plasma outside the cylinder, in which case the external magnetic field is a vacuum field. Under this assumption, we can use the well-known generalized energy stability principle (see, e.g., [3]), which requires that $S_1 + S_2 + S_3 > 0$, where the terms S_i are three integrals. The last (third) term S_3 is a "vacuum" integral, which is taken over the entire outer vacuum region and is always positive. For this reason, it is sufficient to consider only the first two terms. The second term S_2 is a "surface" integral, which is taken over the plasma surface (in the case at hand, the cylinder surface) and is equal to

$$S_2 = \int \xi_r^2 \frac{d\langle P\rangle}{dr} d\sigma,$$
$$\langle P\rangle = P_e - P_i = \frac{B_e^2}{8\pi} - \left(p + \frac{B_i^2}{8\pi}\right), \tag{15}$$

where $B_{e,i}$ are the external and internal magnetic fields, respectively, and p is the plasma pressure. Using the above formulas, we find the difference of the total pressures on the outside and inside of the cylinder:

$$\langle P\rangle = \frac{B_0^2}{8\pi}\left(1 + \frac{a^4}{r^4} + 2\frac{a^2}{r^2}\cos 2\varphi\right)$$
$$- \frac{A_0^2}{8\pi}\left[k^2(J^2 + J'^2)\cos^2\varphi + \frac{J^2}{r^2}\sin^2\varphi\right]. \tag{16}$$

At the cylindrical surface $r = a$, the radial derivative of this pressure difference vanishes,

$$\left(\frac{d\langle P\rangle}{dr}\right)_{r=a} = [(A_0 k J')^2 - 4B_0^2]\frac{\cos^2\varphi}{4\pi a} = 0, \tag{17}$$

so that the surface integral also drops out of our analysis. We are thus left with the first term, which is an integral over the entire plasma volume (or, in the case at hand, the volume of the cylinder).

This volume integral is equal to

$$S_1 = \int \mathcal{L} dV,$$
$$\mathcal{L} = \frac{1}{4\pi}R^2 + \frac{1}{c}(\mathbf{j}\cdot[\boldsymbol{\xi}\times\mathbf{R}]) + \gamma p D^2 + (\boldsymbol{\xi}\cdot\nabla p)D, \tag{18}$$

where $\gamma = 5/3$ is the adiabatic index, $D = \nabla\cdot\xi$, and $\mathbf{R} = \nabla\times[\boldsymbol{\xi}\times\mathbf{B}]$. Here and below, the vector function $\boldsymbol{\xi}$ is treated as a test function (the velocity of the "initial impact") such that the stability condition $S_1 > 0$ should be satisfied for all its values.

Then, following the standard procedure, we resolve the seed perturbation into two components parallel and perpendicular to the magnetic field, $\boldsymbol{\xi} = \boldsymbol{\xi}_\parallel + \boldsymbol{\xi}_\perp$. Since the longitudinal component $\boldsymbol{\xi}_\parallel$ does not enter the expression $\mathbf{R} = \mathbf{R}_* = \nabla\times[\boldsymbol{\xi}_\perp\times\mathbf{B}]$, the Lagrangian can be rewritten as

$$\mathcal{L} = \frac{1}{4\pi}R_*^2 + \frac{1}{c}(\mathbf{j}\cdot[\boldsymbol{\xi}_\perp\times\mathbf{R}_*])$$
$$+ \gamma p(D_\perp + D_\parallel)^2 + (\xi_\perp\nabla p)D_\perp + \delta, \tag{19}$$

where we have singled out the term $\delta = c^{-1}(\mathbf{j}\cdot[\boldsymbol{\xi}_\parallel\times\mathbf{R}_*]) + (\boldsymbol{\xi}_\perp\nabla p)D_\parallel$, which is known to reduce to the total divergence and which vanishes (by virtue of the boundary conditions at the cylinder surface) after integration over the plasma volume. Now, the longitudinal perturbation component $\boldsymbol{\xi}_\parallel$ enters the Lagrangian only through the term with the squared divergence, $\gamma p(D_\perp + D_\parallel)^2$. If $D_\parallel = \nabla\cdot\xi_\parallel \neq 0$, the most dangerous perturbations minimizing the Lagrangian are those that satisfy the condition $\nabla\cdot\xi = 0$, which refers to an incompressible fluid. That is why, in the next section, the stability analysis will be continued in the incompressible fluid approximation.

STABILITY ANALYSIS IN THE INCOMPRESSIBLE FLUID APPROXIMATION

Now, we are left with the terms that contain only the perturbation component $\boldsymbol{\xi}_\perp$, which is transverse to the magnetic field:

$$\mathcal{L}_* = \frac{1}{4\pi}R_*^2 + \frac{1}{c}(\mathbf{j}\cdot[\boldsymbol{\xi}_\perp\times\mathbf{W}]), \quad \mathbf{W} = \mathbf{R}_* - \mathbf{B}D_\perp. \tag{20}$$

In this case, the necessary stability condition has the form $\mathcal{L}_* > 0$. To proceed further, it is convenient to introduce three unit vectors, $\mathbf{t}$, $\mathbf{n}$, and $\mathbf{b} = \mathbf{t}\times\mathbf{n}$—a tangent, a normal, and a binormal to the magnetic field line at each point. We set $\boldsymbol{\xi}_\perp = \mathbf{n}\xi_n + \mathbf{b}\xi_b$ and introduce the notation $f = B\xi_n$ and $g = B\xi_b$ to obtain the relationships

$$\mathbf{R}_* = \mathbf{R}_1 + \mathbf{R}_2,\ \mathbf{R}_1 = \nabla\times[\boldsymbol{\xi}_\mathbf{n}\times\mathbf{B}] = \mathbf{n}\nabla_t f - \mathbf{t}\nabla_n f,$$
$$\mathbf{R}_1^2 = (\nabla_t f)^2 + (\nabla_n f)^2,$$
$$\mathbf{R}_2 = \nabla\times(g\mathbf{n}) = \mathbf{b}\mu - \mathbf{t}\nabla_b g, \quad \mu = g\nabla\cdot\mathbf{t} + \nabla_t g, \tag{21}$$
$$\mathbf{R}_2^2 = \mu^2(\nabla_b g)^2, \quad (\mathbf{R}_1\cdot\mathbf{R}_2) = (\nabla_n f)(\nabla_b g).$$

Here, for brevity, the three components of the nabla operator are conveniently denoted as $\nabla_{t,n,b}$. As a result, the first term of Lagrangian (20) becomes

$$\frac{1}{4\pi}R_*^2 = \frac{1}{4\pi}[(\nabla_f f)^2 + \nu^2 + \mu^2],$$
$$\nu = \nabla_n f + \nabla_b g, \quad \mu = g\nabla\cdot\mathbf{t} + \nabla_t g. \tag{22}$$

Having found the vector

$$\mathbf{W} = \mathbf{n}\nabla_t f + \mathbf{b}\mu - \mathbf{t}\left[2\nu - \frac{f}{B}(\nabla\times\mathbf{B} + 2\nabla_n B)\right], \tag{23}$$

we can determine the second term of the Lagrangian,

$$\frac{1}{c}(\mathbf{j}\cdot[\boldsymbol{\xi}_\perp\times\mathbf{W}]) = \frac{1}{4\pi}(2\nu\psi - \psi^2\Phi), \tag{24}$$

where we have introduced the notation $\psi = (f/B)|\nabla\times\mathbf{B}|$ and $\Phi = 1 + 2(\nabla_n B)/|\nabla\times\mathbf{B}|$.

Using the formulas obtained, we can write the stability condition in a convenient form:

$$4\pi\mathcal{L}_* = (\nabla_t f)^2 + L^2 + M^2 + N > 0, \tag{25}$$

where $L = \nu + \psi = \nabla_n f + \nabla_b g + (f/B)|\nabla\times\mathbf{B}|$, $M = g\nabla\cdot\mathbf{t} + \nabla_t g$, and $N = -\psi^2(1+\Phi) < 0$.

It is also expedient to utilize the relationship

$$\nabla\cdot\mathbf{n} = -\frac{1}{B}(|\nabla\times\mathbf{B}| + \nabla_n B),$$

with which we can rewrite the only negative (last) term in formula (24) as

$$N = -\psi^2(1+\Phi) = 2f^2\frac{|\nabla\times\mathbf{B}|}{B}\nabla\cdot\mathbf{n} < 0. \tag{26}$$

From this relationship, we see that the instability results solely from the negative divergence of the normal, $\nabla\cdot\mathbf{n} < 0$, i.e., from the convexity of the inner magnetic field lines.

Taking into account the fact that an ordinary equilibrium Z-pinch is uniform along the z axis, we can choose the perturbation component in the direction of the binormal in the form $g = g_1\sin kz + g_2\cos kz$, in which case, in the limit of the minimization procedure, $g_{1,2} \longrightarrow 0$, we obtain $M \longrightarrow 0$. As for the quantity L, it contains the derivative $\nabla_b g = \partial g/\partial z = kg_1\cos kz - kg_2\sin kz$; consequently, in the limit $k \longrightarrow \infty$, the factors $kg_{1,2}$ can be assumed to be finite and can be chosen so that $L = 0$.

Then, the stability condition can be rewritten in terms of the effective integral

$$4\pi\mathcal{L}_{\text{eff}} = (\nabla_t f)^2 - \left(\frac{f}{B}\right)^2(\nabla\times\mathbf{B})^2(1+\Phi). \tag{27}$$

Recall that, in order to put expression (24) in a simpler form, we have introduced the notation $f = B\xi_n$ and $b = B\xi_b$, but now it is more convenient to return to the function ξ_n. Introducing the notation $\alpha = \xi_n$, we rewrite formula (27) as

$$4\pi\mathcal{L}_{\text{eff}} = (\nabla_t B\alpha)^2 - \alpha^2(\nabla\times\mathbf{B})^2(1+\Phi) > 0. \tag{28}$$

Here, the first term can be appropriately transformed into

$$(\nabla_t B\alpha)^2 = \nabla\cdot(\mathbf{B}\alpha^2\nabla_t B) + (\mathbf{B}\cdot\nabla\alpha)^2 + \alpha^2 G,$$
$$G = (\nabla_t B)^2 - (\mathbf{B}\cdot\nabla)(\nabla_t B), \tag{29}$$

and the second term with the total divergence vanishes after integration over the volume of the cylinder. As a result, we arrive at the final form of stability criterion (27):

$$4\pi\mathcal{L}_{\text{eff}} = (\mathbf{B}\cdot\nabla\alpha)^2 - \alpha^2 R > 0, \tag{30}$$

where

$$R = (\nabla\times\mathbf{B})^2(1+\Phi) - G.$$

FURTHER ANALYSIS OF THE STABILITY OF A BICYLINDER

We begin by illustrating how the stability criterion is applied to an ordinary Z-pinch of radius a, in which the current density is constant ($j_0 = \text{const}$) over the cross section. Within such a pinch, the magnetic field is equal to $B = B_\varphi = B_0 r/a \sim r$, where $B_0 = 2I/ca$ and $I = \pi a^2 j_0$. Accordingly, we have $\Phi = 0$, $G = 0$, and $R = 4(B_0/a)^2 = \text{const}$, so that the stability criterion reduces to

$$4\pi\mathcal{L}_{\text{eff}} = \left[\left(\frac{\partial\alpha}{\partial\varphi}\right)^2 - 4\alpha^2\right]\left(\frac{B_0}{a}\right)^2 > 0. \tag{31}$$

The axial symmetry of the Z-pinch enables us to choose perturbation in the form $\alpha = \alpha_1\sin m\varphi + \alpha^2\cos m\varphi$ and, in fact, set $(\partial\alpha/\partial\varphi)^2 \longrightarrow m^2\alpha^2$; as a result, the stability criterion for an ordinary pinch (in which the current is distributed uniformly over the cross section) becomes $m_2 \geq 4$. We thus arrive at the well-known results: unstable perturbations are snake-like perturbations with $m = 1$ and constrictions with $m = 0$.

This is also true for the Besselian Z-pinch, considered above, specifically, a pinch in which the current density distribution is described by the zeroth Bessel function, $j = j(0)J_0(kr)$, where $j(0) = (I/\pi a^2)\xi$ and $\xi = N_0/2J_1(N_0) = 2.31$. Let us, however, analyze this problem in more detail. Using stability criterion (27), in which $\nabla_t f = r^{-1}\partial f/\partial\varphi$, we can set $(\nabla_t f)^2 \longrightarrow (fm/r)^2$ and rewrite this criterion as the condition

$$4\pi\mathcal{L}_{\text{eff}} = \left(\frac{f}{r}\right)^2[m^2 - M(r)] > 0,$$
$$M(r) = \left(\frac{r\nabla\times\mathbf{B}}{B}\right)^2(1+\Phi). \tag{32}$$

For a Besselian pinch, we obtain $M(r) = 2zJ_0(z)/J_1(z) \approx 4(1 - z^2/8 + \ldots)$, which indicates that, near the pinch axis, snakelike perturbations with $m = 1$ are unstable. According to criterion (32), the bicylinder under consideration should also be unstable against internal snakelike perturbations.

If, however, further experiments will confirm that tubular structures resembling the bicylinder can actually form in a tokamak, the following three theoretical arguments may be proposed to explain them.

The first argument is that the lifetime of bicylinder-type filaments is too short for the internal snakelike perturbations to grow to any significant amplitude. That the lifetime is short is indirectly confirmed by the fact that, although KRK revealed tubular structures by the method of contrasting photographs on a computer, they look like fairly thin (rather than smoothed) filaments (Fig. 2).

The second argument can be summarized as follows. Recall that the "intermediate" Lagrangian (24) has to be minimized under the following four conditions: (i) the perturbation components in the direction of the binormal should be small ($g_{1,2} \longrightarrow 0$); (ii) the wavelengths of these perturbation components should be short ($k = 2\pi/\lambda \longrightarrow \infty$); (iii) the products ($kg_{1,2}$) should be finite; and (iv) the term L, which has the form $L = \nu + \psi = \nabla_n f + \nabla_b g + (f/B)|\nabla \times \mathbf{B}|$, must vanish. However, it is possible that internal snakelike perturbations with arbitrarily short wavelength, $\lambda \longrightarrow 0$ (which are even difficult to imagine vividly), simply do not break the global structure of bicylinders, which are stable against constrictions because the external integral $J = \int dl/B$ decreases with distance from the cylinder surface.

The last (third) argument may be associated with the finite length l_z of a bicylinder that has the form of a paper clip (Fig. 3) and rapidly "germinates" in a direction perpendicular to the magnetic field B_0. If perturbations $g \sim \sin(2\pi z/\lambda)$ with "quantified" wavelengths $\lambda = l_z/n$ (where n is an integer) appear at a certain time, then the wavelength $\lambda = 2\pi/k$ should also rapidly increase with l_z, as if stretching the perturbation "spring." Under these quasi-steady conditions, it is incorrect to automatically drive the term L^2 in formula (25) to zero by appropriately choosing the values of the finite factors $kg_{1,2}$ in the limit $k \longrightarrow \infty$ and $g_{1,2} \longrightarrow 0$. Presumably, it is this circumstance that is favorable for the stability of the bicylinder against internal snakelike perturbations.

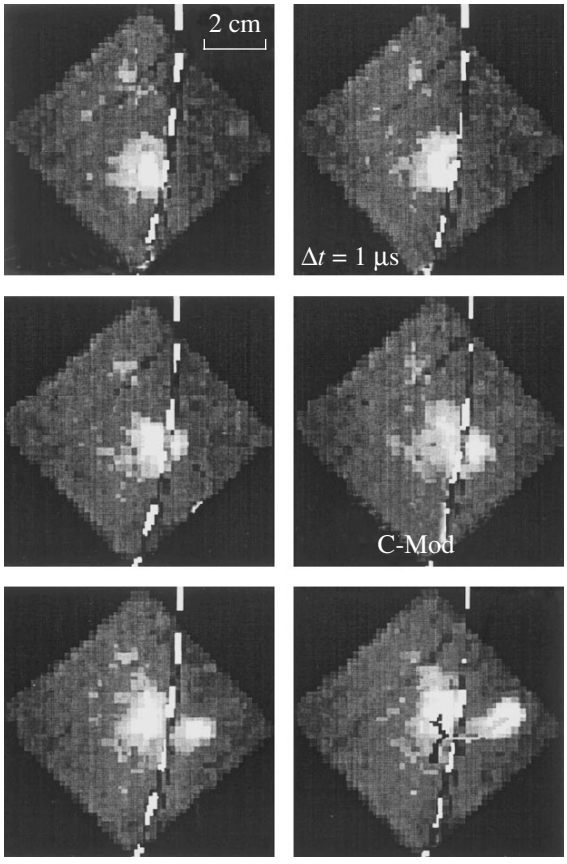

Fig. 4. Six successive film frames of a blob in the Alcator C-Mod tokamak.

NOTE ADDED IN PROOF

After this paper had already been accepted for publication in the *Journal of Technical Physics*, we became aware of the new experimental data on plasma transport in tokamaks that were presented at the 19th IAEA Fusion Energy Conference (Lyon, October 2002). In some tokamak experiments, it was found that the filaments stretched along the main magnetic field—they are commonly referred to as "blobs"—sporadically appeared in the edge plasma. So we decided to supplement this paper, because such filaments seem to be closely connected with the problem under discussion here.

Figure 4, taken from [4], presents six successive film frames of the cross section of an individual blob that emerges into the edge of the plasma column in the Alcator C-Mod tokamak (the frames were taken with an exposure time of 4 μs). We can see that, as the blob crosses the separatrix magnetic surface, it breaks into two parts, one of which remains inside the separatrix and the other passes through the separatrix and continues to move toward the wall. The mechanism for the formation of blobs is still unknown. Krasheninnikov [5] supposed that an individual blob is an overheated magnetic tube that becomes polarized in a nonuniform peripheral tokamak magnetic field by the difference between the gradient drifts of electrons and ions and then continues to move with the velocity $V = cE/B$ toward the wall in the same manner as it does during conventional flute instability.

However, the blob in Fig. 4 is seen to be an isolated structure in the form of a hoop or a strip with a width of about 1 cm; hence, it is more likely to be a self-contracting current filament. The blobs originate in the edge plasma, in which neutral impurities play an important role. In some papers, it was pointed out that the temperature at the center of the blob is close to 10 eV, which seems to be more than mere coincidence. The fact that the blob divides into two parts in crossing the separatrix likely provides evidence for its double structure, which may to some extent resemble the bicylinder under discussion, provided that a uniform toroidal magnetic field, which is parallel to the currents flowing in the bicylinder, is incorporated in the above formulas.

Here, we can propose the following nonlinear mechanism, in which the blobs are formed as current filaments during a sort of thermal–radiative instability that will be described below.

In tokamaks, the blobs originate in the scrape-off layer plasma, which is contaminated with impurities arriving from the wall. As the blobs diffuse inward, they enter the region where the temperature is about 10 eV. In this region, the blobs are ionized. Thereafter, the inward diffusion of the blobs is hindered by the twisting of the magnetic field lines. The inductive voltage around the circumference of the torus and the longitudinal electric field $E_\parallel$ can be assumed to be constant during the discharge. In this case, the specific Joule heating power $W_J = E_\parallel^2 \eta$, where $\eta = n_e e^2/m_e \nu_{ea}$ is the electrical conductivity, should be balanced by the radiative loss power $W_{\text{rad}} = n_e n_i Q$, resulting mainly from dielectronic recombination. The dependence of the factor Q on the electron temperature T_e for typical impurities (such as C, O, Fe, Mo, and W) can be found, e.g., in [6]. From Fig. 19 presented in that paper, we can see that, in the temperature range of interest to us ($5 \le T_e \le 20$ eV), this factor is nearly constant and is approximately equal to $Q \approx 10^{-18}$ erg cm^3/s.

We take into account the quasineutrality of the plasma ($n_i = n_e$) and assume that the electric conductivity is governed by collisions of electrons with neutrals, so that we have $\nu_{ea} = n_a \sigma_{ea} \sqrt{T_e/m_e}$. From the equality $W_J = W_{\text{rad}}$, we deduce the relationship $n_e \sqrt{T_e} = A = e^2 E_\parallel^2 / Q n_a \sigma_{ea} \sqrt{m_e}$ = const and then obtain the dependence of the electron pressure $p = 2 n_e T_e$ on the electron density in the form of a descending hyperbola, $p = 2A^2/n_e$.

An unstable gas obeying the adiabatic equation of state $p \sim \rho^\alpha$ with the adiabatic index $\alpha = -1$ is customarily called Chaplygin gas. A detailed theory of the associated quasi-Chaplygin media is given in monographs [7]. In such media, small perturbations should grow at the rate $\gamma = k c_0 = 2\pi c_0/\lambda$, where $c_0 = \sqrt{2T_e/m_i}$ is the ion thermal velocity (in our case, it is approximately equal to 10 km/s); hence, bloblike structures with dimensions of about 1 cm should develop on microsecond time scales, as is actually observed in experiments.

However, in quasi-Chaplygin media, there are no propagating waves that causally connect neighboring regions. The waves more typical of these media are separate standing fluctuations that are spontaneously generated and grow until they collapse. Moreover, a typical perturbation is a paired disturbance in the form of a well and a hump in the density. In our model, the current density is equal to $j = \eta E_\parallel = (n_e/n_{e0})^2 j_0$ (where n_0 and j_0 are unperturbed electron and current densities). Consequently, against the background of a nearly uniform current density j_0, such perturbation structure is somewhat similar to the double structure of the experimentally observed blobs. This interpretation of blobs will be analyzed in more detail in a separate paper.

ACKNOWLEDGMENTS

We are grateful to V.A. Vershkov and V.S. Lisitsa for useful remarks. This work was supported in part by the Council on the Grants of the President of the Russian Federation and by the federal program "Government Support of Leading Scientific Schools," project no. 00-15-96526.

REFERENCES

1. B. A. Trubnikov, *Plasma Physics and the Problem of Controlled Nuclear Fusion* (Akad. Nauk SSSR, Moscow, 1958), Vol. 1, p. 289.
2. A. B. Kukushkin and V. A. Rantsev-Kartinov, Vopr. At. Nauki Tekh., Ser. Termoyad. Sint., No. 2, 69 (2000).
3. B. A. Trubnikov, *Plasma Theory* (Énergoatomizdat, Moscow, 1996), p. 216.
4. E. S. Marmar, in *Proceedings of the 19th IAEA Fusion Energy Conference, Lyon, 2002*, Report OV/4-1.
5. S. I. Krasheninnikov, Phys. Lett. A **283**, 368 (2001).
6. V. I. Gervids, A. G. Zhidkov, V. S. Marchenko, and S. I. Yakovlenko, in *Reviews of Plasma Physics*, Ed. by B. B. Kadomtsev (Énergoizdat, Moscow, 1982; Consultants Bureau, New York, 1987), Vol. 12.
7. S. K. Zhdanov and B. A. Trubnikov, *Quasi-Gaseous Unstable Media* (Nauka, Moscow, 1991); B. A. Trubnikov, S. K. Zhdanov, and S. M. Zverev, *Hydrodynamics of Unstable Media* (CRC, Boca Raton, 1996).

Translated by O. Khadin

Technical Physics, Vol. 48, No. 7, 2003, pp. 866–872. Translated from Zhurnal Tekhnicheskoĭ Fiziki, Vol. 73, No. 7, 2003, pp. 67–74.

SOLIDS

Domain Structure of (011) Crystalline Garnet Ferrite Plates

R. M. Vakhitov and E. G. Shanina

Bashkortostan Sate University, ul. Frunze 32, Ufa, 450074 Bashkortostan, Russia

e-mail: VakhitovRM@bsu.bashedu.ru

Received November 29, 2002

Abstract—The domain structure in (011) crystalline garnet ferrite plates is studied with allowance for induced uniaxial anisotropy and two-constant cubic anisotropy. It is shown that the inclusion of the second constant of cubic anisotropy greatly affects the orientational phase diagram and also the topology of magnetic inhomogeneities in a given magnet. It is found, in particular, that 180° non-Bloch domain walls may appear in a certain range of combined anisotropy constants, causing a continuous change in the wall orientation. © *2003 MAIK "Nauka/Interperiodica".*

Domain nucleation in a magnet is known to influence significantly its static and dynamic properties. The domain structure depends on many factors, including higher order anisotropic interactions [1, 2]. In this respect, of interest is the domain structure of single-crystal garner ferrites, which usually combine two types of anisotropy with different symmetries: induced uniaxial anisotropy (IUA) and natural cubic anisotropy (CA). These materials offer a number of unique properties and are widely used in applied magnetoelectronics [3].

In this work, we study the structure and properties of magnetic inhomogeneities that may arise in garnet ferrite plates with a developed (011) surface. These magnets exhibit orthorhombic magnetic anisotropy, which significantly improves their dynamic characteristics and generates increased interest in these materials [3, 4]. Earlier [5], the properties of the (011) plates were studied in terms of the phenomenological model that takes into consideration IUA and CA in the single-constant approximation. Later, however, it has been shown [6, 7] that, as the temperature decreases down to helium values, the contribution of the CA second constant K_2 may become comparable to (or even exceed) that of the first constant K_1. This has an effect on the ground state [7, 8] and on the magnetoelastic wave spectrum of the crystal [9]. It should be noted that the inclusion of K_2 in the expansion of the CA energy means a more careful consideration of the CA symmetry and also (in terms of magnetic states) taking into account the effect of ⟨011⟩ axes on the orientational phase diagram of the magnet [6].

In view of the aforesaid, the energy of magnetic inhomogeneities in a sufficiently thick plate can be represented as [5]

$$E = \int_{-\infty}^{\infty} \{A[(d\Theta/dy)^2 + \sin^2\Theta(d\varphi/dy)^2] + [K_u + K_o\sin^2(\varphi-\psi)]\sin^2\Theta + \frac{1}{4}K_1[\sin^4\Theta\sin^2(\varphi-\psi)(\sin^2(\varphi-\psi) + 4\cos^2(\varphi-\psi)) + 2\sin^2\Theta\cos^2\Theta(2\cos^2(\varphi-\psi) - \sin^2(\varphi-\psi)) + \cos^4\Theta] + \frac{1}{4}K_2\sin^2\Theta\cos^2(\varphi-\psi) \times [\cos^4\Theta - 2\sin^2\Theta\cos^2\Theta\sin^2(\varphi-\psi) + \sin^4\Theta\sin^4(\varphi-\psi)] + 2\pi M_s^2(\sin\Theta\sin\varphi - \sin\Theta_\infty\sin\varphi_\infty)^2\}dy. \quad (1)$$

Here, A is the exchange parameter; K_u and K_o are the constants of the uniaxial and orthorhombic anisotropy components, respectively; M_s is the saturation magnetization; Θ and φ are the polar and azimuth angles of the magnetization $\mathbf{M}$; and Θ_∞ and φ_∞ are the same angles in the domains. The coordinate system is selected in such a way that $Oz \parallel [011]$, Oy runs normally to the domain wall (DW) plane, and Ox lies in the DW plane and makes an angle ψ with the [100] axis.

Possible magnetic inhomogeneities are found from the minimum condition for energy (1), i.e., by solving the Euler–Lagrange equations [1, 2, 5]

$$\frac{\delta E}{\delta\Theta} = 0, \quad \frac{\delta E}{\delta\varphi} = 0, \quad \frac{\delta E}{\delta\psi} = 0 \quad (2)$$

subject to the condition

$$\delta^2 E > 0. \quad (3)$$

However, comprehensible analysis of Eqs. (2) in view of condition (3) cannot be performed without knowing the OPD for a magnet under study.

1063-7842/03/4807-0866$24.00 © 2003 MAIK "Nauka/Interperiodica"

HOMOGENEOUS MAGNETIC STATES

For a uniformly magnetized plate, the equilibrium directions of the magnetization **M** in the domains can be found from minimum conditions (2) and (3) by putting $\psi = 0$, $\Theta = \Theta_\infty$, $\varphi = \varphi_\infty$, $d\Theta/dy = 0$, and $d\varphi/dy = 0$ in (1). Calculations show [8] that nine magnetic phases may coexist in the (011) plates, three of which are symmetrical and the other six, disymmetrical [9]. These phases are related to the following solutions.

(1) $\Theta = 0$ or π, $\mathbf{M} \parallel [011]$. The area of stability of this phase ($\Phi_{[100]}$), which is found from condition (3), is given by relationships

$$K_2 > -2(2K_u + K_1), \quad K_1 < K_u + K_o;$$

(2) $\Theta = \pi/2$, $\varphi = 0, \pi$, $\mathbf{M} \parallel [100]$,

$$K_2 > -K_o, \quad K_1 > K_u (\Phi_{[100]});$$

(3) $\Theta = \pi/2$, $\varphi = \pi/2, 3\pi/2$, $\mathbf{M} \parallel [01\bar{1}]$,

$$K_1 < -(K_o + K_u), \quad K_1 > 2K_o - K_2/2 (\Phi_{[01\bar{1}]});$$

(4) $\sin\Theta = \pm\sqrt{[K_1 - (K_u + K_o]/2K_1}$, $\varphi = \pi/2$, or $3\pi/2$, $\mathbf{M} \parallel [0uv]$, $K_1 \geq -(K_0 + K_u)$, $K_1 \geq K_o + K_u$,

$$4K_1^3 + 2K_1^2(K_o - K_u) + K_2(K_o + K_u)^2 > 0.$$

This phase ($\Phi_<^{\mathrm{I}}$) is of the angular type [8]. In angular phases, the magnetization vector **M** changes direction according to the IUA and CA constants but remains within a certain plane of symmetry of the cube. In the phase $\Phi_<^{\mathrm{II}}$, the magnetization lies in the (100) plane;

(5) $\Theta = \pi/2$, $\sin^2\varphi = \{K_2 - 3K_1 \pm [(K_2 - 3K_1)^2 + 12K_2(K_1 + K_o)]^{1/2}\}/3K_2$, $\mathbf{M} \parallel [uv\bar{v}]$.

Here, opposite signs in the expression for φ correspond to two angular phases: $(\Phi_<^{\mathrm{II}})_1$ and $(\Phi_<^{\mathrm{II}})_2$, which belong to the same symmetry group. In both cases, the vector **M** lies in the (011) plane;

(6) $\sin^2\Theta = \{2K_2 + 3K_1 \pm [(2K_2 + 3K_1)^2 - 3K_2(4K_u + 2K_1 + K_2)]^{1/2}\}/3K_2$, $\varphi = 0, \pi$, $\mathbf{M} \parallel [uv\bar{v}]$.

Here again, two solutions correspond to two angular phases: $(\Phi_<^{\mathrm{III}})_1$ and $(\Phi_<^{\mathrm{III}})_2$. In both cases, the vector **M** lies in the $(01\bar{1})$ plane. Otherwise, this situation is similar to the previous one;

(7) $\mathbf{M} \parallel [uvw]$. This phase ($\Phi_<^{\mathrm{IV}}$), which is sometimes called the phase of the general type [5], is also one of noncollinear phases. However, unlike the angular phases considered previously, the associated vector **M** changes direction according to the constants of combined anisotropy, remaining in none of the symmetry planes of the cube. The phase of the general type refers to the lowest symmetry group: whereas the symmetry groups of the angular phases contain some nontrivial symmetry elements (e.g., a plane of reflection), the symmetry group of the general phase lacks them.

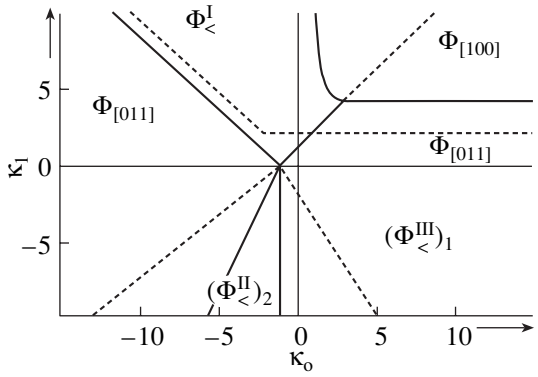

Fig. 1. OPD of the (011) plate for $K_u > 0$ and $\kappa_2 = -4$. Continuous curves, SRPT lines; dashed lines, phase stability boundaries.

Based on the results obtained, including those of the numerical analysis of expressions (2) and (3), one can construct the OPD of the (011) plane (Fig. 1), which provides the most complete picture of the areas of stability for the magnetic phases and of spin-reorientation transitions between them [8]. Without going into the details of the phase diagram, we will only separate out features associated with the effect of the constant K_2. First, this constant is responsible for the occurrence of the angular phases $(\Phi_<^{\mathrm{II}})_2$ and $(\Phi_<^{\mathrm{III}})_2$, as well as the general phase ($\Phi_<^{\mathrm{IV}}$). The last-named phase becomes stable at $K_2 \neq 0$ in the area $\kappa_1 < 0$, $\kappa_2 > 1.7$, $\kappa_o < 0$, $K_u < 0$, where $\kappa_1 = K_1/|K_u|$, $\kappa_2 = K_2/|K_u|$, and $\kappa_o = K_o/|K_u|$. Second, at $K_u > 0$, there appears a quintuple point ($\kappa_o = -1$, $\kappa_1 = 0$, and $\kappa_2 = -4$) which is shared by the areas of stability for five phases (Fig. 1). This is consistent with the Gibbs phase rule, which states that the equilibrium orientation of the vector **M** depends on the action of external and internal fields, including additional internal fields due to orthorhombic and cubic anisotropies. Third, the inclusion of K_2 also changes the areas of stability of the magnetic phases, specifically, $\Phi_{[011]}$. It exists in the area $\kappa_2 > -12$, becoming metastable at $\kappa_2 > 12$. The interval of stability $-12 < \kappa_2 < 12$ for the phase $\Phi_{[011]}$ is split into several parts where the OPD of the (011) plate differs significantly. It makes sense to analyze each of them together with magnetic inhomogeneities that may arise in the magnet studied.

STRUCTURE AND PROPERTIES OF MAGNETIC INHOMOGENEITIES

The magnetization distribution over the crystal is defined by Eqs. (2) in view of (1) and (3). They admit

the existence of the first integral in explicit form. For Bloch DWs ($\varphi = 0$ or π), the expression for this integral is

$$\left(\frac{d\Theta}{d\xi}\right)^2 - r(\sin^2\Theta + p\sin^4\Theta + q\sin^6\Theta) = C, \quad (4)$$

where C is a constant of integration; $\xi = y/\Delta_0$; $\Delta_0 = \sqrt{A/K_u}$; and r, p, and q are parameters given by

$$r = [4(1 + \kappa_p\sin^2\psi) + 2\kappa_1(1 - 3\sin^2\psi) + \kappa_2\cos^2\psi]/4,$$
$$p = [\kappa_1(3 - 10\sin^2\psi + 3\sin^4\psi) + 2\kappa_2(1 - \sin^4\psi)]/4r, \quad (5)$$

$$q = -\kappa_2\cos^2\psi(1 + \sin^2\psi)/4r. \quad (6)$$

Here, the angle ψ specifies the DW orientation relative to crystallographic axes and is found from the last equation of system (2). From a variety of solutions to this equation, three are of interest in the general case: $\psi = 0$, $\psi = \pi/2$, and $\psi = \psi(\kappa_1, \kappa_2, \kappa_o, Q, \varphi)$ (where $Q = K_u/2\pi M_s^2$). These will be analyzed below. Consider the values of K_u, K_o, K_1, and K_2 for which the phase $\Phi_{[011]}$ is stable in the OPD. With $K_u > 0$ and $\kappa_2 > -12$, the associated area consists of several subareas (Fig. 2) where the phase portrait of Eq. (4) is substantially different.

(1) $-4 < \kappa_2 < 3$. From the phase portrait of Eq. (4) for subarea *1* (which is defined by $-2 - \kappa_2/2 < \kappa_1 < 1$, $-1 - \kappa_o < \kappa_1 < 1 + \kappa_o$, and $\kappa_1 < 2\kappa_o - \kappa_2/2$), it follows that separatrices ($C = 0$) passing through singular points $\Theta = \pi n$ ($n \in Z$) of the saddle type correspond to solutions

$$\cot\Theta = \pm\sqrt{1 - p}\sinh(\sqrt{r}\xi). \quad (7)$$

These solutions, in turn, correspond to 180° DWs that separate two domains with $\mathbf{M} \parallel [011]$ and $\mathbf{M} \parallel [0\bar{1}\bar{1}]$. The structure, energy, and width

$$\Delta = \pi\Delta_0/\sqrt{r(1 - p)} \quad (8)$$

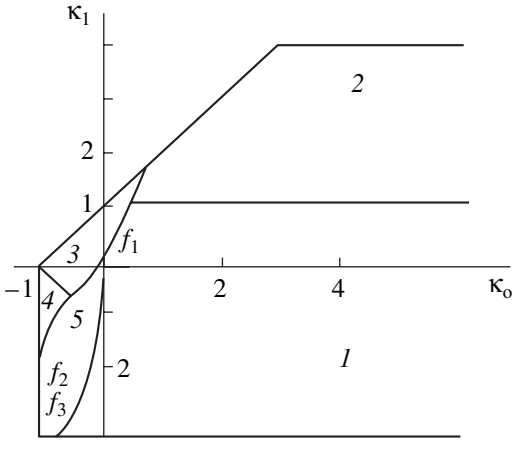

Fig. 2. Phase diagram for DWs of different topology that may occur in the area of existence of the phase $\Phi_{[011]}$ for $-4 < \kappa_2 < 3$.

of such a DW depend on the constants of combined anisotropy and on the DW orientation ψ. The latter parameter is found from condition (3), which, in this case, reduces to the inequality [5, 11]

$$(2K_o - 3K_1 - K_2/2)\cos^2(\varphi - \psi)\int_{-\infty}^{\infty}\sin^2\Theta dy$$
$$+ \{5K_1\cos 2(\varphi - \psi) + (3K_1 - 2K_2)\sin^2(\varphi - \psi)$$
$$\times [\sin^2(\varphi - \psi) - 3\cos^2(\varphi - \psi)]\}\int_{-\infty}^{\infty}\sin^4\Theta dy \quad (9)$$
$$+ \frac{1}{2}K_2[\cos 4(\varphi - \psi) - 3\cos 2(\varphi - \psi)\sin^4(\varphi - \psi)$$
$$- 3\sin^2 2(\varphi - \psi)\sin^2(\varphi - \psi)]\int_{-\infty}^{\infty}\sin^6\Theta dy > 0.$$

Analyzing (9), one can check that a DW with $\psi = 0$ or $\pi/2$ has several areas of stability, which intersect at $\kappa_1 > 0$. This means that, in the region of intersection, the DW may change orientation relative to crystallographic axes, exhibiting hysteresis. The line of change of orientation is found from the energy condition

$$E(\psi = 0) = E(\psi = \pi/2) \quad (10)$$

and has the form $\kappa_1 = f_1(\kappa_o, \kappa_2)$ (Fig. 2). With $\kappa_1 > f_1(\kappa_o, \kappa_2)$ and $\kappa_o < 0$ (a part of subarea *3*), a 180° DW with $\psi = \pi/2$ is stable; with $\kappa_1 < f_1(\kappa_o, \kappa_2)$ and $\kappa_o > 0$, a 180° DW with $\psi = 0$ is stabilized.

At $\kappa_1 < 0$, the situation changes: the areas of stability do not intersect. Moreover, the conditions $\kappa_1 > f_2(\kappa_o, \kappa_2)$ (subarea *4*) and $\kappa_1 < f_3(\kappa_o, \kappa_2)$ (the latter condition also covers the part of subarea *1* lying below the line $\kappa_1 = 0$) are the stability conditions for the DWs with $\psi = \pi/2$ and 0, respectively. In subarea *5*, which is bounded by the curves $\kappa_1 = f_2(\kappa_o, \kappa_2)$, $\kappa_1 = f_3(\kappa_o, \kappa_2)$, $\kappa_1 = -2 - \kappa_2/2$, and $\kappa_o = -1$, both DWs are unstable. In this case, non-Bloch 180° DWs with a noncircular trajectory of the magnetization vector **M** will apparently appear [12], which deserve separate consideration. The curves $\kappa_1 = f_2(\kappa_o, \kappa_2)$ and $\kappa_1 = f_3(\kappa_o, \kappa_2)$ are found from (9) by replacing the nonequality sign by the equality sign for related orientations.

In the area $\kappa_1 > 1$ (subarea *2*), the phase portrait of Eq. (4) changes qualitatively: the shape of the separatrices passing through the singular points $\Theta = \pi/n$ ($n \in Z$) becomes much more complicated. Here, 180° DWs with waists arise (Fig. 3, curve *1*). For such walls, the magnetization distribution exhibits three inflection points. A waist serves as a new-phase nucleus [5, 11, 13] and appears when a metastable axis (the [100] axis in our case) lies in the plane of spin rotation. In addition, the phase portrait shows closed phase trajectories

with self-intersection ($C = \sqrt{(p+q-1)}$), which are associated with solitary magnetic inhomogeneities like 0° DWs or stationary solitons [5, 11]. They, unlike 180° DWs, separate two domains with magnetization vectors of like orientation ($\mathbf{M} \parallel [100]$) and obey the magnetization law (Fig. 3, curve *2*)

$$\tan\Theta = \pm\sqrt{(1-p)/(2p-1)}\cosh[\xi\sqrt{r(2p-1)}]. \quad (11)$$

These features also serve as phase nuclei, which condense on crystal defects, and are central to spin-flip processes in magnets [14]. They have the same orientations as 180° DWs, $\psi = 0$ and $\pi/2$, and their stability is defined by inequality (9). In this case, the line of orientation change is an extension of the line $\kappa_1 = f_1(\kappa_o, \kappa_2)$. Along with this range of κ_1, soliton-like solutions like (11) appear in the interval $-1 - \kappa_o < \kappa_1 < 2\kappa_o - \kappa_o/2$. These solutions have the same properties as the 0° DWs mentioned above, except that the associated domain states are characterized by $\mathbf{M} \parallel [01\bar{1}]$. In this interval of κ_1, the 180° DWs exhibit waists, since the metastable $[01\bar{1}]$ axis lies in the DW plane.

(2) $-6 < \kappa_1 < -4$. In this case, the subrange $-1 - \kappa_o < \kappa_1 < 2\kappa_o - \kappa_o/2$, where the phase $\Phi_{[011]}$ coexists with the phase $\Phi_{[01\bar{1}]}$ (Fig. 2), is absent. Therefore, in the intervals $-2 - \kappa_2/2 < \kappa_2 < 1$ and $\kappa_1 < 1 + \kappa_o$, usual waist-free 180° DWs form. For $\kappa_1 > 1$, the phase $\Phi_{[011]}$ coexists with the phase $\Phi_{[100]}$; as a result, waists appear in the structure of 180° DWs and solitary magnetic inhomogeneities like stationary solitons arise, which were described above.

(3) $-12 < \kappa_2 < -6$. In this range of κ_2, we are dealing with the only situation, namely, with the coexistence of the phases $\Phi_{[011]}$ and $\Phi_{[100]}$, the latter being metastable. Accordingly, the remaining solutions are those corresponding to 180° DWs with one waist and $\psi = 0$ and to 0° DWs of the same orientation.

(4) $3 < \kappa_2 < 12$. The situation here is similar to case (1), except that the metastable angular phase $(\Phi_<^{\mathrm{III}})_2$ arises in the range $(-\kappa_2 + \sqrt{12\kappa_2})/2 < \kappa_1 < 1$ in addition to already existing ones. Because of this, the structure of the 180° DWs exhibits two waists due to two $[uvv]$ metastable axes with $\Theta = \Theta_m$ and $\Theta = \pi - \Theta_m$ (Fig. 4). Accordingly, two extra singular points of saddle type with $\Theta = \Theta_m$ and $\Theta = \pi - \Theta_m$ appear in the phase portrait of Eq. (4), giving rise to phase trajectories in the form of a twisted dumbbell that pass through these points. The parts of the dumbbell that have the form of self-intersecting loops are associated with stationary solitons for which the ground states are $\Theta = \Theta_m$ or $\Theta = \pi - \Theta_m$ (Fig. 4). The phase trajectories connecting the points with $\Theta = \Theta_m$ and $\Theta = \pi - \Theta_m$ correspond to magnetic inhomogeneities like $(180 - 2\Theta_m)°$ DWs with $\mathbf{M} \parallel [uvv]$ in the domains.

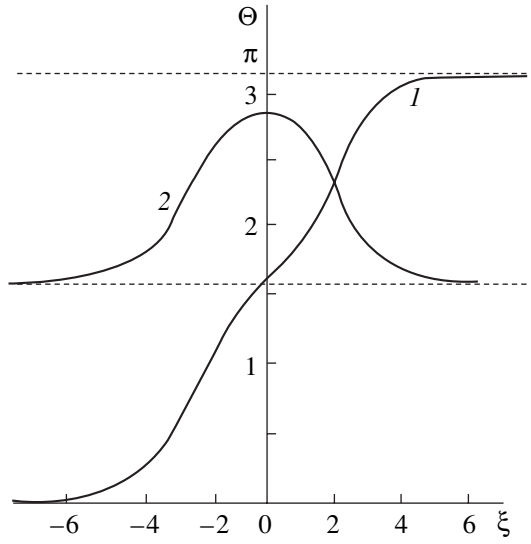

Fig. 3. Magnetization distributions that describe (*1*) 180° DWs with a waist and (*2*) 0° DWs in subarea *2* in Fig. 2.

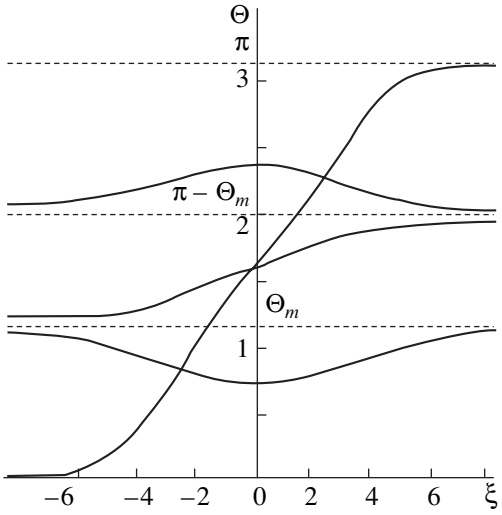

Fig. 4. Magnetic inhomogeneities of different topology that are possible in the area bounded by $(-\kappa_2 + \sqrt{12\kappa_2})/2 < \kappa_1 < 1$ and $3 < \kappa_2 < 12$.

(5) $\kappa_2 > 12$. In this case, the symmetrical phase $\Phi_{[011]}$ becomes metastable in the interval $-(\kappa_2 + 4)/2 < \kappa_1 < [-2\kappa_2 - 2(\kappa_2^2 + 36\kappa_2)^{1/2}]/9$. That is, the line $\kappa_1 = -(\kappa_2 + 4)/2$, which the line of the spin-reorientation phase transition (SRPT) of the second kind between the phases $\Phi_{[011]}$ and $(\Phi_<^{\mathrm{III}})_1$ for $\kappa_2 < 12$, turns into the line $\kappa_1 = [-2\kappa_2 - 2(\kappa_2^2 + 36\kappa_2)^{1/2}]/9$ at $\kappa_1 \geq 12$. The latter line is now the line of the SRPT of first kind between these phases. Thus, the point $\kappa_2 = 12$ is a tricritical point in the OPD of the (011) plate. In the interval $[-2\kappa_2 - 2(\kappa_2^2 + 36\kappa_2)^{1/2}]/9 < \kappa_1 < [-\kappa_2 - (12\kappa_2)^{1/2}]/3$, the angular phase

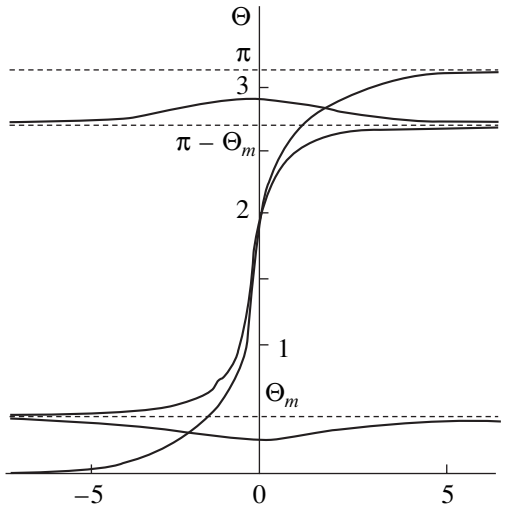

Fig. 5. Magnetic inhomogeneities of different topology that are possible in the area bounded by $[-2\kappa_2 - 2(\kappa_2^2 + 36\kappa_2)^{1/2}]/9 < \kappa_1 < [-\kappa_2 - (12\kappa_2)^{1/2}]/3$ and $\kappa_2 > 12$.

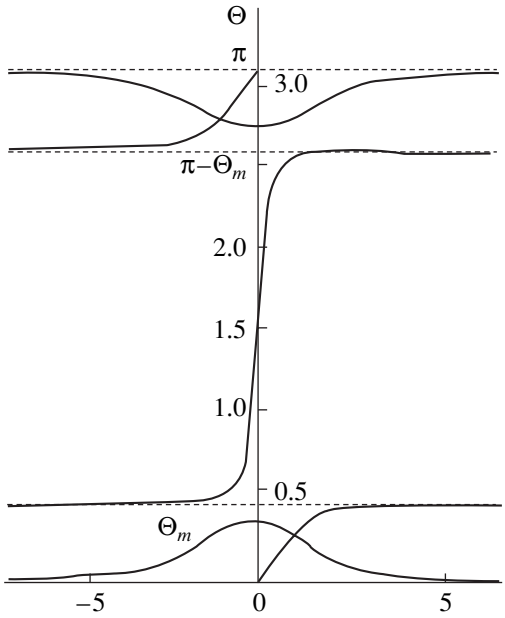

Fig. 6. Possible magnetic inhomogeneities in the area bounded by $-(\kappa_2 + 4)/2 < \kappa_1 < [-2\kappa_2 - 2(\kappa_2^2 + 36\kappa_2)^{1/2}]/9$ and $\kappa_2 > 12$.

$(\Phi_<^{III})_1$ becomes metastable. From the aforesaid it follows that two saddle points with the coordinates $\Theta = \Theta_m$ and $\Theta = \pi - \Theta_m$ appear in the area considered on the phase portrait of Eq. (4) (as in case (4)). These saddles give rise to magnetic inhomogeneities, namely, stationary solitons with their ground states at $\Theta = \Theta_m$ or $\Theta = \pi - \Theta_m$, $(180 - 2\Theta_m)°$ DWs, and 180° DWs with two waists (Fig. 5).

For $-(\kappa_2 + 4)/2 < \kappa_1 < [-2\kappa_1 - 2(\kappa_2^2 + 36\kappa_2)^{1/2}]/9$, the situation changes significantly: phase trajectories in the form of self-intersecting closed loops pass through the points $\Theta = \pi n$ ($n \in Z$). They correspond to 0° DWs with $\mathbf{M} \parallel [011]$ in the domains (Fig. 6). At the same time, one can observe separatrices corresponding to $(180 - 2\Theta_m)°$ DWs, which pass through the points $\Theta = \Theta_m + \pi n$ and $\Theta = \pi(n - 1) - \Theta_m$ ($n \in Z$). However, $(2\Theta_m)°$ DWs also may arise.

It should be noted that the magnetic inhomogeneities considered here in relation to the combined anisotropy parameters are solitary inhomogeneities. However, the analysis of the phase portrait of Eq. (4) indicates that, along with separatrices, there exist other types of phase trajectories. They correspond to the distributions of magnetic inhomogeneities over the whole crystal and, hence, describe various types of periodic domain structure. The consideration of these inhomogeneities goes beyond the scope of this work.

NON-BLOCH 180° DOMAIN WALLS

Let us consider in more detail the range of κ_1, κ_2, and κ_o ($\kappa_1 < 0$) bounded by the curves f_2 and f_3 (subarea *5* in Fig. 2). In this subarea, 180° DWs with $\psi = 0$ and $\pi/2$ are unstable, as was already noted, and 180° DWs with a quasi-Bloch structure may arise [12]. Expression (1) for the DW energy can be recast as [12, 15]

$$E = \sqrt{AK_u} \times \int_{-\infty}^{\infty} \left\{ \left[\left(\frac{d\Theta}{dy} \right)^2 + \sin^2\Theta \left(\frac{d\varphi}{dy} \right)^2 + 2g(\theta, \varphi) \right] \right\} d\xi, \quad (12)$$

where $g(\Theta, \varphi)$ is a function taking into account the densities of the combined anisotropy energy and magnetostatic energy due to the space charge localized at DWs [1].

Set of Eqs. (2), which specifies the structure of magnetic inhomogeneities, will be solved subject to the boundary conditions

$$\Theta|_{\xi \to \pm\infty} = \left\{ \begin{matrix} \pi \\ 0 \end{matrix} \right\}, \quad \frac{d\Theta}{d\xi}, \sin^2\Theta \frac{d\varphi}{d\xi}\Big|_{\xi \to \pm\infty} = 0. \quad (13)$$

Because of the presence of easy magnetic axes in a cubic ferromagnet, the magnetization vector tends to leave the DW plane. Then, its rotation at the domain wall must now be described by two angles $\Theta(\xi)$ and $\varphi(\xi)$. With $|K_1|$, $|K_2|$, and $|K_o| \ll K_u$, the angle $\varphi(\xi)$ can be considered as weakly dependent on the coordinate *y*. In this case, the angles Θ and φ can be represented in the following way:

$$\Theta = \Theta_0(\xi) + \Theta_1(\xi), \quad \varphi = \varphi_0 + \varphi_1(\xi), \quad (14)$$

where Θ_1 and φ_1 are small additions to the zero-order approximation given by Θ_0 and φ_0.

In our case, the zero-order angles are

$$\varphi_0 = 0, \pi, \quad \cot\Theta_0 = \pm\sinh\xi. \tag{15}$$

Linearizing system (13) in the vicinity of Θ_0 and φ_0, we represent the DW energy in the form

$$E = E_0 + E_1, \tag{16}$$

where

$$E_0 = \sqrt{AK_u}[4 + \kappa_2/10 + (2\kappa_o + \kappa_1/3 - 7\kappa_2/30)\sin^2\psi + (2\kappa_2/5 - \kappa_1)\sin^4\psi - (4\kappa_2/15)\sin^6\psi], \tag{17}$$

$$\Delta E_1 = \sqrt{AK_u}\int_{-\infty}^{\infty}\frac{\partial g}{\partial\varphi|_{\Theta=\Theta_0,\,\varphi=\varphi_0}}\varphi_1 d\xi.$$

In the principal approximation in κ_o, κ_1, and κ_2, we obtain from the second equation of (2)

$$(\hat{L}_0 + Q^{-1})u = \frac{\alpha(\psi)}{\cosh\xi} + \frac{\beta(\psi)}{\cosh^3\xi} + \frac{\gamma(\psi)}{\cosh^5\xi}, \tag{18}$$

where

$$\hat{L}_0 = -\frac{d^2}{d\xi^2} + 1 - \frac{2}{\cosh^2\xi}, \quad u = \frac{1}{\cosh\xi}\varphi_1,$$
$$\alpha(\psi) = \sin(2\psi)(4\kappa_o - 6k_1 - \kappa_2)/8,$$
$$\beta(\psi) = \sin(2\psi)(5\kappa_1 - (3\kappa_1 - 2\kappa_2)\sin^2\psi)/4, \tag{19}$$
$$\gamma(\psi) = \sin(2\psi)\kappa_2(1 - 2\sin^2\psi - 3\sin^4\psi)/8.$$

A solution to Eq. (18) is sought in the form of the expansion

$$u = C_u u_0 + \int_0^{\infty} a(k) f(k) dk, \tag{20}$$

where u_0 and $f(k)$ are the eigenfunctions of the operator $\hat{L}_0$ [15, 16]:

$$u_0 = \frac{\sqrt{2}}{2}\frac{1}{\cosh\xi},$$
$$f(k) = \frac{1}{\sqrt{2\pi(1+k^2)}}(\tanh\xi - ik)\exp(ik\xi). \tag{21}$$

After simple calculations, we arrive at

$$C_u = -Q\sqrt{2}\sin(2\psi)[\kappa_o + \kappa_1/2 - 7\kappa_2/60 - (\kappa_1 - 2\kappa_2/5)\sin^2\psi - (2\kappa_2/5)\sin^4\psi]/2, \tag{22}$$

$$\varphi_1 = \frac{\sqrt{2}}{2}C_u - \cosh\xi\left(\frac{1}{3}\beta(\psi)\int_0^{+\infty}\frac{k^2\cos k\xi - k\sin k\xi\tanh k\xi}{(1 + k^2 + Q^{-1})\cosh\frac{\pi k}{2}}dk\right. \tag{23}$$

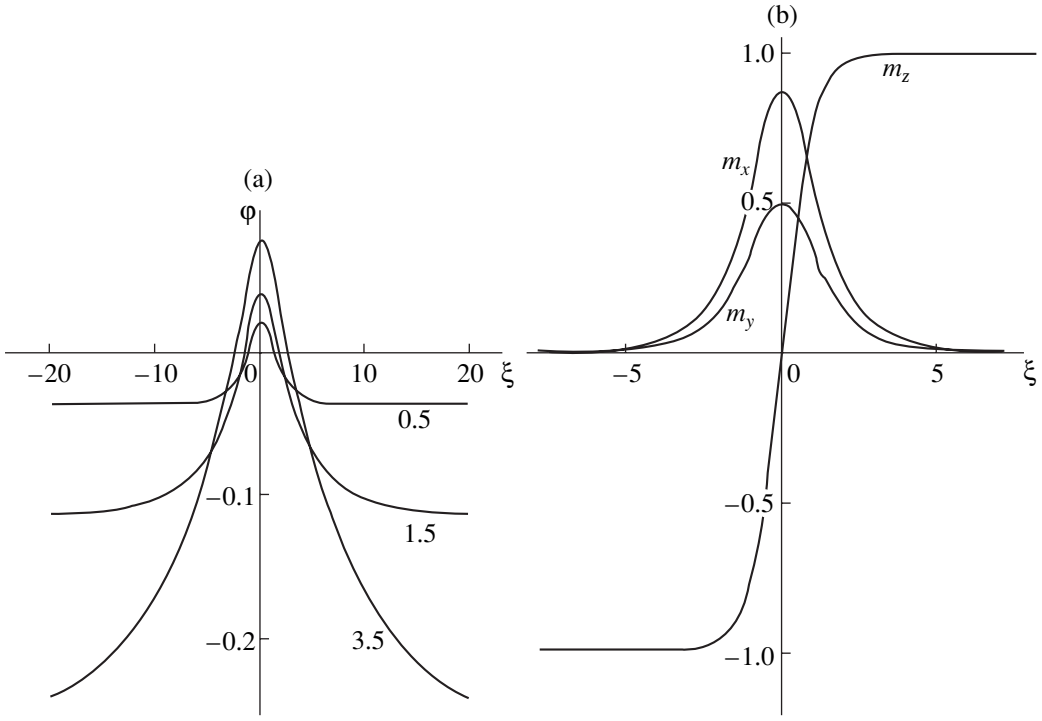

Fig. 7. Magnetization distribution in the transition layer for 180° DWs at $\kappa_o = -0.2$, $\kappa_1 = -0.3$, and $\kappa_2 = -0.3$. (a) Angle φ vs. ξ for different values of Q (the figures by the curves) and (b) magnetization components vs. ξ for $Q = 0.5$.

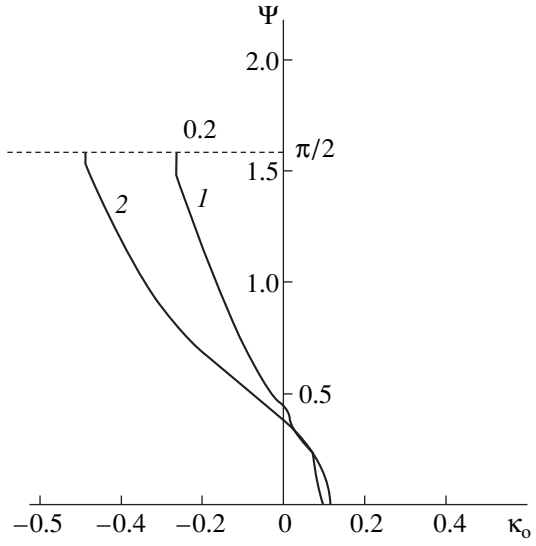

Fig. 8. DW orientation angle ψ vs. κ_o. κ_1 = (*1*) –0.3 and (*2*) –0.5.

$$-\frac{1}{30}\gamma(\psi)\int_0^{+\infty}\frac{(k^2\cos k\xi - k\sin k\xi\tanh k\xi)(k^2+9)}{(1+k^2+Q^{-1})\cosh\dfrac{\pi k}{2}}dk\Bigg).$$

The numerical calculation of the dependence φ = φ(ξ) by formula (23) is shown in Fig. 7. It is seen that the angle at which the magnetization leaves the DW plane varies to the greatest extent near the wall. For $Q \ll 1$, the exit angle of the magnetization vector is given by (in the first order of the perturbation theory)

$$\begin{aligned}\varphi_1 = -\frac{1}{8}Q\sin 2\psi[&4(\kappa_o+\kappa_1)\\ &-2(3\kappa_1-\kappa_2)\sin^2\psi - 3\kappa_2\sin^4\psi\\ &+2(-3\kappa_1-\kappa_2+3\kappa_1\sin^2\psi+3\kappa_2\sin^4\psi)\tanh^2\xi\\ &+\kappa_2(1-2\sin^2\psi-3\sin^4\psi)\tanh^4\xi].\end{aligned} \tag{24}$$

The dependences derived allow one to determine the DW orientation by minimizing (16) in view of (23). In this case, the angle ψ will take different values depending on κ_o, κ_1, and κ_2, including ψ = 0 and π/2 (Fig. 8). Hence, with $\kappa_1 < 0$, a DW continuously changes orientation with the magnetization vector leaving the DW plane as at the phase transition of the second order, while with $\kappa_1 > 0$, the DW changes orientation stepwise as in the case of the phase transition of the first kind. Such a statement is valid when $K_2 = 0$; for K_2 other than zero, the point $\kappa_1 = 0$, at which the DW changes orientation relative to crystallographic axes (this point is akin to the tricritical point in the Landau theory of phase transitions [13]), shifts.

Thus, the study of the effect of the CA second constant on the ground state and domain structure of the (011) crystal plate with combined anisotropy shows that the contribution of ⟨011⟩ axes is essential and complicates the OPD. This, in turn, influences the structure and properties of magnetic inhomogeneities, which may have a nontrivial topology. For example, 0° and 180° DWs with one or two waists may appear. Non-Bloch 180° DWs are also a possibility. In this case, a DW continuously changes orientation. These and other features of the domain structure may also have an effect on other properties of the crystal, specifically, on its behavior upon magnetization and magnetization reversal.

ACKNOWLEDGMENTS

This work was supported by the federal program "Integration" (project no. B00155) and the Ministry of Education of the Russian Federation (grant no. E00-3.4-342).

REFERENCES

1. A. Hubert, *Theorie der Domanenwande in Geordneten Medien* (Springer-Verlag, Berlin, 1974; Mir, Moscow, 1977).
2. V. A. Zaĭkova, I. E. Startseva, and B. N. Filippov, *Domain Structure and Magnetic Properties of Electrical Steels* (Moscow, 1992).
3. V. V. Randoshkin and A. Ya. Chervonenkis, *Applied Magnetooptics* (Moscow, 1990).
4. V. V. Randoshkin, V. I. Kozlov, V. Yu. Mochar, *et al.*, Fiz. Tverd. Tela (St. Petersburg) **41**, 1254 (1999) [Phys. Solid State **41**, 1144 (1999)].
5. R. M. Sabitov, R. M. Vakhitov, and E. G. Shanina, Mikroélektronika **18**, 266 (1989).
6. K. P. Belov, *Rare-Earth Magnets and Their Applications* (Moscow, 1980).
7. A. Mougin, C. Dufour, K. Dumensil, *et al.*, Phys. Rev. B **62**, 9517 (2000).
8. R. M. Vakhitov, Fiz. Met. Metalloved. **89** (6), 16 (2000).
9. R. M. Vakhitov and V. R. Khusainova, Izv. Vyssh. Uchebn. Zaved., Fiz. **44** (6), 90 (2001).
10. Yu. A. Izyumov and V. N. Syromyatnikov, *Phase Transitions and Crystal Symmetry* (Nauka, Moscow, 1984).
11. R. M. Vakhitov, R. M. Sabitov, and R. S. Fakhretdinova, *Dynamics and Statics of Domain Structure in Magnetically Ordered Crystals* (Akad. Nauk SSSR, Ufa, 1988).
12. V. V. Plavskiĭ, M. A. Shamsutdinov, and B. N. Filippov, Fiz. Met. Metalloved. **88** (3), 22 (1999).
13. K. P. Belov, A. K. Zvezdin, A. M. Kadomtseva, *et al.*, *Orientational Transitions in Rare-Earth Magnets* (Moscow, 1979).
14. R. M. Vakhitov and A. R. Yumaguzin, Fiz. Tverd. Tela (St. Petersburg) **43**, 65 (2001) [Phys. Solid State **43**, 65 (2001)].
15. G. S. Kandaurova, L. A. Pamyatnykh, M. A. Shamsutdinov, *et al.*, Fiz. Met. Metalloved. **78** (4), 26 (1994).
16. J. M. Winter, Phys. Rev. **124**, 452 (1961).

Translated by V. Isaakyan

Technical Physics, Vol. 48, No. 7, 2003, pp. 873–879. Translated from Zhurnal Tekhnicheskoĭ Fiziki, Vol. 73, No. 7, 2003, pp. 75–81.

SOLIDS

Thermal Expansion of Polymers Subjected to Low-Amplitude Temperature Cycling

A. I. Slutsker*, V. L. Gilyarov*, Yu. I. Polikarpov, and D. D. Karov****

** Ioffe Physicotechnical Institute, Russian Academy of Sciences, ul. Politekhnicheskaya 26, St. Petersburg, 194021 Russia*

e-mail: Alexander.Slutsker@mail.ioffe.ru

*** St. Petersburg State Technical University, ul. Politekhnicheskaya 29, St. Petersburg, 195251 Russia*

Received December 16, 2002

Abstract—The temperature dependence of the thermal expansion of polymers subjected to small harmonic temperature oscillations about certain base temperatures near the glass transition range is considered. The conformational component of the expansion as a function of temperature is calculated in terms of the conformational transition kinetics. The temperature dependences of the expansion and the expansion vs. oscillation phase shift are analyzed with allowance for the vibrationally anharmonic component. The thermal expansion of polyvinylacetate at base temperatures of 295–320 K, oscillation frequencies of 0.3 and 0.1 Hz, and an oscillation amplitude of 0.8 K are studied experimentally. The measured and calculated data for the expansion and expansion vs. temperature phase shift are shown to be in good agreement. © *2003 MAIK "Nauka/Interperiodica".*

The thermal expansion of solids, i.e., the variation of the object's volume or linear size with temperature, is usually measured under equilibrium conditions.

Along with the obvious methodical requirement that a temperature gradient in the bulk of an object be small (this requirement is satisfied via a trade-off between the thermal diffusivity, sample thickness, and rate of temperature variation), it is necessary that the equilibrium (at a given temperature) parameters of the structure and internal thermal dynamics be established in the object. The approach of a system to the equilibrium state is characterized by the relaxation time. This parameter imposes certain conditions on the measurement of the steady-state thermal expansion (e.g., the temperature should be raised stepwise and kept for a sufficiently long time at each of the steps).

However, a physical investigation where the thermal expansion is measured under *a fortiori* nonequilibrium conditions may give important information on thermal expansion mechanisms and shed light on the features of atomic–molecular dynamics.

The thermal expansion measurement under low-amplitude temperature cycling (the so-called modulation regime [1, 2]) is an example of such investigations. Nonequilibrium conditions here are provided by harmonically varying the temperature relative to a certain base temperature T_b with a frequency ω. The variation (oscillation) amplitude, T_m = 1–3 K, is, as a rule, small compared with the base temperature. By changing T_b and ω, one may gain detailed information on the process. The modulation regime and its applications are described in [3].

The use of the modulation regime makes it possible to study the thermal expansion of solids of various structures.

In low-molecular materials, the vibrational dynamics of atoms (and, accordingly, the vibrationally anharmonic mechanism of thermal expansion) prevails up to the melting point. The relaxation "inertia" of the vibrational dynamics is low; therefore, the dynamic properties are equilibrium over a wide range of temperature oscillation frequencies. For example, in metals, the harmonic oscillations of the thermal expansion have been found to be in phase with the harmonic oscillations of the temperature [4]. In other words, for low-molecular materials, the modulation method does not provide, at moderate temperature oscillation frequencies, any new information compared with "static" measurements of the thermal expansion.

The chain molecular structure of polymers specifies other types of internal dynamics and, hence, other thermal expansion mechanisms [5, 6].

Below the glass transition temperature T_g, the vibrational molecular dynamics dominates and polymers differ little from low-molecular materials in terms of thermal expansion in this temperature range. Above the glass transition temperature, polymers exhibit dynamics of a new type: segmental mobility, or conformational transitions. Conformational transitions are the transitions of chain molecule segments from one (straight *trans*) form to the other (flexed *gauche* (or *gosh*)) form and vice versa. At these transitions, the potential barrier is overcome due to local fluctuations of the thermal energy. Since the potential energy of a *gauche* conformer is usually higher than that of a *trans*

conformer [7], the equilibrium concentration of *gauche* conformers varied with temperature [5–7]. In addition, the effective volume of a *gauche* conformer is larger than that of a *trans* conformer; therefore, an increase in the concentration of *gauche* conformers causes a thermal expansion of a polymer, which adds up to the vibrationally anharmonic expansion.

The thermal fluctuation mechanism of conformational transitions is characterized by the mean expectation time of the transition (or the mean frequency of the transitions), which depends on the transition barrier height. According to this mechanism, the transition kinetics is such that the concentration of *gauche* conformers reaches its equilibrium value (at a given temperature) not instantaneously but after a time, which is named the relaxation time (this time is close to the mean expectation time of the transition).

Thus, at a certain relationship between the temperature oscillation frequency (period) and relaxation time, temperature cycling (oscillation) may establish conditions for measuring the thermal expansion under nonequilibrium conditions. Such measurements reveal the conformational mechanism of expansion and make it possible to determine the relaxation properties of the molecular dynamics in a polymer.

The study of polymers in the modulation regime has not yet been carried out.

In this work, we consider the thermal expansion of polymers under conditions of harmonic temperature oscillations both analytically and experimentally.

OBJECT OF STUDY

The object of study is polyvinylacetate (PVA), whose monomer unit has the form

$$\left[\begin{array}{l}-\mathrm{OCH}-\mathrm{CH_2}-\\ \quad\;\;|\\ \quad\mathrm{OC_2H_3}\end{array}\right]_n.$$

This polymer is convenient to study, because it is completely amorphous and its glass transition temperature is near 300 K [8]. Data for the static (equilibrium) thermal expansion of PVA are given in [9]. They will be used in subsequent calculations.

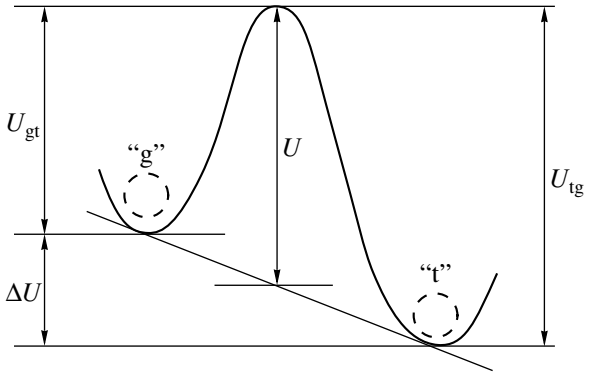

Fig. 1. Potential relief for the *trans* (t)–*gauche* (g) conformational transitions.

ANALYSIS

In this section, we will establish the temperature and frequency dependences of the thermal expansion for polymers subjected to harmonic temperature oscillations. Such calculations have not yet been performed. The basic idea is to obtain the temperature dependence of the *gauche* conformer concentration (as was noted, an increase in this concentration results in the expansion of polymers). The potential relief on conformational transitions is shown in Fig. 1.

The mean expectation time for *gauche–trans* and *trans–gauche* transitions (τ_{gt} and τ_{tg}, respectively) are given by [7, 10]

$$\tau_{gt} = \tau_0 e^{\frac{U_{gt}}{kT}}, \quad \tau_{tg} = \tau_0 e^{\frac{U_{tg}}{kT}},$$

where $\tau_0 \approx 10^{-13}$ s.

Let n_g be the relative concentration of *gauche* conformers: $n_g = N_g/N$, where N_g is the concentration of *gauche* conformers, $N = N_g + N_t$ is the total concentration of the conformers, and N_t is the concentration of *trans* conformers. Then, the relative equilibrium concentration of *gauche* conformers at a temperature T is [7]

$$n_g^e(T) = \left(1 + \exp\frac{\Delta U}{kt}\right)^{-1} = \frac{\tau^*(T)}{\tau_{tg}(T)},$$

where $\Delta U = U_{tg} - U_{gt}$ and $\tau^* = (\tau_{tg}^{-1} + \tau_{gt}^{-1})^{-1}$.

The rate of change (kinetics) of the *gauche* conformer concentration is given by the equation

$$\frac{dn_g}{dt} = \frac{n_t}{\tau_{tg}} - \frac{n_g}{\tau_{gt}},$$

from which follows a differential equation for n_g:

$$\frac{dn_g}{dt} + \frac{n_g}{\tau^*} = \frac{1}{\tau_{tg}}. \tag{1}$$

A solution to this equation is the dependence $n_g(t)$.

Let a polymer have a temperature T_1 and a *gauche* conformer concentration $n_g(T_1)$. If the temperature experiences a step $T_2 - T_1$ at zero time and then remains constant, the analytical solution for the *gauche* conformer concentration tending toward its equilibrium value $n_g^e(T_2)$ at T_2 takes the form

$$\Delta n_g(t) = n_g(t) - n_g(T_1)$$
$$= [n_g(T_2) - n_g(T_1)]\left[1 - \exp\left(\frac{t}{\tau^*(T_2)}\right)\right]. \tag{2}$$

Thus, under these conditions, the polymer will approach its equilibrium state for a time greater than $\tau^*(T_2)$.

Under temperature oscillation conditions, the equilibrium state will not be established for a time t_T (t_T is the temperature oscillation period) if $t_T < \tau^*$. For the temperature varying by the law

$$T(t) = T_b + T_m \sin \omega t,$$

we have

$$\tau_{tg}(t) = \tau_0 \exp \frac{U_{tg}}{kT_b\left(1 + \frac{T_m}{T_b}\sin \omega t\right)},$$

$$\tau_{gt}(t) = \tau_0 \exp \frac{U_{gt}}{kT_b\left(1 + \frac{T_m}{T_b}\sin \omega t\right)}.$$

Because of the high nonlinearity of differential equation (2), an explicit dependence $\Delta n_g(t)$ is impossible to derive analytically. Therefore, it is solved numerically by using the PVA parameters and specifying the parameters of harmonic temperature oscillations (T_m and ω).

When calculating the conformational component of the thermal expansion, we assume that the relative change in the polymer volume because of a change in the *gauche* conformer concentration is expressed as

$$\frac{\Delta V}{V} \approx \frac{\delta V_{gt}}{V_t}\Delta n_g,$$

where V_t is the *trans* conformer volume, V_g is the *gauche* conformer volume, and $\delta V_{gt} = V_g - V_t$ is the difference in the volumes of the conformers.

Then, for the linear expansion of an isotropic polymer by the conformational mechanism, we may write

$$\varepsilon_c(t) \approx \frac{1}{3}\frac{\Delta V(t)}{V} \approx \frac{1}{3}\frac{\Delta V_{gt}}{V_t}\Delta n_g(t).$$

To construct the dependence $\varepsilon_c(t)$ by numerically solving differential equation (1), we used the following parameters of PVA and temperature oscillations: (1) $\delta V_{gt}/V_t \cong 0.3$. Such an estimate results from the data for the "hole" component of the specific heat jump upon PVA devitrification [5] under the assumption that the holes (free volume elements) arise when *trans* conformers pass into looser *gauche* conformers; (2) $U = 0.9$ eV (data of dielectric and mechanical loss spectroscopy and differential scanning calorimetry for PVA [11]); (3) $\Delta U = 3 \times 10^{-2}$ eV (data for PVA-like polymers [11]);

(4) $U_{gt} = U - \frac{1}{2}\Delta U$, $U_{tg} = U + \frac{1}{2}\Delta U$;

(5) $\tau_0 = 10^{-13}$ s;

(6) $T = T_b + T_m \sin \omega t$, $T_m = 1$ K, and $\nu = \omega/2\pi = 10^{-1}$ and 10^{-2} Hz; and

(7) T_b is taken from the 260–360 K interval.

The numerical calculation of $\varepsilon_c(t)$ covered a sufficiently large number of the temperature oscillation periods, including the transition stage (after the onset of the temperature oscillations at $t = 0$) and the establishment of the steady-state thermal expansion process. Below, we discuss the steady-state conditions.

Figure 2 shows $\varepsilon_c(t)$ calculated at $\nu = 0.1$ Hz for three base temperatures. The time dependence of the expansion $\varepsilon_c(t)$ is compared with the sinusoidal temperature variation

$$\Delta T(t) = T(t) - T_b = T_m \sin \omega t.$$

From Fig. 2, it follows that the polymer expansion exhibits oscillations. The correlation analysis showed that the oscillatory component of the expansion is almost harmonic with the expansion oscillation fre-

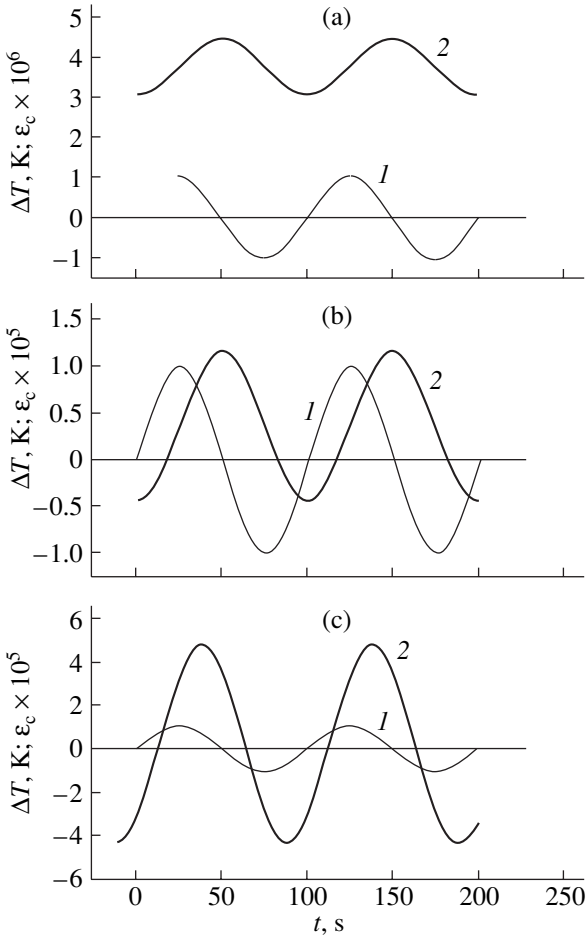

Fig. 2. (*1*) Specified base temperature oscillations $\Delta T(t)$ of frequency 0.1 Hz and amplitude $T_m = 1$ K and (*2*) calculated oscillations of the conformational expansion ε_c. The base temperature is (a) 280, (b) 300, and (c) 320 K.

quency being equal to the temperature oscillation frequency.

It is essential, however, that the phase of the expansion oscillations lags behind that of the temperature oscillations. This phase shift φ varies inversely with the base temperature T_b. In addition, the expansion oscillations have a constant component ε_{con}, which also varies in inverse proportion to the base temperature. The amplitude ε_{cm} of the harmonic component of the expansion increases with base temperature.

Similar calculations were also performed for a number of base temperatures from the 260–360 K interval with $\nu = 10^{-1}$ and 10^{-2} Hz. The temperature dependences $\varphi(T_b)$, $\varepsilon_{cm}(T_b)$, and $\varepsilon_{con}(T_b)$ for these two frequencies are shown in Fig. 3. From Fig. 3a, it is seen that the phase shift $\varphi(T_b)$ varies along an *S*-shaped trajectory from $-\pi/2$ at low temperatures to 0 at high temperatures. This is because the effective relaxation time τ^* falls exponentially with increasing temperature.

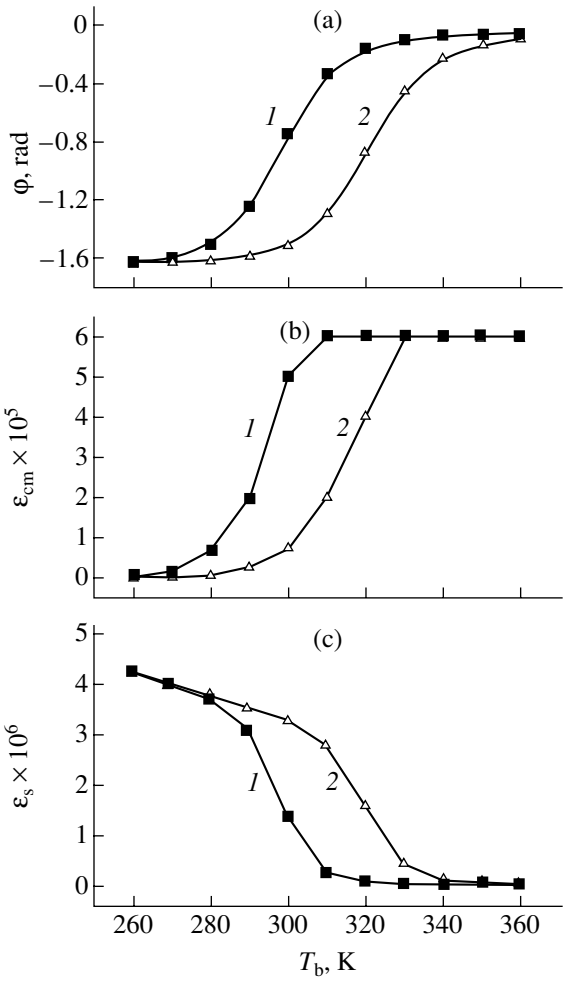

Fig. 3. Calculated dependences of the (a) phase shift, (b) oscillation amplitude, and (c) constant component of the conformational expansion on the base temperature for (*1*) 0.01 and (*2*) 0.1 Hz. The temperature oscillation amplitude is $T_m = 1$ K.

The increase in the expansion oscillation amplitude $\varepsilon_{cm}(T_b)$ with temperature (Fig. 3b) is associated with a greater number of conformation transition events per period; in other words, the system has more time to reach the equilibrium state because of the decrease in the relaxation time.

As the frequency rises, the dependences $\varphi(T_b)$ and $\varepsilon_{cm}(T_b)$ shift toward higher temperatures because of the fluctuation resonance effect, i.e., the resonant relationship between the mean frequency of the conformational transitions and the temperature oscillation frequency.

The appearance of the constant component ε_{con} of the expansion oscillations may be explained as follows. When the number of oscillation cycles is not large, a rise in the *gauche* conformer concentration with a positive change in the temperature (relative to the base temperature) in the exponential dependences of τ_{tg} and τ_{gt} exceeds the decrease in their concentration when the temperature goes down. As the number of cycles grows, the increase in the *gauche* conformer concentration slows down. Eventually, the increase and decrease counterbalance each other (as follows, e.g., from expression (2) when $n_g(T_1)$ rises), causing the constant (steady-state) value $\varepsilon_{con}(T_b)$ to be established. As the base temperature T_b grows, the "asymmetry" in the change of the *gauche* conformer concentration per cycle reduces, the balance is reached faster, and the constant value $\varepsilon_{con}(T_b)$ approaches zero.

According to Fig. 2, the temperature–time dependence of the conformational expansion can be described by the relationship

$$\varepsilon_c(t, T_b) = \varepsilon_g(T_b) + \varepsilon_{cm}(T_b)\sin(\omega t + \varphi(T_b)).$$

In general, the calculated data show that, as the base temperature grows, the conformational expansion oscillations tend to be in phase with the temperature oscillations because of a decrease in the relaxation time with increasing temperature.

Having calculated the behavior of the conformational expansion under temperature oscillation conditions, we will now estimate the total expansion of a polymer under these conditions in order to compare the calculated results with experimental data.

The total thermal expansion ε is the sum of the vibrationally anharmonic, ε_v, and conformational, ε_c, components:

$$\varepsilon(t) = \varepsilon_v(t) + \varepsilon_c(t).$$

As was noted above, the former term can be considered as inertialess, i.e., varying in phase with the temperature variations [12]. Then,

$$\varepsilon_v(t) = \varepsilon_{vm}\sin\omega t.$$

In the classical range (above the characteristic temperature), the coefficient of vibrationally anharmonic

expansion, which is inherent in any solid, depends on temperature only slightly [12]. Therefore, the general expression for the thermal expansion of polymers under the temperature oscillation conditions can be represented as

$$\varepsilon(t, T_b) = \varepsilon_{vm}\sin\omega t + \varepsilon_{con}(T_b) + \varepsilon_{cm}(T_b)\sin(\omega t + \varphi(T_b)). \quad (3)$$

Expression (3), the sum of two sinusoids, can be rearranged into

$$\varepsilon(t, T_b) = \varepsilon_m(T_b)\sin[\omega t + \psi(T_b)] + \varepsilon_{con}(T_b), \quad (4)$$

where

$$\varepsilon_m(T_b) = \sqrt{\varepsilon_{vm}^2 + \varepsilon_{cm}^2 + 2\varepsilon_{vm}\varepsilon_{cm}\cos\varphi}, \quad (5)$$

$$\psi(T_b) = \arctan\frac{\varepsilon_{cm}\sin\varphi}{\varepsilon_{vm} + \varepsilon_{cm}\cos\varphi}. \quad (6)$$

Thus, the total expansion is also a harmonic function that has the same frequency ω but is phase-shifted by ψ relative to the temperature oscillations. The total phase shift φ depends on the phase shift φ of the conformational expansion and on the amplitudes of the vibrational and conformational components (ε_{vm} and ε_{cm}). It is easy to find the limits of $\psi(T_b)$. At low temperatures, $\varphi(T_b) \longrightarrow -(\pi/2)$ (Fig. 3a) and $\varepsilon_{cm}(T_b) \longrightarrow 0$ (Fig. 3b); then, $\psi(T_b) \longrightarrow 0$. At high temperatures, $\varphi(T_b) \longrightarrow 0$ (Fig. 3a) and $\psi(T_b) \longrightarrow 0$. Between the extremes, $\psi(T_b)$ apparently goes through a minimum. The dependence $\psi(T_b)$ will be shown below.

To find the analytical dependence $\varepsilon(T_b)$ from formulas (3)–(6) with the analytical dependences $\varepsilon_{cm}(T_b)$ and $\varphi(T_b)$ known (Fig. 3), it is necessary to determine the amplitude ε_{vm} of the vibrationally anharmonic component of the expansion. To this end, we will use the known experimental value of the thermal expansion coefficient (TEC) α_v for glassy PVA, in which the conformational dynamics is not yet excited and the expansion depends nearly completely on the vibrational dynamics. In the interval 260–280 K, the TEC of PVA is $\alpha_v = 7 \times 10^{-5}$ [9].

Since the vibrationally anharmonic component of the thermal expansion is expressed as $\varepsilon_v(t) = \varepsilon_{vm}\sin\omega t = \alpha_v T_m \sin\omega t$, we find that $\varepsilon_{vm} = \alpha_v T_m$. Since we put $T_m = 1$ K in our calculations, the oscillation amplitude of the vibrationally anharmonic expansion is $\varepsilon_{vm} = 7 \times 10^{-5}$.

The temperature dependences of the oscillation amplitude $\varepsilon(T_b)$ of the total expansion and of the total phase shift $\psi(T_b)$ for 0.1 and 0.01 Hz are given in Fig. 4. Being close to zero at low and high temperatures, the curve $\psi(T_b)$ passes through a minimum as deep as 0.3 rad near 300 K. At the higher frequency, the minimum shifts toward higher temperatures.

The curves $\varepsilon_m(T_b)$ and $\psi(T_b)$ obtained analytically can now be contrasted with thermal expansion data for PVA measured under the temperature oscillation conditions.

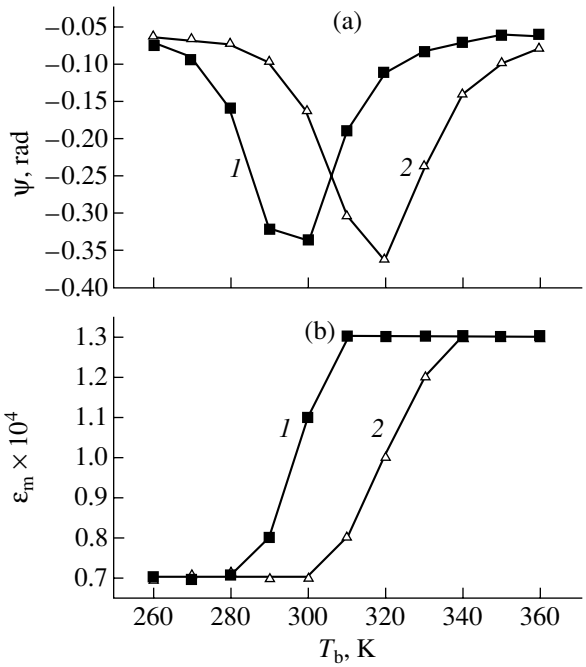

Fig. 4. Calculated dependences of the (a) phase shift and (b) oscillation amplitude of the total (conformational and vibrationally anharmonic) expansion of the polymer at (*1*) 0.01 and (*2*) 0.1 Hz.

EXPERIMENT

As noted above, neither analysis nor experimental studies of the thermal expansion of polymers under temperature cycling have been reported to date. The above calculations have demonstrated what kind of temperature and frequency dependences of the thermal expansion could be expected.

To validate the predictions, we performed experiments with PVA using a specially designed setup for measuring the thermal expansion of polymers under the conditions of a harmonically varying temperature. Temperature variations were produced with planar Peltier cells to which a harmonically varying voltage was applied. The sample temperature was measured by a thermocouple with an accuracy of 0.01 K. The oscillation amplitude was 0.8 K, and the oscillation frequencies were 0.03 and 0.1 Hz. The thickness of the polymer film, 100 μm, was taken such that the temperature field nonuniformity (determined by calculating the thermal diffusivity of PVA [5]) was no more than 10^{-2} for the given oscillation frequencies. The operating length of the sample was L = 20 mm. The thermal expansion $\Delta L(t)$ was detected with a 6MKh1S mechanotronic detector accurate to 0.01 μm. The electrical signals from the thermocouple (sample temperature) and from the mechanotronic detector (sample expansion) were

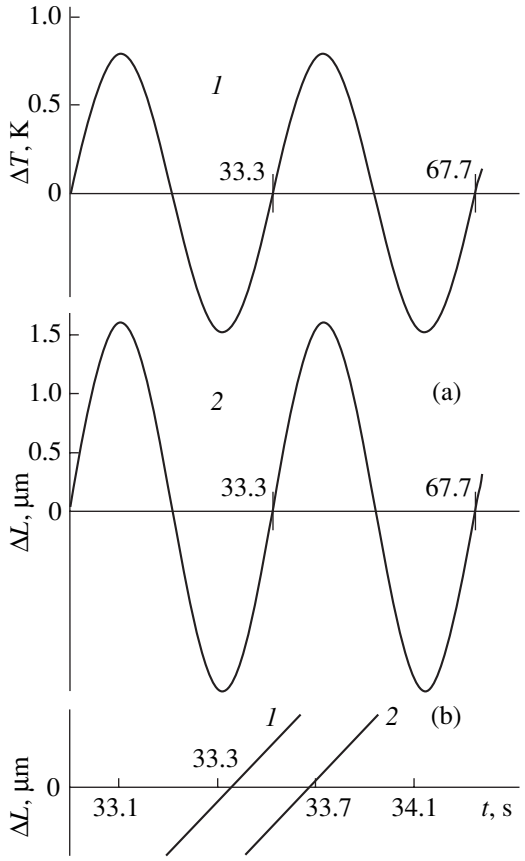

Fig. 5. (*1*) Base temperature oscillations $\Delta T(t)$ at a frequency of 0.03 Hz and an oscillation amplitude of 0.8 K and (*2*) recorded waveforms $\Delta L(t)$ of the total PVA expansion. The base temperature is 305 K. (a) Large-scale time-base sweep and (b) a fragment of the sweep based on the MCC data.

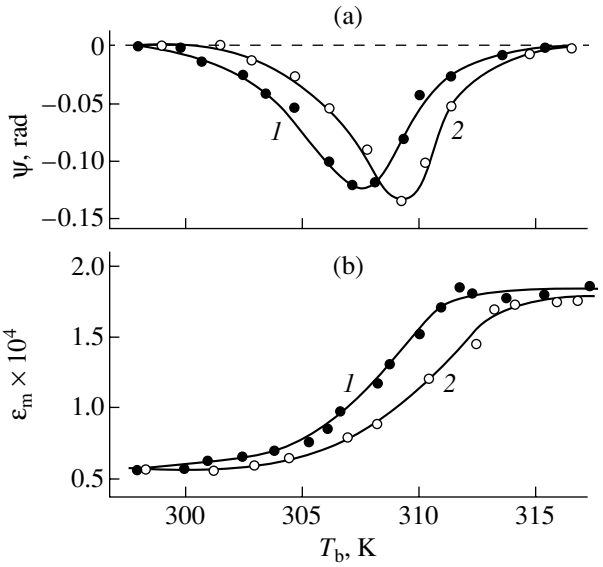

Fig. 6. Experimental dependences of the (a) phase shift and (b) oscillation amplitude of the PVA vibrational expansion on the base temperatures for (*1*) 0.03 and (*2*) 0.1 Hz.

applied to an *X*–*Y* recorder and to a measuring computer complex (MCC), which calculated the expansion vs. temperature phase shift $\psi(T_b)$ and the expansion oscillation amplitude $\varepsilon_m = \Delta L_m/L$. The phase shift was determined with an accuracy of 2 ms.

During the measurements, the base temperature (295–320 K) was changed stepwise. At each step, the sample was kept until the steady-state conditions were established (as a rule, for no more than 20 min).

The records of the temperature oscillations and the vibrational component of the expansion for a frequency of 0.3 Hz and a base temperature of 305 K are shown in Fig. 5. The expansion is seen to harmonically oscillate with the same frequency as the temperature. The presence of the expansion vs. temperature phase shift is impossible to judge visually from large-scale curves *1* and *2* in Fig. 5a. However, the high-resolution MCC reliably reveals it. A fragment of the MCC time-base sweep demonstrates clearly that the expansion lags behind the temperature (Fig. 5b).

Figure 6 shows the expansion, $\varepsilon(T_b)$, and phase shift, $\psi(T_b)$, curves constructed for 0.03 and 0.1 Hz. It is seen that the experimental (Fig. 6) and calculated (Fig. 4) curves $\psi(T_b)$ and $\varepsilon(T_b)$ run in a similar manner.

Obviously, it would be unreasonable to anticipate exact quantitative coincidence. For example, the calculation was carried out for only one transition barrier height, while polymers are known [13] to exhibit the distribution of conformational transition barrier values about the mean. Furthermore, in the devitrification range of polymers (near 300 K for PVA) [8], the conformational transition barriers depend on temperature [13, 14], which was disregarded in the calculations. Finally, the barrier values adopted in the calculations are approximate. Yet the calculation and experiment are in satisfactory quantitative agreement.

For example, the calculations used the experimentally found value of the vibrationally anharmonic component of the PVA expansion, whereas the conformational component was derived analytically from the barrier values and the difference between the volumes occupied by *trans* and *gauche* transformers. The calculated and experimental values of $\varepsilon(T_b)$ are seen to differ insignificantly at high temperatures (315 K or higher).

The minima of the expansion–temperature phase shift calculated and found experimentally for 0.1 Hz are 318 and 309 K, respectively. For other parameters, such as the width and depth of the phase shift minimum and also the temperature shift of the curves with varying frequency, the discrepancy is greater. It is expected that the results will be refined if more realistic values of the transition barriers are used.

As a whole, the agreement between the analytical and experimental data should be considered as acceptable (especially if it is taken into consideration that these results are only tentative).

The data obtained (first of all, the phase shift between the expansion and temperature, as well as the sharp increase in the expansion with temperature) are an independent corroboration of the fact that, at the stage of polymer devitrification, the conformational expansion mechanism plays an increasing part and eventually becomes prevailing. This mechanism is unrelated to the atomic interaction anharmonicity (unlike the low-temperature mechanism of expansion). This is the first result of this work.

Further combined experimental and analytical investigation into the thermal expansion of polymers subjected to temperature cycling of variable frequency and amplitude will give more detailed information on the parameters of elementary events in conformational thermal expansion (transition barriers, the difference between the energy of *trans* and *gauche* conformers, and the difference between their volumes) and on the conformational dynamics as a whole.

To conclude, some comments concerning the well-known parameter of thermal expansion—TEC. The conventional definition of the TEC,

$$\alpha = \left(\frac{d\varepsilon}{dT}\right)_\sigma, \qquad (7)$$

implies that it is measured at a constant pressure σ under equilibrium conditions. Under nonequilibrium conditions, definition (7) exhibits singularities. For a single-step temperature change from T_1 to T_2 and subsequent relaxation to the state equilibrium at T_2, the expansion grows at a constant temperature (see expression (2)). In this case, the TEC $\alpha = d\varepsilon/dT = \infty$ throughout the relaxation period. Under temperature cycling (oscillation), (4) formally yields

$$\alpha(t) = \frac{d\varepsilon}{dT} = \frac{d\varepsilon}{dT}\left(\frac{dT}{dt}\right)^{-1} = \frac{\varepsilon_m}{T_m}\frac{\cos(\omega t + \psi)}{\cos\omega t}.$$

This means that the instantaneous value of the TEC varies from $-\infty$ to ∞ during the oscillation period. These features should be taken into account when the notion TEC is applied to the thermal expansion of nonequilibrium systems.

ACKNOWLEDGMENTS

This work was supported by the Russian Foundation for Basic Research (project no. 00-03-33064a).

REFERENCES

1. Ya. A. Kraftmakher, High Temp. High Press. **5**, 645 (1973).
2. L. P. Filippov, *Measurements of Thermal Physical Properties of Materials* (Énergoatomizdat, Moscow, 1984).
3. Ya. A. Kraftmakher, Obz. Teplofiz. Svoĭstvam Veshchestv, No. 1 (75), (1989).
4. T. N. Johansen, J. Feber, and T. Jossang, High Temp. High Press. **19**, 77 (1987).
5. Yu. K. Godovskiĭ, *Thermal Physics of Polymers* (Khimiya, Moscow, 1982).
6. A. I. Slutsker, L. A. Laĭus, I. V. Gofman, *et al.*, Fiz. Tverd. Tela (St. Petersburg) **43**, 1327 (2001) [Phys. Solid State **43**, 1382 (2001)].
7. M. V. Vol'kenshteĭn, *Configurational Statistics of Polymer Chains* (Akad. Nauk SSSR, Moscow, 1959).
8. V. A. Bershteĭn and V. M. Egorov, *Differential Scanning Calorimetry in Physical Chemistry of Polymers* (Khimiya, Leningrad, 1990).
9. R. Greiner and F. R. Schwarzl, Rheol. Acta **23**, 378 (1984).
10. J. Frenkel, *Kinetic Theory of Liquids* (Nauka, Leningrad, 1945; Clarendon Press, Oxford, 1946).
11. A. I. Slutsker, Yu. I. Polikarpov, and K. V. Vasil'eva, Zh. Tekh. Fiz. **72** (7), 86 (2002) [Tech. Phys. **47**, 880 (2002)].
12. S. I. Novikova, *Thermal Expansion of Solids* (Nauka, Moscow, 1974).
13. P. P. Kobeko, *Amorphous Materials* (Akad. Nauk SSSR, Moscow, 1952).
14. A. I. Slutsker, Yu. I. Polikarpov, and K. V. Vasil'eva, Fiz. Tverd. Tela (St. Petersburg) **44**, 1529 (2002) [Phys. Solid State **44**, 1604 (2002)].

Translated by V. Isaakyan

Technical Physics, Vol. 48, No. 7, 2003, pp. 880–884. Translated from Zhurnal Tekhnicheskoĭ Fiziki, Vol. 73, No. 7, 2003, pp. 82–87.

SOLIDS

Different Types of Dislocation Dynamics Resulting from the Dynamic Aging of Dislocations

B. V. Petukhov

Institute of Crystallography, Russian Academy of Sciences, Leninskiĭ pr. 59, Moscow, 119333 Russia
e-mail: petukhov@ns.crys.ras.ru

Received October 22, 2002

Abstract—The effect of mobile impurities on the dislocation dynamics under static and variable loading of crystals is calculated. It is shown that the dynamic aging of dislocations may produce a specific regime where dislocations are at rest upon static loading and move only under a growing stress. The dislocation mobility in this regime is athermal. The existence conditions for this regime are studied. The dependence of the dislocation path lengths in silicon on the stress pulse rise time that is observed in pulsed-load experiments is explained by the existence of this regime. © *2003 MAIK "Nauka/Interperiodica".*

INTRODUCTION

The dynamic aging of dislocations is an efficient means for hardening doped crystals and improving their mechanical properties. This effect is caused by the impurities, which are entrapped by moving dislocations, thus affecting their mobility. Dynamic aging can be induced by both controllable and uncontrollable impurities or other point defects in crystals. For example, Czochralski-grown silicon with an impurity oxygen concentration of up to 10^{18} cm^{-3} turns out to be more appropriate for microelectronics applications than the pure crystals grown by zone melting (see, e.g., [1, 2]).

The early model describing the dynamic aging of dislocations was the Cottrell–Jaswon model [3]. Subsequently, it was elaborated upon in [4, 5] and other works. Cottrell and Jaswon [3] analyzed impurity diffusion in the elastic force field of a steadily moving dislocation. More recent works considering the Portevin–Le Chatelier effect concentrated on the mechanism of dislocation motion over local barriers, taking into account its steplike nature [6, 7]. Impurities diffuse to a dislocation when it is at rest at an obstacle, waiting for thermal activation, and resulting impurity atmospheres partially relax during a jump to a next obstacle.

Another mechanism of dislocation motion that is characteristic of semiconductors, bcc metals, and a number of other materials assumes that dislocations uniformly overcome the intrinsic small-scale potential relief (Peierls–Nabarro barriers) in the crystal lattice. For this mechanism, the model of dynamic aging might be similar to the original Cottrell–Jaswon model [3], at least at relatively low velocities. However, the continuum approach, which involves the elastic interaction between impurity atoms and dislocations, is known to fail in the vicinity of dislocations: the results of calculation become sensitive to the length of cutoff. This circumstance greatly depreciate the calculations obtained in terms of the continuum approach.

Moreover, elastic forces are not the only ones involved in the impurity–dislocation interaction at short distances. One should not neglect electronic ("chemical") interactions. Maroudas and Brown [8] developed a more general combined approach that takes into account an additional moderating effect of the short-range impurity–dislocation interaction. The energy of the short-range interaction was evaluated by atomistic calculations. This approach significantly clarified the specific role of the dislocation core but failed in completely eliminating the dependence of the results on the length of cutoff.

In [9], the case where dislocations move with a high velocity comparable to the rate of impurity migration D/a (D is the impurity diffusion coefficient, and a is the lattice spacing) was studied. Here, the dimension of the impurity atmosphere decreases to several lattice spacings. Therefore, the contribution from the short-range interaction to the retardation of dislocation motion becomes dominant, and only this contribution was taken into account. In this situation, a discrete approach to describing the impurity redistribution by a moving dislocation seems to be more appropriate. Without the loss of physical justification (which is illusory in the case of the continuum description because of the cutoff length problem), such an approach is much simpler and more illustrative. It will be used in this work.

The model [9] considers primarily an excess impurity content c (per lattice site) in the dislocation core. Its variation is described by the equation

$$\frac{dc}{dt} = \frac{V}{a}\left[rc_0 - c\exp\left(-\frac{a}{\tau_1 V}\right)\right]. \quad (1)$$

1063-7842/03/4807-0880$24.00

Here, $V = a/t_d$ is the average dislocation velocity, t_d is the time it takes for dislocations to overcome the barrier, c_0 is the impurity concentration in the bulk of the crystal, τ_1 is the time of impurity migration in the vicinity of the dislocation core, and r is the impurity entrapment length expressed in lattice parameters. The value of τ_1 may differ substantially from the migration time a^2/D in the bulk of the crystal because of the distorting effect of the dislocation core. The first term on the right-hand side of Eq. (1) describes the increase in the excess concentration in the core due to the impurity entrapment, and the second one describes the decrease in c when the impurities lag behind the dislocation, with a probability proportional to $\exp(-t_d/\tau_1)$.

Along with the entrapment of impurities, the interaction between dislocations and impurities also causes a force that slows down the motion of dislocations, which can be described in terms of a specific "internal stress" σ_i counteracting an applied stress σ. This internal stress is proportional to the excess concentration of impurities in the dislocation core: $\sigma_i = \beta c$. Then, the effective stress σ_{eff} that activates a dislocation is

$$\sigma_{eff} = \sigma - \beta c. \quad (2)$$

The coefficient of proportionality β is specified by the short-range impurity–dislocation interaction and, in specific cases, can be found by atomistic calculations. In this work, β is taken to be a phenomenological parameter. The dislocation velocity is assumed to be a function of the effective stress: $V = V(\sigma_{eff})$. Such a renormalization of the driving force will be considered as the main channel through which impurities affect the dislocation motion, and only this channel is taken into account in this work.

The dislocation dynamics is studied with macroscopic mechanical testing of crystals and in model experiments under both static loading, where long rectangular stress pulses are applied, and under varying loading usually by applying triangular or trapezoidal pulses that have various ratios of their variable and constant components. First, we will consider the effect of mobile impurities on the dislocation dynamics under static loading and then study the possibility for the existence of steady-state motion modes.

STEADY-STATE MODES AND THE THRESHOLD OF DISLOCATION IMMOBILIZATION

The steady motion is characterized by a constant excess impurity content in the dislocation core that is given by Eq. (1) with $dc/dt = 0$. This condition either is satisfied at $V = 0$ or meets the roots of the equation

$$V(\sigma - \beta c) = \frac{a}{\tau_1 \ln(c/rc_0)}. \quad (3)$$

Let us represent graphically the equation

$$\sigma = \beta c + \varphi\left(\frac{a}{\tau_1 \ln(c/rc_0)}\right), \quad (4)$$

which is derived from Eq. (3). Here, $\varphi(V)$ is the function inverse to $V(\sigma)$. For example, if the dislocation velocity is a power function of the stress $V(\sigma) = B\sigma^m$, the inverse function has the form $\varphi(V) = (V/B)^{1/m}$. However, the exact form of the function $\varphi(V)$ is of minor significance for further qualitative considerations; only its general properties are important. If $V(\sigma)$ is naturally considered to be a monotonically increasing function, then $\varphi(V)$ is also a monotonically increasing function of its argument. At $c \longrightarrow rc_0$, this argument grows infinitely; therefore, the plot of the right-hand side in (4) against the concentration takes the form shown in Fig. 1. The straight line here corresponds to $V = 0$; i.e., $\sigma = \beta c$. It is seen that at $\sigma > \sigma_c$, where σ_c is the minimum of the right-hand side in (4), there are three solutions to the stationarity condition $dc/dt = 0$: c_1, c_2, and c_3. In the intervals between the stationary values, c varies as shown by the arrows at the horizontal axis. Thus, the solution c_2 is unstable because any deviation will increase with time, while the solutions c_1 and c_3 are stable. The solution c_1 corresponds to the increase in the excess impurity concentration near a dislocation as the stress decreases and, hence, to the decrease in the dislocation velocity compared with its value in the pure crystal (see Fig. 2).

As the stress decreases to σ_c, the solutions c_1 and c_2 merge together at the point of minimum in Fig. 1 and

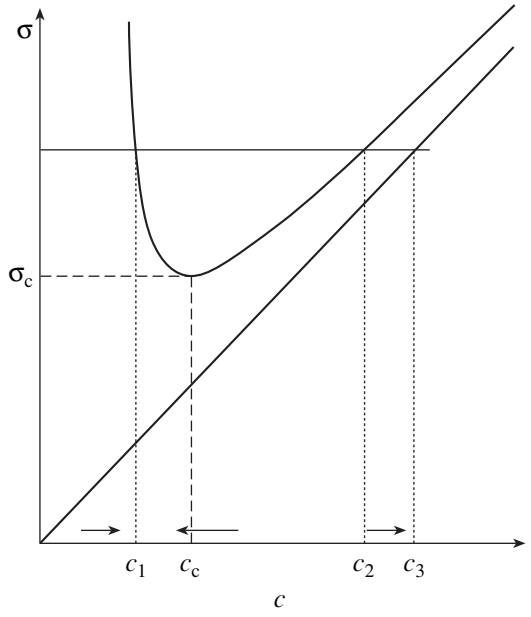

Fig. 1. Solution of Eq. (4) for the steady-state modes of dislocation motion: c_1 and c_3 are stable solutions, c_2 is an unstable solution, and σ_c is the threshold of dislocation immobilization.

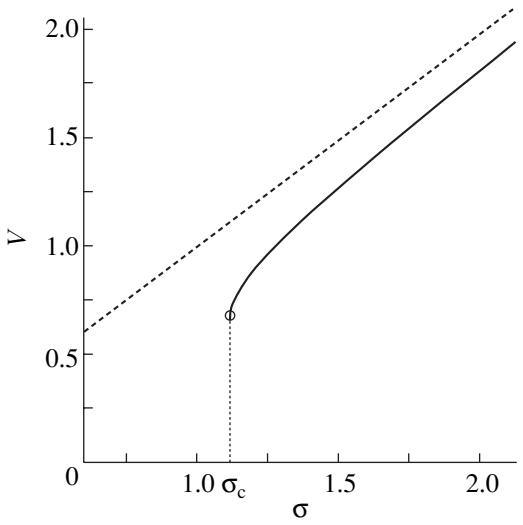

Fig. 2. Dislocation velocity vs. stress dependence with allowance for the effect of mobile impurities. The dashed line is the initial dependence for a pure crystal. The stress is expressed in $a/(\tau_1 B)$; the velocity, in a/τ_1. The calculation was carried out for $m = 1$, $r = 1$, and $c_0 = 0.1a/(\beta\tau_1 B)$.

then disappear, giving rise to the solution c_3, which corresponds to the zero dislocation velocity. The value $c_3 = \sigma/\beta$ is the minimum concentration required to immobilize the dislocation. With time, the concentration of impurities at the pinned dislocation will exceed c_3 owing to the impurity diffusion flux. This leads to the stronger pinning of the dislocation, so that a higher "starting" stress may be required to activate the dislocation again [10]. The consideration of this process of ordinary static aging, as well as the attendant saturation of the impurity atmosphere and complexation [11], is beyond the scope of this work.

At $\sigma < \sigma_c$, the steady motion is impossible; hence, σ_c is the threshold of dislocation immobilization caused by dynamic aging. Such a picture agrees well with the experimental data on the effect of neutral impurities on the dislocation mobility in silicon [10, 12], indicating the qualitative validity of this model.

Figure 1 shows that, at given $\sigma > \sigma_c$, the resulting dynamics can be different depending on the difference between the initial impurity concentration at the dislocation and c_2. Therefore, the issue of how the dislocation approaches the starting state and the behavior of the dislocation–impurity system upon stressing are of crucial importance.

Therefore, we will study the dislocation dynamics under variable loading.

DISLOCATION DYNAMICS UNDER AN INCREASING LOAD

Let us consider the case where the stress rises with a constant rate: $\sigma = \dot\sigma t$, $\dot\sigma$ = const. This situation is observed upon both macroscopic mechanical testing, e.g., at the initial elastic stage of loading and upon studying the dynamics of individual dislocations subjected to triangular or trapezoidal stress pulses. At short times, when the excess impurity concentration is still low and the exponential term in (4) that describes the separation of impurities from the dislocation can be neglected, Eq. (3) is easy to solve. In implicit form, the solution is

$$\int_0^{\dot\sigma t - \beta c} \frac{d\sigma}{V_0 - V(\sigma)} = t\beta r c_0/a, \qquad (5)$$

where $V_0 \equiv (\dot\sigma a)/(\beta r c_0)$. At $t \longrightarrow \infty$, the effective stress tends to a constant value: $\dot\sigma t - \beta c \longrightarrow \sigma_{\text{eff0}}$, which corresponds to the dislocation velocity V_0:

$$V(\sigma_{\text{eff0}}) = V_0 = \frac{\dot\sigma a}{\beta r c_0}. \qquad (6)$$

Thus, after a certain transition time, a constant dislocation velocity $V = V_0$ sets in. Under these conditions, the impurity concentration at the dislocation linearly increases with time:

$$c \approx (\dot\sigma t - \sigma_{\text{eff0}})/\beta. \qquad (7)$$

As is seen from (7), the applicability domain of this solution is bounded below by the condition $t > \sigma_{\text{eff0}}/\dot\sigma$. The upper bound depends on whether or not the exponential term in (1) can be neglected in comparison with rc_0. For the solution obtained, this term is approximately given by

$$\frac{\dot\sigma t - \sigma_{\text{eff0}}}{\beta}\exp\left(\frac{\beta r c_0}{\tau_1 \dot\sigma}\right).$$

Thus, the regime under study occurs in the time interval

$$\frac{\sigma_{\text{eff0}}}{\dot\sigma} < t < t_m = \frac{\sigma_{\text{eff0}}}{\dot\sigma} + \frac{\beta r c_0}{\dot\sigma}\exp\left(\frac{\beta r c_0}{\tau_1 \dot\sigma}\right). \qquad (8)$$

At low rates of load variation, $\dot\sigma < \beta r c_0/\tau_1$, the existence range of this mode may be rather long because of the exponential term in (8). Above the upper boundary of time interval (8), $t > t_m$, the impurities begin to leave the dislocation and their concentration by the dislocation decreases. As a result, the dislocation velocity increases, the impurities lag behind the dislocation still further, and the process becomes catastrophic. Eventually, the dislocation becomes almost free of the impurity atmosphere, as is shown in Fig. 3. The curve $c(t)$ here is obtained by the numerical solution of Eq. (1) at $\sigma = \dot\sigma t$, $\dot\sigma = 0.2a/(\tau_1^2 B)$, $c_0 = 0.1a/(\beta\tau_1 B)$, and $m = r = 1$. This particular example illustrates the existence of the long-term stage where the excess impurity concentration at the dislocation grows linearly with time, which corresponds to solution (7).

The applied stress increases with time linearly; accordingly, c_2, which separates different types of dislocation dynamics, also grows (Fig. 1). The related dashed curve $c_2(t)$ in Fig. 3 passes through the maximum in the curve $c(t)$, since the value $c = c_2$ corresponds to the stationarity condition $\dot{c} = 0$, which coincides with the extremum condition for $c(t)$. This circumstance will be used in following analysis.

Now let us consider the behavior of the dislocation under pulsed trapezoidal loading. First, we will examine the constant amplitude portion. If the loading pulse rise time $t_1 < \sigma_c/\dot{\sigma}$, the stress amplitude σ_a is lower than σ_c and the dislocation motion decays. The same is true for the a pulse rise time in the range $\sigma_c/\dot{\sigma} < t_1 < t_m$, since in this time interval, the impurity concentration at the dislocation obeys the condition $c(t_1) > c_2(t_1)$ (Fig. 3) and relaxes to c_3 in the constant amplitude portion, thus suppressing the dislocation motion.

However, at $t_1 > t_m$, the situation is reversed, $c(t_1) < c_2(t_1)$, and the impurity concentration in the core relaxes to the value c_1, which allows for the steady motion of the dislocation. Based on these considerations, we can construct a diagram in the plane (σ_a, $\dot{\sigma}$) that separates the types of the final dislocation dynamics and makes it possible to find the dependence of the immobilization threshold σ_{th} on the loading rate (Fig. 4).

According to (8), an increase in the threshold stress $\sigma_{th} = \dot{\sigma} t_m$ at $\dot{\sigma} \longrightarrow 0$ is governed by the exponential term. As $\dot{\sigma}$ increases, the maximum in the curve $c(t)$ goes down and eventually becomes equal to c_c (at a certain value $\dot{\sigma} = \dot{\sigma}_p$). At high $\dot{\sigma}$, the stress $\dot{\sigma} t_m$ becomes lower than σ_c and no longer determines the boundary of the dislocation mobility region. In addition, at the end point $\dot{\sigma}_p$ of the dependence of the immobilization threshold σ_{th} on the pulse edge steepness, interval (8), where the regime under study exists, disappears. Hence, we have the order-of-magnitude estimate $\dot{\sigma}_p \sim \beta r c_0/\tau_1$. Let us show that the curve σ_{th} smoothly tends to its constant value σ_c and takes it at $\dot{\sigma} = \dot{\sigma}_p$. As was already noted, the maximum in the curve $c(t)$ is $c_m = c_2$; then,

$$\sigma_{th} = \beta c_m(\dot{\sigma}) + \varphi\left(\frac{a}{\tau_1 \ln(\beta c_m(\dot{\sigma})/r c_0)}\right). \qquad (9)$$

The derivative $d\sigma_{th}/d\dot{\sigma}$ has the form

$$\frac{d\sigma_{th}}{d\dot{\sigma}} = \frac{d}{dc_m}\left[\beta c_m(\dot{\sigma}) + \varphi\left(\frac{a}{\tau_1 \ln(\beta c_m(\dot{\sigma})/r c_0)}\right)\right]\frac{d\beta c_m}{d\dot{\sigma}}. \qquad (10)$$

At $\dot{\sigma} = \dot{\sigma}_p$, $c_m = c_c$ and

$$\frac{d}{dc}\left[c + \varphi\left(\frac{a}{\tau_1 \ln(\beta c_m/r c_0)}\right)\right] = 0.$$

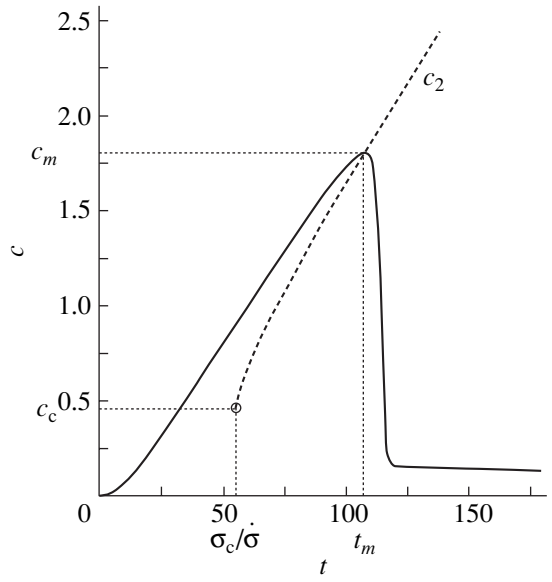

Fig. 3. Time dependence of the excess impurity concentration in the core of a dislocation moving under the action of a stress growing with a constant rate $\dot{\sigma}$. The dashed line shows the related variation of the boundary c_2 of the region where the dislocation moves steadily under static loading.

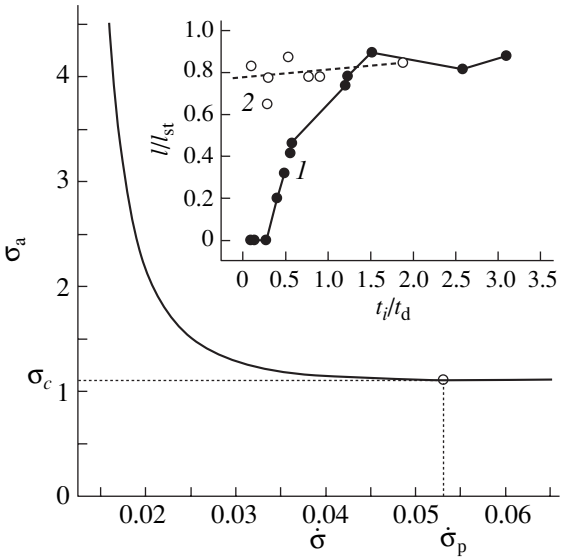

Fig. 4. Diagram separating the regions of mobile and unmoving dislocations in the plane (σ_a, $\dot{\sigma}$) for the flat part of a trapezoidal loading pulse with an amplitude σ_a. The inset shows the normalized dislocation path lengths in silicon [16] as a function of the duration t_i of stress pulses (the total duration is 3600 s) for pulse rise times t_1 = (*1*) 4 and (*2*) 1 ms. σ_a = 7 MPa and T = 600°C.

Hence, $d\sigma_{th}(\dot{\sigma}_p)/d\dot{\sigma} = 0$ and the curve $\sigma_{th}(\dot{\sigma})$ touches the horizontal $\sigma_{th} = \sigma_c$, which proves the statement.

DISCUSSION

Thus, we showed that the dislocation dynamics in impurity and pure crystals differ radically because of dynamic aging. In impurity crystals subjected to loading pulses with an amplitude σ_a, dislocation behave differently at different pulse rise rates. Different modes of behavior are separated by the curve $\sigma_{th}(\dot{\sigma})$ given in Fig. 4. In the region under this curve, dislocations move only during the stress rise time and stop moving on the plateau. The cause of such a radical change in the behavior is that the impurity atmosphere strongly influence the force moving the dislocation. Since the amount of entrapped impurities increases along the dislocation path, so does the retarding force. Therefore, an applied load must grow continuously to sustain the motion. If the applied load rises, the effective steady-state stress acting on the dislocation and, hence, the steady-state mode of dislocation motion may be established. The effective stress turns out to be much lower than the applied stress, and the resulting pattern has little in common with the conventional dislocation dynamics.

Within the stress rise time, the dislocation velocity is expressed as $V = (\dot{\sigma} a)/(\beta r c_0)$. The universality of this expression attracts attention: it is completely independent of the dynamic characteristics of dislocations under the normal conditions that are specified by the function $V(\sigma)$. In most cases, normal dislocation motion is thermally activated and depends strongly on temperature. However, the above expression for the velocity implies that the motion mode under study is athermal. Note that similar qualitative features were observed for the dislocation dynamics in alkali halides KCl [13] and NaCl [14, 15]. However, in the halides, these features may have another nature, since they were convincingly explained by the mechanism of the quasistatic relaxation of dislocations in the internal stress field [15].

Experiments on semiconductor materials add more considerable support for the mechanism of dislocation motion proposed in this work. When studying the dislocation mobility in silicon single crystals under the action of a train of stress pulses, Nikitenko *et al.* [16] found the dependence of the dislocation path length on the pulse edge steepness (see the inset in Fig. 4). At a relatively low steepness, the path length was shorter than under static loading, whereas steep pulses virtually quenched this effect. It seems likely that mobile impurities affect the motion of dislocation kinks, causing their aging only when the stress rise time is long, according to the diagram shown in Fig. 4. It should be noted that our model of dynamic aging is applicable not only to dislocations but also to other objects of any dimension whose dynamics is associated with overcoming a small-scale potential relief. These could be both dislocation kinks and two-dimensional internal boundaries of various physical nature.

CONCLUSIONS

The motion and multiplication of dislocations cause microelectronic devices to fail. The aging of dislocations when they entrap impurities pins dislocations or reduces their mobility, thereby giving a chance to extend the device's service time. In this work, we showed that the interaction with the impurity subsystem makes the dislocation mobility dependent not only on the stress level in the system but also on the system's history (e.g., the formation of an excess impurity concentration in the dislocation core, which is a function of the rate $\dot{\sigma}$ of approach to the steady-state stress). At low $\dot{\sigma}$, the dislocation immobilization threshold was found to increases significantly. This important finding could be useful for applications. We noted experimental facts indicating the dependence of the dislocation mobility in silicon on the pulse steepness during pulsed loading, which qualitatively agrees with the theory developed.

REFERENCES

1. K. Sumino, *Defects and Properties of Semiconductors: Defect Engineering*, Ed. by J. Chikawa, K. Sumino, and K. Wada (KTK Scientific Publishers, Tokyo, 1987), p. 227.
2. M. G. Mil'vidskiĭ and V. V. Osvenskiĭ, *Structural Defects in Semiconductor Single Crystals* (Metallurgiya, Moscow, 1984).
3. A. H. Cottrell and M. A. Jaswon, Proc. R. Soc. **199** (189), 104 (1949).
4. H. Yoshinaga and S. Morozumi, Philos. Mag. **23**, 1351, 1367 (1971).
5. B. V. Petukhov, Fiz. Tverd. Tela (Leningrad) **26**, 3160 (1984) [Sov. Phys. Solid State **26**, 1903 (1984)].
6. Y. Estrin and L. P. Kubin, in *Continuum Models for Materials with Microstructure*, Ed. by H.-B. Mulhaus (Wiley, New York, 1995), p. 395.
7. H. Neuhauser, in *Mechanical Properties of Solid Solutions and Related Topics*, Ed. by J. Lepinoux, D. Maziere, V. Pontikis, and G. Saada (Kluwer, Dordrecht, 2000), NATO ASI Ser. E, Vol. 367, p. 99.
8. D. Maroudas and R. A. Brown, Appl. Phys. Lett. **58**, 1842 (1991).
9. B. V. Petukhov, Zh. Tekh. Fiz. **60** (10), 64 (1990) [Sov. Phys. Tech. Phys. **35**, 1150 (1990)].
10. V. N. Erofeev and V. I. Nikitenko, Fiz. Tverd. Tela (Leningrad) **13**, 146 (1971) [Sov. Phys. Solid State **13**, 116 (1971)].
11. K. Sumino, Phys. Status Solidi A **171**, 111 (1999).
12. K. Sumino and M. Imai, Philos. Mag. A **47**, 753 (1983).
13. G. N. Ermolaev, S. I. Ninenko, and A. A. Urusovskaya, Fiz. Tverd. Tela (Leningrad) **31**, 277 (1989) [Sov. Phys. Solid State **31**, 707 (1989)].
14. G. N. Ermolaev, Fiz. Tverd. Tela (St. Petersburg) **38**, 3375 (1996) [Phys. Solid State **38**, 1841 (1996)].
15. V. I. Al'shits, E. V. Darinskaya, and M. V. Koldaeva, Fiz. Tverd. Tela (St. Petersburg) **43**, 1635 (2001) [Phys. Solid State **43**, 1703 (2001)].
16. V. I. Nikitenko, B. Ya. Farber, and Yu. L. Iunin, Zh. Éksp. Teor. Fiz. **93**, 1314 (1987) [Sov. Phys. JETP **66**, 738 (1987)].

Translated by K. Shakhlevich

Technical Physics, Vol. 48, No. 7, 2003, pp. 885–888. Translated from Zhurnal Tekhnicheskoĭ Fiziki, Vol. 73, No. 7, 2003, pp. 88–92.

SOLID-STATE ELECTRONICS

Modification of GaAs by Medium-Energy N_2^+ Ions

Yu. S. Gordeev, V. V. Bryzgalov, B. N. Makarenko, V. M. Mikushkin, S. G. Konnikov, P. N. Brunkov, V. M. Ustinov, and A. E. Zhukov

Ioffe Physicotechnical Institute, Russian Academy of Sciences, Politekhnicheskaya ul. 26, St. Petersburg, 194021 Russia

Received November 14, 2002

Abstract—The modification of GaAs with a 2500-eV beam containing N_2^+ and Ar^+ ions is examined with Auger electron spectroscopy. Most implanted nitrogen atoms are found to react with the matrix, substituting arsenic atoms to produce a several-nanometer-thick layer of the single-phase $GaAs_{1-x}N_x$ (x = 6%) solid solution. The GaN phase is absent. Displaced arsenic atoms and nitrogen atoms unreacted with the matrix are present in the layer and on its surface. The former segregate, whereas the latter form molecules. © *2003 MAIK "Nauka/Interperiodica".*

The use of $GaAs_{1-x}N_x$ solid solutions in electronics and optoelectronics has aroused considerable interest in recent years. The possibility of controlling the band gap by varying the nitrogen content renders this material extremely promising for controlled luminescence devices based on InAs/$GaAs_{1-x}N_x$ quantum-dot nanoheterostructures, such as long-wavelength injection lasers (see [1, 2] and the references therein). The introduction of an additional (third) $GaAs_{1-x}N_x$ layer with a band gap of about 1 eV into GaAs/$Ga_{0.5}In_{0.5}P$ structures could improve the efficiency of tandem solar cells [3]. Another advantage of the $GaAs_{1-x}N_x$ solid solution is that, for a certain nitrogen content ($x \approx 20\%$), it can be lattice-matched with silicon, which is the basic electronic material, thus making it possible to integrate III–V and silicon devices [4, 5]. Difficulties encountered in reaching this goal are that nitrogen is hard to introduce in amounts more than 2–3% [2, 4, 5] and also that the material becomes unstable, especially at higher nitrogen concentrations [6, 7]. Good films of $GaAs_{1-x}N_x$ solid solutions were grown by molecular beam epitaxy (MBE) or metal-organic chemical vapor deposition (MOCVD) in combination with the activated nitrogen flows containing atoms, radicals, and accelerated nitrogen ions generated by high-frequency or plasma sources (plasma assisted MBE/MOCVD) [1–10]. The single-phase solutions with a nitrogen content x = 1.5–3% were grown by many groups of researchers (over a period of 1993 to 2001) [2–5]. The material grown with a maximal nitrogen content x = 15% (1997), 5.6% (2000), and 8% (2002) was reported [8–10]. The maximal nitrogen content, x = 20%, was reached in [6]; however, the material was not single-phase in this case. Of interest are attempts to solve the problem not by growing the films, but by the nitridation of pure GaAs films with low- and medium-energy (0.5–3 keV) beams of molecular and atomic nitrogen ions [11, 12]. In particular, Hecht *et al.* [12] succeeded in implanting up to 29% of nitrogen into a several-nanometer-thick GaAs layer. However, in both the works cited, almost all the implanted nitrogen formed the GaN phase. In this work, we modify GaAs by bombarding it with a 2500-eV beam containing N_2^+ and Ar^+ ions. Our aim is to see whether nanofilms of the $GaAs_{1-x}N_x$ solid solution with a low nitrogen content can be obtained in a specific implantation process in which the layer being modified is subjected to an additional cascade mixing under the action of inert heavy argon ions. It was assumed that this additional action may not only stimulate the chemical reaction with the implanted nitrogen, but also shift the dynamic equilibrium of the reaction toward the single-phase solution. The latter assumption is based on the fact that the formation of separate chemical phases becomes difficult under conditions of intense cascade mixing of atoms and weak room-temperature diffusion. It should be noted that single-phase $GaAs_{1-x}N_x$ solid solutions, even with a minor nitrogen content, are of great interest, since the most noticeable decrease in the band gap occurs at nitrogen concentrations of no more than x = 5%. Experimental data [8] demonstrate that the band gap of the solution decreases from 1.45 eV (x = 0) to approximately 1.1 (x = 5%), 1.05 (x = 10%), and 1.02 eV (x = 15%).

The object under study was a GaAs(100) MBE-grown film several tens of nanometers thick [1]. The sample was placed in the high-vacuum chamber ($P \sim 10^{-10}$ torr) of an LHS-11 Auger electron spectrometer equipped with a hemispherical energy analyzer. The film surface was repeatedly bombarded (etched) by a mixture of N_2^+ and Ar^+ ions with an energy of 2500 eV. Between the etches, the Auger spectra of C, N, O, Ga, and As were recorded. The surface area scanned by the ion beam was knowingly taken larger than that from

1063-7842/03/4807-0885$24.00 © 2003 MAIK "Nauka/Interperiodica"

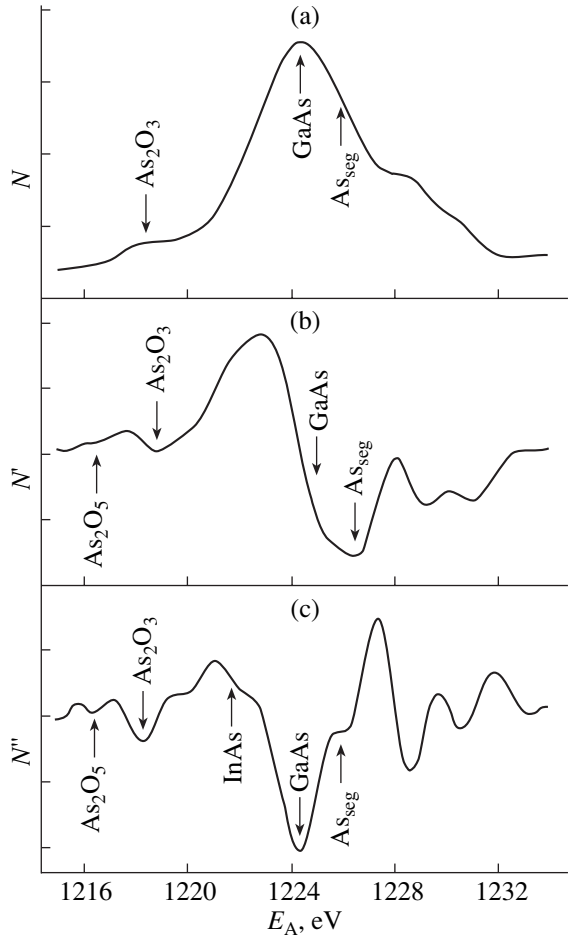

Fig. 1. (a) As [*LMM*] Auger spectrum and its (b) first and (c) second derivatives. The arrows show the Auger peak positions for arsenic in different chemical states.

which Auger electrons were collected. Native oxides and carbon contaminants were totally removed by the argon ion sputtering. The alternate recording of the Auger spectra and ion bombardment made it possible to establish the fact of dynamic equilibrium between the implantation and sputtering; exclude electron-beam-induced oxidation during the long-term irradiation; and, after summation, obtain fairly accurate spectra. As a result, we determined the elemental composition of the modified layer, performed a detailed analysis of the position and shape of the Auger lines, and ascertained the chemical state of the elements incorporated into the layer.

Figures 1–3 present the Auger spectra of arsenic ($L_3M_{45}M_{45}$), gallium ($L_3M_{45}M_{45}$), and nitrogen ($KL_{23}L_{23}$). The spectra were taken with the same relative resolution ($\Delta E/E$ = const). The energy of primary electrons, E_0 = 3000 eV, was high enough to take the spectra of all the elements without electron beam readjustment. In all the spectra, the position of the lines was corrected for the static charge induced by the primary electron beam because of a low sample conductivity. The correction was made by using the energy of the Ga [*LMM*] Auger electron (1066.2 eV), which was obtained on the GaAs surface prepared by cleavage or chemical etching [13]. After the correction, the energy of the As [*LMM*] Auger electron (1224.5 eV) coincided with that found on the cleaved GaAs surface [13]. Both values are close to the energies of Ga [*LMM*] (1065.5 eV) and As [*LMM*] (1224 eV) transitions, which were recently measured *in situ* both on the as-prepared epitaxial GaAs(001) film and on the same film at the early stage of its nitridation by activated nitrogen from an rf source [14]. The atomic percentage of nitrogen and other elements was estimated from the relative intensities of the corresponding Auger lines with regard to the element sensitivity factors. The peak-to-peak signal intensity was determined from the first derivative of the spectrum with the use of the known sensitivity factors obtained in another instrument operating in the constant relative resolution mode [15]. We found that the Ga and As contents in GaAs films are approximately equal to 50%, which confirms the accuracy of these sensitivity factors. It was revealed, in particular, that about 5% of nitrogen atoms were implanted into the GaAs near-surface layer. The introduction of a minor amount of nitrogen into the steady-state implantation–sputtering process was aimed at reducing the phase instability of the forming solid solution. The nitrogen content was small relative to the content of argon in the ion beam. It was also assumed that a small amount of nitrogen will not change the energy position of the Auger lines for the GaAs lattice, making the analysis of the chemical state of the modified layer more accurate.

Obviously, when colliding with the surface, molecular nitrogen ions dissociate, and atomic particles penetrate into the substrate to a depth of several nanometers before they completely lose the kinetic energy. At the end of this process, the nitrogen atoms may occupy matrix interstices or react with the matrix, substituting arsenic. In this bonding process, the matrix temperature is of minor significance, since slowing-down nitrogen atoms (as well as the slow atoms that are accelerated when involved in secondary ion cascades) possess an energy sufficient for such a reaction. Indeed, we found that nitrogen atoms replace arsenic atoms during the implantation. This is evidenced by the As [*LMM*] Auger spectrum (Fig. 1). To reveal the contribution from fine features imposed on the original (true) spectrum, the first and second derivatives of the latter are also shown in Fig. 1. Along with the main GaAs peak (1224.5 eV), the As [*LMM*] spectrum also exhibits an additional component As_{seg} (1226.0 eV), whose intensity is approximately one order of magnitude lower than that of the main peak. The position of this additional component is close to the energy of the As [*LMM*] transition (1225.3 eV), which was evaluated by averaging related data for massive arsenic [13]. This indicates the presence of arsenic segregates on the surface and in the bulk of the layer modified. Most of the segregates are likely

to form on the surface as a result of the diffusion of the substituted arsenic atoms. This is evidenced by the low-intensity peak due to arsenic oxide As_2O_3 (1218.8 eV) [13], which, in our experiment, may form only at the surface by the electron-induced oxidation of the arsenic segregates involving oxygen-containing molecules from the residual atmosphere. The amount of the segregates roughly correlates with the amount of the implanted nitrogen, which also evidences that nitrogen substitutes for arsenic.

When combining with the matrix, nitrogen may form the $GaAs_{1-x}N_x$ solid solution, the GaN phase, a mixture of these two phases in the initial GaAs matrix, or a mixture of the GaN and GaAs phases as a result of the ternary solution decomposition. The following analysis of the gallium and nitrogen Auger spectra suggests that the $GaAs_{1-x}N_x$ solid solution formed is single phase. The initial Ga [*LMM*] spectrum (Fig. 2a), as well as its fourth- and even sixth-order derivatives (Figs. 2b–2d), shows only one GaAs state (1066.2 eV), which actually is the state of the single-phase $GaAs_{1-x}N_x$ solid solution with a minor nitrogen content ($x < 0.05$). Near the Ga [*LMM*] line (1062.7 eV [14]), which corresponds to the GaN phase, no fine features are observed. Taking into account the very low spectral noise level and the position of the GaN line in the immediate vicinity of the GaAs line, we can conclude that the fraction of gallium in the GaN phase does not exceed 5–10%. This estimation follows from the analysis of model spectra with a given contribution from the GaN phase. No signs of metallic gallium (1068.2 eV [13]) and gallium oxide Ga_2O_3 (1061.9–1062.8 eV [13]) are observed in the spectrum. This means that, in spite of the cascade mixing and amorphization of the material, gallium does not change its chemical state, remaining at GaAsN lattice sites.

The almost complete absence of the GaN phase is directly evident from the nitrogen spectrum. Along with the initial N [*KVV*] spectrum, Fig. 3 also shows this spectrum with the background subtracted and its first derivative. The N [*KVV*] peak (383 eV), which corresponds to the $GaAs_{1-x}N_x$ solid solution with a low nitrogen content, dominates in the spectrum. The energy of this transition (383 eV) was obtained in [14] upon studying the early stage of GaAs surface nitridation by activated nitrogen from a high-frequency source. The contribution of the GaN phase to the spectrum is so small that it is hard to separate out even from the known position of the N [*KVV*] line of massive GaN (379.6 eV [14]). The maximal content of this phase estimated from the spectral noise level does not exceed 1–3%.

The high-energy part of the nitrogen spectrum contains one more peak of unknown origin. The spectrum is uniquely resolved into two lines because of the high-energy shoulder present in the initial spectrum (Fig. 1a) and the second minimum in the differential spectrum (Fig. 1c). The energy of the N [*KVV*] Auger electron for

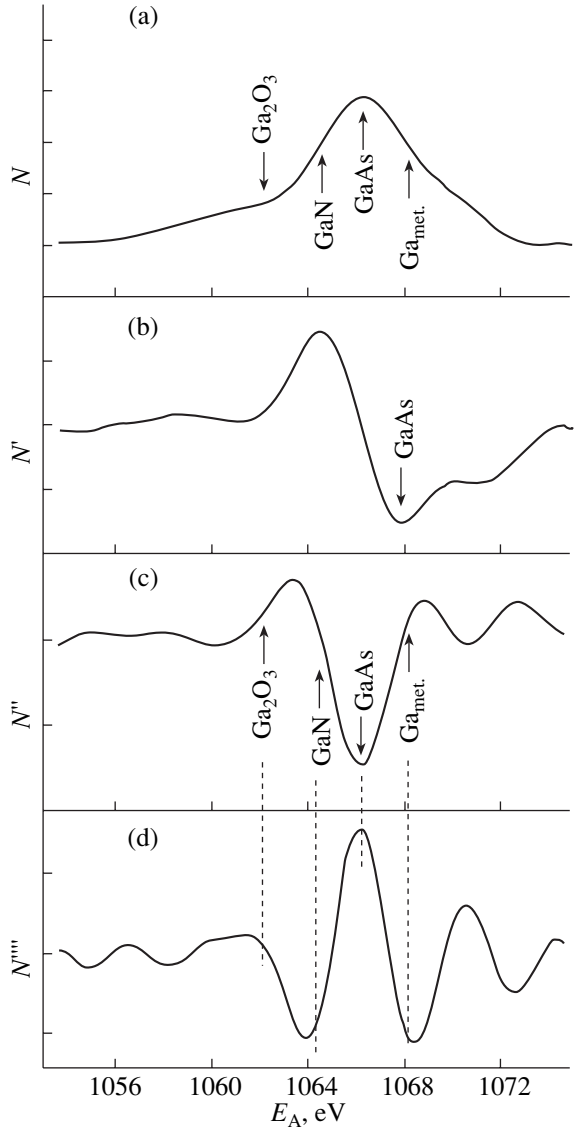

Fig. 2. (a) Ga [*LMM*] Auger spectrum and its (b) first, (c) second, and (d) fourth derivatives. The arrows show the Auger peak positions for gallium in different chemical states.

the unknown line is 5.4 eV higher than the energy of the Auger electron from $GaAs_{1-x}N_x$ and 8.6 eV higher than the energy of the Auger electron from GaN. So high energy shifts are difficult to assign to any nitrogen state chemically bound with matrix atoms, since these shifts considerably exceed normal chemical shifts. Probably, this unknown line can be assigned to molecular nitrogen in the bulk or on the surface of the modified layer. The reason for such an assumption is the following. Hecht *et al.* [12] implanted nitrogen into GaAs and observed the main XPS N1*s* line of GaN (the binding energy of the 1*s* electron is $E_b = 397.4$ eV) and also an additional line ($E_b = 403.8$ eV), which was shifted from the main peak by 6.4 eV and completely disappeared after weak heating of the sample (at 300°C). The very

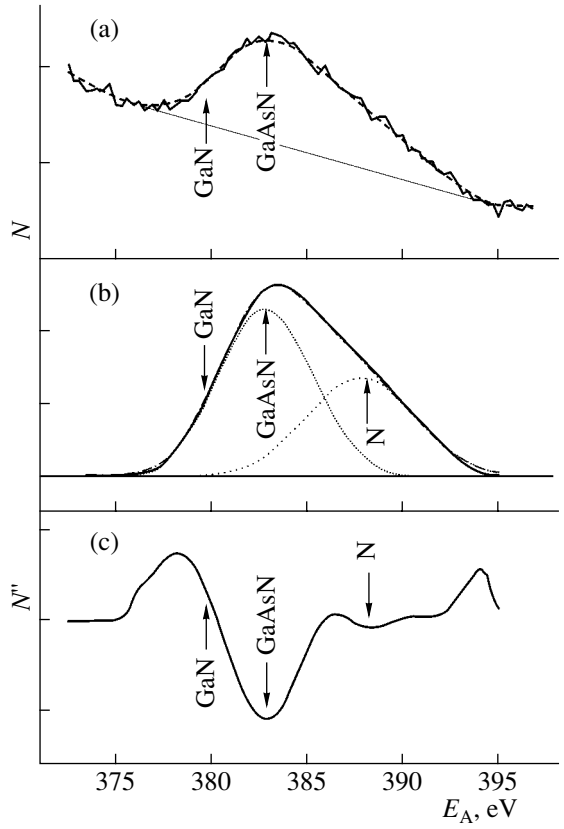

Fig. 3. (a) Initial N [*KVV*] spectrum, (b) the same spectrum without the background, and (c) the second derivative of the spectrum.

low activation energy of the object corresponding to this peak, as well as an analysis of the NEXAFS spectra, made it possible to assign this peak to molecular nitrogen. It is easy to show that the additional high-energy Auger line found in this work corresponds to the additional line of photoelectrons emitted from the inner shell of molecular nitrogen [12]. Indeed, the energy of an Auger electron is equal to the energy difference between the initial state (a vacancy in the 1*s*-shell) and final state (two vacancies in the 2*p* valence shell): $E_A = E_i - E_f = E_b - E(L_{23}L_{23})$. The increase in the binding energy by 6.4 eV in going from GaN to N_2 leads to the same increase in the Auger electron energy. The remaining 2.2 eV may be associated with a reduction of the final state energy due to the increased energy of extraatomic relaxation. It is notable that atomic nitrogen lines were found neither in [12] nor in this work. Apparently, this is because the collision probability for nitrogen atoms in cascade mixing is high and the reaction of molecule formation is exothermic. The relative intensities of the Auger lines for nitrogen (from the solid solution and in molecular form) are 60 and 40%, respectively (Fig. 3). Considering the total amount of nitrogen implanted, we may conclude that the elemental composition of the modified layer is given by the formula $GaAs_{1-x}N_x$, where $x = 0.05 \times 0.6/0.5 = 0.06$.

The modified layer is expected to be considerably amorphized by the argon component of the ion beam. Therefore, the above reasoning concerning the states of the solid solution lattice are valid for short-range order and the character of chemical bonds. However, short-term annealing may recover long-range order and remove segregated arsenic and molecular nitrogen.

Thus, it is shown that the bombardment of GaAs by a beam of low-energy N_2^+ and Ar^+ ions results in the formation of a single-phase $GaAs_{1-x}N_x$ ($x = 0.06$) solid solution layer with a thickness of several nanometers, which contains a low amount of arsenic segregates and molecular nitrogen.

ACKNOWLEDGMENTS

This study was financially supported by the research program "Low-Dimensional Quantum Structures," the research program "Physics of Solid-State Nanostructures" (project no. 97-3-005), and the joint Russian–Ukrainian program "Nanostructures" (project no. 2000-1*D*).

REFERENCES

1. V. M. Ustinov and A. E. Zhukov, Semicond. Sci. Technol. **15**, R41 (2000).
2. A. E. Zhukov, E. S. Semenova, V. M. Ustinov, *et al.*, Zh. Tekh. Fiz. **71** (10), 59 (2001) [Tech. Phys. **46**, 1265 (2001)].
3. S. R. Kurtz, D. Mayers, and J. M. Olsen, in *Proceedings of the 26th IEEE Photovoltaics Spectral Conference, New York, 1997*, p. 875.
4. M. Weyers and M. Sato, Appl. Phys. Lett. **62**, 1396 (1993).
5. M. Sato, J. Cryst. Growth **145**, 99 (1994).
6. J. W. Orton, D. E. Lacklison, N. Baba-Ali, *et al.*, J. Electron. Mater. **24**, 263 (1995).
7. C. T. Foxon, T. S. Cheng, S. V. Novikov, *et al.*, J. Cryst. Growth **150**, 892 (1995).
8. W. G. Bi and C. W. Tu, Appl. Phys. Lett. **70**, 1608 (1997).
9. J. Toivonen, T. Hakkarainen, M. Sopanen, *et al.*, J. Cryst. Growth **221**, 456 (2000).
10. B. F. Moody, P. T. Barletta, N. A. El-Masry, *et al.*, Appl. Phys. Lett. **80**, 2475 (2002).
11. L. A. De Louise, J. Vac. Sci. Technol. A **11**, 609 (1993).
12. J.-D. Hecht, F. Frost, D. Hirsch, *et al.*, J. Appl. Phys. **90**, 6066 (2001).
13. M. P. Sikh and D. Briggs, *Practical Surface Analysis by Auger and X-ray Photoelectron Spectroscopy* (Wiley, New York, 1983; Mir, Moscow, 1987).
14. I. Aksenov, H. Iwai, Y. Nakada, *et al.*, J. Vac. Sci. Technol. B **17**, 1525 (1999).
15. *Handbook of Auger Electron Spectroscopy*, 3rd ed. (Physical Electronics, Eden Prairie, 1995).

Translated by M. Lebedev

Technical Physics, Vol. 48, No. 7, 2003, pp. 889–892. Translated from Zhurnal Tekhnicheskoĭ Fiziki, Vol. 73, No. 7, 2003, pp. 93–96.

OPTICS, QUANTUM ELECTRONICS

Physicotechnical and Spectroscopic Characteristics of Titanium in Aluminaphosphate Phosphors

I. M. Batyaev and Yu. G. Kobezhikov

Hertzen State Pedagogical University, St. Petersburg, 191186 Russia

Received June 5, 2001; in final form, December 2, 2002

Abstract—Aluminaphosphate glasses with different concentrations of matrix and activator components are prepared and investigated. The physicotechnical and spectral properties of titanium ions, the luminescence kinetics, and the dependence of these properties on the matrix composition in the glasses prepared are studied. The crystal field strength as a function of the Al_2O_3 content is determined. It is suggested that the octahedral coordination of the ions in these glasses is distorted. © *2003 MAIK "Nauka/Interperiodica".*

This study continues a series of works concerning the development of novel inorganic materials activated by ions of titanium and some other 3*d* elements in order to use them as active media in tunable lasers [1–17]. In recent decades, many groups of researchers worldwide have studied more than one hundred of solids, liquids, and gases suitable for the production of lasers [18–24]. However, the search for new cheap optical materials, such as glassy systems activated with ions of 3*d* elements, still remains topical. These materials are viewed as alternatives to crystalline lasing elements of frequency-controlled lasers.

Recently, attention has been focused on titanium(III) ions, which, in contrast to chromium(III) ions, have the structure of electronic levels similar to that in Al_2O_3–Ti^{3+} crystals in a certain range of glass compositions. This makes possible intense *d–d* luminescence from Ti^{3+}-activated glasses via the $^2E \longrightarrow {}^2T_2$ channel. In [12–17], titanium(III) ions were studied as sensitizers of luminescence due to rare-earth elements (REEs).

In glasses, the coordination structure of activating agents considerably affects the spectral properties of these optical materials. For 3*d* activators, this influence is the most noticeable. Therefore, the main purpose of this work was to study the electron absorption spectra, the luminescence spectra, and the kinetics of luminescence quenching in the presence of Ti(III) coordination polyhedra in the $(Al_2O_3)_x(P_2O_5)_{1-x}$ glassy system and to determine the structure and symmetry in the neighborhood of titanium(III) ions.

The structural role of aluminum atoms in glasses was discussed in [25–27]. Most researchers are inclined to believe that, at low Al_2O_3 concentrations, aluminum atoms in the octahedral environment serve as modifiers. In phosphate glasses, the presence of aluminum atoms causes the noticeable shortening of polymer phosphate chains. In the case of titanium glasses, this decreases the degree of covalence of the Ti–O bond.

The melting of $(Al_2O_3)_x(P_2O_5)_{1-x}$–$Ti_2O_3$ glasses, where x is the molar percentage, was carried out in the weakly reducing atmosphere at $T = 1450$°C. The starting mixture was prepared by the method of coprecipitation from solution, which ensures a high homogeneity of the glassy system being synthesized.

The glasses thus prepared had a light blue color, which is typical of trivalent titanium. Spectrometric measurements were performed on samples measuring $10 \times 10 \times (4–5)$ mm. The results of spectral analysis were interpreted in terms of the crystal field theory.

The density of the glasses determined by hydrostatic weighing was found to be 2.66 g/cm^3, and their refractive index was 1.497. By chemical resistance, the glasses were rated in hydrolytic class IV.

The absorption spectra of the glasses were recorded with an SF-20 spectrophotometer in the range 340–900 nm. In the electron absorption spectrum (EAS) shown in Fig. 1, a single broad band with a maximum at 595 nm and a pronounced shoulder at 660–770 nm is seen. The absorption band half-width is 8620 cm^{-1}. The fact that it is 2000–2500 cm^{-1} larger than in the crystals is apparently related to structural disordering in the glassy matrix. Compared to the spectra of titanium in sapphire crystals, which have a maximum at about 500 nm, our spectra are shifted to the red region, their maximum being at 595 nm.

The samples exhibited intense luminescence at 700–1000 nm. At a Ti^{3+} concentration of 0.5 wt %, the mean time of luminescence is 10 μs. At a Ti^{3+} content of 1.5 wt %, the excited state lifetime dropped by half. In the luminescence spectrum (Fig. 2) excited by a helium–neon laser (λ = 632 nm) at a temperature of 300 K, a shoulder in the short-wave region at λ = 800 nm with a maximum at λ = 890 nm was observed. The intensity of this shoulder diminishes as the titanium content was increased from 0.5 to 1.5%. This is probably associated with concentration quenching.

1063-7842/03/4807-0889$24.00

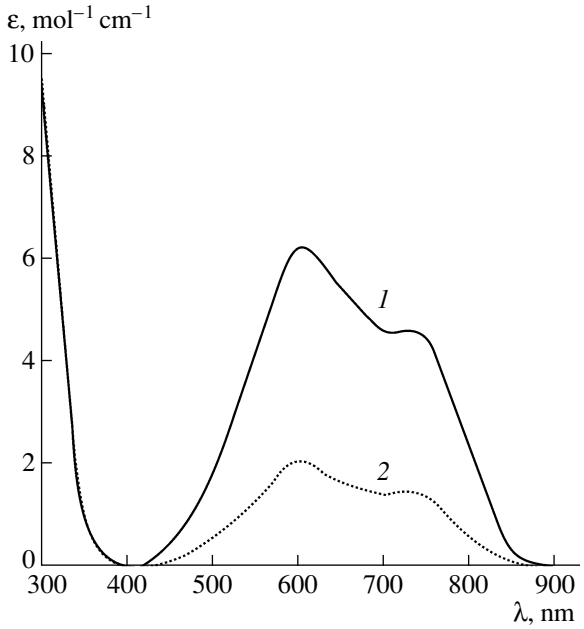

Fig. 1. Absorption spectrum of the $25Al_2O_3$–P_2O_5–Ti^{3+} glass for a titanium concentration of (*1*) 0.5 and (*2*) 1.5 wt %.

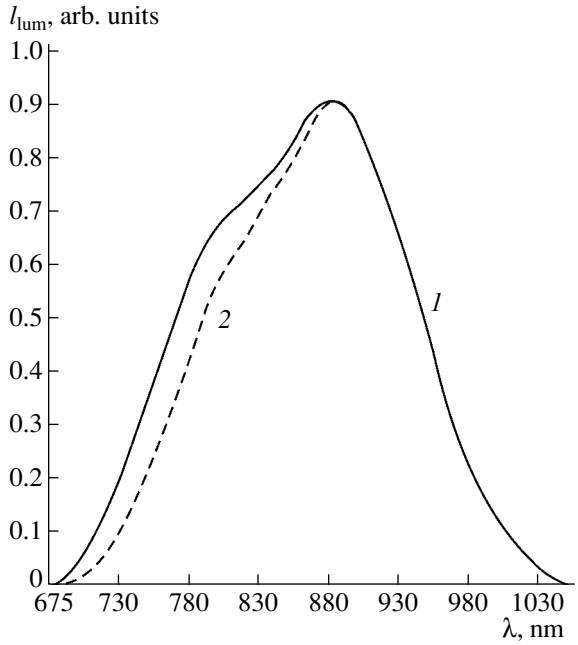

Fig. 2. Luminescence spectrum of the $25Al_2O_3$–P_2O_5–Ti^{3+} glass for a titanium concentration of (*1*) 0.5 and (*2*) 1.5 wt %.

Analysis of the observed bands and energy levels of the Ti(III) ions in different symmetries [28–30] suggests that titanium(III) in the glass has an octahedral coordination. The pronounced shoulder in the visible spectral range testifies to a considerable distortion of the octahedral structure of the [TiO_6] chromophore. This may be attributed to the effect of disordered metaphosphate groups, which produce fields of heavily distorted symmetry. From the EAS data, the crystal field strength (10 Dq) was found to increase from 16 807 to 17 212 cm^{-1} with x increasing from 0.25 to 0.30, and the split of the excited ^2E level into the multiplets $^2A_1$ and $^2B_1$ was found to be 3292 cm^{-1} (at $x = 0.25$). Compared with Al_2O_3–Ti^{3+} crystals, the value of 10 Dq in the Al_2O_3–P_2O_5–Ti^{3+} glass is lower by about 3400 cm^{-1}, which confirms the significant tetragonal distortion of the [TiO_6] chromophore.

Thus, according to the titanium energy level diagram found experimentally, we (for $x = 0.25$) assign to the $^2A_1 \longrightarrow {}^2E$ transition an energy gap of 11 235 cm^{-1}. Next, the shoulder indicates the split of the lower ^2E doublet into two singlets separated by an energy gap of 1015 cm^{-1}. This split results not from spin–orbit interaction but from the low symmetry; otherwise, the split of the ground level $^2T_2$ would be about 200 cm^{-1}. The complete Ti^{3+} energy level diagram in the glass under study is given in Fig. 3.

Considering that the positions of the EAS bands of Ti(III) ions in all phosphate systems are identical and coincide with their positions in $NaPO_3$ [31], and also

Table 1. Spectral characteristics of Ti^{3+} ions in glasses

Glass composition	U_{max}, cm^{-1}	Splitting constant, cm^{-1}	$U_{1/2}$, cm^{-1}	ε_{max}, cm^{-1} mol^{-1}	Oscillator strength $\times 10^{-4}$
$25Al_2O_3$–$75P_2O_5$	16 807	3292	8620	6.2	7.5
Ga_2O_3–P_2O_5	17 241	3037	5493	10.85	2.5
Na_2O–Ga_2O_3–P_2O_5	17 875	3551	5493	12	2.96
Na_2O–ZnO–Ga_2O_3–P_2O_5	17 543	3298	5487	10.9	2.53
K_2O–Al_2O_3–P_2O_5	17 442	–	5820	10	3.4
Al_2O_3 crystals	20 410	2230	4345	–	–

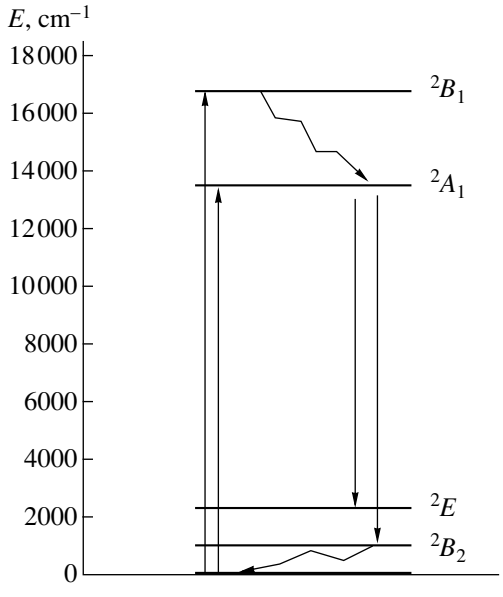

Fig. 3. Titanium(III) energy levels in the $25Al_2O_3$–P_2O_5–Ti^{3+} glass at 300 K.

the fact that the position and shape of the fundamental band in the glass remains unchanged, one may conclude that Ti(III) ions are in all cases coordinated by $(PO_3)_n$ chains.

The basic spectral characteristics of the Al_2O_3–P_2O_5–Ti^{3+} glass and those for several phosphate glasses activated with Ti(III) are listed in Table 1.

Thus, the spectral analysis of the optical material obtained indicates the distorted octahedral coordination of titanium atoms in the glass. The neighborhood of Ti^{3+} consists of $(PO_3^-)_n$ polymer phosphate chains. A distinctive feature of the glass is a wide spectral range of luminescence in near IR (luminescence band half-width $\Delta\lambda$ = 200 nm), exceeding the luminescence band half-width of titanium in other glassy matrices. In this phosphor, four-level lasing occurs, thereby making it possible to create a new glass laser frequency-controlled in a wide range. The complete removal of degeneracy allows one to use titanium(III) as a structure probe to determine the symmetry of the neighborhood. The basic spectral characteristics and behavior of the crystal–glass structural transition are in general similar to earlier results obtained for phosphate glasses (Tables 1, 2).

Table 2. Quenching time of titanium(III) luminescence in various glassy systems

Glass composition	τ_{lum}, μs	References
$25Al_2O_3$–$75P_2O_5$	10	
Ga_2O_3–P_2O_5	6	[6, 7]
Na_2O–Ga_2O_3–P_2O_5	8	[6, 8]
Na_2O–ZnO–Ga_2O_3–P_2O_5	7	[6, 8]
K_2O–Al_2O_3–P_2O_5	5	[3, 4]

REFERENCES

1. I. M. Batyaev and Yu. G. Kobezhikov, Pis'ma Zh. Tekh. Fiz. **22** (11), 81 (1996) [Tech. Phys. Lett. **22**, 472 (1996)].
2. I. M. Batyaev and Yu. G. Kobezhikov, Opt. Spektrosk. **85**, 68 (1998) [Opt. Spectrosc. **85**, 60 (1998)].
3. I. M. Batyaev and S. B. Sukhanov, Opt. Spektrosk. **72**, 1367 (1992) [Opt. Spectrosc. **72**, 765 (1992)].
4. S. B. Sukhanov, Cand. Sci. (Tech.) Dissertation (State Pedagogical University, St.-Petersburg, 1994).
5. I. M. Batyaev and I. V. Golodova, Opt. Spektrosk. **75**, 69 (1993) [Opt. Spectrosc. **75**, 41 (1993)].
6. I. V. Golodova, Cand. Sci. (Tech.) Dissertation (State Pedagogical University, St.-Petersburg, 1994).
7. I. M. Batyaev and I. V. Golodova, Opt. Spektrosk. **77**, 54 (1994) [Opt. Spectrosc. **77**, 45 (1994)].
8. I. M. Batyaev and I. V. Golodova, Opt. Spektrosk. **78**, 468 (1995) [Opt. Spectrosc. **78**, 421 (1995)].
9. I. M. Batyaev, I. V. Golodova, S. V. Levshin, *et al.*, Opt. Spektrosk. **78**, 257 (1995) [Opt. Spectrosc. **78**, 228 (1995)].
10. I. M. Batyaev and E. B. Kleshchinov, Opt. Spektrosk. **81**, 823 (1996) [Opt. Spectrosc. **81**, 753 (1996)].
11. I. M. Batyaev and E. B. Kleshchinov, Zh. Obshch. Khim. **67**, 1207 (1997).
12. I. M. Batyaev and S. B. Sukhanov, Pis'ma Zh. Tekh. Fiz. **20** (10), 38 (1994) [Tech. Phys. Lett. **20**, 403 (1994)].
13. I. M. Batyaev and E. B. Kleshchinov, Pis'ma Zh. Tekh. Fiz. **22** (12), 34 (1996) [Tech. Phys. Lett. **22**, 494 (1996)].
14. I. M. Batyaev and E. B. Kleshchinov, Opt. Spektrosk. **83**, 767 (1997).
15. I. M. Batyaev and E. B. Kleshchinov, Pis'ma Zh. Tekh. Fiz. **23** (21), 7 (1997) [Tech. Phys. Lett. **23**, 820 (1997)].
16. E. B. Kleshchinov, Cand. Sci. Dissertation (State Pedagogical University, St.-Petersburg, 1997).
17. I. M. Batyaev, A. M. Tinus, and E. B. Kleshchinov, Pis'ma Zh. Tekh. Fiz. **24** (3), 38 (1998) [Tech. Phys. Lett. **24**, 97 (1998)].
18. *Handbook of Lasers*, Ed. by A. M. Prokhorov (Sov. Radio, Moscow, 1978).
19. P. F. Moulton, Proc. IEEE **80**, 348 (1992).
20. G. S. Kruglik, G. A. Skripko, A. P. Shkadarevich, *et al.*, Kvantovaya Élektron. **13**, 1207 (1986).
21. D. V. Bakin, L. M. Drozhin, Yu. I. Krasilov, *et al.*, Opt. Spektrosk. **62**, 891 (1987) [Opt. Spectrosc. **62**, 530 (1987)].

22. V. S. Burakov, A. A. Dmidovich, V. I. Kravchenko, *et al.*, Kvantovaya Élektron. **18**, 5 (1991).
23. N. E. Alekseev, V. P. Gapontsev, M. E. Zhabotinskiĭ, *et al.*, *Laser Phosphate Glasses* (Nauka, Moscow, 1980).
24. A. P. Kuznetsov, S. G. Lunter, S. I. Nikitina, *et al.*, Zh. Prikl. Spektrosk. **56**, 90 (1992).
25. E. I. Galant, A. L. Reĭshakhrit, and M. P. Tolstoĭ, Opt. Spektrosk. **31**, 266 (1971).
26. V. I. Mikhaĭlov, T. S. Zhukova, and G. I. Artamonova, Fiz. Khim. Stekla **7**, 718 (1981).
27. O. A. Gladushko, V. V. Gorbachev, and T. A. Zibarova, Fiz. Khim. Stekla **8**, 113 (1982).
28. S. V. Volkov and K. V. Yatsimirskiĭ, *Spectroscopy of Molten Salts* (Naukova Dumka, Kiev, 1977).
29. A. B. P. Lever, *Inorganic Electronic Spectroscopy* (Elsevier, Amsterdam, 1968).
30. S. V. Volkov, V. I. Shapoval, N. I. Buryak, *et al.*, Zh. Neorg. Khim. **25**, 2993 (1980).
31. N. I. Buryak, V. A. Bandur, S. V. Volkov, *et al.*, Teor. Eksp. Khim. **25**, 610 (1989).

Translated by B. Kalinin

Technical Physics, Vol. 48, No. 7, 2003, pp. 893–900. Translated from Zhurnal Tekhnicheskoĭ Fiziki, Vol. 73, No. 7, 2003, pp. 97–104.

ACOUSTIC, ACOUSTOELECTRONICS

Reflection and Refraction of Acoustic Waves from the Insulator–Magnetoacoustic Material Interface

M. M. Karpuk*, D. A. Kostyuk, Yu. A. Kuzavko***, and V. G. Shavrov*****

** Politechnica Kostalinska, 75-620 Koszalin, Poland*

*** Brest State Technical University, Brest, 224017 Belarus*

**** Institute of Radio Engineering and Electronics, Russian Academy of Sciences, Mokhovaya ul. 11, Moscow, 103907 Russia*

Received September 3, 2002; in final form, January 29, 2003

Abstract—The reflection and refraction of longitudinal and transverse acoustic waves by the plane interface between an insulator and an easy-plane antiferromagnet undergoing a magnetic-field-induced orientational phase transition are analyzed. The angles of refraction, as well as all four coefficients of wave conversion, can be effectively controlled by varying the field. Conditions for the appearance of the critical angles of internal reflection and the effect of the magnetic field on these angles are considered. A glancing wave radiated into the material is shown to be a possibility near the phase transition. *© 2003 MAIK "Nauka/Interperiodica".*

When a plane monochromatic elastic wave of certain polarization crosses the interface between two solids, three waves on either side generally appear. The case of two isotropic media is the simplest, since the incident wave gives rise to no more than two waves in either medium and the polarization of these waves is purely longitudinal or purely transverse. In this work, we consider the reflection of elastic waves by the insulator–antiferromagnet interface. For simplicity, both crystals are assumed to be isotropic in elastic and magnetoelastic (ME) properties. It should be noted that, in magnetically ordered crystals, magnetoelastic interaction becomes stronger near the orientational phase transition (OPT) point, causing the long-wave transverse acoustic oscillation spectrum to change from linear to quadratic at the very OPT point [1]. In this case, the anisotropy of dynamic elastic moduli arises even in elastically and magnetoelastically isotropic magnets, decreasing the velocity of longitudinal and especially transverse sound.

Earlier [2], we considered the reflection of magnetoacoustic waves (MAWs) from the free surface of a semi-infinite easy-plane antiferromagnet in the vicinity of the OPT with the magnetic field **H** applied in the *xy* basal plane of the crystal (**H** ∥ **y**, the OPT point is specified by the condition $H = 0$). This magnet displays a high attenuation of sound near the OPT. Magnets with such a property will be called magnetoacoustic materials (MAMs). In the case considered, the MAM surface borders with a semi-infinite insulating space rather than with a vacuum. The propagation of acoustic waves in such layered structures is expected to exhibit intriguing features.

For antiferromagnets mentioned above, the elastic part of the free energy is given by [1]

$$F_{2y} = \frac{1}{2}\lambda_2 u_{2,ii}^2 + \mu_2 u_{2,ik}^2 - 2\mu_2\zeta u_{2,xy}^2, \qquad (1)$$

where λ_2 and μ_2 are the Lamé coefficients for an MAM; $u_{2,ik}$ is the elastic strain tensor; $\zeta = \varepsilon_{me}^2/\varepsilon_{1k}^2$ is the parameter of ME coupling; $\varepsilon_{me} = g\sqrt{2H_eH_{me}}$ is the ME gap in the spin wave spectrum; g is the gyromagnetic ratio; $\varepsilon_{1k} = \sqrt{\Theta_N^2(ak)^2 + \varepsilon_m^2 + \varepsilon_{me}^2}$ is the energy of low-frequency magnons; $\varepsilon_m = g\sqrt{H(H + H_D)}$ is the magnetic part of the gap, which vanishes at the OPT point ($H = 0$); H_e, H_D, and H_{me} are, respectively, the exchange field, the Dzyaloshinski field, and the field of magnetostriction; Θ_N is the Néel temperature; **k** is the wavevector; and a is the lattice constant.

The first two terms in expression (1) will suffice to describe the elastic properties of an insulator.

The material constants for the constituents of the quartz–hematite layered structure are as follows: $s_{1l} = 5000$ m/s, $s_{1t} = 3800$ m/s, and $\rho_1 = 2650$ kg/m^3 for quartz; $s_{2l} = 6760$ m/s, $s_{2t} = 4200$ m/s, and $\rho_2 = 5290$ kg/m^3 for hematite. The fields were $H_e = 9.2 \times 10^6$ Oe, $H_D = 2.2 \times 10^4$ Oe, and $H_{me} = 0.63$ Oe. Based on this values, the ME part of the gap can be estimated as $\omega_{me} = \varepsilon_{me}/\hbar = 34$ GHz. This means that, for frequencies $\omega \ll \omega_{me}$, which are excited by ultrasonic radiators in practice, the approximation where the dynamics of the spin system is not considered in explicit form and its effect on the acoustic system may be reduced to the appropriate renormalization of the elastic moduli (or,

which is the same, of the velocities of longitudinal, $\tilde{s}_{2l}$, and transverse, $\tilde{s}_{2t}$, sound) in MAMs is valid.

Using expressions for the free energies of the insulator and MAM, one can easily obtain wave equations for mechanical displacements. Solutions to these equations in the form of plane harmonic undamped waves give for the velocities of transverse and longitudinal MAWs [3]

$$\tilde{s}_{2t} = \sqrt{\frac{\mu_2}{\rho_2}(1-\zeta\cos^2 2\alpha)}, \quad (2)$$

$$\tilde{s}_{2l} = \sqrt{\frac{\lambda_2+2\mu_2}{\rho_2}(1-n\zeta\sin^2 2\alpha)}, \quad (3)$$

where the angle α is measured from the negative y direction counterclockwise; $s_{2t} = \sqrt{\mu_2/\rho_2}$ and $s_{2l} = \sqrt{\lambda_2+2\mu_2/\rho_2}$ are the velocities of the transverse and longitudinal sound, respectively, away from the OPT; and $n = \mu_2/\lambda_2 + 2\mu_2 = s_{2t}^2/s_{2l}^2$.

Let a longitudinal acoustic wave coming out from the insulator ($y > 0$) be incident on the insulator–MAM interface at an angle α to the normal to the interface ($y = 0$). This wave gives rise to two, longitudinal and transverse, reflected waves and two, longitudinal and transverse, refracted MAWs. The inverse velocity surfaces, from which one can determine graphically the propagation directions of the reflected and transmitted waves, as well as their velocities, are shown in Fig. 1. For plane harmonic waves, the elastic displacements u_i can be represented as (Fig. 1)

$$\begin{pmatrix} u^{I}_{1l,x} \\ u^{I}_{1l,y} \end{pmatrix} = u^{I}_{1l0}\begin{pmatrix} \sin\alpha \\ -\cos\alpha \end{pmatrix} \times \exp[i(k^{I}_{1l}x\sin\alpha - k^{I}_{1l}y\cos\alpha - \omega^{I}_{1l}t)], \quad (4)$$

$$\begin{pmatrix} u^{R}_{1l,x} \\ u^{R}_{1l,y} \end{pmatrix} = u^{R}_{1l0}\begin{pmatrix} \sin\alpha \\ \cos\alpha \end{pmatrix} \times \exp[i(k^{R}_{1l}x\sin\alpha + k^{R}_{1l}y\cos\alpha - \omega^{R}_{1l}t)], \quad (5)$$

$$\begin{pmatrix} u^{R}_{1t,x} \\ u^{R}_{1t,y} \end{pmatrix} = u^{R}_{1t0}\begin{pmatrix} -\cos\beta \\ \sin\beta \end{pmatrix} \times \exp[i(k^{R}_{1t}x\sin\beta + k^{R}_{1t}y\cos\beta - \omega^{R}_{1t}t)], \quad (6)$$

$$\begin{pmatrix} u^{T}_{2l,x} \\ u^{T}_{2l,y} \end{pmatrix} = u^{T}_{2l0}\begin{pmatrix} \sin\gamma \\ -\cos\gamma \end{pmatrix} \times \exp[i(k^{T}_{2l}x\sin\gamma - k^{T}_{2l}y\cos\gamma - \omega^{T}_{2l}t)], \quad (7)$$

$$\begin{pmatrix} u^{T}_{2t,x} \\ u^{T}_{2t,y} \end{pmatrix} = u^{T}_{2t0}\begin{pmatrix} \cos\delta \\ \sin\delta \end{pmatrix} \times \exp[i(k^{T}_{2t}x\sin\delta - k^{T}_{2t}y\cos\delta - \omega^{T}_{2t}t)], \quad (8)$$

where u_0 and ω are the amplitude and frequency of the waves.

The boundary conditions that describe the continuity of the normal components of the mechanical stress tensor T_{iy} and elastic strains u_i are written in this case as [4]

$$T^{I}_{1l,iy} + T^{R}_{1l,iy} + T^{R}_{1t,iy} = T^{T}_{2t,iy} + T^{T}_{2l,iy}, \quad (9)$$

$$u^{I}_{1l,i} + u^{R}_{1l,i} + u^{R}_{1l,i} = u^{T}_{2t,i} + u^{T}_{2l,i}. \quad (10)$$

Here, *I*, *R*, and *T* stand for incident (longitudinal), reflected, and transmitted waves, respectively, and $i = x, y$. Substituting expressions (4)–(8) and the stress tensor $T_{ij} = \partial F/\partial u_{ij}$ into boundary conditions (9) and (10) yields $\omega^{I}_{1l} = \omega^{R}_{1l} = \omega^{R}_{1t} = \omega^{T}_{2t} = \omega^{T}_{2l} = \omega$ at any time instant t and $k^{I}_{1l,x} = k^{R}_{1l,x} = k^{R}_{1t,x} = k^{T}_{2t,x} = k^{T}_{2l,x} = k_x$ at any point on the plane $y = 0$. From the aforesaid, it follows that the propagation directions of the waves are defined by relationships

$$\frac{\sin\alpha}{s_{1l}} = \frac{\sin\beta}{s_{1t}} = \frac{\sin\gamma}{\tilde{s}_{2l}(\gamma)} = \frac{\sin\delta}{\tilde{s}_{2t}(\delta)}, \quad (11)$$

and can be found from (11) graphically by constructing the surfaces of the inverse phase velocities for all the waves (see Fig. 1).

Relationships (11) in view of (2) and (3) yield expressions for wave conversion angles:

$$\sin^2\beta = a\sin^2\alpha, \quad (12)$$

$$\sin^2\gamma = \frac{4\zeta n\sin^2\alpha + b - \sqrt{(4\zeta n\sin^2\alpha + b)^2 - 16\zeta n\sin^4\alpha}}{8\zeta n\sin^2\alpha}, \quad (13)$$

$$\sin^2\delta = \frac{4\zeta c\sin^2\alpha - 1 + \sqrt{(4\zeta c\sin^2\alpha - 1)^2 - 16\zeta(1-\zeta)c^2\sin^4\alpha}}{8\zeta c\sin^2\alpha}, \quad (14)$$

where

$$a = \frac{s_{1t}^2}{s_{1l}^2}, \quad b = \frac{s_{1l}^2}{s_{2l}^2}, \quad c = \frac{s_{1l}^2}{s_{2t}^2}.$$

Figures 2 and 3 show the angles of refraction γ and δ vs. angle of incidence α for various magnetic fields. It is seen that the angles of refraction for the longitudinal and transverse MAWs arising in the MAM can be

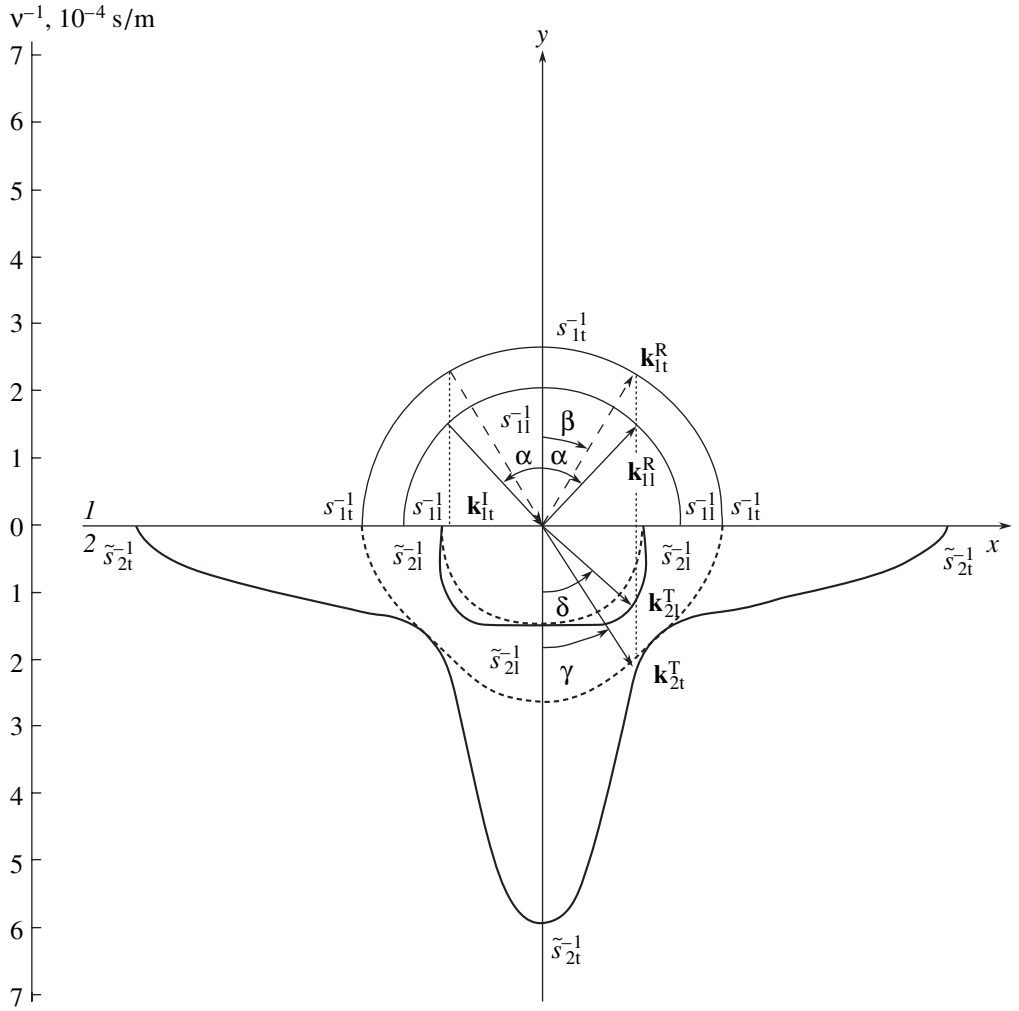

Fig. 1. Geometrical construction of the wavevectors for the incident longitudinal, reflected longitudinal and transverse, and refracted longitudinal and transverse MAWs at the quartz–hematite interface. H = 100 (continuous curve) and 200 Oe (dashed curve).

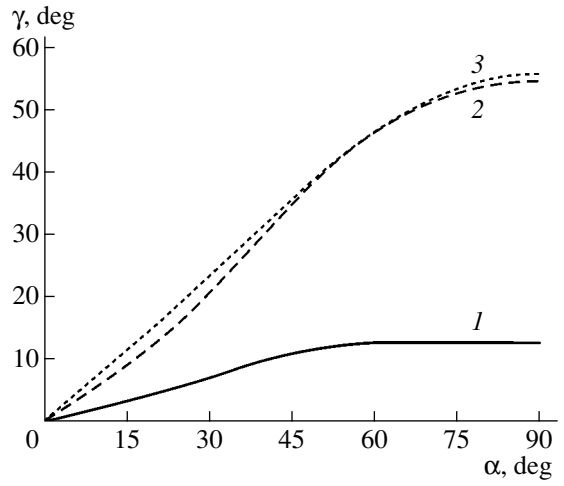

Fig. 2. Angle of refraction γ of the transverse MAW vs. angle of incidence α. H = (*1*) 100, (*2*) 500, and (*3*) 2000 Oe.

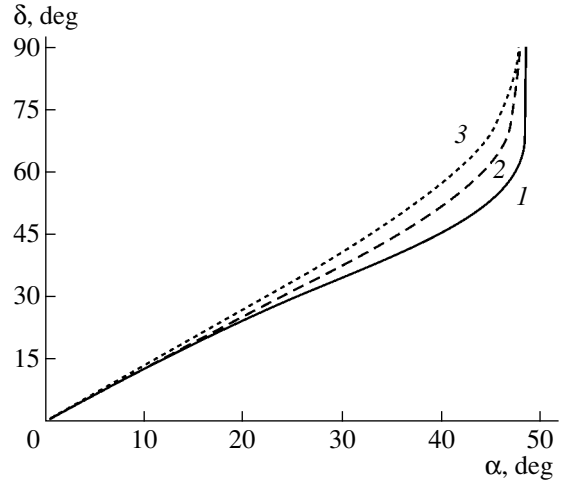

Fig. 3. Angle of refraction δ of the longitudinal MAW vs. angle of incidence of the longitudinal wave. (*1–3*) The same as in Fig. 2.

effectively controlled by varying the applied magnetic field **H**.

Substituting (4)–(8) into Eqs. (9) and (10), one can determine the reflection coefficient for the incident longitudinal wave, $R_{ll} = u^{R}_{1l0}/u^{I}_{1l0}$; the coefficient of its conversion into the transverse wave upon reflection, $R_{tt} = u^{R}_{1t0}/u^{I}_{1t0}$; the coefficient of its transmission into the MAM, $T_{ll} = u^{T}_{2l0}/u^{I}_{1l0}$; and the coefficient of its conversion into the transverse MAW upon refraction, $T_{lt} = u^{T}_{2t0}/u^{I}_{1l0}$. All the four parameters can be found by the Gaussian method from a set of four linear equations derived from boundary conditions (9) and (10):

$$\begin{cases} \mu_1 s_{1l}^{-1}\sin 2\alpha R_{ll} - \mu_1 s_{1t}^{-1}\cos 2\beta R_{lt} \\ + \mu_2(1-\zeta)\tilde{s}_{2l}^{-1}(\gamma)\sin 2\gamma T_{ll} \\ + \mu_2(1-\zeta)\tilde{s}_{2t}^{-1}(\delta)\cos 2\delta T_{lt} = \mu_1 s_{1l}^{-1}\sin 2\alpha, \\ (\lambda_1 + 2\mu_1\cos^2\alpha)s_{1l}^{-1}R_{ll} + \mu_1 s_{1t}^{-1}\sin 2\beta R_{lt} \\ - (\lambda_2 + 2\mu_2\cos^2\gamma)\tilde{s}_{2l}^{-1}(\gamma)T_{ll} + \mu_2\tilde{s}_{2t}^{-1}(\delta)\sin 2\delta T_{lt} \\ = -(\lambda_1 + 2\mu_1\cos^2\alpha)s_{1l}^{-1}, \\ \sin\alpha R_{ll} - \cos\beta R_{lt} - \sin\gamma T_{ll} - \cos\delta T_{lt} = -\sin\alpha, \\ \cos\alpha R_{ll} + \sin\beta R_{lt} + \cos\gamma T_{ll} - \sin\delta T_{lt} = \cos\alpha. \end{cases} \quad (15)$$

We omit solutions to (15) (for R_{ll}, R_{lt}, T_{ll}, and T_{lt}) because of their awkwardness. Note only the conversion of the waves does not occur at normal ($\alpha = 0$) and grazing ($\alpha = 90°$) incidence.

System (15) was solved numerically for specific layered structures. Figures 4–7 show the results of calculation for the quartz–hematite structure at different degrees of closeness to the OPT point.

From (13) and (14), it follows that there may exist two critical angles of incidence $\alpha_{l,\,1cr}$ and $\alpha_{l,\,2cr}$. Starting from $\alpha > \alpha_{l,\,1cr} = \arcsin b^{1/2}$, the longitudinal MAW starts propagating along the interface; then, starting from $\alpha > \alpha_{l,\,2cr} = \arcsin[c/(1-\zeta)]^{1/2}$, the transverse MAW behaves in a similar way. Thus, the threshold value of the angle of total internal reflection from the MAM boundary becomes controllable with an applied magnetic field.

At $\alpha > \alpha_{l,\,1cr}$, the longitudinal MAW, when propagating along the interface, is inhomogeneous: its velocity $\tilde{s}'_{2l}$ and depth of penetration into the MAM Λ_{2i} ($u_{2l} \sim e^{y/\Lambda_{2l}}$) begin to depend on the angle of incidence as

$$\tilde{s}'_{2l} = \frac{s_{1l}}{\sin\alpha}, \quad (16)$$

$$\Lambda_{2l} = \frac{s_{1l}s_{2l}}{\omega\sqrt{s_{2l}^2\sin^2\alpha - s_{1l}^2}}. \quad (17)$$

For $\alpha > \alpha_{l,\,2cr}$, the transverse MAW, propagating along the interface also becomes inhomogeneous: its velocity and depth of penetration are given as

$$\tilde{s}'_{2t} = \frac{s_{1t}}{\sin\alpha}, \quad (18)$$

$$\Lambda_{2t} = \frac{s_{1l}s_{2t}\sqrt{1-\zeta\cos^2 2\alpha}}{\omega\sqrt{s_{2l}^2\sin^2\alpha - s_{1l}^2}}. \quad (19)$$

From (13) and (14), it follows that the heavy distortion of the surfaces of the inverse sound velocity in the MAM causes one more intriguing effect: the radiation of a glancing wave into the material volume, which is observed when ζ exceeds a certain threshold value ζ^*. In this case, the critical angle $\alpha^*_{l,\,cr}$ is given by

$$\alpha^*_{l,\,cr} = \arcsin\sqrt{\frac{b}{4\chi(1-\chi)}}, \quad (20)$$

where $\chi = (\zeta n)^{1/2}$ and depends on the closeness of the MAM to the OPT point.

At $\zeta^* = [2 - b - 2(1-b)^{1/2}]/(4n)$, we have $\alpha^*_{l,\,cr} = 90°$. As the ME coupling parameter ζ grows further, the critical angle $\alpha^*_{l,\,cr}$ decreases. With $\alpha = \alpha^*_{l,\,2}$, the expression under the radical sign in (13) vanishes and becomes negative at $\alpha > \alpha^*_{l,\,cr}$. Formally, this means that $\sin\gamma$ becomes complex and physically that the glancing wave is deflected from its line of travel along the interface toward the insulator volume with the damping coefficient increasing with distance to the interface. It should be noted that this damping is nondissipative (the energy is not absorbed by the medium) and characterizes the structure of a new oscillatory process that also concentrates near the boundary $y = 0$. For the quartz–hematite structure, $\beta_{t,\,lim} = 55°$, $\alpha^*_{l,\,1cr} = 53°$, and $\alpha^*_{2,\,cr}$ is absent at $\zeta^* = 0.1$. With $\zeta = 1$, $\alpha^*_{l,\,cr} = 55°$.

Now we pass to the case where a transverse acoustic wave coming out from the insulator strikes the interface. The reflected and transmitted waves generated are described by expressions (5)–(8) with the substitutions $\alpha \longrightarrow \beta$, $\beta \longrightarrow \alpha$, $\delta \longrightarrow \gamma$, and $\gamma \longrightarrow \beta$, and the transmitted wave is represented as

$$\begin{pmatrix} u^{I}_{1t,\,x} \\ u^{I}_{1t,\,y} \end{pmatrix} = u^{I}_{1t0}\begin{pmatrix} \cos\alpha \\ \sin\alpha \end{pmatrix} \times \exp[i(k^{I}_{1t}x\sin\alpha - k^{I}_{1t}y\cos\alpha - \omega^{I}_{1t}t)]. \quad (21)$$

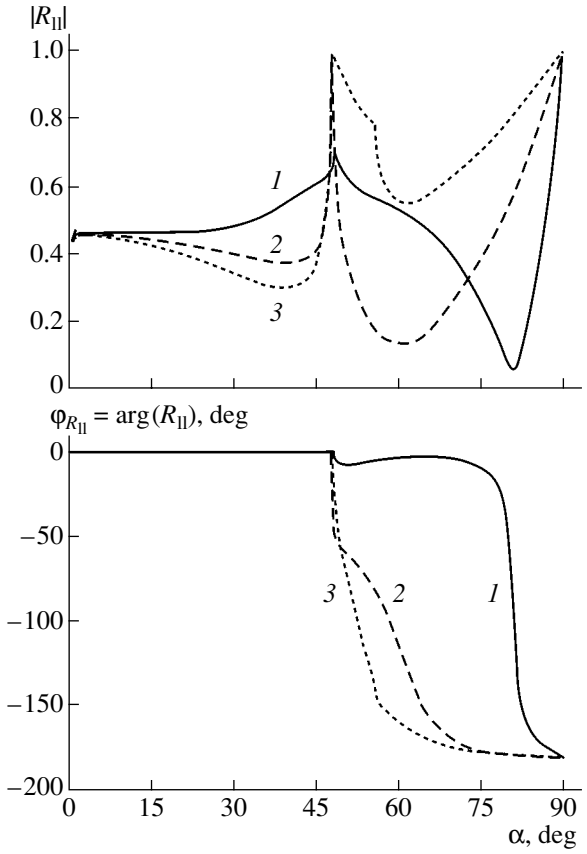

Fig. 4. Magnitude $|R_{ll}|$ and phase $\varphi_{R_{ll}}$ of the reflection coefficient R_{ll} of the longitudinal wave at the quartz–hematite interface vs. angle of incidence α. (*1*–*3*) The same as in Fig. 2.

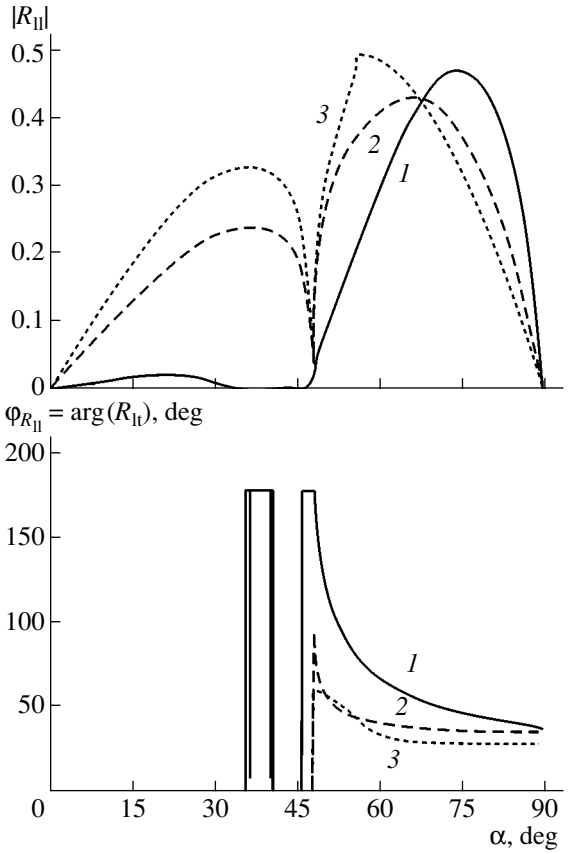

Fig. 5. Magnitude $|R_{lt}|$ and phase $\varphi_{R_{lt}}$ of the coefficient of longitudinal-to-transverse wave conversion R_{lt} at the quartz–hematite interface vs. angle of incidence α. (*1*–*3*) The same as in Fig. 2.

Boundary conditions (9) and (10) are valid if the substitutions $T^{I}_{1l,iy} \longrightarrow T^{I}_{1t,iy}$ and $u^{I}_{1l,i} \longrightarrow u^{I}_{1t,i}$ are made. Proceeding in the same way as above, we find that the propagation directions of the waves are defined by the relationships

$$\frac{\sin\alpha}{s_{1t}} = \frac{\sin\beta}{s_{1l}} = \frac{\sin\gamma}{\tilde{s}_{2l}(\gamma)} = \frac{\sin\delta}{\tilde{s}_{2t}(\delta)}, \qquad (22)$$

and can be determined graphically from these relationships by constructing the surfaces of the inverse phase velocities for all the waves (the wavevector of the incident transverse wave is shown by the dash-and-dot line in Fig. 1).

From (22) in view of (2) and (3), we find the expressions for the angles of wave conversion

$$\sin^2\beta = \frac{\sin^2\alpha}{a}, \qquad (23)$$

$$\sin^2\gamma = \frac{4\zeta n\sin^2\alpha + d - \sqrt{(4\zeta n\sin^2\alpha + e)^2 - 16\zeta n\sin^4\alpha}}{8\zeta n\sin^2\alpha}, \qquad (24)$$

$$\sin^2\delta = \frac{4\zeta n\sin^2\alpha - 1 + \sqrt{(4\zeta n\sin^2\alpha - 1)^2 - 16\zeta(1-\zeta)e\sin^4\alpha}}{8\zeta n\sin^2\alpha}, \qquad (25)$$

where

$$d = \frac{s_{1t}^2}{s_{1l}^2}, \quad e = \frac{s_{1t}^2}{s_{2t}^2}.$$

Figures 8 and 9 demonstrate the angles of refraction γ and δ vs. angle of incidence α (according to (24) and (25)) at different degrees of closeness of the MAM to the OPT point. It is seen that the angles of refraction can be effectively controlled with an applied magnetic field **H**. This is especially true for the transverse wave generated in the MAM, the velocity of which at the

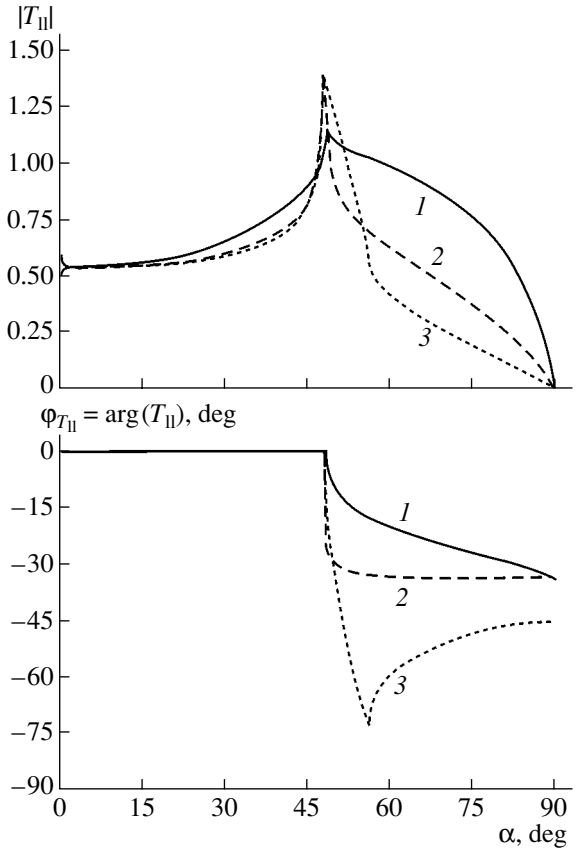

Fig. 6. Magnitude $|T_{ll}|$ and phase $\varphi_{T_{ll}}$ of the transmission coefficient T_{ll} of the longitudinal wave at the quartz–hematite interface vs. angle of incidence α. (*1–3*) The same as in Fig. 2.

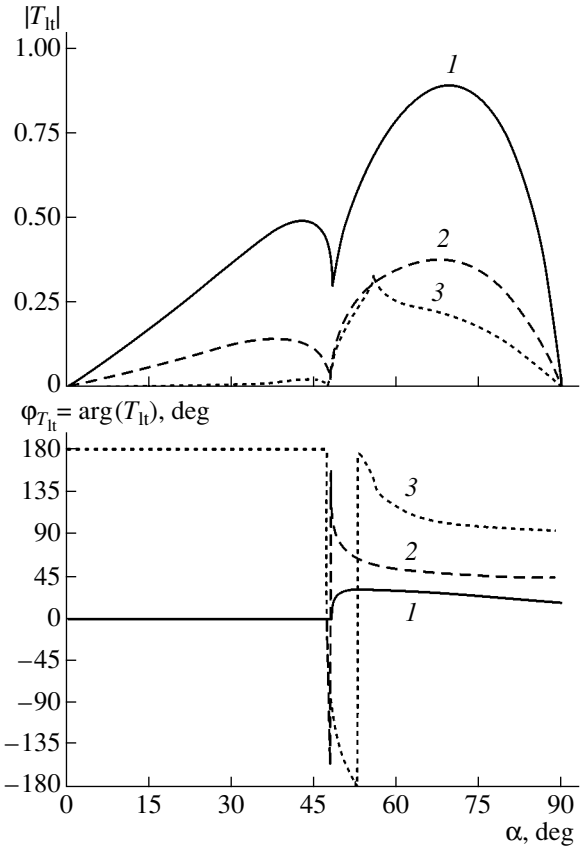

Fig. 7. Magnitude $|T_{lt}|$ and phase $\varphi_{T_{lt}}$ of the coefficient T_{lt} of conversion of the longitudinal wave to the transverse MAW at the quartz–hematite interface vs. angle of incidence α. (*1–3*) The same as in Fig. 2.

OPT point tends to zero.

With (5)–(8) and (21) substituted into the boundary conditions, they represent the set of linear equations

$$\begin{cases} \mu_1 s_{1l}^{-1}\sin 2\beta R_{tl} - \mu_1 s_{1t}^{-1}\cos 2\alpha R_{tt} \\ + \mu_2(1-\zeta)\tilde{s}_{2l}^{-1}(\gamma)\sin 2\gamma T_{tl} \\ + \mu_2(1-\zeta)\tilde{s}_{2t}^{-1}(\delta)\cos 2\delta T_{tt} = \mu_1 s_{1t}^{-1}\sin 2\alpha, \\ (\lambda_1 + 2\mu_1\cos^2\beta)s_{1l}^{-1}R_{tl} + \mu_1 s_{1t}^{-1}\sin 2\alpha R_{tt} \\ - (\lambda_2 + 2\mu_2\cos^2\gamma)\tilde{s}_{2l}^{-1}(\gamma)T_{tl} + \mu_2\tilde{s}_{2t}^{-1}(\delta)\sin 2\delta T_{tt} \\ = \mu_1 s_{1t}^{-1}\sin 2\alpha, \\ \cos\beta R_{tl} + \sin\alpha R_{tt} + \cos\gamma T_{tl} - \sin\delta T_{tt} = -\sin\alpha, \\ \sin\beta R_{tl} - \cos\alpha R_{tt} - \sin\gamma T_{tl} - \cos\delta T_{tt} = -\cos\alpha, \end{cases} \quad (26)$$

where

$$R_{tl} = \frac{u_{1l0}^{R}}{u_{1t0}^{I}}, \quad R_{tt} = \frac{u_{1t0}^{R}}{u_{1t0}^{I}}, \quad T_{tl} = \frac{u_{2l0}^{T}}{u_{1t0}^{I}}, \quad T_{tt} = \frac{u_{2t0}^{T}}{u_{1t0}^{I}}.$$

We omit solutions to (26) (for R_{tl}, R_{tt}, T_{tl}, and T_{tt}) because of their awkwardness. Figures 10–13 show the above coefficients calculated for the quartz–hematite system at different degrees of closeness to the OPT point.

From (23)–(26), it follows that there may exist three critical angles of incidence, $\alpha_{t,\,1cr}$, $\alpha_{t,\,2cr}$, and $\alpha_{t,\,3cr}$. For $\alpha > \alpha_{t,\,1cr} = \arcsin a^{1/2}$, the longitudinal wave in the insulator begins to propagate along the interface; for $\alpha > \alpha_{t,\,2cr} = \arcsin^2\{d^{1/2}\}$, the longitudinal MAW becomes glancing; and for $\alpha > \alpha_{t,\,3cr} = \arcsin^2 c/(1-\zeta)^{1/2}$, the transverse MAW behaves in a similar way. Thus, the threshold value of the angle of total internal reflection from the MAM boundary becomes controllable by an applied magnetic field. At $\zeta > \zeta_{cr} = 1 - c$, total internal reflection disappears.

For $\alpha > \alpha_{t,\,1cr}$, the longitudinal wave, propagating along the interface, is inhomogeneous: its velocity s'_{1l} and penetration depth Λ_{1l} ($u_{1l} \sim e^{y/\Lambda_{1l}}$) begin to depend

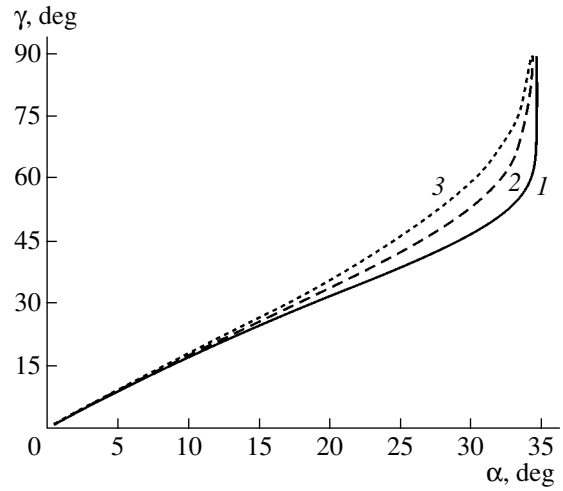

Fig. 8. Angle of refraction γ of the transverse MAW vs. angle of incidence α of the transverse wave. (*1–3*) The same as in Fig. 2.

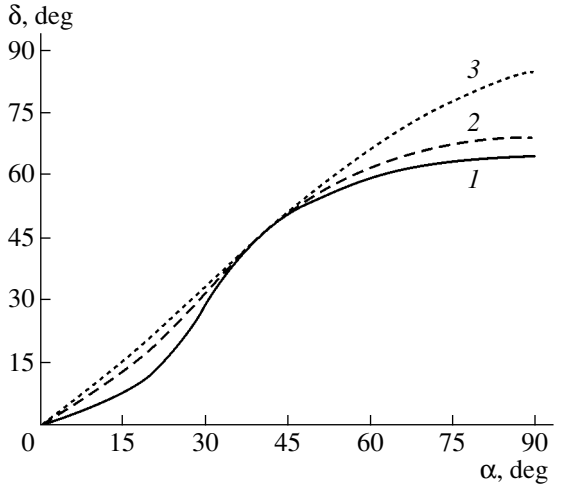

Fig. 9. Angle of refraction δ of the longitudinal wave vs. angle of incidence α of the transverse MAW. (*1–3*) The same as in Fig. 2.

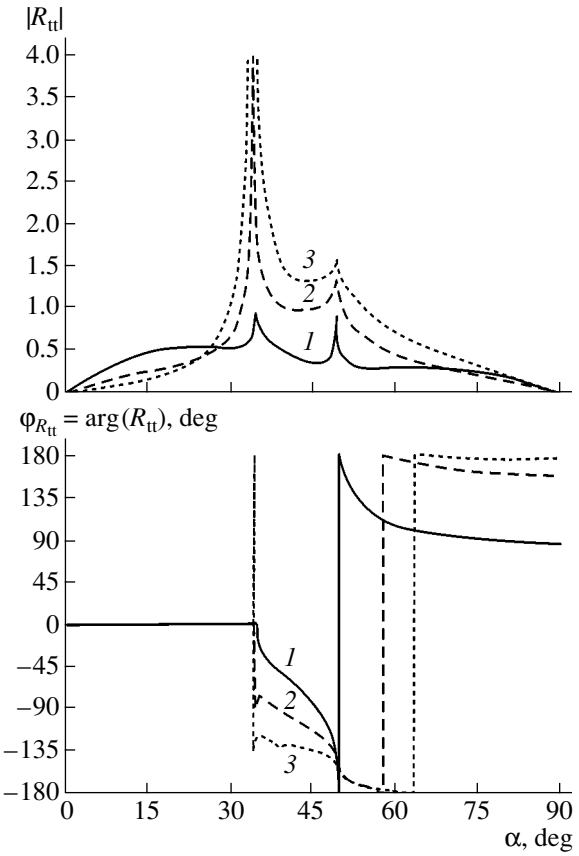

Fig. 10. Magnitude $|R_{tt}|$ and phase $\varphi_{R_{tt}}$ of the reflection coefficient R_{tt} of the transverse wave at the quartz–hematite interface vs. angle of incidence α. (*1–3*) The same as in Fig. 2.

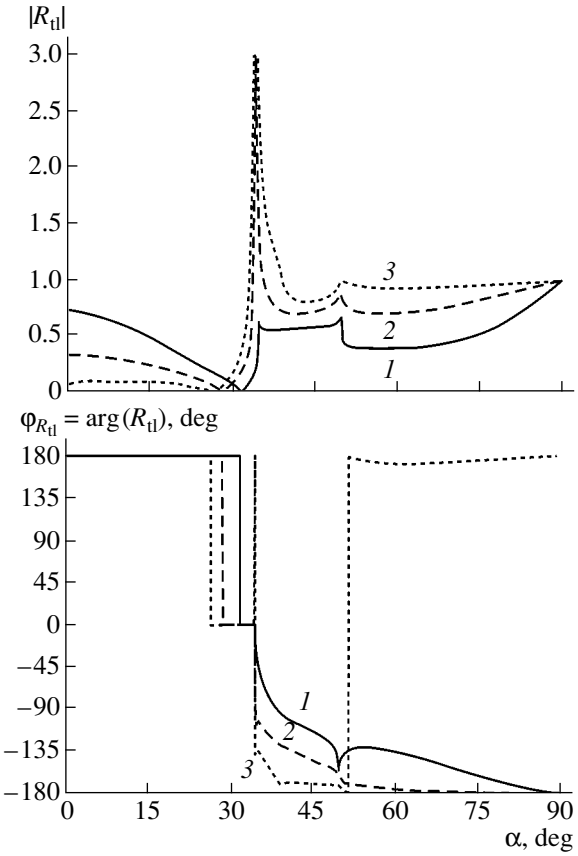

Fig. 11. Magnitude $|R_{tl}|$ and phase $\varphi_{R_{tl}}$ of the coefficient R_{tl} of transverse-to-longitudinal wave conversion at the quartz–hematite interface vs. angle of incidence α. (*1–3*) The same as in Fig. 2.

on the angle of incidence α as follows:

$$s'_{1l} = \frac{s'_{2l}}{\sin\alpha}, \tag{27}$$

$$\Lambda_{1l} = \frac{s_{1l}s_{1t}}{\omega\sqrt{s_{1l}^2\sin^2\alpha - s_{1t}^2}}. \tag{28}$$

At $\alpha > \alpha_{t,\,2cr}$, the longitudinal MAW also becomes

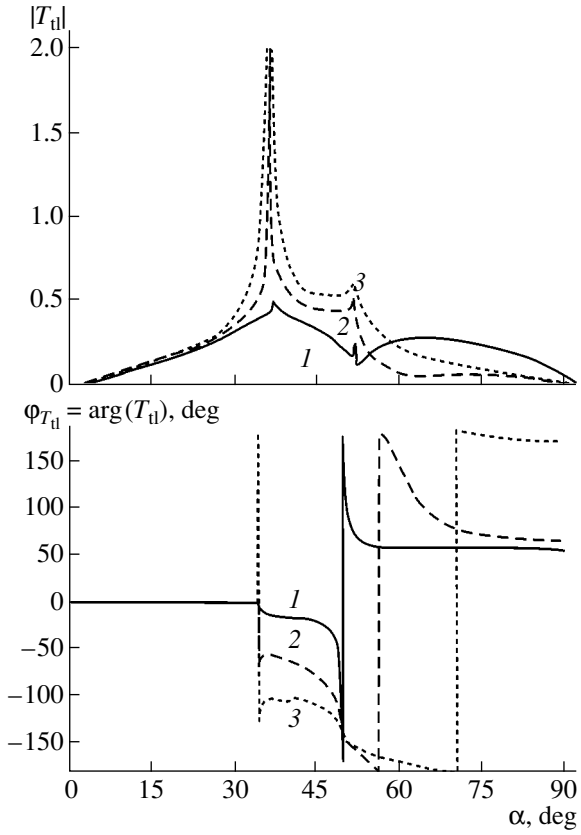

Fig. 12. Magnitude $|T_{tl}|$ and phase $\varphi_{T_{tl}}$ of the coefficient T_{tl} of conversion of the transverse wave to the longitudinal MAW at the quartz–hematite interface vs. angle of incidence α. (*1–3*) The same as in Fig. 2.

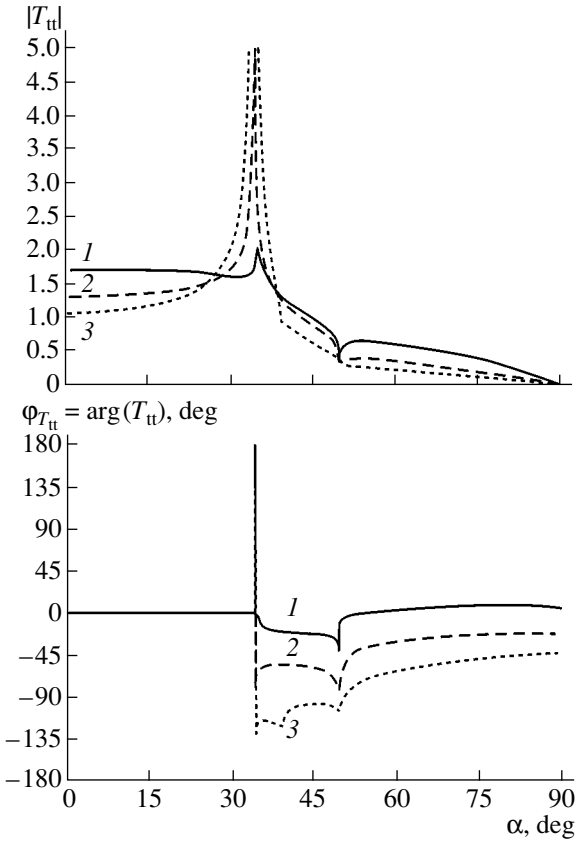

Fig. 13. Magnitude $|T_{tt}|$ and phase $\varphi_{T_{tt}}$ of the transmission coefficient T_{tt} of the transverse wave at the quartz–hematite interface vs. angle of incidence α. (*1–3*) The same as in Fig. 2.

inhomogeneous: its velocity s'_{2t} and penetration depth Λ_{2l} are defined by expressions (16) and (17). At $\alpha > \alpha_{t,\,3cr}$, the transverse MAW behaves in the same way with its velocity and penetration depth found from (18).

From (24) and (25), it follows that the heavy distortion of the surfaces of the inverse sound velocity in the MAM causes the radiation of a glancing wave into the material volume, which is observed when ζ exceeds a certain threshold value ζ*. In this case, the critical angle $\alpha^*_{t,\,cr}$ is defined by (20) where the substitution $b \longrightarrow e$. At $\zeta^* = [2 - e - 2(1 - e)^{1/2}]/(4n)$, we have $\alpha^*_{t,\,cr} = 90°$. As the ME coupling parameter ζ grows further, the critical angle $\alpha^*_{t,\,cr}$ decreases. For the quartz–hematite structure, $\alpha_{t,\,1cr} = 55°$, $\alpha_{t,\,2cr} = 38°$, and $\alpha_{t,\,3cr} = 72°$ at $\zeta = 0$ and 90° at $\zeta = 0.18$. For $\zeta^* \geq 0.31$, $\alpha_{t,\,cr} \leq 90°$; that is, the radiation of the longitudinal magnetostatic wave into the volume begins.

Thus, there appears the possibility of effectively controlling the reflection and refraction coefficients, as well as the mutual conversion of the waves, by a magnetic field. Near the OPT point, the threshold radiation of glancing waves into the MAM volume takes place. According to the relationship between the elastic constants of the constituents, field-controlled total internal reflection from the MAM can be accomplished.

ACKNOWLEDGMENTS

This work was partially supported by the Russian and Belarussian Foundations for Basic Research (grant no. F02R-076).

REFERENCES

1. E. A. Turov and V. G. Shavrov, Usp. Fiz. Nauk **140**, 429 (1983) [Sov. Phys. Usp. **26**, 593 (1983)].
2. Yu. A. Kuzavko and V. G. Shavrov, Akust. Zh. **39**, 1088 (1993) [Acoust. Phys. **39**, 572 (1993)].
3. Yu. A. Kuzavko, H. Roth, and V. Golovko, in *Proceedings of Workshop on Design Methodologies for Signal Processing, Zakopane, 1996*, p. 131.
4. E. Dieulesaint and D. Royer, *Elastic Waves in Solids* (Wiley, New York, 1981; Nauka, Moscow, 1982).

Translated by V. Isaakyan

Technical Physics, Vol. 48, No. 7, 2003, pp. 901–905. Translated from Zhurnal Tekhnicheskoĭ Fiziki, Vol. 73, No. 7, 2003, pp. 105–110.

RADIOPHYSICS

Experimental Study of Complex Dynamics in a Delayed-Feedback Multiple-Cavity Klystron Self-Oscillator

B. S. Dmitriev, Yu. D. Zharkov, D. V. Klokotov, and N. M. Ryskin

Chernyshevsky State University, Moskovskaya ul. 155, Saratov, 410026 Russia

e-mail: knf@sgu.ru

Received March 28, 2002; in final form, January 10, 2003

Abstract—The main characteristics of a delayed-feedback multiple-cavity klystron oscillator with various oscillation modes (single-frequency oscillations, as well as regular and chaotic self-modulations) are studied experimentally. Maps of dynamic modes on the beam current–accelerating voltage plane are presented. Basic scenarios of transition to chaos are considered. As the beam current and amount of feedback increase, regular and chaotic oscillation modes are found to alternate in a complex manner. It is shown that one can significantly increase the power of chaotic oscillations by appropriately tuning the control parameters. © *2003 MAIK "Nauka/Interperiodica".*

INTRODUCTION

The study of complex dynamics and chaos in various vacuum-tube microwave oscillators is a topical problem of modern radiophysics and electronics. Interest in this problem arises, on the one hand, from the necessity to suppress various undesired instabilities and, on the other hand, from the need for high-power wide-spectrum microwave sources, which must operate in chaotic oscillation modes. Such sources may find a number of applications, such as particle linacs, microwave plasma heating, process equipment, and modern data transmission and processing systems that use dynamic chaos.

In these applications, it is very promising to use delayed-feedback multiple-cavity klystron oscillators, which feature a high output power and high efficiency. However, the complex dynamics of such oscillators is still poorly understood. Of special note is the lack of experimental data.

Tentative experimental studies on the chaotic behavior of a multiple-cavity klystron oscillator and its theoretical model that is built around a two-cavity klystron and qualitatively agrees with experiments were considered in [1]. In this paper, we report detailed experimental investigations of a multiple-cavity klystron oscillator operating in single-frequency, quasi-harmonic multifrequency, and chaotic self-oscillation modes.

EXPERIMENTAL SETUP

The schematic of the experimental setup is given in Fig. 1. The object of study is medium-power 10-cm-range commercial klystron *1* with power supply *10*. The klystron uses five double-gap cavities operated in the antiphase oscillation mode. The input cavity is coupled to the catcher through a coaxial feedback loop. Through directional couplers *2*, the feedback loop is connected to crystal detector *6* for observing the signal envelope on oscilloscope *7*, second crystal detector *6* for observing the two-dimensional projection of the phase portrait of an oscillatory process on the screen of oscilloscope *9* by using the delay method, spectrum analyzer *5* for studying the complete spectrum of microwave signals over a wide frequency band, digital frequency meter *8* for measuring the quasi-harmonic oscillation frequency, and thermistor power meter *4* with polarization attenuator *3*. Another polarization attenuator *3* is included in the feedback circuit to control the amount of feedback.

The electrical length of the feedback loop with the dielectric filling equals 105 wavelengths. The loaded Q factor of the klystron's input cavity is $Q_{in} = 250$; that of the catcher, $Q_{out} = 125$. The unloaded Q factor of both cavities is $Q_0 = 460$, and their natural frequency is $f_0 =$

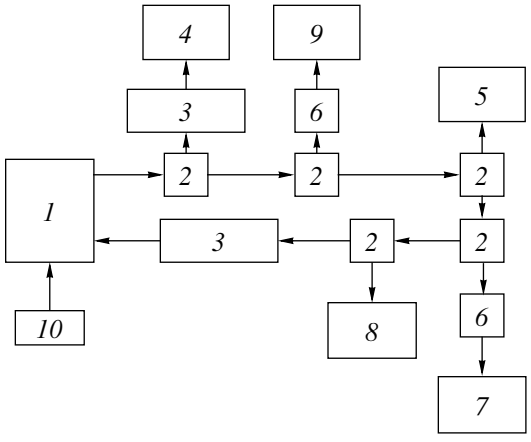

Fig. 1. Schematic of the experimental setup.

1063-7842/03/4807-0901$24.00 © 2003 MAIK "Nauka/Interperiodica"

2800 MHz. The total delay in the feedback loop, which is determined in view of its length, the electron transit time through the drift space, and the *Q* factors of the klystron cavities, is about 0.3 μs. The time constants of the cavities are about 0.05 μs. As control parameters, the setup uses the electron beam current and attenuation in the feedback loop.

Using this setup, one can study the operation of the oscillator by observing the envelope, entire spectrum, and phase portrait of the signal, and measuring the frequency and output power. Thus, the setup provides fairly accurate identification of oscillatory processes, including regular and chaotic self-modulations.

EXPERIMENTAL RESULTS

First, the starting current was studied as a function of accelerating voltage. This dependence specifies the operating range of the accelerating voltage (1000–3000 V). As in other delayed-feedback oscillators (see, e.g., [2]), oscillation zones, which correspond to phase conditions of self-excitation, are discrete. Figure 2 shows the boundaries of the oscillation zones on the beam current (I_0)–accelerating voltage (U_0) plane (without attenuation in the feedback loop). In the range of accelerating voltages shown in Fig. 2, there are five oscillation zones.

The positions of the oscillation zone centers, i.e., U_0 at which the starting current is minimal, can be estimated theoretically from the phase condition of self-excitation. For a multicavity klystron oscillator in the simplest case of synchronous tuning, this condition is

$$m\Theta_0 + \omega_0\delta t = 2\pi n - \pi m/2. \quad (1)$$

Here, $\Theta_0 = \omega_0 l/\sqrt{2\eta U_0}$ is the unperturbed transit angle between two adjacent cavities, ω_0 is the natural frequency of the cavities, δt is the time of signal propagation through the feedback loop, η is the electronic charge, l is the cavity spacing (in the klystron under study, the cavities are equispaced), m is the number of stages (in our case four), and n is an integer. The physical meaning of relationship (1) is straightforward: at optimal tuning, the phase delay due to the feedback loop is an integer multiple of 2π. The second term on the right of (1) reflects the fact that each of the cavities introduces a phase shift of $\pi/2$. In the klystron under study, the intermediate cavities were detuned to increase its efficiency in the amplification mode. A special physical experiment showed that the detuning is small (less than 1%). The positions of the zone centers calculated from formula (1) are in good agreement with the experiment.

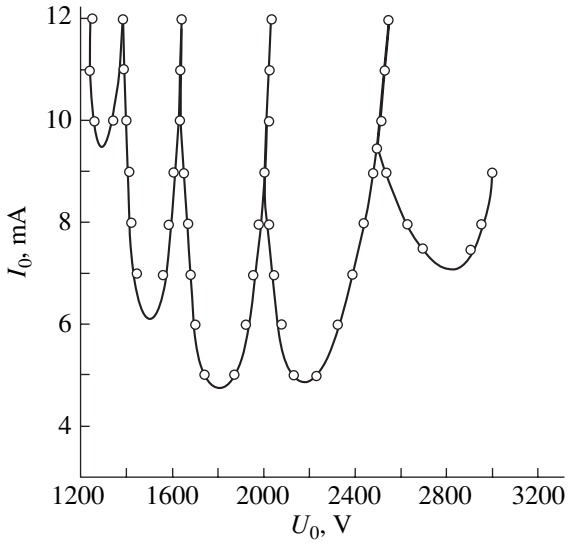

Fig. 2. Boundaries of the oscillation zones on the beam current (I_0)–accelerating voltage (U_0) plane.

As can be seen from Fig. 2, the lowest starting currents are observed in the zones near the middle of the operating voltage range. This is explained as follows. It is known that the klystron gain K depends on the gain parameter [2, 3]

$$\alpha = \rho M^2 I_0 \Theta_0 / 4U_0, \quad (2)$$

which has the meaning of the gain per stage at the resonant frequency. Here, ρ is the characteristic impedance of the cavities and M is the gap factor. In particular, $K \sim \alpha^m$ at the center of the oscillation zone. Then, the amplitude condition of self-excitation can be written in the simple form $\mu\alpha^m > 1$, where μ is the amount of feedback ($0 < \mu < 1$). This condition predicts that the starting current at the center of the zone grows as $U_0^{3/2}$. On the other hand, for double-gap gridless cavities, which were used in the klystron, the parameter M decreases in the low-voltage part of the operating range. Because of this, the starting current starts increasing.

The above reasoning is speculative and explains the experimental results only qualitatively. A rigorous theory that allows for cavity detuning and agreement between experimental data and results of simulations will be published later.

When the beam current exceeds the self-excitation threshold, stationary single-frequency oscillations are observed. Figure 3 plots the (a) power and (b) frequency of the oscillations versus accelerating voltage for several beam currents. At the current 6 mA, only two zones are excited. With increasing current, the power grows, the zones expand, and their number increases (cf. Fig. 2). Simultaneously, the zones change their shape and the power maxima in the zones move toward higher voltages.

A further increase in the current causes the zones to overlap. Near their boundaries, the U_0 dependences of the power and frequency become ambiguous. In these regions, the oscillator is bistable: at the same parameters, one of two adjacent eigenmodes may arise depend-

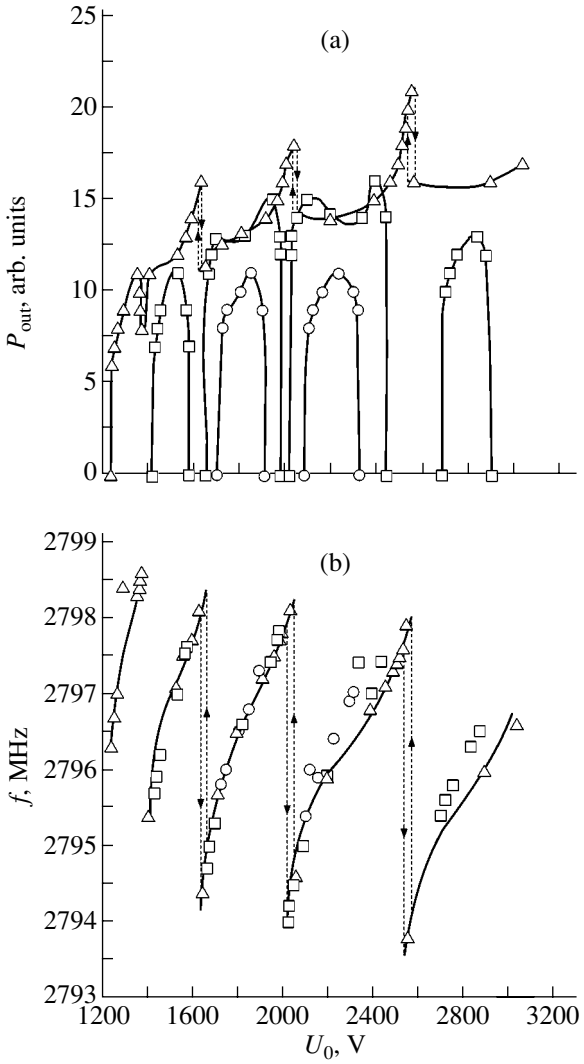

Fig. 3. (a) Power and (b) frequency of the oscillations versus accelerating voltage for the beam current (circles) 6, (squares) 8, and (triangles) 12 mA.

ing on the initial conditions. Such behavior is typical of oscillators with delay (see, e.g., [4–6]). As the accelerating voltage is gradually increased, the oscillator sharply switches from one zone to another, exhibiting hysteretic (Fig. 3). At the points of sharp switching, clear-cut maxima of the output power are observed.

When the current significantly exceeds the self-excitation threshold, the single-frequency mode becomes unstable and changes to the periodic self-modulation regime with the output signal amplitude oscillating about a constant value. Simultaneously, a limit cycle appears smoothly in the phase portrait of the signal envelope and two satellites, which are symmetrically offset from the fundamental frequency by $f_{sm} \approx$ 3.6 MHz, arise in the spectrum. The minimum (threshold) current of self-modulation is $I_{sm} \approx 13$ mA.

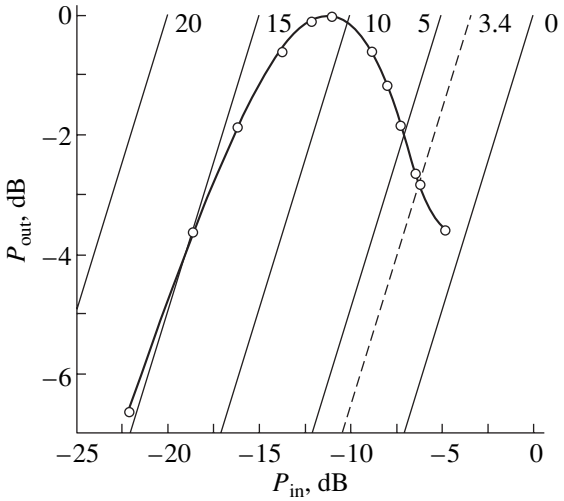

Fig. 4. Amplitude characteristic of the klystron. The straight lines are the lines of constant amount of feedback. The figures by the curves indicate the attenuation in the feedback loop (decibels).

It was noted [1] that, physically, the self-modulation stems from the steeply descending portion in the amplitude characteristic of the amplifier. This portion reflects the rebunching of electrons at strong input signals. Such a self-modulation mechanism is usually called the amplitude mechanism [7–9]. Figure 4 shows the experimental amplitude characteristic of the klystron obtained by the self-excited oscillator method: the output power P_{out} plotted as a function of input power P_{in} on the log–log scale. This figure also shows the feedback isolines $L = P_{out,\,dB} - P_{in,\,dB}$, where $L = -20\log\mu$ is the decibel attenuation in the feedback loop. The points where these lines cross the amplitude characteristic correspond to the power generated in the steady oscillation mode [10]. The regular self-modulation appears at $L = 3.4$ dB: the corresponding isoline crosses the characteristic in the negative-slope portion. This indicates that the amplitude mechanism is actually responsible for the loss of stability.

A further increase in the beam current randomizes the oscillations. As is known, systems with the amplitude self-modulation mechanism usually pass to chaos following the Feigenbaum scenario, i.e., through a number of period-doubling bifurcations (see, e.g., [6–9, 11, 12]). Figure 5 is a map of dynamic modes on the (I_0, U_0) plane, which is divided into regions of oscillations of different types. The map is generated for $L =$ 20 dB and shows the regions of single-frequency oscillations, periodic self-modulation, double- and quadruple-period self-modulation, and chaotic dynamics. The self-modulation regions appear as isolated areas separated by extended segments of single-frequency oscillations. As the beam current grows, some of the zones merge (e.g., near $U_0 \approx 1500$ V in Fig. 5).

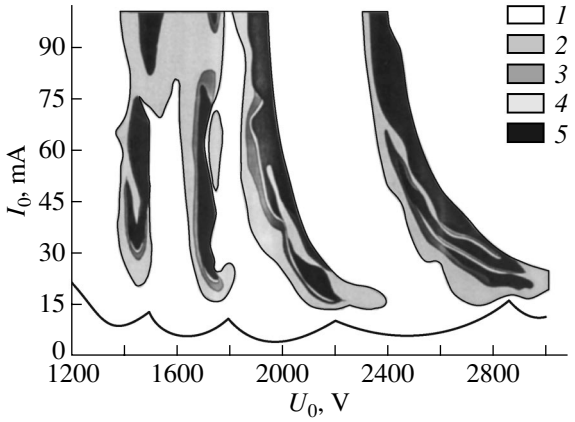

Fig. 5. Map of dynamic modes on the (I_0, U_0) plane: (*1*) single-frequency oscillation, (*2*) periodic self-modulation, (*3*) double-period self-modulation, (*4*) quadruple-period self-modulation, and (*5*) chaotic dynamics.

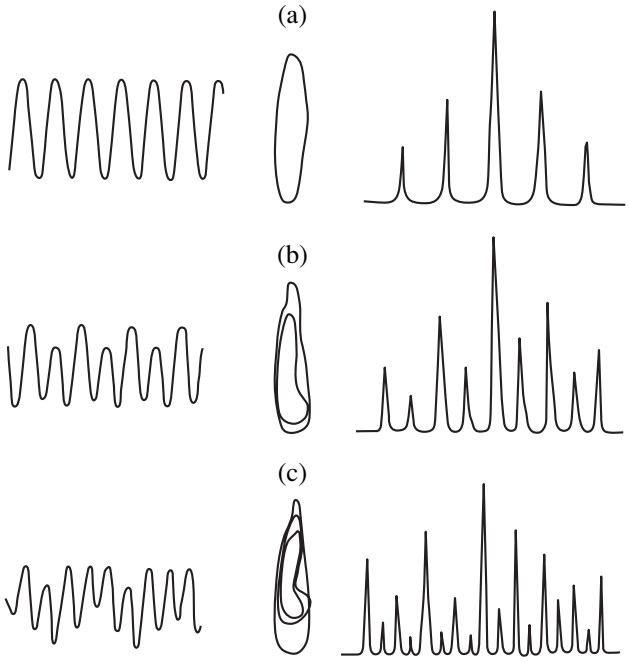

Fig. 6. Envelopes, phase portraits, and spectra of the signals for the attenuation L = (a) 1.7, (b) 0.9, and (c) 0.4 dB in the feedback loop.

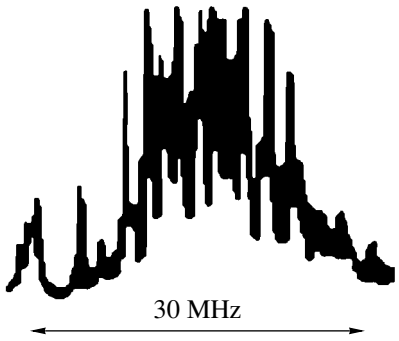

Fig. 7. Oscillation spectrum in the developed chaos regime.

Expectedly, the transition to chaos proceeds largely through period-doubling cascades. Figure 6 illustrates the change in the signal spectrum, phase portrait, and envelope as the system passes to chaos. The control parameter in this case was taken to be the amount of feedback L. Due to fluctuations, no more than three period-doubling bifurcations are readily observed. In Fig. 5, even quadruple-period oscillation regions are very narrow and difficult to detect.

It should be noted that the lines of different bifurcations run in a sufficiently complex manner (which is typical of systems with several control parameters). Therefore, the Feigenbaum scenario may be observed only by properly moving over the parameter plane. If we keep, for example, the accelerating voltage constant and increase the beam current, we may, in general, observe the oscillation modes giving way to one another in an arbitrary sequence. For example, sharp transitions to chaos that exhibit hysteretic phenomena may occur from the regular self-modulation and even single-frequency oscillation regimes. On the other hand, there are accelerating voltage intervals where single-frequency oscillations persist over the available range of currents and even regular self-modulation does not arise.

In the majority of the oscillation zones, the periodic self-modulation areas have the form of narrow "tongues," which penetrate deeply into the chaotic regions. Inside the tongues, the projections of the phase portrait are cycles of topologically different shape. The shape, as a rule, becomes more complicated with increasing beam current. On an initially smooth cycle (like, e.g., the one shown in Fig. 6a), loops are formed. Accordingly, the temporal realization of the output signal also becomes more complex: several local maxima are observed within a period of the oscillations. Simultaneously, the self-modulation frequency decreases. Such behavior is typical of self-excited oscillators with delay (for more detail, see [6]).

The regions with the complex dynamics also contain numerous windows of regular behavior. They form a complex pattern and are not shown in Fig. 5 because of their small size. Near the boundaries where the system passes to chaos, the chaotic oscillation spectrum is pronouncedly irregular with clear-cut maxima at the self-modulation frequencies. At high beam currents, the system starts oscillating with a much more uniform spectrum, which is approximately 32 MHz wide (Fig. 7). In this case, the phase portrait lacks any distinguishable large-scale features. Such a regime, which can be classified as developed chaos, is a distinctive feature of systems with a large number of degrees of freedom and is typical of many other vacuum-tube microwave oscillators [6, 11, 12]. The maximum power generated in this regime was 41 W at an efficiency of 35%.

CONCLUSIONS

A resonant multiple-cavity klystron oscillator is a relatively simple and extremely convenient object for the experimental study of self-sustained chaotic microwave oscillations. The device is a typical delayed-feedback oscillation system and demonstrates the complex behavior inherent in such systems [4–6, 11, 12] (multistability and hysteresis, the complicated shape of limit cycles, multiple alternation of regular and chaotic regimes, transition to developed chaos, etc.). We may expect that this oscillator will join the ranks of conventional models of microwave electronics with a complex dynamics, such as backward-wave oscillators and traveling-wave tubes.

Our experimental results show that various regular and chaotic oscillation modes can be accomplished by appropriately tuning the control parameters (beam current, accelerating voltage, amount of feedback, etc.). The chaotic behavior is observable over a wide range of control parameters. With other oscillators, to observe such a behavior would require designing special mockups (see, e.g., [5, 13]). It is important to note that there are a great number of chaotic regimes characterized by different strange attractors. The fine structure of chaotic oscillations, which will furnish insight into common features of the complex dynamics of distributed systems, is the aim of our further research.

ACKNOWLEDGMENTS

This work was supported by the Russian Foundation for Basic Research (grant no. 03-02-16269), the program “Russian Universities” (grant no. 01.01.021), and CRDF (award no. REC-006).

REFERENCES

1. B. S. Dmitriev, Yu. D. Zharkov, N. M. Ryskin, *et al.*, Radiotekh. Élektron. (Moscow) **46**, 604 (2001).
2. V. N. Shevchik, *Fundamentals of Microwave Electronics* (Sov. Radio, Moscow, 1959; Pergamon, London, 1963).
3. V. I. Gaĭduk, K. I. Palatov, and D. M. Petrov, *Physical Grounds of Microwave Electronics* (Sov. Radio, Moscow, 1971).
4. V. I. Kalinin, N. N. Zalogin, and V. Ya. Kislov, Radiotekh. Élektron. (Moscow) **28**, 2001 (1983).
5. V. A. Kats, Izv. Vyssh. Uchebn. Zaved. Radiofiz. **28**, 161 (1985).
6. N. M. Ryskin and A. M. Shigaev, Zh. Tekh. Fiz. **72** (7), 1 (2002) [Tech. Phys. **47**, 795 (2002)].
7. S. P. Kuznetsov, Izv. Vyssh. Uchebn. Zaved. Radiofiz. **25**, 1410 (1982).
8. Yu. P. Bliokh, A. V. Borodkin, M. G. Lyubarskiĭ, *et al.*, Izv. Vyssh. Uchebn. Zaved. Prikl. Nelineĭnaya Din. **1**, 34 (1993).
9. Yu. P. Bliokh, M. G. Lyubarskiĭ, V. O. Podobinskiĭ, *et al.*, Fiz. Plazmy **20**, 718 (1994) [Plasma Phys. Rep. **20**, 648 (1994)].
10. V. V. Migulin, V. I. Medvedev, E. R. Mustel’, and V. N. Parygin, *Fundamentals of the Vibration Theory* (Nauka, Moscow, 1978).
11. N. M. Ryskin, V. N. Titov, and D. I. Trubetskov, Dokl. Akad. Nauk **358**, 620 (1998) [Dokl. Phys. **43**, 90 (1998)].
12. N. M. Ryskin and V. N. Titov, Izv. Vyssh. Uchebn. Zaved. Prikl. Nelineĭnaya Din. **6**, 75 (1998).
13. B. P. Bezruchko, L. V. Bulgakova, S. P. Kuznetsov, *et al.*, Radiotekh. Élektron. (Moscow) **28**, 1136 (1983).

Translated by A. Khzmalyan

Technical Physics, Vol. 48, No. 7, 2003, pp. 906–913. Translated from Zhurnal Tekhnicheskoĭ Fiziki, Vol. 73, No. 7, 2003, pp. 111–118.

RADIOPHYSICS

Thermal Analysis of Atmosphere–Ocean Interaction by Means of Satellite Microwave Radiometry in the 0.5- and 1.35-cm Resonance Bands

A. G. Grankov

Institute of Radio Engineering and Electronics (Fryazino Branch), Russian Academy of Sciences, pl. Vvedenskogo 1, Fryazino, Moscow oblast, 141190 Russia

e-mail: agrankov@ms.ire.rssi.ru

Received December 17, 2002

INTRODUCTION

Modern diagnostics of large-scale ocean–atmosphere thermal interaction from microwave satellite radiometry data is built upon the idea of using the semiempirical global aerodynamic approach (the so-called bulk formulas), which links the radiative and thermal properties [1–3]. This approach rests on the fact that the basic parameters involved in the bulk formulas (the ocean surface temperature, the temperature and humidity of air, and the wind velocity in near-water atmospheric layers) are responsible (directly or indirectly) for the generation and transformation of the self-microwave radiation from the ocean–atmosphere system (OAS).

In this work, we discuss the efficiency of using the self-microwave radiation intensity of the OAS as a direct characteristic of heat-and-moisture exchange between the ocean and atmosphere on a synoptic (weekly) scale, where the intensity of the ocean–atmosphere interaction in the middle latitudes of the Earth is maximum. Our analysis employs oceanographic, meteorological, and aerological observations made aboard the vessels *Viktor Bugaev*, *Musson*, and *Volna* (State Institute of Oceanography; April, 1990) in the Newfoundland energy-active zone of the North Atlantic region during the NEUFOUEX-88 and ATLANTEX-90 experiments. Based on these data, we calculate the brightness temperature of OAS's microwave radiation in the cm- and mm-wave ranges (by simulating satellite, aircraft, and ship measurements). Also, we consider its dependence on the synoptic variation of vertical turbulent fluxes of evolved and latent heat at the ocean–atmosphere interface. Finally, we compare the heat fluxes recorded in the ship experiments with the microwave radiometry data obtained simultaneously with an SSM/I radiometer aboard the US F-08 satellite. This radiometer was the only instrument for sounding the ocean during the NEUFOUEX-88 and ATLANTEX-90 experiments. The combination of the measurements aboard the *Viktor Bugaev*, *Musson*, and *Volna* with the data of the satellite-borne SSM/I radiometer allowed us to account for the intimate linkage between the OAS's brightness temperature and processes at the ocean–atmosphere interface.

SOLUTION OF THE PROBLEM

From the entire array of data gained afloat, we used only those obtained during the stationary phases of the experiments (March, 1988 and April, 1990). Unlike other phases, these two (i) feature regular oceanographic, meteorological, and aerological observations and (ii) are expected to give the most reliable results on the time evolution of the ocean and atmosphere parameters, since the vessels were anchored within definite areas.

Over that time interval, the vessels made measurements in the Gulf Stream delta and in the eastern branch of the Labrador Current, where the synoptic variability of the ocean and atmosphere parameters is very high [4, 5].

To calculate the radiative properties of the OAS, we use the plane-layer model of radiation. In terms of this model, for observations in the nadir direction from an altitude H, the brightness temperature of the OAS's microwave radiation consists of three components:

$$T_\Sigma^b = T_1^b + T_2^b + T_3^b, \quad (1)$$

where

$$T_1^b = T_s^b \exp(-\tau_\Sigma)$$

is the brightness temperature of the atmosphere-attenuated radiation from the ocean surface (the quantity T_s^b is proportional to the emissivity of the water surface and to its thermodynamic temperature T_s);

$$T_2^b = \int_0^H T(h)\gamma_\Sigma(h)\exp[\tau_\Sigma(h) - \tau_\Sigma(H)]dh$$

is the brightness temperature of the atmosphere's

1063-7842/03/4807-0906$24.00

ascending radiation;

$$T_3^b = \exp[-\tau_\Sigma(H)]R\int_0^H T(h)\gamma_\Sigma(h)\exp[\tau_\Sigma(h)-\tau_\Sigma(H)]dh$$

is the brightness temperature of the atmosphere's descending radiation reflected by the water surface; $T(z)$ is the thermodynamic temperature of the atmosphere at a level z;

$$\tau_\Sigma(h) = \int_0^h \gamma_\Sigma(z)dz$$

is the integral absorption of the radiation by the atmosphere, which depends on the absorption per unit length γ_Σ and the thickness z of the absorbing layer measured from the ocean surface ($z = 0$); and R is the coefficient of reflection of the atmosphere's descending radiation from the water surface.

With this model, we analyzed the daily and synoptic variations of the OAS's brightness temperature in the wavelength range 0.5–5.0 cm at the stationary phases of the ATLANTEX-90 experiment aboard the *Viktor Bugaev*, *Musson*, and *Volna*. From the filed data gathered at the stationary phases, we extracted the following: (i) hourly values of the ocean surface temperature T_s and wind velocity V at the water surface to calculate the brightness temperature of the ocean surface; (ii) the total (integral) moisture content in the troposphere to evaluate the water-vapor-related integral absorption of the underlying surface both with and without cloudiness (the measurements were made aboard the *Volna* at 15–20 min intervals with a set of microwave radiometers (Voeĭkov Main Geophysical Observatory, MGO) at wavelengths of 0.8 and 1.35 cm; (iii) the temperatures T_a, relative humidities q (water vapor pressures e), and pressures P of air (measured at 20 levels between 10 and 16000 m every six hours) to estimate not only the total absorption τ but also the absorption per unit length $\gamma(z)$ in the troposphere, from which refined estimates of the atmosphere's transfer function and, hence, the brightness temperature can be found; and (iv) the estimates of turbulent heat, qh, and moisture, qe, fluxes at the ocean–atmosphere interface, which were calculated in the State Institute of Oceanography by using MGO parametrizations [6] based on hourly observational data for T_s, T_a, V, and e.

The contributions from different layers to the radiation properties of the OAS and their effect on the interplay between the radiative properties and thermal fluxes at the interface on the synoptic scale were evaluated with radiation detectors arranged at different altitudes. In the first case, detectors (microwave radiometers designed for the cm- and mm-wave ranges) with downward-directed antennas were placed in free air to simulate satellite observations. In the second case, detectors with downward-directed antennas were placed at the boundary between free air and the atmospheric boundary layer (a turbulent layer of thickness from 0 to 1000 m), which simulates measurements aboard an aircraft at altitudes of 1000–1500 m above sea level. In the third case, detectors with downward-directed antennas were placed 10–20 m above the ocean–atmosphere interface to simulate observations afloat.

CALCULATION OF THE BRIGHTNESS TEMPERATURE AND COMPARISON WITH HEAT FLUXES

The response of the OAS's microwave radiation field to the variability of heat fluxes at the ocean–atmosphere interface was the most distinct in April 8–13, 1990. Over this period, the variation of the (evolved + latent) heat fluxes were more than 800 W/m^2 for the *Viktor Bugaev*, 500 W/m^2 for the *Musson*, and about 400 W/m^2 for the *Volna* [4, 5]. Among the spectral ranges used to calculate the OAS's brightness temperature (5.4, 5.6, 5.9, 0.8, 1.0, 1.35, 1.6, 3.2, and 5.0 cm), the luminance contrast over this time interval was found to be the greatest in the wavelength range 0.59–1.60 cm, which corresponds to the resonant radiation from (absorption by) atmospheric oxygen and water vapor (Fig. 1).

In the case of the satellite observational data, the OAS's brightness temperature in the ranges of the paramount effect of atmospheric oxygen (5–6 mm) and water vapor (1.35 cm) was calculated with two approaches. The former used the indirect measurements of the integral atmospheric absorption that were made by the MGO's set of microwave radiometers. The latter approach employed direct radiometric data for the temperature, humidity, and pressure of the troposphere measured at different horizons and altitudes varying from 10 to 16000 m. Comparative analysis was of

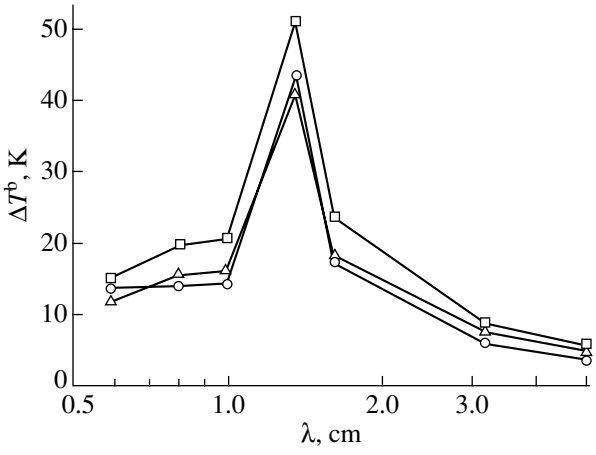

Fig. 1. Spectral dependence of the OAS's luminance contrast ΔT^b in the range 0.5–5.0 cm during the passage of a cyclone (April 8–13) through the places of location of the (–○–) *Viktor Bugaev*, (–△–) *Musson*, and (–□–) *Volna*.

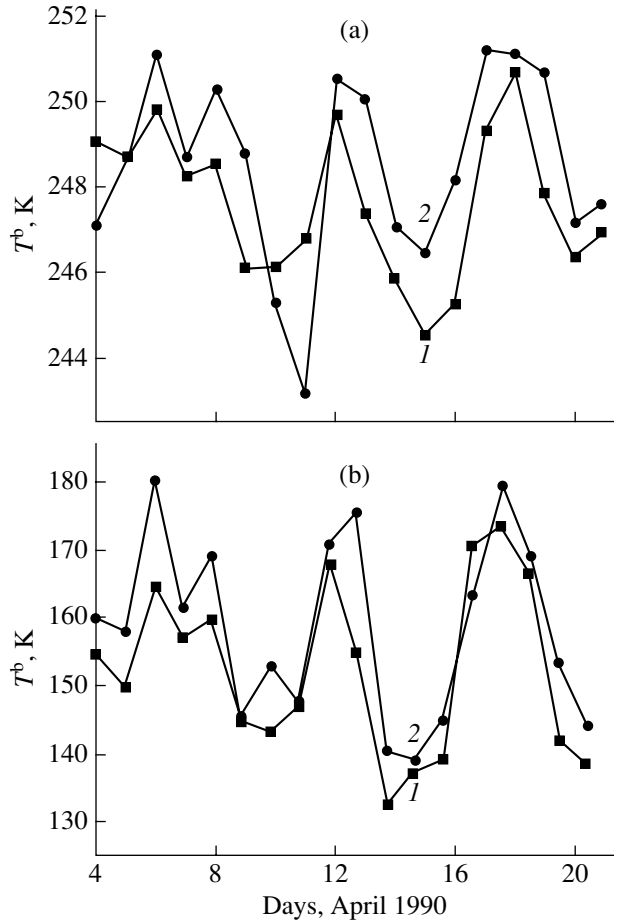

Fig. 2. OAS's brightness temperature calculated from (*1*) integral microwave radiometric and (*2*) aerological (layer-by-layer) measurements of the temperature and humidity properties of the atmosphere at (a) 0.56 and (b) 1.35 cm.

interest, since the time period between measurements that was used to calculate the daily average brightness temperature was 15–20 min in the former case and as long as 6 h in the latter. However, the radiometric measurements carry more detailed information about the vertical distribution of the atmosphere parameters that control the OAS's microwave radiation field.

Comparing the calculation results (Fig. 2) demonstrates that both approaches give the same variation of the daily average brightness temperature at wavelengths of 5.6 mm and 1.35 cm for the stationary phase of the ATLANTEX-90 experiment, although the discrepancy may reach several degrees Kelvin at a wavelength of 5.6 mm and 15–20 K at 1.35 cm.

We studied regression relationships in the form of linear correlations between six-hour samples (Fig. 3) of the total heat flux *qhe* at the ocean–atmosphere interface and the brightness temperature of the OAS's microwave radiation (the simulation of satellite measurements) at wavelengths of (a) 5.9 mm and (b) 1.35 cm (the temperature was calculated from the oceanographic and aerological measurements aboard the *Volna*). It is seen that there is an intimate relation between the synoptic variation of the heat fluxes (recorded by the *Volna*) and the model estimates of the OAS's brightness temperature. For the six-hour samples of the parameters *qhe* and T^b in the resonance ranges of molecular oxygen and atmospheric water vapor, the least absolute error of approximating the total heat flux *qhe* by the brightness temperature T^b is 26–28 W/m^2 for a flux variation amplitude of 320 W/m^2. The relative variations of the regression coefficients c_1 and c_2 are 13–15%, with the regression coefficient c_2 being negative in both cases. This means that the heat flux and the brightness temperature vary in antiphase: an increase in the parameter *qhe* causes T^b to decrease and vice versa. It is remarkable that the intensity variation of the OAS's microwave radiation correlates well with the variation of the heat fluxes in this case, although the accuracy of finding the brightness temperature and especially the heat fluxes is not very high. The relative error involved in model brightness temperature values found under the hydrometeorological conditions of the ATLANTEX-90 experiment is estimated as 5–10%, while that of the heat fluxes determined by the parametrizations [6] may be as great as several tens of percent [4]. This substantiates the idea of using remote microwave radiometry data as natural characteristics of ocean–atmosphere thermal interaction.

Next, we studied the importance (priority) of water surface parameters and parameters of different atmospheric strata in terms of their effect on the interplay between the heat-and-moisture exchange characteristics and the microwave radiation of the system on the synoptic time scale. To this end, the regression analysis of the relationships between the daily average values of the brightness temperature T^b and the total heat flux *qhe* was made based on the data gathered at the ATLANTEX-90 stationary phase. We used the ordered elimination method to reveal the contribution of one or another parameter simultaneously to the heat exchange process and the radiation in different parts of the microwave range. Table 1 lists the errors due to the approximation of the total heat fluxes *qhe* by the brightness temperature of the system's radiation in the wavelength range 0.56–3.2 cm. Here, the column *d* takes into account the synoptic variations of all the basic thermodynamic parameters of the OAS (T_s, T_a, V, and Q). In the columns d_T_s, d_V, d_T_a, and d_Q, the effects of the ocean surface temperature T_s, the water-wind velocity V, the water-air temperature T_a, and the total moisture content Q, respectively, are excluded.

The results of the analysis show that the parameters T_a and Q should be taken into account in the first place when a correlation between the heat-and-moisture exchange parameters and the self-microwave radiation intensity in the ocean–atmosphere system is established

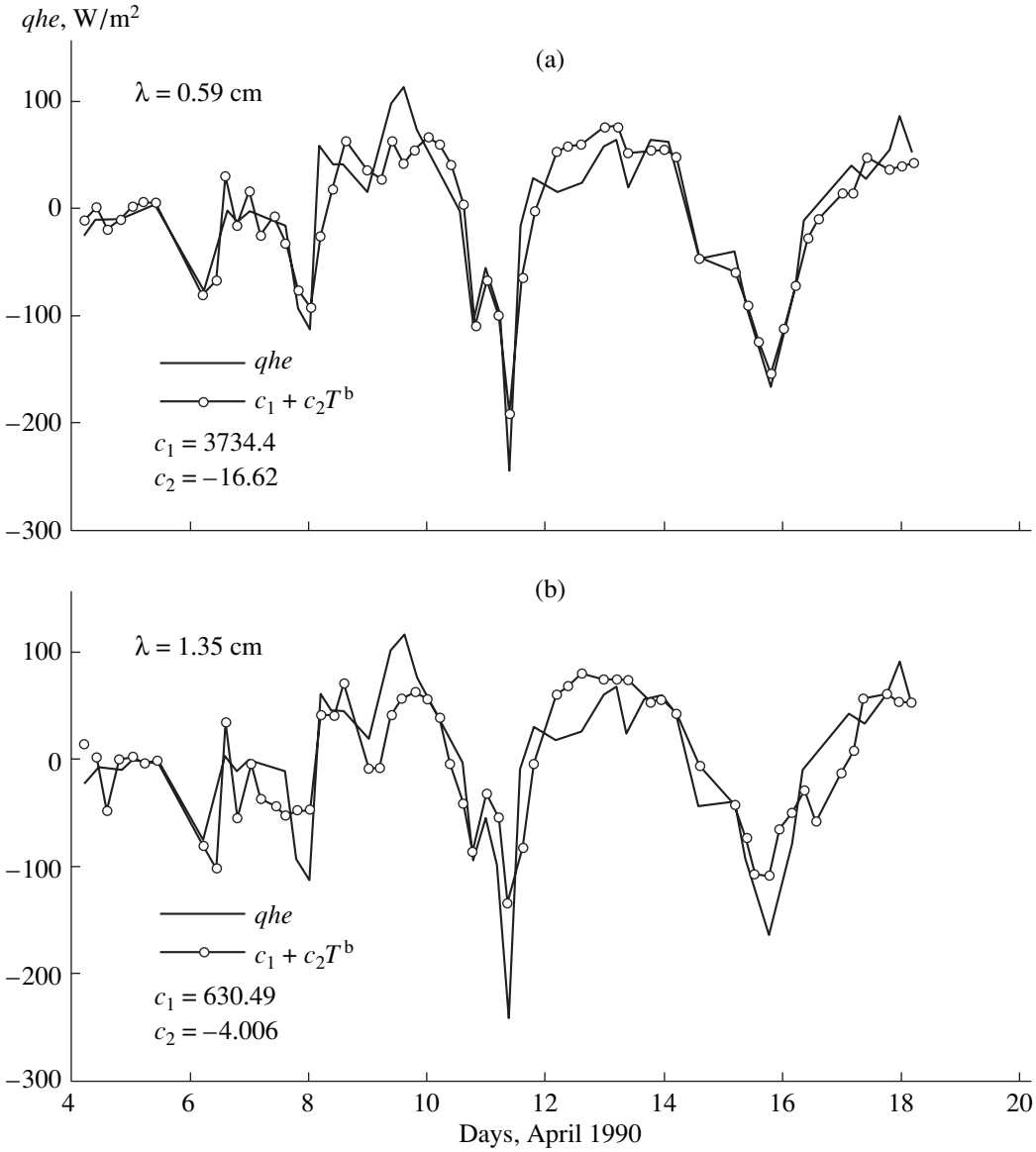

Fig. 3. Six-hour samples of the total heat fluxes *qhe* vs. their satellite (model) estimates at wavelengths of (a) 0.59 and (b) 1.35 cm. The ATLANTEX-90 stationary stage at the location of the *Volna*.

on a synoptic time scale. This correlation shows up largely in the bands of resonant absorption by molecular oxygen and water vapor.

ON A MECHANISM BEHIND A CORRELATION BETWEEN THE BRIGHTNESS TEMPERATURE AND INTERFACIAL HEAT FLUXES IN THE OCEAN–ATMOSPHERE SYSTEM

The problem of how the OAS's brightness temperature (simulated or satellite-measured), for which an effectively radiating 2- to- 5-km-thick atmospheric stratum is responsible, can be related to the temperature and humidity properties of a much thinner (roughly 10-m-thick) near-water atmospheric layer has been repeatedly discussed by teams at the Institute of Radio Engineering and Electronics, Russian Academy of Sciences; the Institute of Space Research, Russian Academy of Sciences; and the Institute of Oceanography, Russian Academy of Sciences. The processing of the aerological data array gained afloat has made it possible to put forward a concept of horizontal (advective) heat-and-moisture transfer as a factor generating ascending (vertical) heat and electromagnetic fluxes. The essence of this idea is that horizontal heat transfer leads to a periodical sharp heating (cooling) of air in a given ocean area. This effect (i) intensifies heat fluxes from the atmosphere to the ocean (or vice versa) because of a greater temperature difference between the water and air and (ii) increases (or decreases) the integral absorp-

Table 1

Wavelength, cm	Approximation error, W/m^2				
	d	d_T_s	d_V	d_T_a	d_Q
0.56	27.8	27.8	28.2	48.5	27.8
0.8	26.6	26.8	27.3	27.0	37.8
1.35	27.0	27.2	28.4	27.5	35.9
1.6	26.1	26.3	27.8	26.5	35.9
3.2	34.2	34.2	30.2	34.3	39.4

tion of electromagnetic fluxes and, in view of (1), the system's brightness temperature. Such a supposition follows from the comparison of the enthalpy (heat content) variation in the atmospheric boundary layer, which experiences the regular influence of the horizontal heat-and-moisture transfer, with the vertical heat fluxes at the ocean–atmosphere interface and the system's brightness temperature.

By way of example, Fig. 4 compares the estimates of the boundary layer enthalpy (calculated from the aerological sounding data for horizons at an altitude of 10, 100, 200, 300, 400, 500, 600, 900, and 1000 m gathered aboard the *Viktor Bugaev* and *Musson*) with the total heat fluxes during the passage of a deep cyclone (the ATLANTEX-90 stationary phase; April 8–13, 1990). Simultaneously, Fig. 5 compares the values of *qhe*, T_-^b 0.59 (the brightness temperature at a wavelength of 5.9 mm), and T_-^b 1.35 (the brightness temperature at a wavelength of 1.35 cm) obtained aboard the *Viktor Bugaev* and *Musson*. It is seen that, in response to the increase in the fluxes *qhe*, the OAS's microwave radiation field diminishes its brightness temperature T^b and vice versa: as the value of *qhe* decreases, T^b grows. This observation supports the validity of the formal analysis the results of which are illustrated in Fig. 3. Over this period, the brightness temperature variation is, on average, 15–20 K at a radiation wavelength of 5.9 mm and 30–40 K at 1.35 cm. Also, the response of the brightness temperature lags behind the heat flux variation by 6–12 h. The response to the limiting values of the heat fluxes does not depend on the place where the measurements were taken: in the water atmospheric layer, at the upper boundary of the atmospheric boundary layer, or in free air. The brightness temperature differs only in magnitude and is the greater, the higher the level of observation.

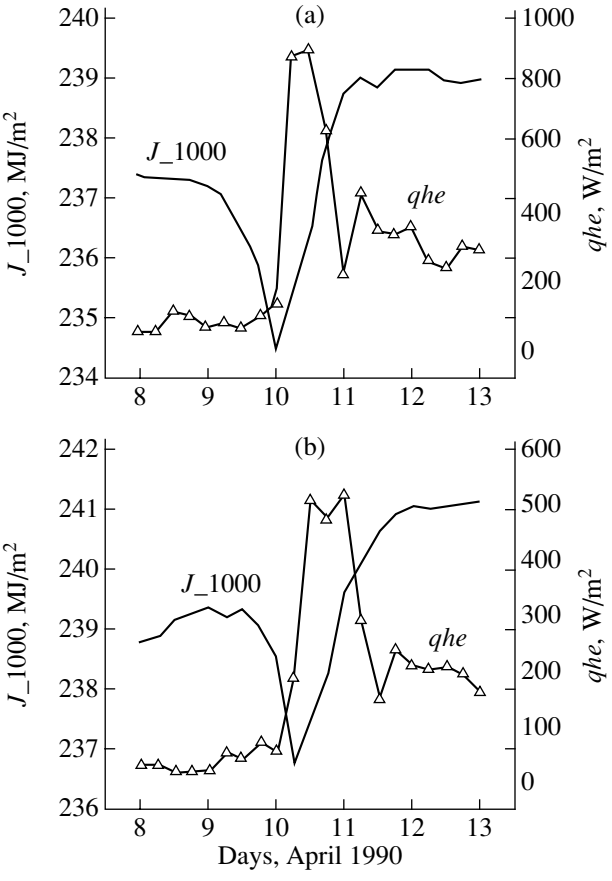

Fig. 4. Total heat fluxes *qhe* vs. the enthalpy *J*_1000 of the atmospheric boundary layer during the passage of a cyclone (April 8–13, 1990) through the location of the (a) *Viktor Bugaev* and (b) *Musson*.

Based on the results of analysis performed in various North Atlantic regions over different time periods, one may safely suggest that the enthalpy variation in the atmospheric boundary layer due to the horizontal heat-and-moisture transfer (advection) controls the variability of heat-and-moisture exchange between the ocean and atmosphere and also specifies the OAS's brightness temperature. In addition, the enthalpy variation defines the relationship between them on the synoptic scale. Some issues, such as the delay between the response of the system's brightness temperature to the variation of the thermal conditions due to the horizontal and vertical heat fluxes in the water and boundary atmospheric layers, need special investigation. To date, we have gained experience in solving such problems by mathematically simulating vertical heat and electromagnetic fluxes and in analyzing their interplay on a daily scale [7].

Table 2

Frequency, GHz	Wavelength, cm	Polarization (*V*/*H*)	Spatial resolution, km	Fluctuation sensitivity, K
19.35	1.55	*V, H*	43 × 69	0.7
22.235	1.35	*V*	40 × 60	0.7
37.0	0.81	*V, H*	29 × 37	0.4
85.5	0.35	*V, H*	13 × 15	0.8

Note: *V*, vertical polarization; *H*, horizontal polarization.

CORRELATION BETWEEN SSM/I RADIOMETRIC MEASUREMENTS AND HEAT FLUXES

An SSM/I (Special Sensor Microwave/Imager) multichannel scanning radiometer is a most promising representative of satellite-borne microwave radiometric systems that have been used over the last 13 years within the framework of the Defense Meteorological Satellite Program, DMSP), which is sponsored by the US Department of Defense. The aim of this program is the long-term monitoring of the Earth in order to provide the US armed forces with global meteorological, oceanographical, and solar–geophysical on-line information (in December 1992, the DMSP data were declassified and became open to the scientific community). DMSP satellites have a solar-synchronized circular orbit at an altitude of about 850 km with an inclination of 98.8°. Today, six satellites of this series (F-10, F-11, F-12, F-13, F-14, and F-15), which have a service time of four years, are in orbit.

An SSM/I satellite-borne radiometer is a scanning seven-channel four-frequency system (Table 2), which measures the brightness temperature of the OAS's microwave radiation over a range of 1400 km and provides complete coverage of the Earth within three days (incomplete coverage is reached within a day) [8].

Since 1987, SSM/I radiometers aboard the F-08, F-10–F-15 satellites have been one of the most important instruments for the meteorological sounding of the atmosphere and the Earth's surface. The SSM/I radiometer aboard the F-08 satellite is of particular interest for our study, since it was the only satellite-borne tool for the microwave monitoring of the ocean in 1988 and 1990, when the NEUFOUEX-88 and ATLANTEX-90 experiments were carried out.

Figure 6 contrasts the total heat fluxes *qhe* and momentum $q\nu$ estimated afloat at the ATLANTEX-90 stationary stage with the satellite estimates, which are represented as the linear combinations of the brightness temperature data from different SSM/I channels. The channels provide information on the total water vapor content in the atmosphere (channel 22*V*), integral water supply in clouds (37*V, H*), and water-wind velocity (19*V, H*). For weak cloudiness, the brightness temperature provided by channel 22*V* alone is a good quantitative estimate of the heat fluxes; in general, however, the data from channel 37*V, H*, which include the effect of cloudiness, should be taken into consideration.

Although the character of ocean–atmosphere thermal interaction at the places of observation within the Newfoundland energy-active zone of the North Atlantic region is quantitatively and even qualitatively different, the estimates of the parameter *qhe* made afloat and aboard the satellite are in good agreement. The correlation coefficients *r* for the heat fluxes and their satellite

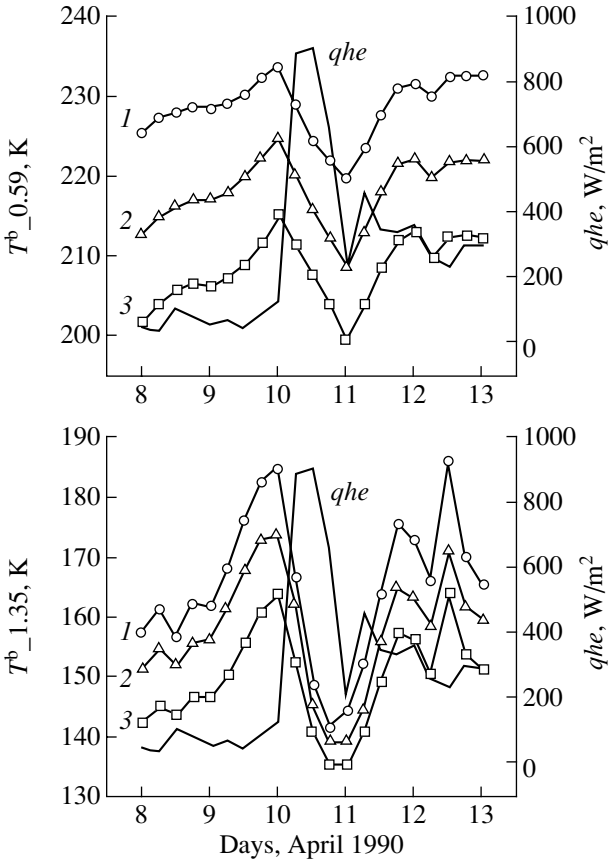

Fig. 5. Total heat fluxes *qhe* vs. OAS brightness temperature estimates $T^b_{\_}0.59$ and $T^b_{\_}1.35$ at the location of the *Viktor Bugaev* (April 8–13, 1990). Simulations of (*1*) satellite, (*2*) aircraft, and (*3*) ship observations.

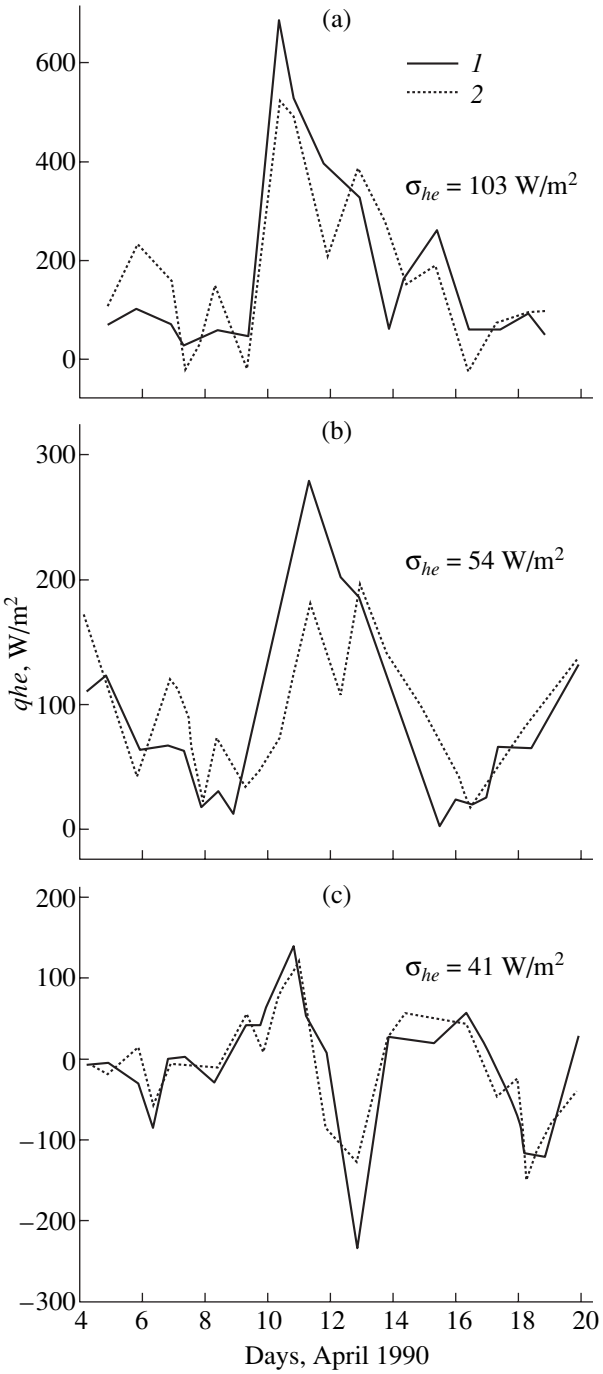

Fig. 6. (*1*) Total heat fluxes *qhe* and momentum qv vs. (*2*) their estimates obtained by linear regressions applied to the data from SSM/I radiometer channels 22*V*, 37*V*, *H*, and 19*V*, *H*37*V*, *H*. (a) the *Viktor Bugaev*, (b) *Musson*, and (c) *Volna*.

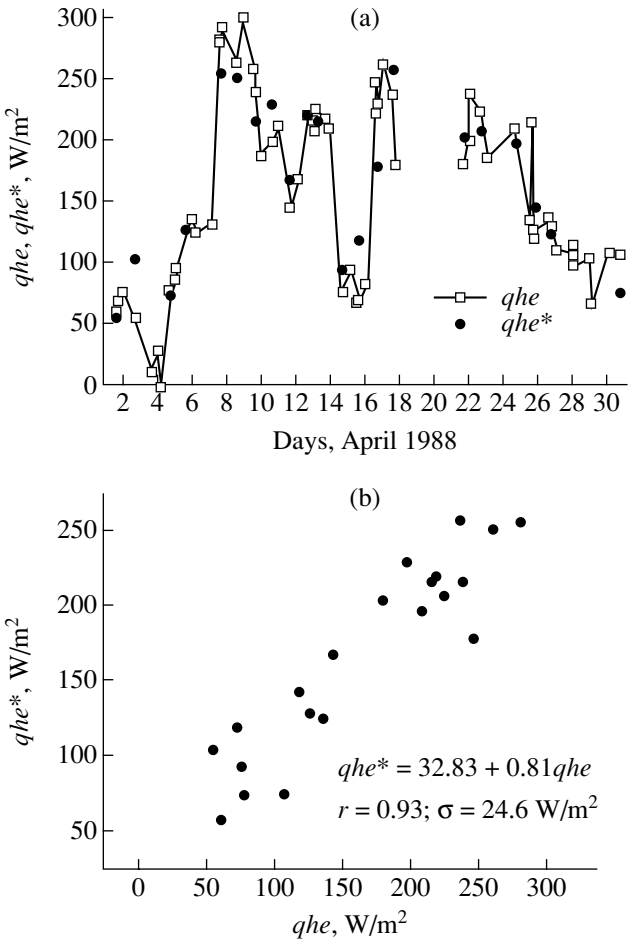

Fig. 7. Total heat fluxes measured directly (afloat), *qhe*, and estimated aboard the satellites, *qhe**, at the point *M* of the North Atlantic region. (a) Variations of the quantities *qhe* and *qhe** in April, 1988, and (b) linear regression for *qhe* and *qhe**.

microwave radiometric estimates reach 0.85 for the *Viktor Bugaev* and 0.84 for the *Volna*. For the fluxes measured afloat and estimated remotely, the ratio of the rms residual σ_{he} to the maximal natural variations of the fluxes lies between 12% (the *Volna*) and 19% (the *Musson*).

The total heat fluxes estimated afloat at higher latitudes, at the point *M* of the Norwegian–Greenland energy-active zone (the materials are submitted by courtesy of Jorgen Schultz from the Remote Sensing Center, Germany), also closely correlate with the satellite estimates made by linear regressions applied to the data obtained simultaneously from channels 22*V*, 37*V*, *H*, and 19*V* of the F-08-borne SSM/I radiometer (Fig. 7).

The stability of the relationships between the total heat fluxes and their satellite estimates constructed by linear regressions applied to the data from channels 22*V*, 37*V*, *H*, and 19.35*V* of the F-08-borne SSM/I radiometer is readily apparent from comparing the parameters *qhe* and *qhe** that were determined with a two-year shift in time (i.e., during the NEWFOUEX-88 and ATLANTEX-90 stationary stages) in nearly the same areas of the Newfoundland energy-active zone (Fig. 8).

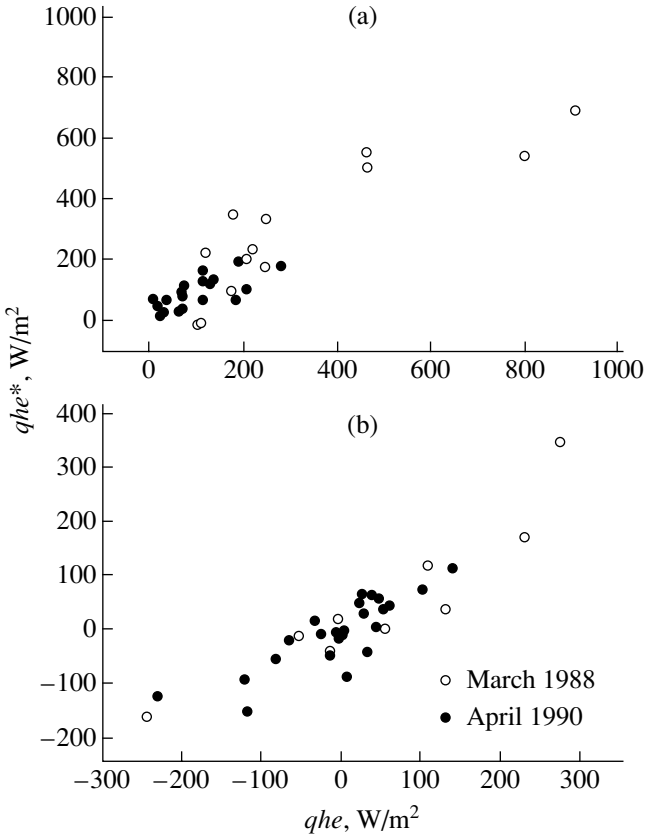

Fig. 8. Total heat fluxes measured directly, *qhe*, and estimated aboard the satellites, *qhe**, at the locations of the (a) *Musson* and (b) *Volna* during the NEUFOUEX-88 and ATLANTEX-90 stationary stages.

CONCLUSIONS

The brightness temperature of the self-microwave radiation of the ocean–atmosphere system that is measured on satellites in the resonant absorption bands of water vapor (1.35 cm) and molecular oxygen (5 mm) allows researchers to quantitatively estimate the intensity of vertical turbulent fluxes of the evolved and latent heat in the "thin" (in terms of the satellite scale) water atmospheric layer over different time intervals. The integral heat fluxes in the entire ocean–atmosphere system and the local heat and moisture fluxes at the ocean–atmosphere interface are related through the moisture and temperature characteristics of the atmosphere.

The relationship between the OAS's brightness temperature and vertical interfacial turbulent fluxes at middle and high latitudes of the ocean is governed largely by horizontal fluxes (advection) of moisture and heat in the boundary atmospheric layer. This effect is responsible for the direct correlation between the brightness temperature of the OAS and the boundary values of the heat fluxes.

In this work, we used the data previously obtained within the framework of contract NAS15-10110 concluded between NASA and the Russian Space Agency. Of inestimable value for this study were the archives of the NEWFOUEX-88 and ATLANTEX-90 experiments and also archival data on long-standing microwave radiometric measurements aboard DMSP satellites (the latter were submitted by the Marshall Space Flight Center).

ACKNOWLEDGMENTS

The author is indebted to A.A. Mil'shin and N.K. Shelobanova (Institute of Radio Engineering and Electronics, Russian Academy of Sciences) and S.K. Gulev (Institute of Oceanography, Russian Academy of Sciences) for assistance in the experiments.

REFERENCES

1. W. T. Liu, J. Geophys. Res. **93**, 6749 (1988).
2. A. G. Grankov, Izv. Akad. Nauk, Fiz. Atmos. Okeana **28**, 1189 (1992).
3. A. G. Grankov and E. P. Novichikhin, Meteorol. Gidrol., No. 1, 81 (1997).
4. S. K. Gulev, A. V. Kolinko, and S. S. Lappo, *Synoptic Interaction of Ocean and Atmosphere in Middle Latitudes* (Gidrometeoizdat, St. Petersburg, 1994).
5. S. K. Gulev, Yu. A. Ivanov, A. V. Kolinko, *et al.*, Meteorol. Gidrol., No. 5, 51 (1992).
6. *Turbulent Fluxes of Heat, Moisture, and Momentum over the Sea: Methods of Calculation* (Main Geophysical Observatory, Leningrad, 1981).
7. A. G. Grankov and Yu. D. Resnyanskiĭ, Meteorol. Gidrol., No. 11, 78 (1997).
8. P. H. Hollinger, J. L. Peirce, and G. A. Poe, IEEE Trans. Geosci. Remote Sens. **28**, 781 (1990).

Translated by V. Isaakyan

Technical Physics, Vol. 48, No. 7, 2003, pp. 914–919. Translated from Zhurnal Tekhnicheskoĭ Fiziki, Vol. 73, No. 7, 2003, pp. 119–124.

ELECTRON AND ION BEAMS, ACCELERATORS

Effect of Beam–Plasma Interaction on Ion Transport through a Cyclotron Injector

S. V. Grigorenko and S. Yu. Udovichenko

Efremov Research Institute of Electrophysical Equipment, St. Petersburg, 196641 Russia

Received September 9, 2002

Abstract—The influence of collective effects associated with transverse plasma oscillations excited by a beam of negative ions on the neutralization of the space charge due to fast ions is studied. Conditions for the dynamic deneutralization of an unstable ion beam are refined. Analytic expressions for the plasma ion density distribution and for the stationary electric field in a partially neutralized beam are obtained. The equation of motion of a beam in the self-electric field and in an external magnetic field is used to determine the effect of secondary charged particles on the transport of negative ions through the injector of a cyclotron. © *2003 MAIK "Nauka/Interperiodica".*

INTRODUCTION

External systems injecting H^- ions into a cyclotron-like accelerator are intended for generating 20- to 30-keV beams of current higher than 1 mA and transporting them over a distance of several meters. The system contains a plasma source of ions; an electrostatic optics to focus the beam; a transport channel with a magnetic focusing system; and an inflector, which matches the beam to the cyclotron's accelerating channel. In such an injector, the neutral gas enters the transport channel from the plasma source. Its density decreases as it approaches the cyclotron: downstream from the system of electrostatic focusing and final acceleration, the pressure is about 10^{-4} torr; in the magnetic focusing system, about 10^{-5} torr; and near the cyclotron, 10^{-6} torr. The beam ionizes the gas, and secondary charged particles, accumulating in the transport channel, neutralize the beam's space charge. In the electrostatic beam-forming system, the charge remains unneutralized, because the plasma is scattered to the electrodes, whose potential is high.

At the exit from the injector, the beam forming and guiding system must provide a beam of H^- ions with an emittance matched to the acceptance of a cyclotron-like accelerator. The match to the acceleration channel is the best when, at the entrance to the accelerator, the beam converges and has an optimum major-to-minor axis ratio of an ellipse that represents the beam in the phase space.

The significant pressure drop across the injector, as well as the presence of the stationary beam–plasma field, the field of plasma oscillations, and the field of the space charge of negative ions in the neutralization region, make the beam transportation difficult. The self-consistent beam–plasma electric field [1] may affect the dynamics of precision ion beams with a small phase volume and low angular divergence [2]. Collective processes associated with the spectrum of beam-induced plasma oscillations heat up fast ions [1] and dynamically deneutralize the beam's space charge [3]. Earlier, the effect of secondary charged particles on the ion beam transport through the cyclotron injector was disregarded [4].

In this paper, we determine conditions of beam–plasma interaction and use an equation of beam motion to study the effect of secondary charged particles on the transport of negative ions. This could be a help for a designer in correcting the injector parameters and matching the beam's emittance to the cyclotron's acceptance.

CONDITIONS OF BEAM–PLASMA INTERACTION IN THE TRANSPORT CHANNEL

When the gas pressure is low ($P \le 10^{-4}$ torr), in the free drift space and in the region of the magnetic optics, the space charge of the negative ion beam is completely neutralized by positive ions of the plasma within time $\tau_n = (n_g \sigma_i v_b)^{-1}$, where n_g is the concentration of gas molecules, σ_i is the cross section of ionization of a gas molecule by a beam's ion, and v_b is the longitudinal beam velocity. Over short free drift paths, strong static or variable fields in the beam, as well as negative ion density oscillations, are absent. However, when the path is on the order of several tens of centimeters, the neutralization breaks: the negative potential starts oscillating with an amplitude reaching several tens of percent of the potential of the completely deneutralized beam. This phenomenon is attributed to ion–ion instability in the beam [5].

Let us study the effect of low-frequency plasma oscillations on the stationary electric field and positive ion concentration in the neutralized beam and find conditions for the dynamic deneutralization of the beam.

1063-7842/03/4807-0914$24.00 © 2003 MAIK "Nauka/Interperiodica"

To this end, we will refine the hydrodynamic model of a beam plasma proposed in [3].

In the hydrodynamic approximation, which disregards the thermal spread in velocities, the equation for the transverse ion velocity of plasma ions in the Cartesian coordinates system takes the form

$$u_{ix}\frac{du_{ix}}{dx} = \frac{e}{m_i}E_A(x) - \frac{Su_{ix}}{n_i} - \frac{e^2}{4m_i^2\omega_{pi}^2}\frac{d\tilde{E}_x^2}{dx}. \quad (1)$$

Here, $E_a(x) = -(T_e/en_e)dn_e/dx$ is the stationary ambipolar field of the plasma; T_e is the electron temperature; n_e and n_i are the electron and ion concentrations in the plasma; $\tilde{E}_x$ and ω_{pi} are the electric field and Langmuir frequency of ion oscillations, respectively; and $S = d(n_iu_{ix})/dx = \sigma_i n_g v_b n_b$.

At gas pressures indicated above, the ion density in the beam $n_b \approx n_i \gg n_e$ and the ambipolar field is weak: $E_a(x) \approx 2m_i(\sigma_i n_g v_b)^2 x/e$. This expression follows from Eq. (1), where the known value of the plasma ion flux n_iu_i at $\tilde{E}_x = 0$ is taken into account. Experiments [6] show that the transverse electric field strength in a neutralized beam is much greater than this theoretical prediction. The last term on the right of (1) is due to the Miller force produced by the field of the plasma oscillations. In the field fast oscillating with high frequency ω_{pi}, plasma ions experience the stationary ambipolar field and also an additional constant electric field, which varies quadratically with the amplitude of the variable field. The maximum strength of this field,

$$E_M = -\frac{e}{4m_i\omega_{pi}^2}\frac{d\tilde{E}_x^2}{dx} = -\frac{m_i}{2e}\frac{d\omega_{pi}^2/k_\perp^2}{dx} \approx \frac{T_e}{2ex_b}, \quad (2)$$

is comparable with the estimate given in [6]. In (2), $\tilde{E}_x = k_\perp\tilde{\varphi}$; $\tilde{\varphi}_{max} \approx m_i(\Delta v)^2/e \approx m_i v_{\phi\perp}^2/e$ is the potential amplitude in saturated ion oscillations with the plasma ions captured by them; $v_{\phi\perp} = \omega_{pi}/k_\perp$ is the phase velocity of the oscillations, which becomes equal to the ion sound velocity $v_s = (T_e/m_i)^{1/2}$ at low gas pressures [7]; $\omega_{pi} = (4\pi e^2 n_i/m_b)^{1/2}$; $k_\perp$ is the transverse wavenumber; and x_b is the cross-sectional dimension of the beam, $n_i(x) > n_i(x_b)$. When the beam charge is completely neutralized, the condition $k_\perp x_b \gg 1$ is valid at low gas pressure and the ion oscillations propagate in the x-axis direction in the form of plane traveling waves ($\sim\exp(ik_\perp x)$). We assume that the transverse ion oscillations ($k_\perp \gg k_z$), which drift along the beam, grow exponentially with a linear increment ($\sim\exp(\int \mathrm{Im}\, k_z dz)$, where k_z is the longitudinal wave number) until the limit value of the potential amplitude is reached. The distance over which the oscillations become saturated is defined as $z_n = (1/\mathrm{Im}k_z)\ln(\tilde{\varphi}_{max}/\tilde{\varphi}_0)$, where $\tilde{\varphi}_0$ is the amplitude of initial fluctuations in the plasma, $\mathrm{Im}k_z = \omega_{bi}(\omega_{pi}\tau_i)^{1/2}/2v_b$ is the spatial growth increment, $\omega_{bi} = (4\pi e^2 n_b/m_b)^{1/2}$, and $\tau_i = \sigma_i n_g v_b$ is the life time of a plasma ion.

Integrating equation of motion (1) and the equation of plasma ion continuity yields a set of equations for the plasma parameter distributions across the ion beam:

$$n_i(x)u_i^2(x) - n_i(x_b)u_i^2(x_b) = 2A\frac{v_s}{x_b}\int_{x_b}^{x} n_i(x)u_i(x)dx + \frac{v_{\phi\perp}^2}{4}[n_i(x_b) - n_i(x)], \quad (3)$$

$$n_i(x)u_i(x) = An_b v_s\frac{x}{x_b} + n_1 v_{\phi\perp}, \quad (4)$$

where $A = \sigma_i n_g v_b x_b/v_s$ and the ion concentration in the beam, n_b, is assumed to be constant for simplicity.

The first term on the right of (3) is proportional to the integral of $E_a n_i$ with $E_a/u_i = 2(m_i/e)Av_s/x_b = \mathrm{const}$. A relationship between E_a and the linear function $u_i(x)$ is derived under the condition $n_i \approx n_b$ from the equation $d(n_iu_i^2)_0/dx = (e/m_i)E_a n_i$, which is the zeroth-order approximation of (1) in the oscillation field $\tilde{E}_x$. In Eq. (4), the flux $n_1 v_{\phi\perp}$ is a constant of integration and is related to the electric field produced by an external source (the beam). The transverse ion oscillations enhance the ion flux toward the chamber wall. Measurements [6] show that the plasma ion flux at the beam boundary is three times as high as the theoretical value obtained when the plasma oscillations are ignored. Assuming that $n_i(x_b)u_i(x_b) \approx 3An_b v_s$ and $v_{\phi\perp} \approx v_s$, we find that $n_1 \approx 2An_b$.

The same value of n_1 can be obtained by solving the set of Eqs. (3) and (4) with appropriate boundary conditions imposed on the plasma at the beam surface. In the region of the quasi-neutral plasma outside the beam, $n_i \approx n_e$, $\tilde{E}_x = 0$, the ion flux is $n_iu_i \approx 3An_b v_s = \mathrm{const}$, and the velocity with which the ions strike the wall is v_s. Equation (1) yields the boundary condition $u_i(x_b) \approx v_s$. Assuming that $v_{\phi\perp} \approx v_s$ and $n_i(x = 0) \approx n_b$, we find from Eqs. (3) and (4) an equation for $\eta_1 = n_1/n_b$:

$$\eta_1^2 - \left(\frac{5}{4} - 2A\right)\eta_1 + A^2 + \frac{1-5A}{4} = 0. \quad (5)$$

From (5), it follows that $\eta_1 = 2/3 = 2A$ at $A = 1/3$. According to Eq. (4), when $A < 1/3$, $n_i(x_b) < n_b$, which means the onset of the ion beam deneutralization mode. This condition yields the critical gas density

$$n_{g,cr} \approx \frac{v_s}{3\sigma_i v_b x_b}, \quad (6)$$

which is in good agreement with the value measured in [6].

Consider the dynamic deneutralization of an ion beam that is associated with beam instability [5]. It was found [8] that the transverse oscillations of plasma ions that are triggered by a beam of negative ions in a rarefied gas make a major contribution to the radial drift of positive ions when the oscillation amplitude is high enough. In this case, the drift velocity is proportional to the oscillation amplitude. As a result, the average negative potential grows with beam length.

Let us study the distributions of plasma ions and stationary electric field along and across a cylindrical beam of negative ions when the space charge is deneutralized. When the gas density is $n_g < n_{g,cr}$, the density of plasma electrons drops abruptly and their Debye length exceeds the beam radius: $d_e > r_b$. Under these conditions, the beam excites the zeroth-order radial mode ($k_\perp \gg k_z$) of the plasma ion oscillations [7]. The electron density meets the inequality $n_e/n_i \gg v_s^2/v_b^2$, which is typical of the cyclotron's injector. The possibility of developing the longitudinal ($k_z > k_\perp$) oscillations of plasma ions when the opposite inequality is valid was considered in [3].

Let us represent the radial distribution of the standing wave potential as $\tilde{\varphi}(r, z) = \tilde{\varphi}(0, z)J_0(k_\perp r)$, where $\tilde{\varphi}(0, z) = \tilde{\varphi}_0 \exp(\int \mathrm{Im}\, k_z dz)$ is the amplitude of the potential at the beam's axis, $k_\perp = \alpha_0/r_b$, and $\alpha_0 = 2.4$ is the first zero of the Bessel function J_0. Then, expression (2) for the electric field becomes

$$E_M(r, z) = -\frac{\tilde{\varphi}^2(0, z)\alpha_0^2}{16\pi e n_i(r, z) r_b^2}\frac{dJ_1^2(\alpha_0 r/r_b)}{dr}. \qquad (7)$$

In formula (7), $J_1(\xi) = -dJ_0(\xi)/d\xi$ is the first-order Bessel function, $dJ_1^2/d\xi = 2J_1(J_0 - J_1/\xi)$, and $\xi = \alpha_0 r/r_b$. The spatial increment $\mathrm{Im}\, k_z$ of the oscillations in the deneutralized beam for $n_g < n_{g,cr}$ is defined by attenuation due to a finite life time of plasma ions and attenuation due to the spread in their thermal velocity [8, 9]. The minimum of either of two expressions corresponding to these attenuation modes specifies the rate of beam instability buildup:

$$\mathrm{Im}\, k_z = \min\left\{\begin{array}{l} \dfrac{\omega_{bi}}{2v_b}(\omega_{pi}\tau_i)^{1/2} = \alpha_0^{1/2}\dfrac{\omega_{bi}}{2v_b} \\ \left(\dfrac{2}{\pi}\right)^{1/4}\dfrac{\omega_{bi}}{v_b}\dfrac{\exp(a^2/4)}{a^{3/2}}, \end{array}\right.$$

where $\tau_i = r_b/v_{\phi\perp}$, $v_{\phi\perp} = \omega_{pi}/k_\perp$, $a = \omega_{pi}r_b/\alpha_0 v_{Ti}$, $v_{Ti} = (T_i/m_i)^{1/2}$, and T_i is the temperature of plasma ions.

The average energy of plasma ions is assumed to be approximately equal to the depth of the potential well that is determined by the negative potential drop across the beam radius.

The ambipolar field E_a of the plasma is absent when the beam is deneutralized, because the electron density is low. By substituting expression (7) into the Poisson equation, we obtain the equation that describes the radial plasma ion distribution $\eta = n_i/n_b$:

$$\eta^2 - \eta + f_1(\xi, z) - \frac{f_2(\xi, z)}{\eta}\frac{d\eta}{d\xi} = 0, \qquad (8)$$

where $f_1(\xi, z) = 2B(z)(J_0^2 - J_1^2 - 2J_0J_1/\xi + 2J_1^2/\xi^2)$, $f_2(\xi, z) = 2B(z)J_1(J_0 - J_1/\xi)$, $B(z) = [\alpha_0^2\tilde{\varphi}(0, z)/8\varphi_b]^2$, and $\varphi_b = \pi e n_b r_b^2$ is the potential drop across the radius of the completely deneutralized beam.

When solving the Poisson equation, we assumed that $dE_M/dr \gg dE_M/dz$ in a long narrow beam. In the approximation $d\ln\eta/d\xi \ll |f_1/f_2|$, Eq. (8) yields

$$\eta_0 = \frac{1}{2}\{1 + [1 - 4f_1]^{1/2}\}. \qquad (9)$$

The solution η_0 may be used to refine η by finding the derivative $d\eta_0/d\xi$ in Eq. (8). Thus,

$$\eta \approx \frac{1}{2}\left\{1 + \left[1 - 4f_1 + 4f_2\frac{d\ln\eta_0}{d\xi}\right]^{1/2}\right\}. \qquad (10)$$

The approximation used here is valid everywhere in the beam where $4f_1 \leq 1$. The maximum difference between expressions (9) and (10), $\ll 10\%$, is observed near the beam axis at the boundary of the applicability domain ($\eta_0 = 1/2$). Radial distribution (10) of the plasma ion density for several values of the z coordinate is shown in Fig. 1. It can be seen that the beam of negative ions is in the deneutralized state with the negative potential drop across the radius. At the circumference

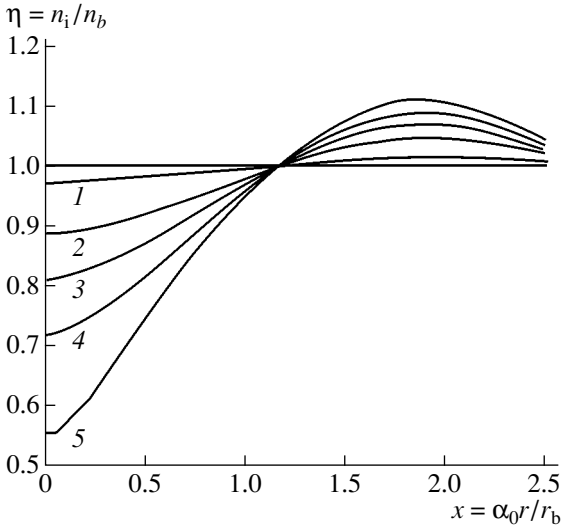

Fig. 1. Radial distribution of the plasma ion density in the beam at z = (*1*) 50, (*2*) 127, (*3*) 132, (*4*) 135, and (*5*) 138 cm.

of the beam, the weak overneutralization of the space charge is observed. The state of the beam–plasma system with positively and negatively charged channels present in the cross section of the negative ion beam at $n_g < n_{g,cr}$ was experimentally discovered in [10].

BEAM TRANSPORT IN THE CASE OF COMPLETE AND PARTIAL SPACE CHARGE NEUTRALIZATION

The parameters of the beam–plasma system and transport channel are taken as follows: the beam current $I_b = 30$ mA, the energy of negative ions $W_b = 30$ keV, the radius of the quasi-parallel beam downstream from the electrodes of the primary beam-forming system ($z = 0$) $r_b = 1.5$ cm, the normalized emittance $\varepsilon = 5 \times 10^{-5}$ cm rad, the radius of the ion guide $R = 5$ cm, the potential drop across the charged beam radius $\varphi_b = 112.5$ V, and the plasma ion temperature $T_i = 0.03$ eV.

If the transport channel is filled with xenon, the space charge of the ion beam is completely compensated at a pressure of $P \geq 3 \times 10^{-6}$ torr, as follows from (6). The xenon plasma parameters, $T_e = 3$ eV and $\sigma_i(\chi_e) \approx 8 \times 10^{-16}$ cm^2, we take from [6]. The above gas pressure is not too different from the residual gas pressure in the cyclotron itself. However, the penetration of heavy xenon particles into the evacuated space of the cyclotron is undesirable. Therefore, the beam's space charge is neutralized with molecular hydrogen, which enters the injector from the plasma source of H^- ions. In this case, the critical (initial) pressure of beam deneutralization is $P_{cr} = 1.2 \times 10^{-4}$ torr ($n_{g,cr} = 4.3 \times 10^{12}$ cm^{-3}). In our calculations, we used $T_e = 1$ eV and $\sigma_i(H_2) = 1.5 \times 10^{-16}$ cm^2.

The maximum gas pressure in the injector is limited, because too high a pressure may cause breakdowns in the final acceleration system of the plasma source. Also, as the density of the gaseous medium increases, the beam particle density in the transport channel decreases as a result of the inelastic conversion of negative ions into neutral atoms and positive ions. The associated cross sections are $\sigma_{-10} = 7.3 \times 10^{-16}$ cm^2 and $\sigma_{-11} = 0.43 \times 10^{-16}$ cm^2, respectively.

A typical distribution of the molecular hydrogen density along the injector downstream of the final acceleration system is plotted in Fig. 2. Estimates show that, as the beam passes through the gaseous medium in the injector, the density of negative ions

$$n_b(z) = n_b(0)\exp\left[-(\sigma_{-10} + \sigma_{-11})\int_0^z n_g(z)dz\right], \quad (11)$$

decreases by only 10–11%.

As can be seen from Fig. 2, the gas density is on the order of or less than the critical density $n_{g,cr}$, even in the initial portion of the transport channel. However, the beam's charge remains neutralized over the length $z_n \approx 23$ cm until the amplitude of plasma ion oscillations reaches $\tilde{\varphi}_{max} \approx m_i v_s^2/e \approx 1$ eV. The oscillation increment, which is determined by the finite lifetime of H_2^+ ions in the quasi-neutral plasma, is $\mathrm{Im}\,k_z \approx 0.2$ cm^{-1}, the ion Langmuir frequency is $\omega_{pi} = 9.3 \times 10^6$ s^{-1}, and $\omega_{bi} = 1.3 \times 10^7$ s^{-1}. The minimum potential amplitude for the spontaneously excited oscillations of plasma ions is assumed to be $\tilde{\varphi}_0 \approx 10^{-2}$ V. The space charge neutralization in the initial portion of the beam drift path at a low gas pressure was observed in [5].

For the given parameters of the beam–plasma system, attenuation due to the leakage of plasma ions is the basic factor controlling the increment of the ion oscillations in the region of space charge deneutralization. Therefore, when simulating the beam dynamics in the region $z > z_n$, one should use the expression $\mathrm{Im}\,k_z = \alpha_0^{1/2}\omega_{bi}/2v_b \approx 0.77\omega_{bi}/v_b$, assuming that the negative ion concentration at the axis remains constant when the beam radius changes insignificantly. In the experiment conducted under similar conditions [8], the increment was measured to be $0.7\omega_{bi}/v_b$ and remained constant in the region of the deneutralized beam, where the amplitude of the plasma ion oscillations grows exponentially.

As follows from Fig. 2, the space charge deneutralization reaches 50% at $z = 140$ cm. The amplitude of the transverse potential oscillations at the beam axis increases from 1 V (at $z \approx 23$ cm) to 80 V if the instability increment is set equal to 3.8×10^{-2} cm^{-1}. Such high-amplitude oscillations of the potential were reported in [5].

The dynamics of the negative ion beam was simulated based on the equation for the beam envelope in the Cartesian coordinates (the beam-plasma interaction in the free drift channel and in four quadrupole magnetic

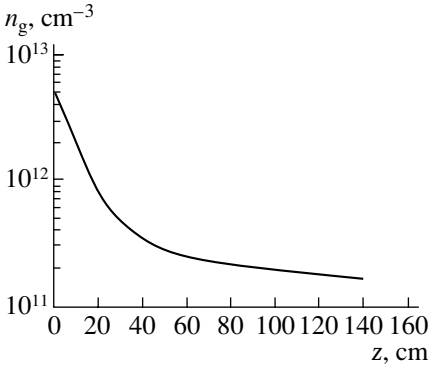

Fig. 2. Distribution of H_2 particle density along the injector axis.

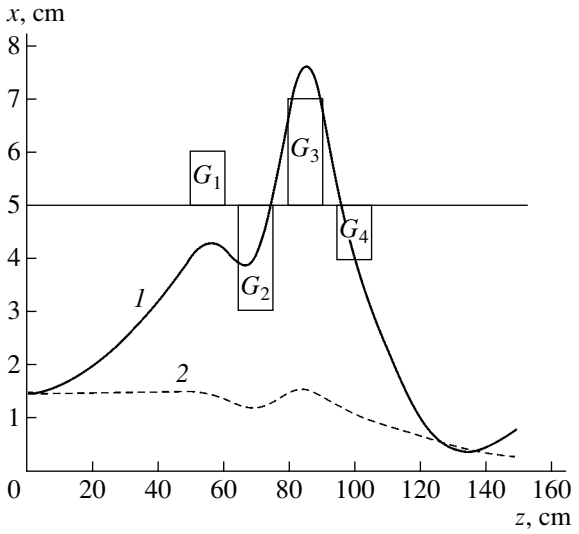

Fig. 3. Envelope of the beam (*1*) with the space charge and (*2*) with the charge completely neutralized in the injector with four quadrupoles.

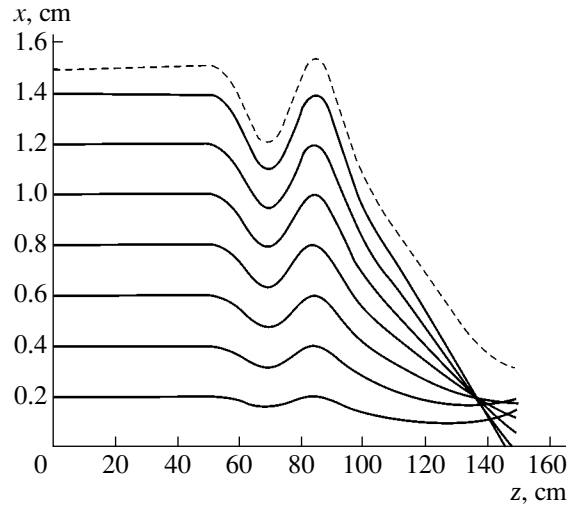

Fig. 4. Trajectories of the beam ions (solid lines) with allowance for the beam–plasma interaction and envelope of the completely charge neutralized beam (dashed line, corresponding to curve *2* in Fig. 3).

lenses ignored)

$$\frac{d^2x_b}{dz^2} = \frac{\varepsilon^2}{x_b^3} + \frac{e\varphi_b}{x_b W_b} - \frac{e\nu_b x_b G}{2W_b}, \qquad (12)$$

where G is the magnetic field gradient in the quadrupole lens.

The first and second terms on the right of Eq. (12) define the defocusing of the ions due to the finite value of the beam emittance ε and Coulomb repulsion, respectively. In the yz plane, the equation for the envelope has the same form except that the last term on the right is taken with a plus sign.

Equation (12) was integrated numerically by the Runge–Kutta method. Figure 3 plots the envelopes of the beam propagating in a vacuum and when the space charge is completely neutralized. In the first case, the magnetic field gradients in the four quadrupole lenses were G_1 = 0.9 T/m, G_2 = –2.2 T/m, G_3 = 2.2 T/m, and G_4 = –0.9 T/m. These optimum magnetic field gradients in the lenses do not eliminate the wall loss of the beam current. With the space charge completely neutralized at G_1 = 0.45 T/m, G_2 = –1.2 T/m, G_3 = 1.2 T/m, and G_4 = –0.45 T/m, the radius of the beam is minimal and the beam converges to the axis. However, as was shown above, the beam charge cannot be neutralized completely at a low gas pressure in the injector.

The dynamics of the negative ion beam in the transport channel with allowance for beam–plasma interaction was simulated by the coarse particle method applied to the equation of motion in the Cartesian coordinates:

$$\frac{d^2x}{dz^2} = -\frac{eE_M(x)}{2W_b} - \frac{e\nu_b xG}{2W_b}. \qquad (13)$$

In the region where the beam charge is completely neutralized ($z \le z_n$), the effect of weak focusing field (2) ($E_M \le 1$ V/cm) on the dynamics of the negative ions was disregarded.

Upon simulating the ion dynamics in the region of deneutralization, the plasma ion density was evaluated by formula (10) at each step along the z coordinate. The ion densities found were used to determine Miller force (7): $eE_M = -\alpha_0^3 J_1(J_0 - J_1/\xi)\tilde{\varphi}^2(0, z)/8\varphi_b r_b \eta$. The adopted approximation that a change in the radius (density) of the initially cylindrical beam is small allows us to apply the axisymmetrical model when calculating the Miller force.

Figure 4 shows the trajectories of the particles injected at different distances from the axis of the system. The magnetic field gradients in the quadrupoles are the same as in the case of a completely neutralized beam. In the paraxial region, where a negatively charged channel is present, the negative ions are defocused. Conversely, peripheral particles move toward the beam's axis under the action of the self-consistent beam–plasma field E_M. As a result, the particle concentration decreases near the axis and increases at the periphery. This effect, as well as the significant change in the cross-sectional dimension of the beam (Fig. 4), disagrees with the initial approximation. In this case, one should take into account the variation of the beam particle concentration when calculating the instability increment and the potential amplitude at the axis. Such a necessity has been corroborated experimentally and is

beyond question. This fact cannot be neglected when the beam dynamics in long transport systems is simulated.

Thus, we found conditions for beam–plasma interaction when negative ions pass through the cyclotron's injector and refined conditions for the dynamic deneutralization of the ion beam, which excites plasma oscillations. A value of the critical gas pressure (below which the space charge of the beam becomes deneutralized) that is more accurate than the one reported in [3] was found. The distributions of the plasma ion density and stationary electric field for the partially neutralized beam in the presence of developed transverse ion–ion instability and intense flow of positive ions across the beam were obtained. The beam dynamics was studied numerically in the regions where the space charge is neutralized completely or partially. The beam–plasma interaction was shown to affect noticeably the dynamic characteristics of the beam at the exit from the transport channel. This effect must be taken into consideration when it is necessary to match the injector and the cyclotron. To minimize the transverse beam dimensions and provide a desired convergence of the negative ions to the axis requires the adjustment of the magnetic field in the quadrupoles and the parameters of the beam–plasma system.

REFERENCES

1. S. Yu. Udovichenko, Zh. Tekh. Fiz. **65** (4), 31 (1995) [Tech. Phys. **40**, 307 (1995)].
2. N. G. Vaganov, V. P. Sidorov, and S. Yu. Udovichenko, Vopr. At. Nauki Tekh., Ser. Termoyad. Sint., No. 4, 36.
3. S. Yu. Udovichenko, Zh. Tekh. Fiz. **64** (8), 104 (1994) [Tech. Phys. **39**, 802 (1994)].
4. Yu. V. Afanas'ev, M. F. Vorogushin, S. V. Grigorenko, *et al.*, in *Proceedings of the 8th Conference on the Industrial and Medical Applications of Charged Particles Accelerators, St. Petersburg, 1995*, p. 150.
5. M. D. Gabovich, D. G. Dzhabarov, and A. P. Naĭda, Pis'ma Zh. Éksp. Teor. Fiz. **29**, 536 (1979) [JETP Lett. **29**, 489 (1979)].
6. J. Sherman, E. Pitcher, R. Stevens, *et al.*, in *Proceedings of the 6th International Symposium on the Production and Neutralization of Negative Ions and Beams, Brookhaven, 1992*, p. 686.
7. M. D. Gabovich, L. S. Simonenko, I. A. Soloshenko, *et al.*, Zh. Éksp. Teor. Fiz. **67**, 1710 (1974) [Sov. Phys. JETP **40**, 851 (1975)].
8. D. G. Dzhabarov and A. P. Naĭda, Zh. Éksp. Teor. Fiz. **78**, 2259 (1980) [Sov. Phys. JETP **51**, 1132 (1980)].
9. I. A. Soloshenko, Fiz. Plazmy **8**, 103 (1982) [Sov. J. Plasma Phys. **8**, 58 (1982)].
10. V. P. Goretskiĭ and A. P. Naĭda, Fiz. Plazmy **11**, 394 (1985) [Sov. J. Plasma Phys. **11**, 227 (1985)].

Translated by A. Khzmalyan

Technical Physics, Vol. 48, No. 7, 2003, pp. 920–927. Translated from Zhurnal Tekhnicheskoĭ Fiziki, Vol. 73, No. 7, 2003, pp. 125–132.

EXPERIMENTAL INSTRUMENTS AND TECHNIQUES

High-Current Plasma Opening Switch Fed by a Magnetic Explosion Generator

K. I. Almazova, A. S. Boriskin, V. V. Borovkov, E. P. Volkov, V. A. Demidov, V. S. Zhdanov, A. V. Ivanovsky, S. A. Kazakov, V. G. Kornilov, S. Yu. Kornilov, V. D. Selemir, D. A. Tolshmyakov, A. A. Khizhnyakov, E. A. Tsareva, V. I. Chelpanov, and E. V. Shapovalov

All-Russia Research Institute of Experimental Physics, Russian Federal Nuclear Center, Sarov, Nizhni Novgorod oblast, 607190 Russia

e-mail: mailbox@ntc.vniief.ru

Received August 28, 2002; in final form, January 10, 2003

Abstract—A plasma opening switch fed by a helical magnetic explosion generator is developed. A plasma sheath with an axial length of ≈4 cm and an electron density of ~10^{17} cm^{-3} is produced in the electrode gap of the switch by six coaxial gaseous-plasma injectors. A series of explosion experiments shows that the system developed allows one to study the switch at currents of about 2 MA. © *2003 MAIK "Nauka/Interperiodica".*

INTRODUCTION

In the past decade, plasma opening switches (POSs) have advanced into the megaampere current range at a conducting phase duration of 1 μs [1, 2]. In these devices, voltage pulse generators based on capacitive energy storages serve as primary energy sources.

A generator with a POS where a magnetic explosion generator (MEG) is used as a primary energy source was first suggested in [3]. Such an approach had become possible owing to great advances in decreasing the current rise time in the termination. Recent developments have made it possible to transfer currents of amplitudes as high as several tens of megaamperes with a typical current rise time of several microseconds by using disk-shaped MEGs. Currents of amplitudes up to 10 MA with a rise time of <1 μs can now be transferred by means of helical MEGs with cumulative current switches [4].

The use of helical MEGs to form a current pulse of amplitude up to several millions of amperes with a rise time of ≈1 μs suggests a low impedance of the generator termination, i.e., a low inductance (no higher than several tens of nH) and resistance (<10 mΩ). This restriction limits the longitudinal dimension of the POS plasma sheath and requires the sheath to be localized near a feedthrough insulator between the MEG and plasma chamber. Also, it implies the generation of an ultra-high-density plasma.

Erosion plasma injectors, which are currently in common use, generate plasmas in the electrode gap of a POS with densities at a level of $(4–6) \times 10^{15}$ cm^{-3} [5]. In view of conditions imposed on MEG-fed POSs, it seems reasonable to apply coaxial plasma injectors with intermittent gas delivery. It has been shown that such injectors provide plasma channels with an electron density of ~10^{17} cm^{-3}.

A limited number of POS elements implies that the current density per plasma channel (injector) must increase. The transfer of a megaampere current in a device that markedly differs from conventional ones needed experimental verification. Since the experimental technique is very sophisticated and associated explosion experiments are destructive, much theoretical and experimental preliminary work with capacitive storages on laboratory benches had to be done. In the laboratory experiments, we considered the plasma current channels of a POS as electrically independent and studied the properties of only one channel. When selecting the bench parameters, we assumed that the current rise time τ is on the order of 1 μs and the voltage U_0 across the capacitor bank does not exceed the maximum value $U_m \sim 150$ kV, which is typical of a plasma current channel in explosion experiments. Among available benches, the one based on a current pulse generator with $U_0 = 80$ kV and the bank capacitance $C_0 = 8$ μF, the source circuit inductance $L_s \approx 0.2$ μH (which provides the maximal current $J_m = U_0/(L_s/C_0)^{1/2} \approx 500$ kA), and $\tau = (L_sC_0)^{1/2}/4 \approx 1.25$ μs, was the most appropriate.

Below we report the refined design, numerical simulation, and early results of explosion experiments with an MEG-fed POS operating in the conducting mode.

EXPLOSION EXPERIMENT DESIGN

The lack of experience in experimentation with MEG-fed plasma opening switches influenced the design of early experiments and limited the scope of the problems to be solved. The main goals at this stage of investigation were (i) to select an experimental tech-

nique of MEG-induced explosion directed into a vacuum chamber with a spatially confined dense plasma sheath, (ii) evaluate the feasibility of passing a current of ≈2 MA through this plasma sheath, (iii) test the detection system, and (iv) verify the results of the laboratory experiments and model calculation. The plasma chamber was directly connected to the MEG and, accordingly, was destroyed in each of the runs. The vacuum system and the power supply circuit of the plasma injectors were preserved intact.

At a current of ≈2 MA, the POS was fed by a helical MEG with a conic liner. The inner diameter of stator turns is 100 mm. The terminating loop of the helical generator includes a cylindrical explosive switch. Such an arrangement is similar to a VMG-100 device with an explosive switch [4]. The schematic representation of the energy source for a POS is shown in Fig. 1. The initial inductance of the MEG is equal to 20 μH. The destructible conductor of the switch has the form of a cylinder of diameter 100 mm and is made of 0.3-mm-thick copper foil. Inside the helical MEG, differentiating transducers recording the generator current derivative are arranged.

Figure 2 depicts the plasma chamber designed for studying the POS operation in the conducting mode during explosion experiments. The chamber contains coaxial injectors generating a plasma sheath in the electrode gap. Transducers Tr1–Tr3 (not shown) placed in sections S_1–S_3 measure the parameters of the electrical pulse. The current derivative is recorded with differentiating probes. The current pulse amplitude and shape are determined with integrating Rogowski loops.

The experimental design, as well the plasma sheath parameters that ensure the transfer of a ≈2-MA current with a rise time of ≈1 μs, were substantiated by scaling on laboratory benches with capacitive energy storages.

CONDUCTING STAGE OF A PLASMA OPENING SWITCH: NUMERICAL SIMULATION ON LABORATORY BENCHES

When conducting the numerical simulation of the conducting stage, we assumed that the magnetic field penetrates into the plasma via the magnetized plasma region, which compensates for the longitudinal component j_z/σ. In the generalized Ohm's law, this term corresponds to the Hall term $([\mathbf{j} \times \mathbf{B}]_z/(en_e c))$.

The conduction current is compensated for by the Hall current near the anode, where the Hall field is short-circuited. As the electron temperature grows, the plasma magnetization increases; consequently, so do the channel resistance and the rate of penetration of the magnetic field into the plasma. With rising channel resistance, the energy deposition into the magnetized plasma region increases still further, and so on. During this process, the plasma density drops because of gasdynamic relief in the transverse direction. This effect favors, but does not control, the penetration of the magnetic field into the plasma [5, 6].

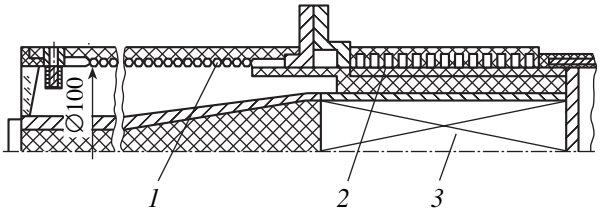

Fig. 1. VMG-100 magnetic explosion generator with an explosive switch. (*1*) Helical VMG, (*2*) explosive electric switch, and (*3*) shaper of divergent cylindrical shock wave.

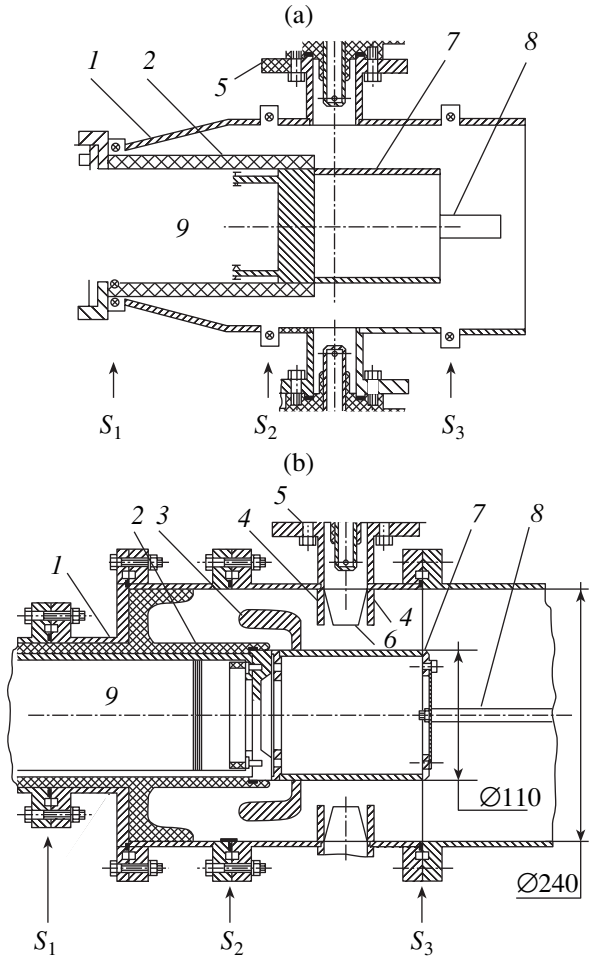

Fig. 2. Plasma chamber. (a) First experiment and (b) second experiment: (*1*) chamber body, (*2*) insulator, (*3*) protecting screen, (*4*) anode rings, (*5*) plasma injector, (*6*) nozzle extensions, (*7*) cathode, (*8*) simulator of termination, and (9) helical MEG.

The numerical calculations were based on a locally planar plasma channel model. An injection-induced plasma channel resulting on the anode side was represented as a parallelepiped with a base area $h \times l$, which equals the contact area between the plasma column and

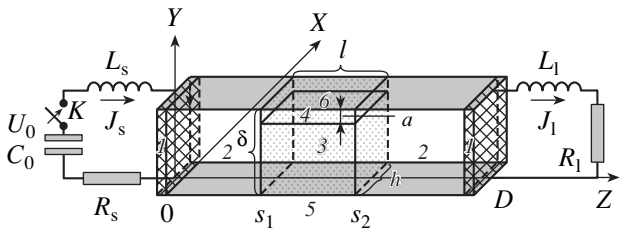

Fig. 3. Geometry used in the calculations: (*1*) solid insulator, (*2*) vacuum, (*3*) plasma, (*4*) magnetized plasma region, (*5*) cathode, and (*6*) anode.

the cathode. The height of the parallelepiped is equal to the electrode gap δ (Fig. 3). Taking into account that the transverse dimension a of the magnetized plasma region is small, ignoring the transverse gasdynamic relief, and neglecting electronic and ionic heat fluxes, one can write the following one-dimensional equations for the dynamics of the magnetized plasma and the component B_x of the magnetic field [6]:

$$\begin{cases} \dfrac{\partial \rho}{\partial t} + \dfrac{\partial(\rho u_z)}{\partial z} = 0, \\ \dfrac{\partial u_z}{\partial t} + u_z\dfrac{\partial u_z}{\partial z} = -\dfrac{1}{\rho}\dfrac{\partial}{\partial z}\left(p + \dfrac{B_x^2}{2\mu_0}\right), \\ \dfrac{\partial B_x}{\partial t} + \dfrac{\partial}{\partial z}(u_z B_x) = \dfrac{\partial}{\partial z}\left[\dfrac{1}{\mu_0\sigma}\dfrac{\partial B_x}{\partial z}\right], \\ \dfrac{\partial \varepsilon_e}{\partial t} + u_z\dfrac{\partial \varepsilon_e}{\partial z} + \dfrac{p_e}{\rho}\dfrac{\partial u_z}{\partial z} = \dfrac{j_y E_y'}{\rho} - 3\dfrac{m_e}{m_i^2}\dfrac{k(T_e - T_i)}{\tau_r/Z}, \\ \dfrac{\partial \varepsilon_i}{\partial t} + u_z\dfrac{\partial \varepsilon_i}{\partial z} + \dfrac{p_i}{\rho}\dfrac{\partial u_z}{\partial z} = 3\dfrac{m_e}{m_i^2}\dfrac{kT_e - kT_i}{\tau_r/z}. \end{cases} \quad (1)$$

Here, z and u_z are the coordinate and mass velocity of the plasma, respectively, along the channel; ρ is the plasma density; $p = p_e + p_i$ is the total pressure, which is the sum of the electronic, p_e, and ionic, p_i, components; ε_e and ε_i are the respective electron and ion internal energies per ion; T_e and T_i are the respective electron and ion energies; m_e and m_i are the respective electron and ion masses; τ_r is the momentum relaxation time; Z is the mean ion charge;

$$\sigma = e^2\frac{Z\rho}{m_i}\frac{\tau_r}{m_e}$$

is the Spitzer plasma conductivity; $\sigma' = \sigma/(1 + \omega^2\tau_r^2)$ is the conductivity of the magnetized plasma; $\omega = e|B_x|/m_e$ is the electron Larmor frequency; $j_y = 1/\mu_0\partial B_x/\partial z$ is the current density; and $E_y' = j_y/\sigma'$ is the electric field in the frame of reference related to the plasma.

Equations (1) are supplemented by the equations of state

$$p_e = Z\frac{\rho}{m_i}kT_e, \quad p_i = \frac{\rho}{m_i}kT_i,$$
$$\varepsilon_e = \frac{3}{2}ZkT_e + \int_0^z I(Z')dZ', \quad \varepsilon_i = \frac{3}{2}kT_i. \quad (2)$$

The mean ion charge Z is determined from the electron temperature T_e [7]:

$$I(Z + 1/2) = kT_e\ln\left[\frac{2m_i}{Z\rho}\left(\frac{2\pi m_e kT_e}{h^2}\right)^{3/2}\right], \quad (3)$$

where the ionization potential $I(Z)$ is considered to be a continuous function of the ion charge.

At the boundaries of the plasma with the source, $z = s_1$, and with the termination, $z = s_2$, the pressure $p|_{z = s_1, s_2} = 0$ and the magnetic fields are defined by the currents in the source circuit, $B_x|_{z = s_1} = \mu_0 J_s/h$, and in the termination circuit, $B_x|_{z = s_2} = \mu_0 J_l/h$. The currents are calculated from the circuit equations

$$\begin{cases} U_s = R_s J_s + \dfrac{d}{dt}(L_s J_s) + \dfrac{d}{dt}(L_s' J_s) + V_s, \\ \dfrac{dU_s}{dt} = -\dfrac{J_s}{C_0}, \quad V_s = E_y'|_{z = s_1} a \end{cases} \quad (4)$$

for the source circuit and

$$V_l + R_l J_l + \frac{d}{dt}(L_l J_l) + \frac{d}{dt}(L_l' J_l) = 0,$$
$$V_l = E_y'|_{z = s_2} a$$

for the termination circuit.

Here, V_s and V_l are the plasma surface voltages on the source side and termination side, respectively; U_s and C_0 are the voltage and the capacitance of the capacitive source; R_s, R_l, L_s, and L_l are the resistances and inductances of the source and termination circuits, respectively; and $L_s' = \mu_0 s_1(t)a/h$ and $L_l' = \mu_0(D - s_2(t))a/h$ are the inductances of the waveguide lines on the source and termination sides, respectively. At zero time, $U_s|_{t = 0} = U_0$ and the current and magnetic field are zero.

The value of the parameter a is related to the skin depth. It was shown [6] that both the critical current J_m and the time taken to achieve this current depend on the initial plasma temperature and parameter a only slightly. In the calculations, it was assumed that, at the initial time instant, $T_e = T_i = T_0 = 1$ eV, the plasma density $\rho = \rho_0$ is uniformly distributed over the channel's cross section, and $a \cong 1$ cm. Such a value of a provides

the best agreement with the experiments on current breaking performed on the Kovcheg setup [8].

Prior to the experiments on the laboratory bench, we carried out three series of scaling calculations with varying source and plasma channel parameters. The geometrical parameters $h \times l$ of the channel were 3.14×4.4 cm (first series), 4.4×4.4 cm (second series), and 6.2×6.2 cm (third series). The parameters of the source circuit $C_0 = 8$ μF and $R_s = 0.015$ Ω were the same in all three series. In the first series, $U_0 = 70$ kV and $L_s = 240$ nH; in the second series, $U_0 = 80$ kV and $L_s = 180$ nH; and in the third series, $U_0 = 80$ kV and $L_s = 200$ nH. Also, it was assumed that $R_l = R_s$ and $L_l = L_s$.

Figure 4 shows typical waveforms of the source current and the current in the termination. Current breaking is observed at $t = \tau_m \approx 1$ μs. At this time instant, the maximal (critical) current is $J_m \approx 300$ kA.

The calculations show the strong dependence of the critical current on the plasma channel geometry $h \times l$ and plasma density ρ_0. The J_m vs. linear plasma density $S_0 = \rho_0 l$ dependence is depicted in Fig. 5. In simulations, current breaks were observed at $S_0 \le 5$ μm/cm^2.

The critical current is seen to grow with plasma density, its value being dependent on the channel–cathode contact area.

To determine the plasma parameters and the conductivity of the plasma current channel induced by coaxial plasma injectors, we carried out a number experiments.

PARAMETERS OF THE PLASMA INDUCED BY A COAXIAL PLASMA INJECTOR: EXPERIMENTAL DETERMINATION

The plasma induced by a plasma injector [9] was studied in the vacuum chamber evacuated to $(5–8) \times 10^{-5}$ torr. A coaxial plasma injector with intermittent gas delivery (Fig. 6) was mounted on one side wall of the chamber. With electromagnetic valve *1*, the gas is delivered to central (inner) electrode *2* of the injector, which is made in the form of a closed tube with an outer diameter of 2 cm. The gas duct diameter is 1.4 cm. The gas leaves the tube through four side openings and enters a cylindrical tube with an inner diameter of 4 cm, which serves as the external electrode of plasma injector *3*. The distance between the gas inlet (the end of the central electrode) and the injector nozzle is 5 cm. In the experiments, a negative voltage of 25 kV from a 12-μF capacitor was applied to the central electrode of the injector. The maximal amplitude and half-period of the current were 125 kA and 6.5 μs, respectively.

The plasma produced by the injector was studied with a Michelson interferometer (He–Ne laser radiation with $\lambda = 0.63$ μm). The interference pattern was recorded by means of a slit-scan streak camera with time and space resolutions of 0.1 μs and 0.3 mm, respectively.

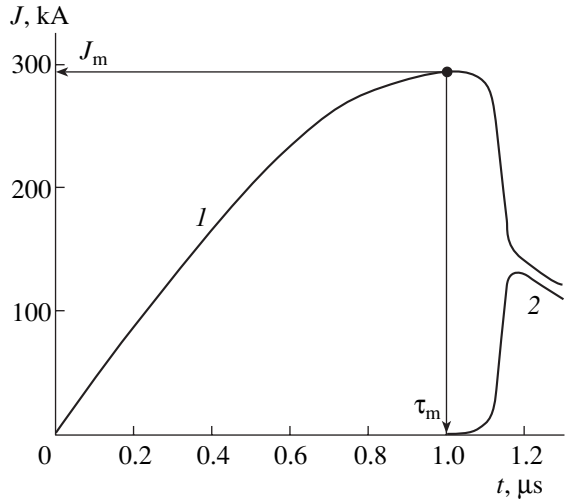

Fig. 4. Time dependences of the (*1*) source current and (*2*) current in the termination (second series, $S_0 = 0.3$ μg/cm^2).

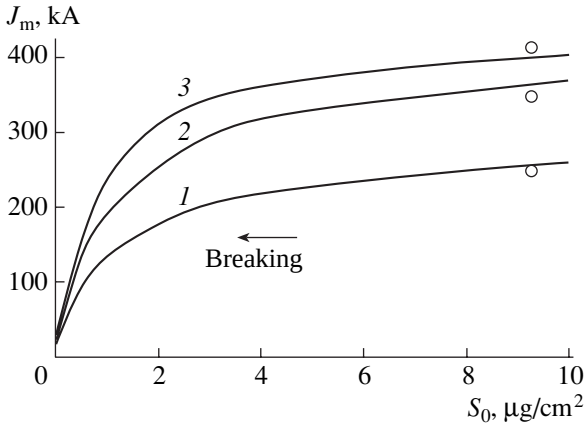

Fig. 5. Calculated dependences of the current on the linear plasma density. The channel dimensions $h \times l$ are (*1*) 3.14×4.4, (*2*) 4.4×4.4, and (*3*) 6.2×6.2 cm. The circle denoted experimental current values related to $S_0 = 9.3$ μg/cm^2.

Tentative results showed that the gas entering the vacuum chamber from the injector does not cause the fringes to shift if the capacitor bank of the plasma injector is switched off. With the bank on, the refractive index of the injected plasma diminished. Therefore, the change in the refractive index was presumably associated with the dominant effect of free plasma electrons.

The integral (along the line of probing) electron concentration (hereafter linear electron concentration) was calculated by the formula

$$n_e l = -1.76 \times 10^{17} \Delta k \ (\text{cm}^{-2}), \qquad (5)$$

where n_e is the optical-path-averaged electron concentration, l is the geometrical length of the plasma object along the line of probing, and Δk is the shift of the fringe relative to its width.

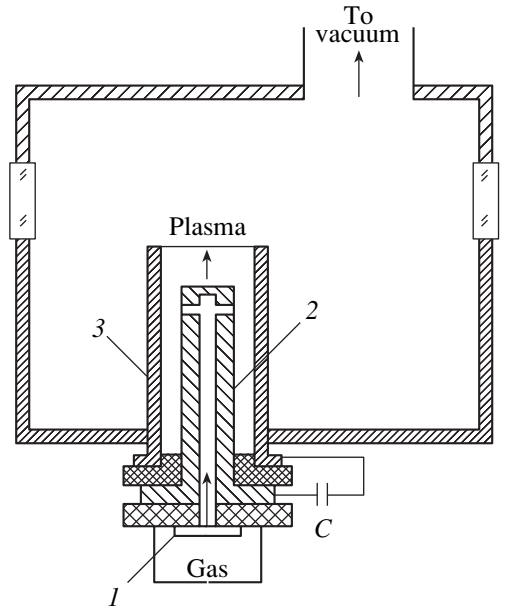

Fig. 6. Plasma injector. (*1*) Electromagnetic valve for intermittent gas delivery, (*2*) inner electrode of plasma injector, and (*3*) outer electrode of plasma injector.

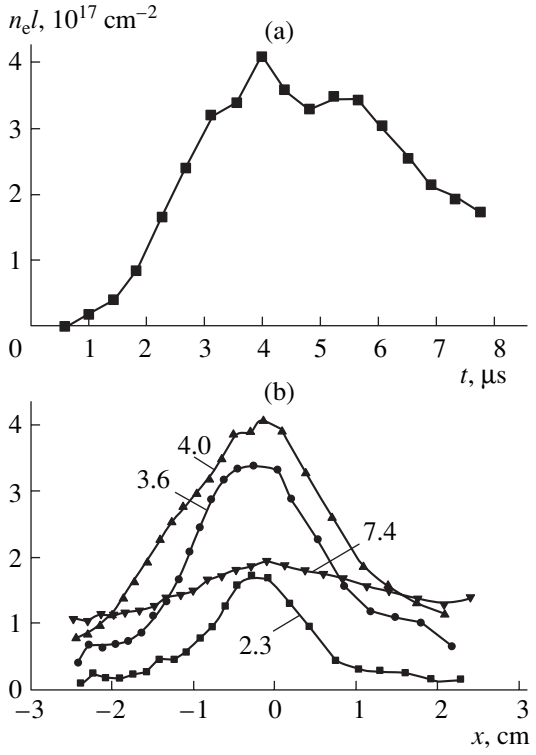

Fig. 7. (a) Time dependence of the linear electron concentration at a distance of 1.5 cm away from the injector and (b) the distribution of the plasma electron concentration across the plasma channel. The figures by the curves are the time instants (μs) at which the distributions of $n_e l$ are taken.

The sensitivity of the method in determining $n_e l$ equals 9×10^{15} cm^{-2}. The numerical coefficient in (5) was found by the double passage of the radiation through the plasma object in view of the electron polarizability at the probing laser wavelength.

The investigations performed allowed us to determine both the optimal delay of gas delivery and the optimal time shift between the instant of initiating the discharge of the capacitive storage of the POS and the instant the plasma injector is switched on. Figure 7 shows the time dependence of the linear electron density at a distance of 1.5 cm away from the injector and the electron density distribution over the cross section of the plasma channel at the exit from the injector under its optimal operating conditions.

From Fig. 7 it follows that the linear electron concentration reaches a maximum of $\approx 4 \times 10^7$ cm^{-2} roughly by the fourth microsecond. For single ionization, this agrees with the linear plasma density $S_0 \approx 9.3$ μg/cm^2 and with three calculated values of the critical current in the POS circuit (J_m = 260, 360, and 400 kA, respectively, for the first, second, and third series of calculations) (Fig. 5).

EXPERIMENTAL INVESTIGATION OF THE PLASMA CURRENT CHANNEL CONDUCTIVITY

The aim of this investigation was to find the maximal current that can pass through the plasma channel upon using various replaceable electrodes.

We employed a POS with two, generally misaligned, cylindrical electrodes. The plasma channel was produced by a single plasma injector and filled the electrode gap only partially. The channel–cathode contact area was varied by varying the geometry of the internal electrode (cathode). The configurations of the POS electrodes used in three series of experiments are schematically depicted in Fig. 8. The diameter of the cathode was 20 mm (the first series), 85 mm (the second series), and 250 mm (the third series). The former two were placed at a distance of 30 mm away from the nozzle of the injector; the cathode with a diameter of 250 mm, 80 mm away from the injector. Based on the interferometry data, the channel–cathode contact areas were estimated as ≈14, 20, and 40 cm^2, respectively. These values are close to those used in the three series of calculations (Fig. 5).

The setup used for studying the plasma current channel conductivity is represented in Fig. 9. It includes a capacitive storage (a GIT-100 current pulse generator), which is connected to the POS via a feedthrough insulator. The GIT-100 parameters are as follows: the capacitance is 8 μF; the self-inductance, 35–40 nH; the charging voltage, 70–90 kV; and resistance of the GIT gaps, 15–20 mΩ. A plasma injector is mounted on the 480-mm-diameter outer tube (POS anode) of the vacuum chamber. The total inductance of

the circuit with the 20-mm-diameter cathode is 240 nH; in the other two configurations, 160–180 nH. The vacuum chamber is evacuated to $\approx 2 \times 10^{-4}$ torr. The plasma is generated by a high-current discharge in the electrode gap of a coaxial injector with intermittent gas (air) delivery. The amplitude and half-period of the discharge current in the injector are, respectively, ≈120 kA and 6.5 μs. One Rogowski loop is placed at the beginning of the feedthrough insulator to measure the total current and another, in the vacuum chamber to measure the current through the plasma channel. The range of maximal current was sought by varying the plasma injection time and also the time delay between gas delivery to the channel and energizing the capacitor bank of the injector.

The current waveforms for the three electrode configurations are shown in Fig. 10. The current is maximal for the 250-mm-diameter cathode and an electrode gap of 80 mm, i.e., for the case when the plasma–cathode contact area is the largest.

It should be noted that the plasma injection times and delays between injection bank switching and gas delivery that correspond to the maximal currents in the experiments coincided with the times taken to achieve the maximal plasma density. The current amplitudes that were measured in the experiments with the 20-, 85, and 250-mm-diameter cathodes (I_m = 250, 350, and 410 kA, respectively) agree well with those calculated for the measured linear plasma density $S_0 \approx 9.3$ μg/cm^2 (Fig. 5).

Thus, the comprehensive analytical and experimental investigations of the plasma parameters and the parameters of the plasma channel provided a complete consistent set of the properties of a single-plasma-channel POS operating in the conducting mode. This made it possible to substantiate the number and operating conditions of MEG-fed POSs in explosion experiments aimed at transferring a current of amplitude ≈2 MA and rise time of ≈1 μs.

RESULTS OF EXPLOSION EXPERIMENTS

In these experiments, we tested the VMG-100 magnetic explosion generator terminated by a POS-equivalent termination and carried out two runs with plasma injectors. It was found that a current of amplitude ≈2 MA may be achieved if five plasma injectors operate synchronously under optimal conditions. The plasma bridge was produced by six plasma injectors. The waveforms of the current recorded by Tr1 in the section S_1 in three runs are demonstrated in Fig. 11.

The test where the VMG-100 was terminated by a POS-equivalent termination shed light on the efficiency of operation with an explosive switch. This test differed from subsequent ones in that plasma injectors were absent and plasma channels were replaced by conducting jumpers. In the explosive switch, a 190-mm-long destructible conductor was used.

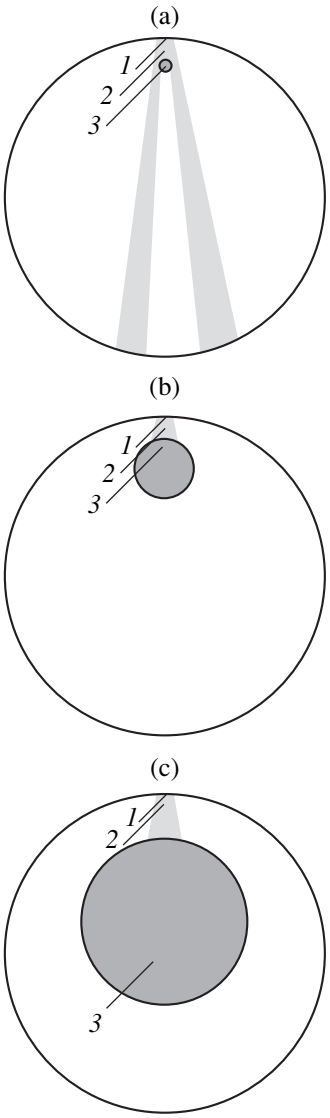

Fig. 8. Electrode configurations in (a–c) three series of runs: (*1*) anode, (*2*) plasma current channel, and (*3*) cathode.

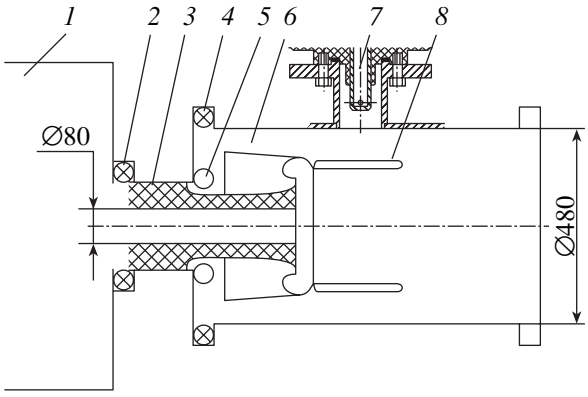

Fig. 9. Experimental setup: (*1*) current pulse generator, (*2*) Rogowski loop to measure the generator current, (*3*) feed through insulator, (*4*) Rogowski loop to measure the current in the vacuum chamber, (*5*, *6*) guide electrodes, (*7*) plasma injector, and (*8*) replaceable electrode.

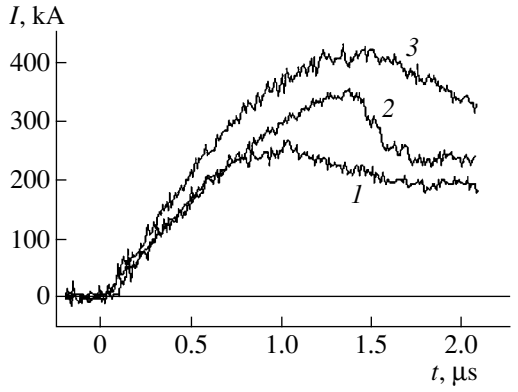

Fig. 10. Characteristic current pulse waveforms for a cathode diameter of (*1*) 20, (*2*) 85, and (*3*) 250 mm.

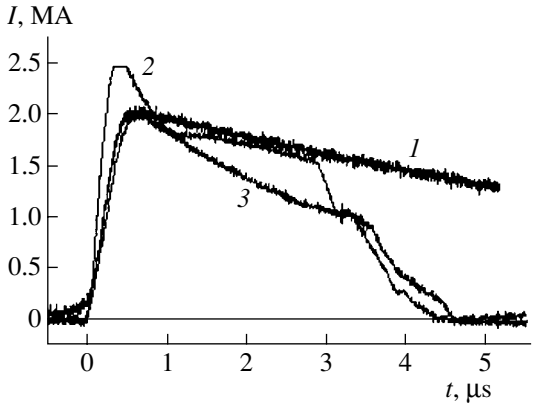

Fig. 11. Current waveforms in the section S_1. (*1*) Run with the equivalent terminating load, (*2*) run 1 with the plasma terminating, and (*3*) run 2 with the plasma terminating load.

In the terminating loop of the helical MEG with an inductance of ≈20 nH, a current pulse of amplitude 6.9 MA and characteristic rise time of ≈10 μs (at the final stage of generator operation) was observed. The maximal value of the current derivative in the helical generator was found to be 7.4×10^{11} A/s. Note that, in subsequent experiments, the output parameters of the helical MEG were almost the same.

In the presence of the POS, the termination with an inductance of 40 nH formed a current pulse of amplitude ≈2 MA and rise time of 0.7 μs (Fig. 11, curve *1*). The maximal value of the current derivative in this case is 5.2×10^{12} A/s, which corresponds to a voltage of ≈200 kV across the switch.

The waveforms of the signals from Tr1 obtained in the first run with the plasma termination (Fig. 2a) indicate that, when the electrical loop of the VMG-100 breaks, the current rise time is shorter than in the test with the inductive termination 40 nH. In the explosive switch circuit, the pulse rise time is ≈0.5 μs. Because of such a short rise time, Tr1 failed to measure the maximal current derivative. However, from the set of data obtained, it follows that the operation of the switch in the section S_1 generated a current of amplitude >2.6 MA (Fig. 11, curve *2*). The high amplitude and the short rise time of the current pulse that are recorded by Tr1 can be explained by the presence of the conducting region on the surface of insulator *2*, which appears when the switch is terminated by the loop with an inductance of 20–30 nH (this value is lower than the inductance of the loop bounded by the sections S_1 and S_2). This statement is also substantiated by the readings of Tr2, which show that, within initial ≈0.5 μs of switch operation, the current amplitude in the termination rises to only ≈50 kA, while within subsequent ≈0.7 μs, it grows to ≈300 kA.

The waveforms obtained can be treated as follows. Since the end part of the feedthrough insulator is exposed to the plasma from the injector, a plasma cloud has formed over the insulator on the injector side by the time of switch operation. This cloud shunts the cavity where Tr2 are placed. On operation of the switch, feedthrough insulator *2* undergoes surface breakdown. In the plasma sheath produced by the injectors, the current grows slowly and does not reach the value that can pass through the plasma. The spread in the Tr2 readings may be associated with the asymmetry of the current related to the surface breakdown. In the section S_3, the current appears 2.5 μs after the appearance of the current in the section S_2 and even its peak value is twice as low as the current in the section S_2. This points to a high conductivity of the plasma sheath.

Thus, the breakdown of insulator *2* increases the amplitude of the current pulse and shortens its rise time in the termination. Currents above 2.6 MA are observed when the initial inductance of the termination is ≈20 nH. The subsequent fast fall of the current to ≈1.8 MA may be associated with the expansion of the plasma sheath under the action of the magnetic field, causing a higher inductance loop to form.

In the second run with the plasma termination, the design of the experimental setup was somewhat modified. The length of the foil used in the explosive switch was shortened to 100 mm in order to decrease the maximal output voltage of the MEG. The vacuum chamber was that shown in Fig. 2b. Insulator *2* of the vacuum chamber was made in the form of a bicylinder and covered the cathode and a part of the anode. To protect the insulating surface against the plasma radiation, the cylindrical cathode was equipped with screen *3*, which, together with anode rings *4*, retards the propagation of the plasma toward the insulator. Injectors *5* were shifted to the right from the insulator by 30 mm. Nozzle extensions *6* serve to improve the azimuth homogeneity of the plasma sheath in the gap between the cathode and anode rings *4*. At the exit from the injectors, the extensions have a circular cross section of diameter 40 mm; on the cathode side, they have an elliptical cross section with minor and major axes of 30 and 60 mm, respectively. The anode–cathode gap is 30 mm. The interfer-

ometric data confirmed that conical nozzles generate plasma jets with a desired shape of the cross section.

In this experiment, all the energy systems, including the MEG, behaved as expected. Comparing the current signals with the readings of the transducers in section S_1 (Fig. 11) shows the absence of the surface breakdown in this experiment. As follows from the run with the POS-equivalent termination, the current amplitude 2 MA is observed at an inductance of 40 nH. Assuming that the inductance remains constant, one can estimate the total resistance of the loop from the rate of fall of the current. It turned out to be 13–15 mΩ in this experiment and 5–6 mΩ in the experiment with the equivalent termination. Hence, the resistive contribution of the plasma to the terminating load is 7–10 mΩ. The fall of the current may be related to both the plasma resistance and an increase in the terminating inductance because of the drift of the current channel. These two reasons cannot be distinguished from each other without special diagnostics. If it is assumed that the rate of fall of the current varies only because of an increase in the inductance of the loop, $dL/dt = 10$ nH/μs. It is then easy to check that the maximal rate of the axial drift of the current channel is no higher than several cm/μs at a current level of ≈2 MA.

CONCLUSIONS

The comprehensive analytical and experimental investigation of the plasma parameters and the parameters of the plasma current channel allowed us to refine the design of explosion experiments where a plasma opening switch is fed by an MEG.

The successful experiments on ≈2-MA current transfer through the POS make it possible to study conditions for current breaking at this and higher levels of energy applied to the plasma chamber.

The results obtained in this work open up possibilities for creating unique devices based on an inductive storage with an MEG-fed POS. These devices are expected to generate currents with amplitudes as high as several tens of megaamperes and rise times of several tens of nanoseconds.

ACKNOWLEDGMENTS

This work was supported by the Sandia National Laboratories (USA) (contract no. 17665).

REFERENCES

1. W. Rix, P. Coleman, J. R. Thompson, *et al.*, IEEE Trans. Plasma Sci. **25**, 169 (1997).
2. S. P. Bugaev, A. M. Volkov, A. A. Kim, *et al.*, Izv. Vyssh. Uchebn. Zaved. Fiz., No. 12, 38 (1997).
3. N. F. Popkov, V. Ya. Averchenkov, A. S. Pikar', *et al.*, in *Proceedings of the 7th International Conference "Megagauss Magnetic Fields Generation and Related Topics" (MG-VII)*, Ed. by V. K. Chernyshev, V. D. Selemir, and L. N. Plyashkevich (VNIIÉF, Sarov, 1997), Vol. 2, p. 736.
4. V. D. Selemir, V. A. Demidov, L. N. Plyashkevich, *et al.*, in *Proceedings of the 7th International Conference "Megagauss Magnetic Fields Generation and Related Topics" (MG-VII)*, Ed. by V. K. Chernyshev, V. D. Selemir, and L. N. Plyashkevich (VNIIÉF, Sarov, 1997), Vol. 1, p. 248.
5. B. V. Weber, D. D. Hinshelwood, and R. J. Commisso, IEEE Trans. Plasma Sci. **25**, 189 (1997).
6. V. F. Bukharov, Yu. V. Vlasov, V. A. Demidov, *et al.*, Zh. Tekh. Fiz. **71** (3), 57 (2001) [Tech. Phys. **46**, 326 (2001)].
7. Yu. P. Raĭzer, Zh. Éksp. Teor. Fiz. **36**, 1583 (1959) [Sov. Phys. JETP **9**, 1124 (1959)].
8. V. I. Chelpanov, V. A. Adakin, V. F. Bukharov, *et al.*, in *Proceedings of the 12th IEEE International Pulsed Power Conference (PPC'99), Monterey (California), 1999*, Vol. 2, p. 1029.
9. S. Yu. Kornilov, V. V. Borovkov, V. I. Chelpanov, *et al.*, in *Proceedings of the 1st International Congress on Radiation Physics, High Current Electronics, and Modification of Materials, Tomsk, 2000*, Vol. 2, p. 332.

Translated by V. Isaakyan

Technical Physics, Vol. 48, No. 7, 2003, pp. 928–930. Translated from Zhurnal Tekhnicheskoĭ Fiziki, Vol. 73, No. 7, 2003, pp. 133–135.

BRIEF COMMUNICATIONS

Inequalities for Electrostatic Energy

V. A. Antonov

Main (Pulkovo) Astronomical Observatory, Russian Academy of Sciences, Pulkovskoe shosse 65, St. Petersburg, 196140 Russia

Received November 20, 2002

Abstract—The potential energy for a set of a finite number of point charges that are assumed to be aligned is calculated. The lower estimate of the energy is formally obtained by calculating the interactions between neighboring charges, with each interaction considered as attraction. In another (quantum mechanical) approach, the three-dimensional problem of N bodies is studied. It is established that the lower energy level rises in absolute value no faster than N. This result is extended to the case when the particles have different masses. © *2003 MAIK "Nauka/Interperiodica".*

INTRODUCTION

The calculation of the energy of nonrelativistic electrostatic interaction in a set of elementary charges is of interest for a number of problems in solid-state physics and plasma physics. As a rule, specific cases where the charges are regularly arranged at lattice sites are studied. However, there may appear the need for investigating more general configurations. In this work, we will analyze a linear but not strictly uniform arrangement of charges in terms of the classical approach and find the lower estimate of the potential energy. Since the kinetic energy makes only positive contribution, there is no point in including it in the calculations.

In the quantum-mechanical approach, on the contrary, the particle motion cannot be neglected according to the Heisenberg relations. Mathematically, to obtain the lower estimate of the total energy of N particles interacting electrostatically means to minimize a certain functional of the wave function ψ in the $3N$-dimensional configuration space (we consider the three-dimensional case).

In both approaches, we use the same auxiliary inequality for an exponential law of interaction taken by convention.

BASIC INEQUALITY

Consider an arbitrary number of points with coordinates x_j $(1 \le j \le N)$ such that

$$x_1 < x_2 < \ldots < x_N. \tag{1}$$

These points are assigned charges $\varepsilon_j = \pm 1$ in any combination. We will prove that

$$\sum_{i<j} \varepsilon_i \varepsilon_j e^{-|x_i - x_j|} \ge -\sum_{j=1}^{N-1} e^{-(x_{j+1} - x_j)} \quad (\varepsilon_j = \pm 1) \tag{2}$$

by applying induction in N. At $N = 2$, the statement is obvious. Consider the case $N > 2$. Let L be the difference between the left- and right-hand sides of Eq. (2). This quantity is a function of $N - 1$ variables $u_i = \exp(x_i - x_{i+1})$, has the domain of definition $0 \le u_i \le 1$ $(i = 1, 2, \ldots, N - 1)$ (by virtue of (1)), and is linear in each of the arguments u_i. As any polylinear form, L reaches a maximum at one of the vertices of this cube. However, if at least one of the quantities u_i vanishes, the statement is proved, since the set of N particles is virtually portioned into subsets consisting of a smaller number of particles. It remains to check the vertex $u_1 = u_2 = \ldots = u_{n-1} = 1$, to which there corresponds $x_1 = x_2 = \ldots = x_N = x$; hence,

$$L = \sum_{i<j} \varepsilon_i \varepsilon_j + N - 1 = \frac{1}{2}\left(\sum_{i=1}^{N} \varepsilon_i \sum_{j=1}^{N} \varepsilon_j - N\right) + N - 1 > 0,$$

which proves the statement.

Obviously, each of the exponents can be multiplied by an arbitrary positive factor:

$$\sum_{i<j} \varepsilon_i \varepsilon_j e^{-k|x_i - x_j|} \ge \sum_{j=1}^{N-1} e^{-k(x_{j+1} - x_j)} \tag{3}$$
$$(\varepsilon_j = \pm 1, k > 0).$$

CLASSICAL CHARGED PARTICLES

Integrating (3) over k from 0 to ∞, we arrive at

$$\sum_{i<j} \frac{\varepsilon_i \varepsilon_j}{|x_i - x_j|} \ge -\sum_{i=1}^{N-1} \frac{1}{x_{i+1} - x_i} \quad (\varepsilon_i = \pm 1) \tag{4}$$

subject to previous condition (1). Thus, for the energy, for example, of a system of electrons and protons located along an axis, the lower estimate is obtained if we take into account only the negative energy of pairwise interaction between particles.

1063-7842/03/4807-0928$24.00 © 2003 MAIK "Nauka/Interperiodica"

The authors of [1], elaborating upon an idea in [2], derived a similar inequality for the spatial distribution of point charges of any value and sign:

$$\sum_{i<j}\varepsilon_i\varepsilon_j r_{ij}^{-1} \geq -\sum_{i=1}^{N}\frac{\varepsilon_i^2}{\alpha_i}, \tag{5}$$

where r_{ij} is the distance between relevant point and $\alpha_i = \min_{j\neq i} r_{ij}$.

In our case of the nonlinear distribution of unit charges, expression (4) is a better estimator than expression (5), although the right-hand sides differ only by a factor of no more than 2.

QUANTUM CHARGED PARTICLES IN SPACE

Consider the Hamiltonian for the one-dimensional motion of N particles that have identical masses and obey an exponential law of interaction:

$$\hat{H} = \sum_{j=1}^{N}\frac{\hat{p}_i^2}{2m} + \sum_{i<j}\varepsilon_i\varepsilon_j k e^{-k|x_i - x_j|} \quad (k>0,\ \varepsilon_j = \pm 1). \tag{6}$$

The least eigenvalue H_m of operator (6) can be evaluated from the conventional variational definition

$$H_m = \min\frac{\int\psi^*\hat{H}\psi d\Omega}{\int\psi^*\psi d\Omega} \tag{7}$$

(where $d\Omega = dx_1, dx_2, \ldots, dx_n$) in the class of continuously differentiable normalizable complex functions $\psi(x_1, x_2, \ldots, x_N)$. The entire N-dimensional configuration space is divided into $N!$ zones differing by the mutual order of quantities x_j. We weaken the continuity conditions for the wave function in the sense that we abandon the necessary coincidence of its values when approaching the boundary between the zones on both sides. In this case, the minimum in (7) may only decrease. Then, the numerator and the denominator of fraction (7) are split into the sums of $N!$ terms, the pairs corresponding to different zones being totally identical and unrelated to each other. It is easy to check that taking the integrals over one typical zone defined by (1) would suffice to evaluate H_m. From inequality (2), it follows that

$$H_m \geq \min\frac{\int\psi^*\hat{H}\psi d\Omega}{\int\psi^*\psi d\Omega},$$

where

$$\hat{H}_i = \sum_{j=1}^{N}\frac{\hat{p}_j^2}{2m} - k\sum_{j=1}^{N-1}e^{-k(x_{j+1}-x_j)}$$

and integration is performed over domain (1). Next, we apply the transformation $\hat{P}_1 = \hat{p}_1$, $\hat{Q}_1 = \hat{q}_1$, $\hat{P}_j = (1/2)(\hat{p}_j - \hat{p}_{j-1})$, and $\hat{Q}_j = (1/2)(\hat{q}_j - \hat{q}_{j-1})$ $(2\leq j\leq N)$ (the operator $\hat{q}_j$ is known to mean mere multiplication by x_j) under which the Heisenberg relations

$$\hat{Q}_j\hat{P}_j - \hat{P}_j\hat{Q}_j = \hat{q}_j\hat{p}_j - \hat{p}_j\hat{q}_j = i\hbar \quad (1\leq j\leq N) \tag{8}$$

remain valid.

Accordingly, using the commutativity of $\hat{p}_j$ with various j, we find

$$\frac{\hat{p}_{j-1}^2 + \hat{p}_j^2}{2} = \left(\frac{\hat{p}_j^2 - \hat{p}_{j-1}^2}{2}\right)^2 + \left(\frac{\hat{p}_{j-1}^2 - \hat{p}_j^2}{2}\right)^2 \quad (2\leq j\leq N), \tag{9}$$

$$\hat{H}_1 \geq \hat{H}_2 = \sum_{j=2}^{N}\left(\frac{\hat{P}_1^2}{m} - ke^{-k\hat{Q}_j}\right).$$

In going to the Hamiltonian $\hat{H}_2$, the coordinate Q_1 becomes of no significance, so that integration over it can be omitted. The remaining $N-1$ coordinates obey only the positiveness condition independently of one another. Thus, we have separated the variables and, consequently,

$$H_m \leq -(N-1)\lambda,$$

$$\lambda = \min\frac{\int\psi^*\left(\frac{\hat{P}^2}{m} - ke^{-kQ}\right)\psi d\Omega}{\int\psi^*\psi d\Omega}$$

now with one-dimensional wave functions. However, in view of (9), the determination of λ is equivalent to finding the eigenvalue for the Schrödinger equation

$$\frac{\hbar^2}{m}\frac{d^2\psi}{dx^2} + (\lambda + ke^{-kx})\psi = 0, \tag{10}$$

where the function $\psi(x)$ does not have nodes and meets the "free" boundary condition $\psi'(0) = 0$. We virtually need only the asymptotics at $k\longrightarrow\infty$. It can be easily found by expressing a desired solution to (10) through the Bessel functions. However, for physical problems of such a kind, the conventional approximation (at $x \gg k^{-1}$)

$$\psi(x) = ce^{-\mu x}, \quad \mu = \frac{\sqrt{-m\lambda}}{\hbar} \tag{11}$$

is more illustrative.

We integrate the left-hand side of (10) over a narrow potential well in the vicinity of the origin, taking into account that the function $\psi(x)$ has no time to vary significantly and the term $\lambda\psi$ is relatively small. Then,

$$\frac{\hbar^2}{m}\psi'(x) + \psi(x) = 0 \quad (k^{-1} \ll x \ll \mu^{-1}).$$

Comparing with (11) gives approximately

$$\mu = \frac{m}{\hbar^2}, \quad \lambda = -\frac{m}{\hbar^2}.$$

Eventually, we find that

$$H_m \geq -(N-1)\frac{m}{\hbar^2} + o(1) \tag{12}$$

with large k.

However, the above reasoning holds if the motion of the particles is considered to be three-dimensional and x_j and $\hat{p}_j$ in (6) are replaced by the projections of the radius vector and vector momentum operator onto a fixed axis. Actually, this means that x_j and $\hat{p}_j$ ($j = 1, 2, \ldots, N$) are viewed as $\alpha x_j + \beta y_j + \gamma z_j$ and $\alpha \hat{p}_{jx} + \beta \hat{p}_{jy} + \gamma \hat{p}_{jz}$, respectively.

Let us average Hamiltonian (6) (with the above substitution) over the directions of the unit vector (α, β, γ). After averaging Hamiltonians with the same spectra, the lower estimate of (6) can only rise. Performing straightforward calculations on the assumption that all the directions are equivalent, we come from (12) to

$$\frac{1}{6m}\sum_{j=1}^{N}(\hat{p}_{jx}^2 + \hat{p}_{jy}^2 + \hat{p}_{jz}^2) + \sum_{i<j}\varepsilon_i\varepsilon_j\frac{1-e^{-kr_{ij}}}{r_{ij}}$$
$$\geq -(N-1)\frac{m}{\hbar^2} + o(1)$$

(where $r_{ij} = \sqrt{(x_i - x_j)^2 + (y_i - y_j)^2 + (z_i - z_j)^2}$), which is the inequality for the spectrum edge.

Finally, if k tends to ∞, we find the exact, rather than asymptotical, inequality

$$\frac{1}{2m}\sum_{j=1}^{N}\hat{p}_j^2 + \sum_{i<j}\frac{\varepsilon_i\varepsilon_j}{r_{ij}} \geq -\frac{(N-1)m}{3\hbar} \tag{13}$$

(here, $3m$ was replaced by m). Thus, the ground-state energy of a set of a large number N of oppositely charged elementary particles with a given mass m rises in absolute value no faster than N. This conclusion (easily predictable by intuition has been drawn under different simplifying assumptions (splitting into $N/2$ isolated pairs, etc.), but the general proof seems to be lacking in the literature.

Note that no assumptions concerning the similarity of the particles were used.

We believe that the frequently cited result for a dense gas of particles that obey the general statistics is incorrect and misleading. In [3], the (negative) asymptotical estimate of the lower energy level was derived. It is proportional to $N\rho^{1/4}$ (ρ is the spatial plasma density), which is in obvious disagreement with inequality (13), since we said nothing about either restrictions on the density of the system or the identity of electrons.

The inconsistency involved in the calculations performed in [3] can be found in the following way. If we assume that the corresponding result is true, the average kinetic energy of an individual particle in its ground state must then be roughly equal (according to the virial theorem) to

$$T_0 = \rho^{1/4} \tag{14}$$

in the system of units where $m = \varepsilon = \hbar = 1$. Accordingly, the relaxation time must be on the order of $\rho^{-5/8}$ or somewhat less (due to the logarithmic factor). However, in view of the uncertainty relation, energy T is not a strictly determined quantity in the range of $T < \rho^{5/8}$ and can hardly serve as the argument of the quantum-mechanical propagator. However, quantity (14) falls into this "bad" range at large ρ. In other words, in this model, fluctuations evolve so rapidly that one cannot pass from the inertial to true motion by the summation of perturbations. Such contradictions are absent in the case of fermion gas and in the theory of hot plasma [4], where, as a rule, the characteristic specific kinetic energy considerably exceeds that defined by formula (14).

DIFFERENT MASSES

When the particles have different masses $m_1, m_2, \ldots, m_N$, an estimate like (13) is the simplest to derive by replacing all the masses by the largest one. However, it is possible to apply a more elegant expedient. Generalizing (9), one may take advantage of the fact that

$$\frac{p_j^2}{2m_j} + \frac{p_{j-1}^2}{2m_{j-1}} - \frac{(p_j - p_{j-1})^2}{2(m_j + m_{j-1})}$$

is a positive definite form.

Next, in the expression for H_2, m is replaced by $(1/2)(m_j + m_{j-1})$. Note that the numbering of the masses in each of the $N!$ zones will be different. However, the result of replacing the same m by pairwise arithmetic means on the right of (12) makes it possible to express the general estimate from below in the form

$$-\frac{m_1 + m_2}{2} - \frac{m_2 + m_3}{2} - \ldots - \frac{m_{N-1} + m_N}{2}$$
$$\geq -(m_1 + m_2 + \ldots + m_N).$$

Eventually, expression (13) is generalized as

$$\sum_{j=1}^{N}\frac{1}{2m_j}\hat{p}_j^2 + \sum_{i<j}\frac{\varepsilon_i\varepsilon_j}{r_{ij}} \geq -\frac{1}{3\hbar^2}\sum m_j.$$

REFERENCES

1. F. J. Dyson and A. Lenard, J. Math. Phys. **8**, 423 (1963).
2. L. Onsager, J. Phys. Chem. **43**, 189 (1939).
3. M. J. Stephen, Proc. Phys. Soc. **79**, 994 (1962).
4. V. S. Lisitsa, Usp. Fiz. Nauk **122**, 449 (1977) [Sov. Phys. Usp. **20**, 603 (1977)].

Translated by Yu. Vishnyakov

Technical Physics, Vol. 48, No. 7, 2003, pp. 931–933. Translated from Zhurnal Tekhnicheskoĭ Fiziki, Vol. 73, No. 7, 2003, pp. 136–138.

BRIEF COMMUNICATIONS

Self-Consistent Thermodynamic Approach to Calculating the Grüneisen Parameters of the Crystal Lattice in Solids

V. Yu. Bodryakov and A. A. Povzner

Ural State Technical University, ul. Mira 19, Yekaterinburg, 620002 Russia

e-mail: povz@kf.ustu.ru

Received December 17, 2002

Abstract—For a nonmetallic isotropic paramagnetic solid, a set of generalized Grüneisen parameters γ_i that are suitable in applied computations is introduced. Exact thermodynamic expressions for the temperature dependences of the Grüneisen parameters γ_θ and γ_θ^* are derived, and basic factors responsible for these dependences are found. Thermodynamic conditions under which the parameter γ_θ changes sign and the Invar effect shows up in the material are determined. © *2003 MAIK "Nauka/Interperiodica".*

(1) The dimensionless Grüneisen parameter Γ, together with the characteristic Debye temperature θ, is a basic parameter in the solid-state theory. It is defined as the isothermal logarithmic derivative of the Debye temperature with respect to volume V [1, 2]:

$$\Gamma = -\left(\frac{\partial \ln\theta}{\partial \ln V}\right)_T. \quad (1)$$

Generally speaking, the parameter Γ characterizes the average "distortion" of the phonon spectrum of acoustic oscillations in the lattice by an applied voltage, which changes the solid volume. For most solids, the Grüneisen parameter is positive and close to unity. In some cases, however, Γ may change sign and become negative. It is believed (see, e.g., [2]) that such a reversal may be responsible for the unusual behavior of the thermal expansion coefficient in a number of materials, such as Si and Ge. In these materials, the thermal expansion coefficient changes sign, becoming negative in a rather wide range of low temperatures (the so-called Invar anomaly). This fact has been known for a long time and is explained [2] by the features of the phonon spectrum. However, an adequate thermodynamic interpretation of this phenomenon is still lacking. Even thermodynamic conditions under which the Grüneisen parameter changes sign remain unclear. Thermodynamic properties whose anomalous behavior is responsible for the Invarness of the materials mentioned above are also unknown.

The aim of this work is to calculate the Grüneisen parameters of the first and second order for a nonmetallic isotropic paramagnet by using a self-consistent thermodynamic approach. This study elaborates upon the authors' ideas put forward in previous publications [3–6].

Let us introduce for convenience generalized Grüneisen parameters γ_i of the first (γ_i) and second (γ_i^*) order, which are defined as

$$\begin{cases} \gamma_i = \dfrac{V}{i}\left(\dfrac{\partial i}{\partial V}\right)_T, \\ \gamma_i^* = \dfrac{V^2}{i}\left(\dfrac{\partial^2 i}{\partial V^2}\right)_T, \end{cases} \quad (2)$$

where $i = \theta$, θ_l, θ_t, K, K_0, K_{ph}, σ, Ξ, Ξ_l, and Ξ_t (see the text). It is easy to check that the Grüneisen parameter γ_θ from (2) coincides with conventional definition (1) up to the sign.

As was already mentioned, we are interested in the temperature dependences of the parameters γ_θ and γ_θ^*.

(2) The parameter specifying the value of the Grüneisen parameter γ_θ is the Debye temperature, which is conveniently represented as the average over one longitudinal and two transverse branches of the phonon spectrum of acoustic oscillations in the crystal lattice [1]:

$$\theta = \left(\frac{3}{1/\theta_l^3 + 2/\theta_t^3}\right)^{1/3}. \quad (3)$$

The partial Debye temperatures θ_l and θ_t that correspond to longitudinal and transverse acoustic oscillations, respectively, are given by

$$\theta_l = \frac{\hbar(6\pi^2 N_A)^{1/3}}{k_B}\sqrt{\frac{K + \frac{4}{3}G}{\mu}}V^{1/6}; \quad (4)$$

1063-7842/03/4807-0931$24.00

$$\theta_t = \frac{\hbar(6\pi^2 N_A)^{1/3}}{k_B}\sqrt{\frac{G}{\mu}}V^{1/6}. \quad (5)$$

In (4) and (5), $\hbar$, N_A, and k_B are the Planck constant, the Avogadro number, and the Boltzmann constant, respectively; μ and V are the molar weight and volume, respectively; and K and G are the bulk and shear moduli, respectively. The well-known relationships of the elasticity theory [7],

$$K + \frac{4}{3}G = 3\frac{1-\sigma}{1+\sigma}K,$$

$$G = 3\frac{1-2\sigma}{1+\sigma}K,$$

allow us to express the so-called longitudinal elastic modulus K and the transverse elastic (shear) modulus G through the Poisson's ratio σ and the bulk modulus. Since the Poisson's ratio lacks the thermodynamic definition and there is no reliable data for its temperature dependence, we will assume it to be a temperature independent material constant. Then, the temperature dependences of the partial Debye temperatures given by (4) and (5) are related largely to the temperature dependences of the bulk modulus and molar volume.

In view of the aforesaid, the partial Debye temperatures can be expressed in the mathematically convenient form

$$\theta_i = \text{const}\,\Xi_i^{1/2}K^{1/2}V^{1/6}, \quad (6)$$

where the subscript $i = l, t$ for the longitudinal and transverse phonon oscillation modes, respectively. The constant in (6), which is of no significance for the subsequent calculations, is given by

$$\text{const} = \sqrt{\frac{3}{\mu}}\hbar(6\pi^2 N_A)^{1/3}/k_B,$$

and

$$\Xi_i = \begin{cases} \dfrac{1-\sigma}{1+\sigma}, & i = l \\ \dfrac{1-2\sigma}{1+\sigma}, & i = t. \end{cases} \quad (7)$$

Thus, expression (6) contains in explicit form the thermodynamic parameters that are functions of volume (Ξ, K, and V) and those depending on temperature (K, V). For the molar volume and bulk modulus, we will employ the thermodynamically exact expressions derived previously:

$$V = V_0 + V_{ph} = V_0 + 3R\left[\frac{3}{8} + \frac{D(z)}{z}\right]\left(\frac{\partial\theta}{\partial P}\right)_T, \quad (8)$$

$$K = K_0 + K_{ph} = K_0 + \frac{3R}{V}\left\{\frac{3}{8}\gamma_\theta^*\theta - T[\gamma_\theta^2 C_{VR}(z) - \gamma_\theta^* D(z)]\right\}. \quad (9)$$

In (8) and (9), V_0 and K_0 are the initial molar volume and bulk modulus extrapolated to $T = 0$; V_{ph} and K_{ph} are the phonon (lattice) contributions to related quantities; $z = \theta/T$; and $D(z)$ and $C_{VR}(z)$ are the tabulated Debye functions and the Debye heat capacity at constant volume normalized to unity. The baric isothermal derivative of the Debye temperature in (9) can be expressed through γ_θ by means of the well-known thermodynamic relationships [1]:

$$\left(\frac{\partial\theta}{\partial P}\right)_T = -\frac{\theta}{K}\gamma_\theta. \quad (10)$$

Eventually, we will arrive at a consistent set of expressions that relate the thermodynamic parameters V, K, σ, θ, γ_θ, and γ_θ^* to each other. Next, one may devise an iterative scheme to find consistent values of these parameters in a sufficiently wide temperature range by the method of successive approximations and determine the temperature dependences of γ_θ and γ_θ^*.

(3) Omitting simple mathematical manipulations based on (2) and (3), we write averaging expressions for γ_θ and γ_θ^*:

$$\begin{cases} \gamma_\theta = \dfrac{\gamma_{\theta l}/\theta_l^3 + 2\gamma_{\theta t}/\theta_t^3}{1/\theta_l^3 + 2/\theta_t^3}, \\ \gamma_\theta^* = \dfrac{\gamma_{\theta l}^*/\theta_l^3 + 2\gamma_{\theta t}^*/\theta_t^3}{1/\theta_l^3 + 2/\theta_t^3}. \end{cases} \quad (11)$$

With (6)–(10), it is easy to obtain a set of four expressions for $\gamma_{\theta l}$, $\gamma_{\theta t}$, $\gamma_{\theta l}^*$, and $\gamma_{\theta t}^*$:

$$\begin{cases} \gamma_{\theta i} = \dfrac{1}{2}\gamma_{\Xi i} + \dfrac{1}{2}\gamma_K + \dfrac{1}{6}, \\ \gamma_{\theta i}^* = -\dfrac{1}{4}(\gamma_{\Xi i} - \gamma_K)^2 + \dfrac{1}{6}(\gamma_{\Xi i} + \gamma_K) \\ \quad + \dfrac{1}{2}(\gamma_{\Xi i}^* + \gamma_K^*) - \dfrac{5}{36}; \quad i = l, t. \end{cases} \quad (12)$$

Omitting mathematical manipulations again, we write the basic relationships for $\gamma_{\Xi l}$ and $\gamma_{\Xi t}$:

$$\begin{cases} \gamma_{\Xi l} = -\dfrac{2}{(1+\sigma)(1-\sigma)}\gamma_\sigma, \\ \gamma_{\Xi t} = -\dfrac{3}{(1+\sigma)(1-2\sigma)}\gamma_\sigma, \end{cases} \quad (13)$$

for $\gamma_{\Xi l}^*$ and $\gamma_{\Xi t}^*$:

$$\begin{cases} \gamma_{\Xi l}^* = -\dfrac{2\sigma}{(1+\sigma)^2(1-\sigma)}[2\sigma\gamma_\sigma^2 - (1+\sigma)\gamma_\sigma^*], \\ \gamma_{\Xi t}^* = -\dfrac{3\sigma}{(1+\sigma)^2(1-2\sigma)}[2\sigma\gamma_\sigma^2 - (1+\sigma)\gamma_\sigma^*], \end{cases} \tag{14}$$

and for γ_K:

$$\gamma_K = \frac{\gamma_{K0}K_0 + \gamma_{K\mathrm{ph}}K_{\mathrm{ph}}}{K_0 + K_{\mathrm{ph}}}. \tag{15}$$

Finally, the parameter $\gamma_{K\mathrm{ph}}$ is given by the awkward expression

$$\gamma_{K\mathrm{ph}} + 1 = \frac{3PT}{V}\left\{\left[\left(\frac{3}{8} + D'(z)\right)\gamma_\theta^* - \gamma_\theta^2 C'_{VR}(z)\right]z\gamma_\theta + \left[\frac{3}{8} + \frac{D(z)}{z}\right](2\gamma_\theta^* - \gamma_\theta\gamma_\theta^* + \gamma_\theta^{**}) - 2\gamma_\theta C_{VR}(z)(\gamma_\theta + \gamma_\theta^* - \gamma_\theta^2)\right\}. \tag{16}$$

Here, the prime means differentiation in respect to the argument

$$\gamma_\theta^{**} = \frac{V^3}{\theta}\left(\frac{\partial^3\theta}{\partial V^3}\right)_T.$$

Thus, expressions (12)–(16), together with (3)–(5), (8), and (9), completely determine the temperature dependence of the Grüneisen parameters γ_θ and γ_θ^*. In the iterative process, the parameters σ, γ_σ, γ_σ^*, γ_{K_0}, and γ_θ^{**} may be used as variable material constants if experimental data for them are absent. Such data may be found, e.g., for σ or γ_{K_0}. The latter parameter depends on the baric derivative of the bulk modulus and in principle can be measured. It is seen from the above relationships that the temperature dependence of the Grüneisen parameters γ_θ is specified largely by the temperature dependences of the thermodynamic quantities K_{ph} and $\gamma_{K\mathrm{ph}}$.

Expression (12) clarifies the thermodynamic conditions under which the usually negative Grüneisen parameter γ_θ changes sign subsequent to $\gamma_{\theta l}$ and $\gamma_{\theta t}$; namely,

$$\gamma_{\Xi l} + \gamma_K = -\frac{1}{3}$$

and/or

$$\gamma_{\Xi t} + \gamma_K = -\frac{1}{3}.$$

More detailed calculations (for example, the calculation of γ_θ^{**}) can be made following the same scheme; however, they seem to be unjustified in the light of the experimental accuracy.

The results of this work can be summarized as follows. A set of generalized Grüneisen parameters γ_i that are convenient in applied computations is introduced. As far as we know, the thermodynamically exact temperature dependences of the Grüneisen parameters γ_θ and γ_θ^* for a nonmetallic isotropic paramagnetic solid are derived for the first time. The main reasons for the temperature dependences of γ_θ and γ_θ^* are established correctly in terms of thermodynamics. Thermodynamic conditions under which the parameter γ_θ changes sign and, accordingly, a nonmetallic isotropic paramagnet acquires the Invar properties are established.

REFERENCES

1. L. D. Landau and E. M. Lifshitz, *Course of Theoretical Physics*, Vol. 5: *Statistical Physics* (Nauka, Moscow, 1976; Pergamon, Oxford, 1980), Part 1.
2. S. I. Novikova, *Thermal Expansion of Solids* (Nauka, Moscow, 1974).
3. V. Yu. Bodryakov, A. A. Povzner, and O. G. Zelyukova, Fiz. Tverd. Tela (St. Petersburg) **40**, 1581 (1998) [Phys. Solid State **40**, 1433 (1998)].
4. V. Yu. Bodryakov, A. A. Povzner, and O. G. Zelyukova, Metally, No. 2, 79 (2000).
5. V. Yu. Bodryakov, V. V. Petrushkin, and A. A. Povzner, Fiz. Met. Metalloved. **89** (4), 5 (2000).
6. V. Yu. Bodryakov and A. A. Povzner, Fiz. Met. Metalloved. **89** (6), 21 (2000).
7. L. D. Landau and E. M. Lifshitz, *Course of Theoretical Physics*, Vol. 7: *Theory of Elasticity* (Nauka, Moscow, 1987; Pergamon, New York, 1986).

Translated by V. Isaakyan

Technical Physics, Vol. 48, No. 7, 2003, pp. 934–937. Translated from Zhurnal Tekhnicheskoĭ Fiziki, Vol. 73, No. 7, 2003, pp. 139–142.

BRIEF COMMUNICATIONS

Closed Geodesics on Part of a Toral Surface

S. S. Romanov

Kharkov Institute of Physics and Technology, Ukrainian Scientific Center, Akademicheskaya ul. 1, Kharkov, 61108 Ukraine

Received January 9, 2003

Abstract—Geodesics in that part of a toroidal manifold containing the major equator of a torus are studied. The local and global properties of the geodesics are analyzed by taking the integrals along them. Maximal geodesics are used to construct closed trajectories that have integer global invariants. © *2003 MAIK "Nauka/Interperiodica".*

INTRODUCTION

Any information on trajectories is useful for motion control. In low-energy physics, electromagnetic interactions play a central part. The direction and focusing of particles with a magnetic moment can be varied with a magnetic field. Such an approach has long been used to advantage in the physics of atomic beams and has been recently suggested for neutron beams [1].

Neutrons are accumulated more readily if the magnetic field is configured into a torus. In a torus, the allowable energy of trapped neutrons is higher than in a sphere. No barrier is encountered by incoming neutrons if they move in a trap over a limited surface area [2]. In the absence of external forces, the neutrons naturally follow geodesics. In the case of a toroidal manifold, maximal geodesics are not all defined on the entire manifold. Therefore, the toral surface on the set R^3 is geodesically incomplete. Geodesics are characterized by local and global invariants. A relationship between global invariants along geodesics on toroidal manifolds has been found in [3, 4].

In this work, equations for geodesic trajectories on limited toroidal manifolds are derived.

CLAIRAUT INTEGRAL

A set of differential equations for geodesics [5] include two integrals. In the toroidal coordinate system η, ϕ, θ, the first integral, Clairaut integral has the form [6]

$$\sin\alpha = h(\cosh\eta_0 - \cos\phi),$$

where h is a constant along a geodesic γ on a torus $\eta = \eta_0$ (Clairaut constant).

The angle α between the geodesic and meridian of the torus varies within the closed interval $\alpha \in [0, \pi/2]$. If the right of the Clairaut integral exceeds unity, the geodesic is situated within a limited part of the toroidal manifold. The upper bounds of h for several values of ϕ are listed in the table.

Note that a geodesic path may wind around the azimuth axis of a torus, crossing the major and minor equators, only if $h < (\cosh\eta_0 + 1)^{-1}$. The equation for a geodesic for this case is given in [4]. This geodesic is maximal on the entire toroidal manifold [7] and is defined on the whole set R^3. For other h, geodesics are located on part of the toroidal manifold and, if closed, may be only piecewise smooth.

With $h \le (\tanh\eta_0 \sinh\eta_0)^{-1}$, geodesics are placed in the convex part of the manifold and cross the major equator of the torus.

The Clairaut integral establishes a local relationship between the properties of geodesics.

ANALYSIS OF THE SECOND INTEGRAL

Let us derive equations for maximal geodesic paths that are defined on a limited toroidal manifold.

The relationship between the surface coordinates of geodesics has the integral form [4]

$$\theta(\phi) = \int \frac{h(\cosh\eta_0 - \cos\phi)d\phi}{\sinh\eta_0\sqrt{1 - h^2(\cosh\eta_0 - \cos\phi)^2}}.$$

When considering trajectories that either densely cover the manifold R^2 or are periodic, we must stay in the real vector space R. In this case, geodesics described by these two integrals are smooth paths without self-intersections and nodes.

Table

φ	h
0	$(\cosh\eta_0 - 1)^{-1}$
$\arccos(1/\cosh\eta_0)$	$(\tan\eta_0\sinh\eta_0)^{-1}$
$\pi/2$	$(\cosh\eta_0)^{-1}$
π	$(\cosh\eta_0 + 1)^{-1}$

1063-7842/03/4807-0934$24.00

For further analysis of the second integral, it is convenient to introduce a new variable $x = \tan(\phi/2)$. Then, the integral can be represented as the sum of two terms:

$$\theta(x) = 2h\frac{\cosh\eta + 1}{\sinh\eta}(A_1 + A_2).$$

Hereafter, the subscript 0 by η is omitted; however, it is assumed that we are in the set R^2. The integrand of the first term

$$A_1 = \int \frac{\{1 - h(\cosh\eta - 1) + [1 - h(\cosh\eta + 1)]x^2\}^{-1/2}}{\sqrt{1 + h(\cosh\eta - 1) + [1 + h(\cosh\eta + 1)]x^2}}dx$$

is the product of two factors. The expression under the radical sign in the first factor vanishes when the Clairaut constant exceeds $(\cosh\eta + 1)^{-1}$. Therefore, h decreases with increasing ϕ (see table). The second factor does not vanish.

The second term

$$A_2 = -\frac{2}{\cosh\eta + 1}$$

$$\times \int \frac{\{1 - h(\cosh\eta - 1) + [1 - h(\cosh\eta + 1)]x^2\}^{-1/2}}{(1 + x^2)\sqrt{1 + h(\cosh\eta - 1) + [1 + h(\cosh\eta + 1)]x^2}}dx$$

does not add any singularities.

With $h = (\cosh\eta - 1)^{-1}$, the major equator of the torus is a geodesic.

When $h = (\tanh\eta\sinh\eta)^{-1}$, the first term

$$A_1 = \frac{(\cosh\eta + 1)^{-1/2}\sinh^2\eta}{\sqrt{2\cosh^2\eta + \cosh\eta - 1}}$$

$$\times \int \frac{\left(\frac{\cosh\eta - 1}{\cosh\eta + 1} - x^2\right)^{-1/2}dx}{\sqrt{\frac{2\cosh^2\eta - \cosh\eta - 1}{2\cosh^2\eta + \cosh\eta - 1} + x^2}}$$

$$= \frac{\sinh\eta}{2\sqrt{\cosh\eta}}(K(k) - F(\varphi, k))$$

is expressed through the elliptic integral $K(k)$ and the elliptic function $F(\varphi, k)$. The squared magnitude of the latter is

$$k^2 = \frac{2\cosh^2\eta + \cosh\eta - 1}{4(\cosh\eta + 1)\cosh\eta},$$

and the argument of the elliptic function is

$$\varphi = \arccos\left(\sqrt{\frac{\cosh\eta + 1}{\cosh\eta - 1}}x\right).$$

The second term can be recast as

$$A_2 = -\frac{2(\cosh\eta + 1)^{-3/2}\sinh^2\eta}{\sqrt{2\cosh^2\eta + \cosh\eta - 1}}$$

$$\times \int \frac{\left(\frac{\cosh\eta - 1}{\cosh\eta + 1} - x^2\right)^{-1/2}dx}{(1 + x^2)\sqrt{\frac{2\cosh^2\eta - \cosh\eta - 1}{2\cosh^2\eta + \cosh\eta - 1} + x^2}}.$$

It does not have any singularities, unlike the first term. The effect of the third factor on A_2 can be estimated asymptotically. The calculation result is

$$A_2 \approx -\frac{\sqrt{2}(\cosh\eta + 1)^{-1}\sinh^2\eta}{\sqrt{(2\cosh^2\eta + \cosh\eta - 1)\cosh\eta}}$$

$$\times \arctan\left(\sqrt{\frac{2\cosh\eta}{\cosh\eta - 1 - (\cosh\eta + 1)x^2}}x\right).$$

With $h = (\tanh\eta\sinh\eta)^{-1}$, the geodesic path runs between the upper and lower parabolic lines of the torus,

$$\theta(\phi) \cong \frac{\sqrt{\cosh\eta}}{\sinh^2\eta}\Bigg((\cosh\eta + 1)$$

$$\times\left(1 - \frac{2}{\pi}\arctan\sqrt{2\frac{\cosh\eta - \cos\phi}{(\cosh\eta + 1)(1 - \cos\phi)}}\right)K(k)$$

$$-\frac{2\sqrt{2}\sinh\eta}{\sqrt{2\cosh^2\eta + \cosh\eta - 1}}\arctan\sqrt{\frac{(1 - \cos\phi)\cosh\eta}{\cosh\eta\cos\phi - 1}}\Bigg),$$

and crosses the major equator of the torus.

Another case where a maximal geodesic path is defined on a limited toroidal manifold is $h = (\cosh\eta)^{-1}$. The domain of definition for the trajectory is bounded by the upper ($\phi = \pi/2$) and lower ($\phi = -\pi/2$) parallels and covers the major equator of the torus.

The terms of the second integral,

$$A_1 = \frac{\cosh\eta}{\sqrt{2\cosh\eta + 1}}\int \frac{dx}{\sqrt{1 - x^2}\sqrt{\frac{2\cosh\eta - 1}{2\cosh\eta + 1} + x^2}},$$

$$A_2 = -\frac{2(\cosh\eta + 1)^{-1}\cosh\eta}{\sqrt{2\cosh\eta + 1}}$$

$$\times \int \frac{dx}{(1 + x^2)\sqrt{1 - x^2}\sqrt{\frac{2\cosh\eta - 1}{2\cosh\eta + 1} + x^2}},$$

have singularities at the points $x = \pm 1$.

The maximal geodesic

$$\theta(\phi) \cong \frac{1}{\sinh\eta}\left(\frac{\cosh\eta + 1}{\sqrt{\cosh\eta}}\left(1 - \frac{2}{\pi}\arctan\sqrt{\frac{2\cos\phi}{1-\cos\phi}}\right)K(k_0)\right.$$
$$\left. - \frac{2\sqrt{2}}{\sqrt{2\cosh\eta - 1}}\arctan\sqrt{\frac{1-\cos\phi}{\cos\phi}}\right)$$

touches the upper parallel from the side of smaller ϕ and the lower parallel from the side of larger ϕ. The elliptic integral magnitude squared is in this case

$$k_0^2 = \frac{2\cosh\eta + 1}{4\cosh\eta}.$$

This trajectory does not have singularities along the parabolic lines of the torus.

Both trajectories densely cover a part of the toroidal manifold when the initial values of the surface coordinates vary continuously [8].

CLOSED GEODESICS

Let us construct an equation of closed trajectory based on the expressions for maximal geodesics. The curves discussed above are smooth, except for the vicinities of the points of contact. According to the Darboux theorem [9], the necessary and sufficient condition for the closeness of all toroidal-metric geodesics is the fulfillment of the equality

$$\int_{i(h)} \frac{h(\cosh\eta - \cos\phi)d\phi}{\sinh\eta\sqrt{1 - h^2(\cosh\eta - \cos\phi)^2}} = \frac{p(i)}{q(i)}\pi$$

for all i (p and q are integers). Any geodesic γ consists of $2q$ geodesic segments between the points of contact with the parallels.

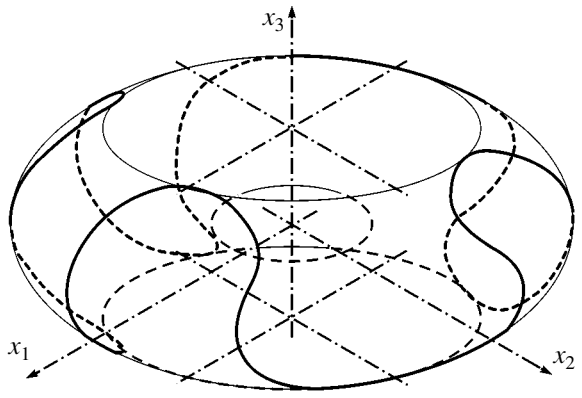

Fig. 1. Toroidal geodesic with $p = 1$, $q = 4$, and $i = \arccos(1/\cosh\eta)$. For this torus, the aspect ratio is slightly above unity ($\cosh\eta = 3/2$). Dashed line, the invisible part of the geodesic; continuous line, a segment of the geodesic lying on the most distant (from the center) part of the toroidal surface.

The geodesic rounds the torus axis p times. The limits of integration $i(h)$ depend on the normalization of the Clairaut constant.

With $h = (\tanh\eta\ \sinh\eta)^{-1}$, a geodesic lies between the parallels $i = \pm\arccos(1/\cosh\eta)$, which are the parabolic lines of the torus.

A geodesic is closed if and only if the condition

$$\theta\left(\frac{\pi}{2}\right) = \frac{2\sqrt{\cosh\eta}}{\sinh^2\eta}\left((\cosh\eta + 1)\right.$$
$$\times\left(1 - \frac{2}{\pi}\arctan\sqrt{\cosh\eta}\right)K(k)$$
$$\left. - \frac{\sqrt{2}\pi\sinh\eta}{\sqrt{2\cosh^2\eta + \cosh\eta - 1}}\right) = \frac{p}{q}\pi$$

is met for a certain rational p/q.

When $h = (\tanh\eta\ \sinh\eta)^{-1}$, the equation of geodesic paths

$$\varepsilon_1\theta(\phi) \cong \frac{\varepsilon\sqrt{\cosh\eta}}{\sinh^2\eta}\left((\cosh\eta + 1)\right.$$
$$\times\left(1 - \frac{2}{\pi}\arctan\sqrt{\frac{2(\cosh\eta - \cos\phi)}{(\cosh\eta + 1)(1-\cos\phi)}}\right)K(k)$$
$$\left. - \frac{2\sqrt{2}\sinh\eta}{\sqrt{2\cosh^2\eta + \cosh\eta - 1}}\arctan\sqrt{\frac{(1-\cos\phi)\cosh\eta}{\cosh\eta\cos\phi - 1}}\right)$$

consists of piecewise maximal geodesics that are continuous curves. The sign of $\varepsilon_1 = \pm 1$ specifies the orientation of a geodesic.

The sign of $\varepsilon = \pm 1$ is fixed within the segment between $i = \arccos(1/\cosh\eta)$ and $i = -\arccos(1/\cosh\eta)$ and changes each time i takes the value $\arccos(1/\cosh\eta)$ or $-\arccos(1/\cosh\eta)$.

Figure 1 shows a three-dimensional piecewise maximal closed trajectory between the parabolic lines of the torus for $p = 1$, $q = 4$, and the scale factor $c = 15\sqrt{5}$. The upper and lower parallels touched by the trajectory are shown.

When $h = (\cosh\eta)^{-1}$, the angle $\theta(\pi/2)$ between two successive points of contact with extreme parallels is

$$\theta\left(\frac{\pi}{2}\right) \cong \varepsilon_1\frac{\varepsilon}{\sinh\eta}\left(\frac{\cosh\eta + 1}{\sqrt{\sinh\eta}}K(k_0) - \frac{\sqrt{2}\pi}{\sqrt{2\cosh\eta - 1}}\right).$$

The closeness condition for a trajectory turning around the torus axis p times and consisting of $2q$ geo-

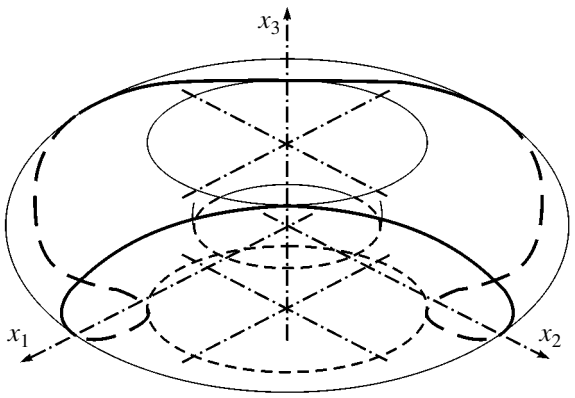

Fig. 2. Geodesic trajectory turns around the torus axis once ($p = 1$) and consists of four geodesic segments ($q = 2$). The torus is relatively thick ($\cosh\eta = 3/2$) The parallels that are in contact with the geodesic are positioned at $i = \pm\pi/2$.

desic segments is given by

$$\varepsilon_1\varepsilon\theta(\pi/2) = \frac{p}{q}\pi.$$

A closed trajectory consisting of piecewise maximal geodesics,

$$\varepsilon_1\theta(\phi) \cong \frac{\varepsilon}{\sinh\eta}\left(\frac{\cosh\eta + 1}{\sqrt{\cosh\eta}}\left(1 - \frac{2}{\pi}\arctan\sqrt{\frac{2\cos\phi}{1-\cos\phi}}\right)K(k_0)\right.$$
$$\left. - \frac{2\sqrt{2}}{\sqrt{2\cosh\eta - 1}}\arctan\sqrt{\frac{1-\cos\phi}{\cos\phi}}\right)$$

runs between the parallels $\phi = \pm\pi/2$ and covers the major equator of the torus (see Fig. 2).

CONCLUSIONS

(1) A toroidal manifold is a widely met natural physical object of investigation.

(2) Geodesic trajectories on a limited toroidal manifold open up fresh opportunities for particle trapping.

(3) The first (Clairaut) integral allows one to discriminate between the situations where a geodesic is maximal and when it is placed on a part of the toral surface.

(4) Singularities of the second integral in the geodesic equation mean that a geodesic is located on a limited part of a toroidal manifold.

(5) Singularities of the second integral specify the positions of the extreme parallels of the torus that are in contact with a geodesic.

(6) A closed trajectory has global invariants: p, the number of turns about the torus axis to closure, and $2q$, the number of geodesic segments.

(7) A closed geodesic is a piecewise smooth curve without self-intersections and nodes.

REFERENCES

1. K.-J. Kugler, W. Paul, and U. Trinks, Phys. Lett. B **72B**, 422 (1978).
2. V. Paul', Usp. Fiz. Nauk **160** (12), 109 (1990).
3. S. S. Romanov, Dokl. Akad. Nauk Ukr., No. 9, 84 (2001).
4. S. S. Romanov, in *Collection of Scientific Works* (Inst. Nucl. Res., Moscow, 2001), Vol. 4, p. 169.
5. S. P. Finikov, *Course of Differential Geometry* (GITTL, Moscow, 1952).
6. E. W. Hobson, *The Theory of Spherical and Ellipsoidal Harmonics* (Cambridge University, Cambridge, 1931; Inostrannaya Literatura, Moscow, 1952).
7. J. A. Thorpe, *Elementary Topics in Differential Geometry* (Springer, New York, 1979; Mir, Moscow, 1982).
8. J. Palis, Jr. and Welington de Melo, *Geometric Theory of Dynamic Systems* (New York, 1982).
9. A. Besse, *Manifolds: All of Whose Geodesics are Closed* (Springer-Verlag, Heidelberg, 1978; Mir, Moscow, 1981).

Translated by V. Isaakyan